

**A STUDY ON HIGH TEMPERATURE PHASE STABILITY
AND PHASE TRANSFORMATION CHARACTERISTICS IN
Ti-Ta AND Ti-Ta-Nb ALLOYS USING CALORIMETRY AND
MICROSCOPY TECHNIQUES**

By

MADHUSMITA BEHERA

Enrolment No: CHEM02200704012

*Microscopy and Thermophysical Properties Division
Physical Metallurgy Group
Metallurgy and Materials Group
Indira Gandhi Centre for Atomic Research
Kalpakkam, Tamil Nadu, India, 603 102*

*A thesis submitted to the
Board of Studies in Chemical Sciences
In partial fulfillment of requirements
For the Degree of*

DOCTOR OF PHILOSOPHY

of

HOMI BHABHA NATIONAL INSTITUTE



November, 2012

Homi Bhabha National Institute

Recommendations of the Viva Voce Board

As members of the Viva Voce Board, we certify that we have read the dissertation prepared by **Madhusmita Behera** entitled "A study on high temperature phase stability and phase transformation characteristics in Ti-Ta and Ti-Ta-Nb alloys using calorimetry and microscopy techniques" and recommend that it may be accepted as fulfilling the dissertation requirement for the Degree of Doctor of Philosophy.

K. Nagarajan Date: 23/4/13
Chairman- Dr. K. Nagarajan

S. Sai Date: 23/04/2013
Convener- Dr. Saroja Saibaba

B. S. Murthy Date: 23/4/13
External Examiner-Prof. B. S. Murthy

M. Vijayalakshmi Date: 23.4.13
Member 1 - Dr. M. Vijayalakshmi

Mallika Date: 23.04.13
Member 2 - Dr. C. Mallika

S. Raju Date: 23/04/13
Technology Advisor - Mr. S. Raju

Final approval and acceptance of this dissertation is contingent upon the candidate's submission of the final copies of the dissertation to HBNI.

I hereby certify that I have read this dissertation prepared under my direction and recommend that it may be accepted as fulfilling the dissertation requirement.

Date: April 23, 2013

Place: KALPAKKAM

STATEMENT BY AUTHOR

This dissertation has been submitted in partial fulfillment of requirements for an advanced degree at Homi Bhabha National Institute (HBNI) and is deposited in the Library to be made available to borrowers under rules of the HBNI.

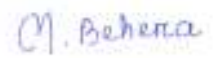
Brief quotations from this dissertation are allowable without special permission, provided that accurate acknowledgement of source is made. Requests for permission for extended quotation from or reproduction of this manuscript in whole or in part may be granted by the Competent Authority of HBNI when in his or her judgment the proposed use of the material is in the interests of scholarship. In all other instances, however, permission must be obtained from the author.

M. Behera

Madhusmita Behera

DECLARATION

I, hereby declare that the investigation presented in the thesis has been carried out by me. The work is original and has not been submitted earlier as a whole or in part for a degree/diploma at this or any other Institution/University.



Madhusmita Behera

This thesis is dedicated to

My Parents

ACKNOWLEDGEMENTS

At the outset, I would like to express my whole hearted and deep sense of gratitude to my supervisor **Prof. (Dr.) Saroja Saibaba** and technology advisor **Mr. S. Raju** IGCAR for their guidance, help and encouragement throughout my research work. I greatly admire their dedication or interest towards research, creative thinking, hard work and dedication in work. These are the great source of inspiration for me in all my endeavours. I am highly grateful to them for patiently checking all my manuscripts and thesis. This thesis would not have been possible without their bounteous effort. More than supervisor, Prof. (Dr.) Saroja Saibaba is my mentor for shaping my personal and professional life, without whom I would not have been in this position. Her helps are immeasurable. I owe my profound gratitude to **Prof. (Dr.) Saroja Saibaba** for her supports in all spheres. **Mr. S. Raju's** constant guidance, constructive discussions on day to day basis and his whole-hearted involvement in the project has helped me to carry out my research work smoothly.

I would like to thank **Dr. R. Mythili**, SO/F, PMG, IGCAR for her constant help in carrying out the work using microscopy and useful discussions at the need.

My heartfelt thank to Shri. L. Meenakshi Sundaram, for his continuous help in melting the alloys for my research work. I am extremely thankful to Dr. N. V. Chandrasekhar and Dr. P. C. Sahu for providing access to their melting facilities of their laboratory. I am also thankful to Dr. G. Paneerselvam, SO/E, Fuel Chemistry Group, RCL, IGCAR for helping me in XRD characterization.

I am grateful to my doctoral committee chairman Dr. K. Nagarajan and members Dr. M. Vijayalakshmi and Dr. C. Mallika for their punctilious evaluation of the progress of my research work and valuable suggestions.

My sincere thanks to Dr. T. Jayakumar, Director, MMG, IGCAR, Shri S. C. Chetal, Director, IGCAR and Dr. Baldev Raj, former Director, IGCAR for their support and for providing the research facilities in the centre for carrying out this research work.

I would like to express my sincere gratitude to Dr. B. Jeya Ganesh for his kind help in carrying out the experimental work as well as for making me learn to analyze the result. Besides, I am grateful to him for his moral support at difficult situations without which it is impossible for me to reach at this stage of my research carrier.

I wish to thank Mr. Arun Kumar Rai, SO/D, MTPD, PMG, IGCAR, Mrs. A. Josephine Prabha, Assistant Professor, Bishop Heber College, Tiruchirapalli, and Mr.

Harapasanna Tripathy, SO/C, MTPD, PMG, IGCAR for their timely help in the laboratory and useful discussions. Also I am thankful to Mr. Raj Narayan Hajra and N. Vijayashanthi for their moral support during this period.

My sincere thanks to Dr. Arup Das Gupta, SO/F, Mr. V. Thomas Paul, SO/E, and Thirumurugesan, SA/E of PMD, for providing sample cutting and mounting facilities in PMG. I would also thank to Mr Pradyumna Kumar Parida SO/C and Mr. Chanchal Ghosh SO/D to teach me the Transmission Electron Microscopy sample preparation methods. I thank to Dr. R. Anand and Mr. Ravi Kirana for their technical support. laboratory. I would also like to thank all other PMG members for their support during the course of research work.

I would like to thank Dr. M. Saibaba, Associate Director, Resource Management Group for providing me a comfortable stay at Research Scholar enclave.

I would also like to thank Department of Science and Technology (DST) and Homi Bhabha National Institute for the financial support to attend an international conference (19th ECTP) in Greece during my research period.

I am grateful for the financial support provided by the Department of Atomic Energy research fellowship scheme from Indira Gandhi Centre for Atomic Research for the duration of the work.

My affectionate thanks to my special friends Subhra, Bishnu, Suranjan, Nithila, Sudeepta, Sulata, and Sanatan Maharana and his family who have given me a family like environment during my stay in Kalpakkam. I would like to thank Dr. Nilamadhab Padhy, Maneesha, Pradeep, Pravati, Rajini, Prasanna, Alok, Girish, Kuheli, who have helped me in various ways during my stay.

I would like to thank my parents for their unconditional support and encouragement throughout my academic career which made me to come up in my life. In particular, the patience and understanding shown by my parents and brothers during my Ph.D is greatly appreciated. Last but not least, thanks be to God for my life through all tests in the past six years. You have made my life more bountiful. May your name be exalted, honoured, and glorified.

CONTENTS

	Page No.
Synopsis	vi
List of figures	xiv
List of tables	xxii
List of abbreviations	xxiv
CHAPTER 1 INTRODUCTION	1
1.1 Genesis of Titanium Era	2
1.2 Titanium & Alloys: Basic Characteristics	2
1.3 Role of Phase Transformation in Microstructure Design	3
1.4 Necessity of Basic Research on Phase Stability & Related Issues on Ti-Ta and Ti-Ta-Nb alloys	12
1.5 Phase Equilibria of Ti alloys: Further details	13
1.5.1 α -Alloys	13
1.5.2 $\alpha+\beta$ -Alloys	14
1.5.3 β -Alloys	15
1.6 Classification of phase transformation in Titanium alloys	16
1.6.1 Diffusional transformation	17
1.6.2 Displacive transformation	18
1.7 Ti-Ta binary system	20
1.8 Organization of the Thesis	25
References	28
CHAPTER 2 EXPERIMENTAL METHODS	33
2.1 Introduction	34
2.2 Organization of the chapter	34
2.3 Alloy preparation	35
2.4 Specimen preparation	37
2.5 Primary experimental techniques	37
2.5.1 Basic principle of calorimetry	37
2.5.2 Classification of calorimeters	38

2.6	Drop Calorimeter	39
2.6.1	General principle	39
2.6.2	Inverse Drop Calorimeter	41
2.6.2.1	High temperature furnace	42
2.6.2.2	Multi-sample introducer and the drop tube	42
2.6.2.3	Measurement head	42
2.6.2.4	Gas, Vacuum, Chill-water Circuit Controller	43
2.6.2.5	Experimental procedure	43
2.6.3	Calibration of the drop experiment	46
2.6.4	Estimation of enthalpy	47
2.6.5	Limitation of drop calorimeter	48
2.7	Differential Scanning Calorimetry (DSC)	48
2.7.1	General principle	48
2.7.2	High temperature furnace	49
2.7.3	DSC probe	49
2.7.4	Vacuum pump, Gas circuit, Chill-water cooling circuit	51
2.7.5	Mass flow controller	51
2.7.6	Experimental procedure	51
2.7.7	Determination of phase transformation temperature	53
2.7.8	Determination of phase transformation enthalpy	54
2.7.9	Temperature calibration in DSC	55
2.8	Microstructural characterization	56
2.8.1	X-ray diffraction study: Identification of phases	56
2.8.2	Optical Microscopy	57
2.8.3	Scanning Electron Microscopy (SEM)	57
2.8.4	Transmission Electron Microscopy	57
2.8.5	Analysis of microstructural parameters	58
2.8.6	Phase analysis using electron diffraction pattern	58

2.8.7	Analysis of composition	59
2.8.8	Microhardness measurements	60
	References	61
CHAPTER 3	MEASUREMENT OF	63
	THERMODYNAMIC PROPERTIES OF	
	Ti-xTa (x = 5, 10, 15, 20 mass %) ALLOYS	
	USING DROP CALORIMETRY	
3.1	Introduction	64
3.2	Organization of the chapter	64
3.3	Brief description of Ti-Ta binary system	65
3.4	Structural and microstructural characterization of the starting material	66
3.5	Enthalpy increment ($H_T - H_{298.15}$) measurement	73
3.5.1	Enthalpy increment data for Ti-5mass% Ta alloy	73
3.5.2	Enthalpy increment data for Ti-10, 15, 20 mass% Ta alloys	75
3.6	Microstructural evolution in $\alpha \rightarrow \beta$ transformation zone	78
3.6.1	Microstructural characterization of post drop samples of Ti-5Ta alloy	78
3.6.2	Microstructural characterization of post drop samples of Ti-15Ta alloy	81
3.7	Analytical representation of enthalpy increment $\Delta^{\circ}H(T)$ data for Ti-5Ta alloy	83
3.7.1	$\alpha + \beta$ domain: $463 \leq T \leq 1083$ K	84
3.7.2	$\alpha \rightarrow \beta$ transformation region: $1083 \leq T \leq 1183$ K	84
3.7.2.1	Estimation of $\alpha \rightarrow \beta$ transformation enthalpy	84
3.7.2.2	Model for temperature driven $\alpha \rightarrow \beta$ transformation kinetics	87
3.8	Analytical representation of enthalpy increment $\Delta^{\circ}H(T)$ data for Ti-10, 15, 20 Ta alloy	90
3.9	Theoretical estimate of C_p in low temperature region	97
3.10	Estimation of thermodynamic functions	102
3.11	Conclusions	105

	References	108
CHAPTER 4	STUDY OF PHASE TRANSFORMATION KINETICS IN Ti-xTa (x = 5, 10, 15, 20 mass %) ALLOYS USING DIFFERENTIAL SCANNING CALORIMETRY	110
4.1	Introduction	111
4.2	Organization of the chapter	112
4.3	Structural and microstructural characterization of initial alloy	112
4.4	DSC results: Transformation temperatures and transformation peak profiles	112
4.5	Composite nature of transformation peak profiles	122
4.6	$\alpha+\beta \rightarrow \beta$ Transformation temperatures and transformation enthalpy	129
4.7	Kinetics of $\alpha \leftrightarrow \beta$ phase transformation	134
	4.7.1 Ta diffusion as the rate controlling step	136
	4.7.2 KJMA Modelling of transformation kinetics	139
4.8	Conclusions	152
	References	154
CHAPTER 5	THERMODYNAMICS, KINETICS AND MECHANISM OF PHASE TRANSFORMATION IN Ti-5Ta-1.8Nb ALLOY	157
5.1	Introduction	158
5.2	Organization of the chapter	158
5.3	Structural and microstructural characterization of the starting alloy	159
5.4	Enthalpy Increment ($H_T-H_{298.15}$) variation with temperature	161
5.5	Microstructural changes during $\alpha \rightarrow \beta$ transformation	163
5.6	Analytical representation of enthalpy increment ($H_T-H_{298.15}$) data	166
	5.6.1 α phase: $463 \text{ K} \leq T \leq 1072 \text{ K}$	166
	5.6.2 $\alpha \rightarrow \beta$ transformation region: $1072 \text{ K} \leq T \leq 1156 \text{ K}$	166
	5.6.3 Enthalpy representation in β region: 1156 K	169

	$\leq T \leq 1457 \text{ K.}$	
5.7	Neumann-Kopp approximation for C_p evaluation	169
5.8	Differential Scanning Calorimetry result: Transformation peak profile and transformation temperatures	172
5.9	Kinetics of $\alpha \leftrightarrow \beta$ transformation	177
5.10	Microstructural evolution during $\beta \rightarrow \alpha$ transformation	182
	5.10.1 Microstructural changes during cooling from high temperature β - phase field	182
	5.10.2 Secondary transformation of high temperature β phase on continuous cooling	192
5.11	Conclusion	197
	References	199
CHAPTER 6 SUMMARY AND SCOPE FOR FUTURE WORK		202
6.1	Summary of the work	203
6.2	Scope for future work	205
	Publications	206

SYNOPSIS

1. Motivation

In the world of engineering materials, titanium and its alloys occupy a unique position in that they are extensively used in wide ranging applications, which include, aerospace, chemical, petrochemical, bio-medical and also in some strategic sectors such as processing of radioactive nuclear waste in highly corrosive environments [1]. Such versatility of titanium alloys stems from the synergetic combination of physical, chemical and processing characteristics, the latter being extremely important from the point of view of fabricating advanced engineering components and strong structures that are expected to have good high temperature phase and microstructure stability, adequate corrosion resistance, excellent biocompatibility etc. [2-5]. It is well known in alloy design that successful tailoring of microstructure to suit the desired end application through carefully structured thermomechanical and other processing schedules, depends on the ready availability of reliable and accurate thermo-kinetic database [6, 7]. This is especially true in the case of $\alpha+\beta$ or β alloys of titanium containing refractory transition metals like Nb, Ta, Mo, Zr, Hf etc [8]. The available literature information on Ti-(Nb, Ta, Hf, Zr, W) multi-component systems, although meagre, suggest that these alloys are indeed challenging to process through standard and conventional routes in bulk quantities. Achieving a homogeneous microstructure and preserving through section property uniformity calls for a chemically homogeneous β -phase at the end of solution anneal treatment, which in these alloys is difficult due to sluggish diffusion of refractory solutes. Hence, a thorough understanding of the physical metallurgy, in particular the energetics and kinetics aspects of both diffusional and displacive $\alpha\leftrightarrow\beta$ phase changes is essential for proper engineering of various processing steps like: ingot melting, solution anneal, β -forging which is followed by multi step thermomechanical treatments, before

the desired two phase $\alpha+\beta$ microstructure is realised in the final work piece. From a fundamental physical metallurgy point of view also, a study of $\alpha\leftrightarrow\beta$ phase transformation characteristics is extremely rewarding. It is observed very often that the forward $\alpha\rightarrow\beta$ and the reverse $\beta\rightarrow\alpha$ reactions that take place during heating and cooling cycles respectively exhibit certain interesting kinetic asymmetry that is dictated by composition, cooling rate and the magnitude of stresses present. The intricate interplay between many of these factors contributes to the final and finer details of processing induced microstructure development.

Thus in summary, it may be said that a fundamental investigation on **HIGH TEMPERATURE PHASE STABILITY AND PHASE TRANSFORMATION CHARACTERISTICS**, of Titanium base alloys containing elements like Ta, Nb etc., is relevant and appropriate from both basic and applied contexts.

2. Scope of Present Investigation

For the reasons stated above a fundamental investigation on high temperature thermodynamic and kinetic aspects of phase stability, especially with regard to $\alpha\leftrightarrow\beta$ phase transformation behaviours of Ti-xTa (x= 5, 10, 15 20 mass %) and Ti-5 mass% Ta-1.8 mass % Nb alloys has been undertaken as a part of this thesis. The major experimental techniques that are chosen for this purpose are isothermal drop calorimetry and high temperature differential scanning or dynamic calorimetry, the results of which are supplemented by microstructural characterization of post calorimetry samples. It must also be mentioned that to the best of the candidate's knowledge, there exists virtually very little information on thermodynamic and kinetic aspects of phase change in Ti-Ta (Nb) alloys. In particular, no literature in the past two decades or so could be traced to any calorimetry based characterization of Ti-Ta (Nb) alloys. Thus, it may be stated that the present investigation is aimed at adding some useful input to the existing

thermodynamic property database on titanium alloys [9, 10], which is expected to be of interest to material scientists working towards designing advanced titanium base alloys.

3 Organization of Thesis

The organisation of the thesis is schematically illustrated in Figure 1. The thesis consists of six chapters. *Chapter 1* provides a comprehensive summary of the existing knowledgebase on phase stability and phase transformation issues of titanium base alloys. As this is a vast field, the focus of the present summary is oriented towards highlighting the major advantages of employing calorimetry as the principal technique for investigating the relatively unexplored research themes in the high temperature phase stability of $\alpha+\beta$ titanium alloys. It is described in detail as to how a set of carefully performed and (near) equilibrium isothermal calorimetry measurements on well characterised and calibrated samples, offers the unique advantage of tracing the transformation onset and offset temperatures precisely, and in conjunction with the associated heat or enthalpy effects. In other words, how the experimental determination of thermodynamic quantities such as relative enthalpy or enthalpy increment ($H_T - H_{298.15}$) as measured in the present study by sensitive drop calorimetry technique, in pre-transformation, transformation and post transformation domains can be used to establish the thermodynamics of $\alpha \rightarrow \beta$ phase change, has been described in detail. In particular, the most useful thermodynamic quantities like, $\Delta^{\circ}H_{tr}^{\alpha \rightarrow \beta}$ the enthalpy change due to $\alpha \rightarrow \beta$ transformation, and, $\Delta C_p^{\alpha \rightarrow \beta}$ its specific heat counterpart are determined to ± 5 to 8% accuracy for a few Ti-Ta and Ti-5Ta-1.8Nb compositions. Hence, this chapter presents a brief recapitulation of the essence of various aspects of $\alpha \leftrightarrow \beta$ phase transformation in $\alpha+\beta$ titanium alloys, as viewed from the literature [11, 12]. In brief, the physical metallurgy aspects with a focus on thermodynamic and kinetic aspects of high temperature phase stability forms the subject matter of Chapter 1.

The focus of *Chapter 2* is on the description of experimental methods adopted in this investigation. This is preceded by details with regard to melting of alloys, basic compositional characterization and sample preparation for calorimetry and microscopy investigations, including the details of compositional homogenisation and room temperature phase characterization by x-ray diffraction. However, the major portion of chapter 2 deals with the detailed descriptions of the drop and dynamic calorimetry methods, within the scope of the investigations for which they have been used. Accordingly, the description lays emphasis on the subtle issues involved in the physical and phenomenological interpretation of adopting calorimetry both as an energetic and kinetic tool for characterizing phase transformations. For this purpose, it is necessary to link the interpretation of processed calorimetry signal with physically plausible models of solid state phase changes. The methods of treating the effects of thermal history, starting grain size, holding temperature and time on phase transformation thermal arrests are dealt with in detail in this chapter. In particular, the limitation of adopting standard iso-conversional methods like Kissinger or Ozawa type analysis of dynamic calorimetry data for treating the heterogeneous metallurgical reactions, such as the ones encountered in titanium base alloys is brought out.

The details of data analysis of the temperature dependence of the measured enthalpy increment variation with temperature in the light of models for vibrational heat capacity like Debye or Einstein and the issues involved in the determination of the Debye θ etc. are also dealt with in this chapter. This chapter also contains details of calibration methods adopted in the calorimetry characterization. The determination of error limits for both temperature and heat effects are elucidated with a few standard calibrants.

Chapter 3, presents and discusses in full perspective the drop calorimetry

measurements of enthalpy increment ($H_T - H_{298.15}$) for four Ti-xTa ($x = 5, 10, 15, 20$ mass %) alloys. The temperature range of this study is restricted to 463 – 1257 K, which includes $\alpha+\beta$ two phase field and also the $\alpha+\beta \rightarrow \beta$ phase change. The measured enthalpy variation in the transformation domain is used to obtain the energetic quantities of $\alpha+\beta \rightarrow \beta$ phase change, and this is accomplished by invoking an appropriate description of the diffusional kinetics involved. This modelling has been performed for all the four compositions and a systematic trend for the energetic parameters is explored by combining the present data with limited literature based information on related Ti-base alloys. An interesting systematics implying a homologous character for $\alpha \rightarrow \beta$ phase transformation energetics is obtained in the present study. This is expected to provide an incentive for undertaking further fundamental theoretical studies on understanding phase transitions in $\alpha+\beta$ alloys.

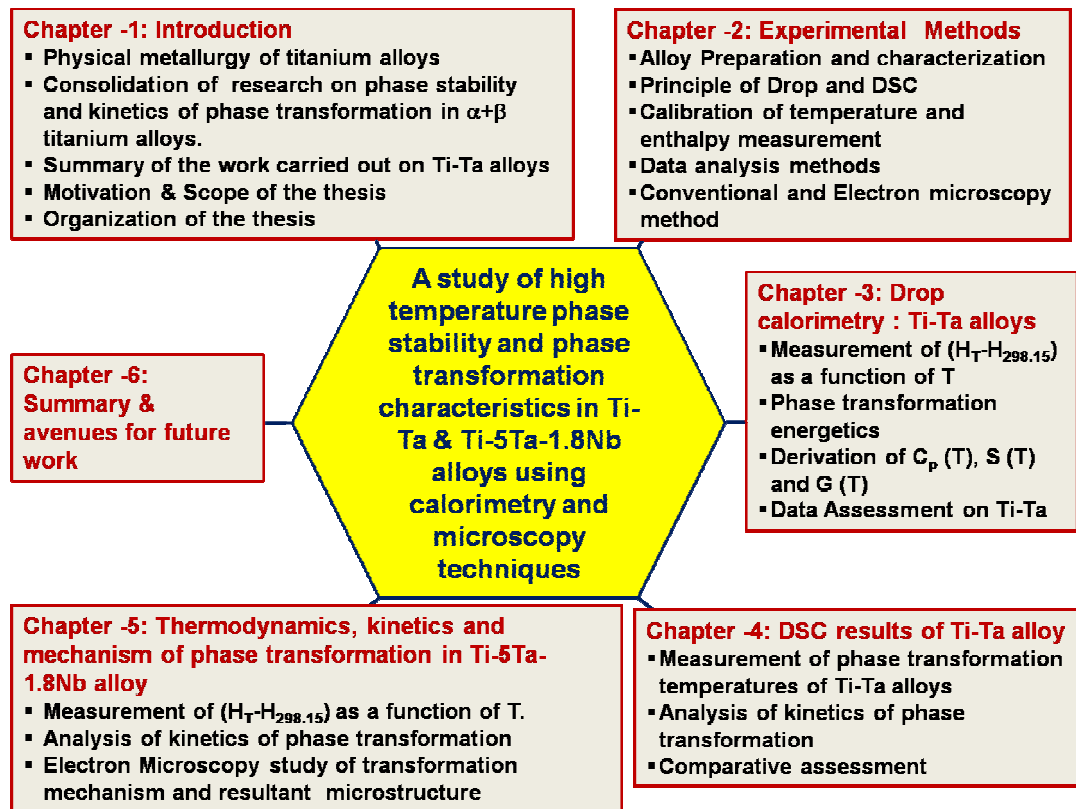


Figure -1 Organization of thesis

Chapter 3 also presents the comprehensive compilation of the critically assessed thermodynamic data for Ti-5, 10, 15 and 20 mass% Ta alloys for the temperature range of 0 – 1273 K. It is important to add that the present high temperature enthalpy measurements have been extensively compared and critically analysed for its smooth compatibility with limited low temperature data, wherever available, so that the desired objective of arriving at a reliable thermodynamic database for at least some alloys in Ti-Ta binary system is facilitated.

Chapter 4 presents the results on kinetics of phase transformation in Ti-5, 10, 15, 20 Ta alloys. Most importantly, this chapter brings out the subtle differences involved in the kinetics of thermally activated $\alpha \rightarrow \beta$ and $\beta \rightarrow \alpha$ transformation, probed using dynamic calorimetric as a function of several scan rates in the range 3-99 K min⁻¹. The pronounced non-linear variation of the $\alpha \rightarrow \beta$ transformation finish temperatures with increasing heating rate and its physical implication in achieving good chemical homogeneity of the high temperature β -phase has been elucidated in terms of the sluggish diffusion of Ta as the principal rate controlling step. On the other hand, the $\beta \rightarrow \alpha$ cooling induced phase change has been shown to be governed by a competition between grain boundary mediated and grain interior prompted heterogeneous nucleation of α . It is suggested that at high cooling rates the higher undercooling achieved can catalyse the grain interior nucleated α , in addition to a small fraction of grain boundary allotriomorphic α . The role of β -grain size as affected by holding temperature and time at the β -phase field has also been taken into account in the modelling scheme of $\beta \rightarrow \alpha$ phase change. An extensive post calorimetry microscopic investigation of transformed microstructures has also been discussed in detail in Chapter 4. The kinetic modelling has been done by adopting a suitable version of Kolmogorov-Johnson-Mehl-Avrami (KJMA) formalism and the estimated kinetic parameters are discussed in the light of

available diffusivity data for transition metals in titanium. Useful data on continuous heating transformation (CHT) and continuous cooling transformation (CCT) have been reported for all the alloys.

Few typical sample results of Chapter 3 and 4 are highlighted in the following table.

S. No.	Ti –5 Ta	Ti–10 Ta	Ti–15 Ta	Ti–20 Ta
T_s/K	1083	1059	1029	991
T_f/K	1183	1168	1154	1144
$\Delta^\circ H_{tr} /J g^{-1}$	66	61	47	25
$\Delta^\circ C_p^r /J kg^{-1} K^{-1}$	667	561	376	161
θ_D / K	366	370	360	348
$\gamma_c /J kg^{-1} K^{-2}$	0.127	0.134	0.141	0.144
$Q_{eff} / kJ mol^{-1}$ (DROP)	284 ± 14	301 ± 15	325 ± 16	336 ± 12
$Q_{eff} / kJ mol^{-1}$ (DSC / $3 K min^{-1}$)	280 ± 5	300 ± 5	325 ± 5	342 ± 8

Chapter 5 presents the results of calorimetry –cum modelling investigation of Ti-5Ta-1.8Nb alloy. The scope of the investigation on Ti-5Ta-1.8Nb is along the same lines of that on Ti-Ta alloys. It is necessary to mention here that the difficulties encountered in interpreting the results of Ti-5Ta-1.8Nb alloy, an alloy developed for a high corrosion resistance application in this laboratory provided the motivation to undertake a systematic investigation on Ti-Ta and Ti-Nb binaries, of which the results on Ti-Ta forms the core of this thesis. Chapter 5 dealing with this ternary alloy also contains the results of electron microscopy characterization of transformation microstructures, to identify the transformation mechanisms as it is expected that metastable transformation products such as ω and or α'' martensites form in this alloy on fast cooling. Hence, it became necessary to perform an electron microscopy characterization of transformation induced microstructure development in Ti-5Ta-

1.8Nb. However, such formation of metastable ω or α'' martensite phases are not reported so far in Ti-Ta alloys up to 20 Ta, for the range of slow cooling rates employed in this study.

Chapter 6 presents the summary of the research findings presented in Chapter 3-5. It is realized that the presented findings have provided a brief insight into the Ti-Ta(Nb) phase equilibria; suggesting that much work remains to be done in identifying the phase stability under non equilibrium conditions. Further, the present results reveal in the light of existing database one major issue, namely that the phase equilibria of Ti-Ta binary system needs to be freshly assessed, especially with new experimental input on high Ta alloy compositions and also with fresh high temperature liquidus data. This calls for more experimental work with higher Ta content alloys. Achieving true thermodynamic equilibrium in Ti-Ta alloys is very difficult, due to sluggish diffusion of Ta. Prolonged annealing is generally required and this results in appreciable grain growth of β -grains, which gives rise to poorly defined thermal arrests for very slow cooling in dynamic calorimetry. Thus there is an inherent experimental difficulty associated with getting equilibrium phase boundary data by dynamic or even static isothermal calorimetry data. It is possible that computational methods may be employed for supplementing the crucial input needed for further conceptual understanding of phase stability in Ti-Ta (Nb) systems.

Chapter 6 is therefore devoted to exploring the further avenues of research which can be profitably continued from what limited data has been accrued in this study.

LIST OF FIGURES

Figure No.	Figure Captions	Page No
Figure 1.1	(a) unit cell of hexagonal closed packed structure for α - phase. (b) unit cell of body centered cubic structure for β - phase. The transition from the low temperature α (hcp) phase to high temperature β (bcc) phase occurs at 1155 K.	3
Figure 1.2	Optical micrograph showing the basket weave morphology	5
Figure 1.3	Optical micrograph showing the cooling induced cracks in the microstructure	5
Figure 1.4	Simple equilibrium phase diagram for (a) α , (b) β eutectoid and (c) β isomorphous alloy additions	16
Figure 1.5	Equilibrium phase diagram of Ti-Ta binary system obtained using the ThermoCalc [®] program is shown. The approximate compositional range for formation of α' , α'' and metastable β phases are marked in this figure [86].	21
Figure 2.1	Schematic of enthalpy increment variation with temperature. This is referred to as 'drop curve' in this thesis	40
Figure 2.2	Schematic representation of Inverse Drop	41
Figure 2.3	The experimental set up of drop calorimeter	41
Figure 2.4	Snapshot of the drop experiment output ΔV vs t obtained in this study.	45
Figure 2.5	Illustration of the temperature variation of Q for a typical experimental schedule and Calibration constant (inset)	46
Figure 2.6	The experimental set up of heat flux DSC [6]	48
Figure 2.7	(a) Setaram high temperature DSC furnace (b) Heat flux DSC plate-rod [6]	50
Figure 2.8	Typical DSC thermogram showing start (T_s) and finish (T_f) temperatures of phase transformation on cooling	53
Figure 2.9	Temperature calibrations with Al and Cu	55
Figure 3.1	Equilibrium phase diagram of Ti-Ta binary system obtained using the ThermoCalc [®] program is shown. The dotted lines stand for the compositions investigated in this study. The circles represent the experimental $\alpha/\alpha+\beta$, $\alpha+\beta/\beta$ solvus temperatures	65

	obtained in this study. The approximate compositional domains of α' , α'' , and metastable β phases are also marked in the figure [12,13].	
Figure 3.2	Room temperature X-ray diffraction profiles of Ti - xTa (x = 5, 10, 15, 20 mass %) alloys. The shoulder like feature adjacent to $(00.2)_\alpha$ indicates the presence of β -bcc phase	67
Figure 3.3	Lattice parameter variation with Ta-content.	68
Figure 3.4	A comparison of the lattice parameters of Ti-Ta alloys obtained in this study is made with the literature data on related Ti-base alloys. The numbers given in the square bracket stand for the respective references	68
Figure 3.5	Back Scattered Electron images of solution annealed Ti-Ta alloys corresponding to (a) 5 Ta, (b) 10 Ta, (c) 15 Ta, (d) 20 Ta.	70
Figure 3.6	Volume fraction of β measured in present study is compared with the equilibrium phase diagram estimate.	71
Figure 3.7	EDX spectra showing the relative enrichment of Ta in the β phase of Ti-Ta alloy.	72
Figure 3.8	Variation of microhardness with Ta content is shown for the solution annealed alloys.	72
Figure 3.9	Enthalpy increment variation with temperature for Ti-5Ta alloy is graphically illustrated. T_s and T_f represent $\alpha \rightarrow \beta$ transformation start and finish temperature respectively.	73
Figure 3.10	Slow scan DSC on-heating and cooling profile obtained for Ti -5Ta alloy.	74
Figure 3.11	Variation of enthalpy increment with temperature is plotted for (a) Ti-10 Ta, (b). Ti-15 Ta (c). Ti-20 Ta alloys. In (d) the data for all the compositions are compared for the $\alpha + \beta$ domain.	76-78
Figure 3.12	Collage of transformation microstructures (a-e) obtained for Ti-5Ta alloy. Each micrograph corresponds to different temperature T in the transformation zone, $T_s \leq T \leq T_f$, and hence exhibit different extents of $\alpha:\beta$ phase fraction as shown in (f)	80
Figure 3.13	Variation of microhardness of the quenched-in microstructure with temperature in the transformation zone for Ti-5 Ta alloy.	81

Figure 3.14	Collage of transformation microstructures (a-e) obtained for Ti-15Ta alloy. Each micrograph corresponds to different temperature T in the transformation zone, $T_s \leq T \leq T_f$ and hence exhibit different extents of $\alpha:\beta$ phase fraction as shown in (f).	82
Figure 3.15	Variation of microhardness of the quenched-in microstructure with the temperature in the transformation zone is shown for Ti-15 Ta alloy.	83
Figure 3.16	Graphical description of the method employed for estimating the $\alpha \rightarrow \beta$ transformation enthalpy, $\Delta^\circ H_{tr}$	86
Figure 3.17	Comparison of the model and experimental values of enthalpy increment in the transformation domain for Ti-5 Ta alloy	89
Figure 3.18	Effect of Ta concentration on the $\alpha \rightarrow \beta$ transformation onset (T_s) and offset (T_f) temperatures	96
Figure 3.19	Effect of Ta concentration on the $\alpha \rightarrow \beta$ transformation enthalpy ($\Delta^\circ H_{tr}^{\alpha-\beta}$)	97
Figure 3.20 (a)	Selection of γ_e and θ_E to obtain a good agreement between the experimental high temperature CP and the simulated low temperature CV data	99
Figure 3.20 (b)	The calculated low temperature C_v for Ti-5Ta alloy is presented together with the experimental high temperature C_p obtained in the present study.	100
Figure 3.21	The C_p data for Ti-Ta alloys estimated in this study are summarized. (a) 10 Ta, (b) 15 Ta, (c) 20 Ta. In (d) comparison of C_p for all compositions in the $\alpha + \beta$ region is shown.	101-102
Figure 3.22	The variation of H°_T , $-TS^\circ_T$ and G°_T with temperature T in the $\alpha + \beta$ region of Ti-Ta alloys (a) 5 Ta, (b) 10 Ta, (c) 15 Ta, (d) 20 Ta.	103-104
Figure 4.1	The on-heating and cooling DSC profiles for (a) Ti-5Ta, (b) Ti-10Ta, (c) Ti-15Ta & (d) Ti-20Ta alloys, recorded at 20 K min^{-1} .	113-114
Figure 4.2	Graphical representation of heating and cooling rate variation of transformation start (T_s), peak (T_p) and finish (T_f) temperatures for (a) Ti-5Ta, (b) Ti-10Ta, (c) Ti-15Ta and (d) Ti-20Ta alloys.	117-118
Figure 4.3	The composition dependence of the width ($\Delta T_{tr}^{\alpha \leftrightarrow \beta}$) of the (a) $\alpha \rightarrow \beta$ transformation and (b) $\beta \rightarrow \alpha$ transformation domain measured at 3 K min^{-1} . The	119

	vertical bars denote the typical spread of the measurement data.	
Figure 4.4	(a) & (b) The $\alpha \rightarrow \beta$ transformation and (c) & (d) The $\beta \rightarrow \alpha$ transformation peak profiles for Ti-5Ta alloy. The dotted ellipse outlines the shallow peak seen at the start of the $\alpha \rightarrow \beta$ thermal arrest for low heating rates.	122-123
Figure 4.5	(a) & (b) The $\alpha \rightarrow \beta$ transformation and (c) & (d) $\beta \rightarrow \alpha$ transformation peak profiles for Ti-20Ta alloy.	126-127
Figure 4.6	Optical microstructures of the post DSC samples of Ti-20Ta alloy showing the effect of cooling rate on microstructures that have undergone $\beta \rightarrow \alpha$ diffusional phase transformation	128
Figure 4.7	Microhardness data from post $\beta \rightarrow \alpha$ transformation microstructures showing the effect of cooling rate and Ta concentration.	129
Figure 4.8	A comparison of measured $T_s^{\alpha \rightarrow \beta}$ and $T_f^{\alpha \rightarrow \beta}$ temperatures in the present study with select literature data on phase boundaries is made.	131
Figure 4.9	Variation of measured $\alpha \rightarrow \beta$ transformation enthalpy ($\Delta H_{tr}^{\alpha \rightarrow \beta}$) with Ta content is graphically presented.	132
Figure 4.10	Correlation between measured $\alpha \rightarrow \beta$ transformation enthalpy ($\Delta H_{tr}^{\alpha \rightarrow \beta}$) and ($\Delta S_{tr}^{\alpha \rightarrow \beta}$). The value for titanium is taken from reference [27], while for others from our previously published data [28-30]. The dash dotted line indicates the linear relation between these two quantities for few Ti-alloys containing Ta, Zr, and Nb.	133
Figure 4.11	Experimentally obtained transformation plots for $\alpha \rightarrow \beta$ (left) and $\beta \rightarrow \alpha$ (right) transformations in Ti-5Ta alloy. The line stands for the experimental data, while the symbols are non-isothermal KJMA fit.	134
Figure 4.12	Experimentally obtained transformation plots for $\alpha \rightarrow \beta$ (left) and $\beta \rightarrow \alpha$ (right) transformations in Ti-10Ta alloy. The line stands for the experimental data, while the symbols are non-isothermal KJMA fit.	135
Figure 4.13	Experimentally obtained transformation plots for $\alpha \rightarrow \beta$ (left) and $\beta \rightarrow \alpha$ (right) transformations in Ti-15Ta alloy The line stands for the experimental	135

	data, while the symbols are non-isothermal KJMA fit.	
Figure 4.14	Experimentally obtained transformation plots for $\alpha \rightarrow \beta$ (left) and $\beta \rightarrow \alpha$ (right) transformations in Ti-20Ta alloy. The line stands for the experimental data, while the symbols are non-isothermal KJMA fit.	135
Figure 4.15	Kissinger plot for the $\alpha \rightarrow \beta$ transformation in Ti-x Ta (x = 5, 10, 15, 20 mass %) alloys	141
Figure 4.16	The variation of effective activation energy, Q_{eff} , for (a) $\alpha \rightarrow \beta$ and (b) $\beta \rightarrow \alpha$ transformations with Ta concentration is graphically displayed.	143
Figure 4.17	The continuous heating transformation (CHT) diagram for $\alpha \rightarrow \beta$ and (b) continuous cooling transformation (CCT) diagram for $\beta \rightarrow \alpha$ transformations obtained in the present study for Ti-5Ta alloy	148
Figure 4.18	The continuous heating transformation (CHT) diagram for $\alpha \rightarrow \beta$ and (b) continuous cooling transformation (CCT) diagram for $\beta \rightarrow \alpha$ transformations obtained in the present study for Ti-10Ta alloy.	149
Figure 4.19	The continuous heating transformation (CHT) diagram for $\alpha \rightarrow \beta$ and (b) continuous cooling transformation (CCT) diagram for $\beta \rightarrow \alpha$ transformations obtained in the present study for Ti-15Ta alloy.	150
Figure 4.20	The continuous heating transformation (CHT) diagram for $\alpha \rightarrow \beta$ and (b) continuous cooling transformation (CCT) diagram for $\beta \rightarrow \alpha$ transformations obtained in the present study for Ti-20Ta alloy	151
Figure 5.1	The room temperature XRD pattern of the Ti-5mass% Ta-1.8mass%Nb alloy showing the presence of α - phase peaks.	159
Figure 5.2	(a) Optical and (b) TEM micrograph showing fine equiaxed grains, (c) SAD pattern showing a polycrystalline pattern corresponding to α – hcp phase.	160
Figure 5.3	Variation of enthalpy increment with temperature for Ti-5mass%Ta-1.8 mass%Nb alloy.	162
Figure 5.4	Slow scan DSC profile obtained for Ti-5mass%Ta-	163

	1.8 mass% Nb alloy	
Figure 5.5	(a) Back scattered electron image showing predominately equiaxed primary α phase at 1060 K, (b) EDS spectra obtained from α and β phases, (c-f) Back scattered electron images showing the variation in microstructural features with Temperature; (c) 1083 K, (d) 1120 K, (e) 1133 K and (f) 1158 K.	165
Figure 5.6	Variation of specific heat C_p with temperature for Ti-5 mass%Ta-1.8 mass% Nb alloy and its comparison with Ti-4Nb-4Zr alloy and the estimation using Neumann-Kopp approximation.	170
Figure 5.7	On-heating and cooling DSC profile for Ti-5 mass%Ta-1.8 mass%Nb alloy recorded at 20 K min^{-1} .	172
Figure 5.8 (a)	The $\alpha \rightarrow \beta$ transformation peak profiles for slow heating rate.	173
Figure 5.8 (b)	The $\alpha \rightarrow \beta$ transformation peak profiles for high heating rate.	174
Figure 5.8 (c)	The $\beta \rightarrow \alpha$ transformation peak profiles for low cooling rate.	174
Figure 5.8 (d)	The $\beta \rightarrow \alpha$ transformation peak profiles for high cooling rate	175
Figure 5.9	Graphical representations of heating and cooling rate variation of transformation start (T_s), peak (T_p) and finish (T_f) temperatures for Ti-5 mass% Ta-1.8 mass% Nb alloy	177
Figure 5.10	Experimentally obtained transformation plot for (a) $\alpha \rightarrow \beta$ transformation, (b) for $\beta \rightarrow \alpha$ transformation. The line stands for the experimental data, while the symbols are the non-isothermal KJMA fit.	178
Figure 5.11	(a) The continuous heating transformation (CHT) diagram for $\alpha \rightarrow \beta$ and (b) continuous cooling transformation (CCT) diagram for $\beta \rightarrow \alpha$ transformations obtained in the present study for Ti-5mass%Ta-1.8 mass% Nb alloy.	181-182
Figure 5.12	SEM micrographs showing lamellar morphology of the products of $\beta \rightarrow \alpha$ transformation at different cooling rates such as (a) 5, (b) 10, (c) 20, (d) 40, (e) 75 and (f) 99 K min^{-1} . Decrease in lamellae size with increase in cooling rate is evident in the micrographs.	183

Figure 5.13	(a-e) TEM micrographs of alloy cooled at (a) 20, (b) 40, (c) 50, (d) 75, (e) 99 K min ⁻¹ showing alternate lamella of α and β phases, (f) & (g) represent the SAD pattern for the sample cooled at 99 K min ⁻¹ corresponding to α -hcp and β -bcc phases along and zone axis respectively, (h) represents the EDS spectrum showing the enrichment of Ta and Nb in the β lamella as compared to α lamella.	184-185
Figure 5.14	Variation of α and β lamella size and grain boundary α thickness as a function of cooling rate.	186
Figure 5.15	The effect of cooling rate on microhardness of $\beta \rightarrow \alpha$ transformation microstructure.	186
Figure 5.16	Variation of volume fraction of α and β phase as a function of cooling rate.	187
Figure 5.17	Variation of Ta equivalent of α and β phases as a function of cooling rate and the dotted line parallel to X-axis represents the alloy composition.	188
Figure 5.18	Schematic illustration of the effect of cooling rate in shifting of α and β solvus lines under non equilibrium conditions	190
Figure 5.19	Variation of composition of α and β phases at transformation finish (T_f) temperature with cooling rate in Ti-5Ta-1.8 Nb alloy.	191
Figure 5.20	Microstructure of the alloy cooled at 40 K min ⁻¹ . (a) BF image showing the lamellar $\alpha+\beta$ structure, (b) SAD pattern from the β lamella in (a) showing the presence of α phase along $[\bar{1}10\bar{1}]$ zone axis (c) DF image with $(01\bar{1}1)$ reflection (circled in (b)) showing the alternate lamellae α and β phases within a primary β lamella (arrow marked)	193
Figure 5.21	DF images showing the decomposition of primary β phase into a lamellar $\alpha+\beta$ structure on cooling at (a) 20 K min ⁻¹ (b) 50 K min ⁻¹ and (c) 75 K min ⁻¹ .	194
Figure 5.22	(a) BF image of β lamella of the alloy cooled at 99K min ⁻¹ showing a mottled contrast (b) & (c) SAD pattern and its key confirming the presence of two different variants of ω along $[\bar{1}2\bar{1}3]$ zone axis; (d) DF image taken with $(10\bar{1}0)_\omega$ reflection (circled in (b)) showing fine ω particles; (e) BF image of β lamella with fine plate like features within it and (f)	195

SAD pattern confirming the presence of two different variants of face centered orthorhombic martensite α'' along $[3\bar{2}1]$ and $[3\bar{1}2]$ zone axes.

LIST OF TABLES

Table No.	Table captions	Page No.
Table 1.1	Review of the work done on thermodynamics and kinetics of phase transformation in pure Ti and Ti-X (X= Nb, Mo, Zr, V) alloys.	9
Table 1.2	Review of the work done on Ti – Ta alloys.	22
Table 2.1	Chemical compositions of Ti-xTa (x= 5, 10, 15, 20 mass %) alloys.	36
Table 2.2	Chemical composition of Ti-5Ta-1.8Nb ternary alloy.	36
Table 2.3	Conditions adopted for quantification of EDS spectra.	58
Table 3.1	Room temperature X-ray diffraction data and estimated lattice parameters of Ti-xTa (x = 5, 10, 15, 20 mass %) alloys.	69
Table 3.2	The $\alpha \rightarrow \beta$ transformation temperatures & the fit parameters of Eq.2 for the enthalpy increment data for all Ti-Ta alloys.	91
Table 3.3	Experimental and derived thermodynamic properties for Ti-5Ta alloys.	92
Table 3.4	Experimental and derived thermodynamic properties for Ti-10Ta alloys.	93
Table 3.5	Experimental and derived thermodynamic properties for Ti-15Ta alloys.	94
Table 3.6	Experimental and derived thermodynamic properties for Ti-20Ta alloys.	95
Table 3.7	Thermodynamic and kinetics parameters pertaining to $\alpha \rightarrow \beta$ phase transformation are tabulated for all the alloy compositions investigated in this study.	96
Table 3.8	Elastic and Thermodynamic properties of $Ti_{1-x} Ta_x$ (x=5, 10, 15, 20 mass %) alloys at 298.15 K.	107
Table 4.1	$\alpha \leftrightarrow \beta$ transformation temperatures for Ti-5 mass% Ta alloy.	119
Table 4.2	$\alpha \leftrightarrow \beta$ transformation temperatures for Ti-10 mass% Ta alloy.	120
Table 4.3	$\alpha \leftrightarrow \beta$ transformation temperatures for Ti-15 mass% Ta alloy.	121
Table 4.4	$\alpha \leftrightarrow \beta$ transformation temperatures for Ti-20 mass% Ta alloy.	121
Table 4.5	Kinetics parameters for $\alpha \rightarrow \beta$ transformation obtained by fitting experimental data to non-isothermal KJMA model.	144

Table 4.6	Kinetics parameters for $\beta \rightarrow \alpha$ transformation obtained by fitting experimental data to non-isothermal KJMA model.	145
Table 5.1	Room temperature X-ray diffraction data on Ti-5mass%Ta-1.8 mass% Nb alloy.	160
Table 5.2	Experimental enthalpy, fit enthalpy and the derived specific heat data for Ti -5 mass% Ta – 1.8 mass% Nb alloy.	171
Table 5.3	$\alpha \leftrightarrow \beta$ transformation temperatures for Ti-5 mass%Ta-1.8 mass%Nb alloy.	176
Table 5.4	Kinetics parameters for $\alpha \leftrightarrow \beta$ phase transformation obtained by fitting experimental data to non-isothermal KJMA model.	180

LIST OF SYMBOLS AND ABBREVIATIONS

DSC	Differential Scanning Calorimetry
XRD	X-Ray Diffraction
SEM	Scanning Electron Microscopy
TEM	Transmission Electron Microscopy
SAD	Selected Area Diffraction
SE	Secondary Electron
BSE	Back Scattered Electron
EDAX	Energy Dispersive X-ray analysis
$N(E_F)$	electron density of state at the Fermi level
θ_E	Einstein temperature
C_P	Heat capacity at constant pressure
C_V	Heat capacity at constant volume
θ_D	Debye temperature
γ_e	Electronic specific heat coefficient
α_V	Volume coefficient of thermal expansion
γ_G	Gruneisen parameter
B_T	Isothermal bulk modulus
k_B	Boltzman constant
K	Kelvin
k_0	frequency factor
Q_{eff}	Apparent / effective activation energy
n	transformation exponent
CHT	Continuous Heating Diagram
CCT	Continuous Cooling Diagram
T_s	start temperature
T_f	finish temperature
$H^{\circ}_{298.15}$	enthalpy at 298.15 K
$S^{\circ}_{298.15}$	entropy at 298.15 K
$G^{\circ}_{298.15}$	Gibbs energy at 298.15 K

CHAPTER-1

Introduction

1.1 Genesis of Titanium Era

Titanium was first discovered in the year 1791 by William Gregor of England in an impurity form and the naming of the element by Martin Klaproth, a German chemist derived quite later, after the Greek mythological word “Titan” [1]. Nevertheless, until about 1910, titanium had turned out to be quite difficult to separate from its compounds and it was only in 1946 that Dr. Wilhelm J. Kroll developed the new famous method – Kroll’s Process, known after him, to produce titanium commercially [1]. This singular process metallurgical discovery initiated the torrent of developments that were soon to constitute a new metallurgical industry – that is concerned exclusively with the science, engineering and technology of titanium alloys [2-4]. These classical developments in the science and technology of titanium alloys have been nicely captured in many reviews and conference proceedings [5]. Today, the potential application of titanium and its alloys as structural materials spans such a wide array of industrial and more recently bio-medical and nuclear reprocessing applications that only few materials can match.

1.2 Titanium & Alloys: Basic Characteristics

Titanium alloys extensively with many transition and non transition metallic elements to produce a spectrum of alloys that are well known for high strength to weight ratio with adequate measure of fracture toughness, excellent fabricability, good corrosion resistance and a fair degree of weldability, although requiring special precautions and joining practices. Titanium alloys are comparatively costly, nevertheless their versatility and specialty status for high – end applications justifies their unique position. About 80 to 90 % of the titanium produced is used for making the components in aero engines and space shuttles in aerospace industry [2, 6, 7].

In recent years, non-aerospace applications such as chemical, marine, nuclear,

petro-chemical, power, bio-medical, and energy industries also abound [1, 8-18] because of titanium's high corrosion resistance [19, 20], good high temperature thermal and microstructural stability, low density, high strength, low elastic modulus and excellent biocompatibility. Titanium is well-known for its high affinity towards oxygen and hydrogen. Many Ti-alloys are potential H₂-absorber/ storage candidates. The ready hydriding capability on the other hand poses some problems in the form of low thermal conductivity and brittleness and several other challenges are encountered in production and fabrication of titanium alloys due to its hydrogen pick-up [21]. Considering the scope of this study these special issues are not elaborated in detail here. This chapter mainly focuses on presenting a comprehensive account on the physical metallurgy aspects of Ti-and its alloys.

1.3 Role of Phase Transformation in Microstructure Design

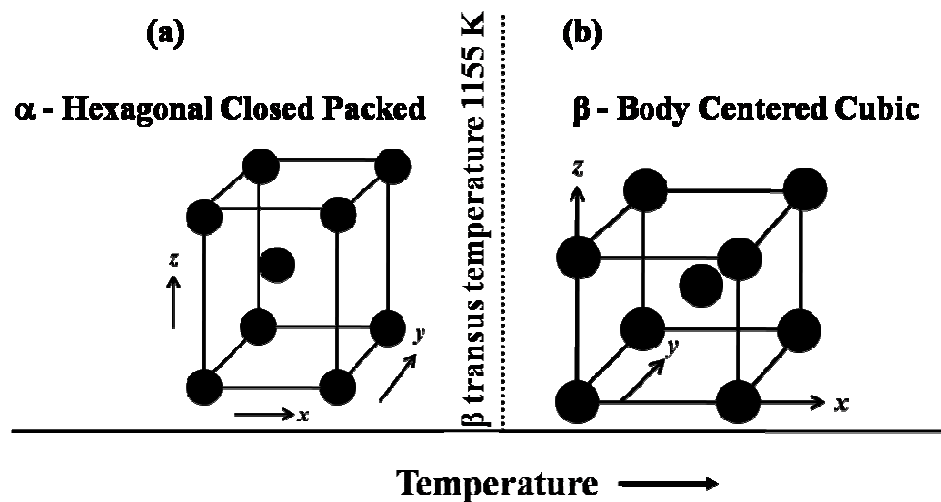


Figure 1.1 (a) unit cell of hexagonal closed packed structure for α - phase. (b) unit cell of body centered cubic structure for β - phase. The transition from the low temperature α (hcp) phase to high temperature β (bcc) phase occurs at 1155 K.

Titanium undergoes a structural phase change from low temperature α (hcp) to high temperature β (bcc) polymorph at 1155 K (882 °C) and 1 atm. pressure (**Fig. 1.1**). This hcp-bcc polymorphic transition is normally of nucleation and growth type, although

the martensitic - displacive mode of structural phase change is also observed [22]. Besides, there is another crystal structure form called ω , which is hexagonal but not close packed and of AlB_2 type, to which the α -hcp - titanium transforms upon application of external pressure [23]. The athermal ω transformation from high temperature β phase is displacive in nature in that it is brought about by a set of coordinated shuffles of a small number of (group) atoms. In fact, ω structure can be thought of as due to the collapse of alternate $\{111\}$ planes in the $[111]$ direction. In this sense, the ω phase as a distinct crystal structure modification can be thought of as an intermediate state during the *continuous* transition from the open bcc structure to the close packed hcp structure, with the extent of $\{111\}$ plane collapse serving as a pseudo transformation progress index or the so-called order parameter [24]. The overview by Sikka and Chidambaram gives more interesting crystallographic details of the ω transformation in Ti-alloys [25].

The structural transformations as well microstructure development in Titanium and in Ti-base alloys are considerably influenced by strain energy considerations. The nucleation of crystallographically anisotropic α from elastically isotropic cubic β during cooling introduces certain issues arising out of strain energy accommodation. These transformation crystallography related structures play a crucial role in the final microstructural development during decomposition of β -bcc phase. It is generally the case that the elastically soft directions are preferred from the growth point of view, and that result in some times, the production of co-aligned α -plates in mutually orthogonal crystallographic habits, which give rise to so called basket weave morphology in many $\alpha+\beta$ alloys. A typical microstructure of this category is shown in **Fig. 1.2**. If for some reasons, the cooling from β is rather rapid and that adequate strain minimizing

nucleation and accommodation of α could not be realized due to hard impingement considerations, then considerable transgranular cracking (cracks inside the prior β -grain) follows, especially in thick sections due to gradients in cooling.

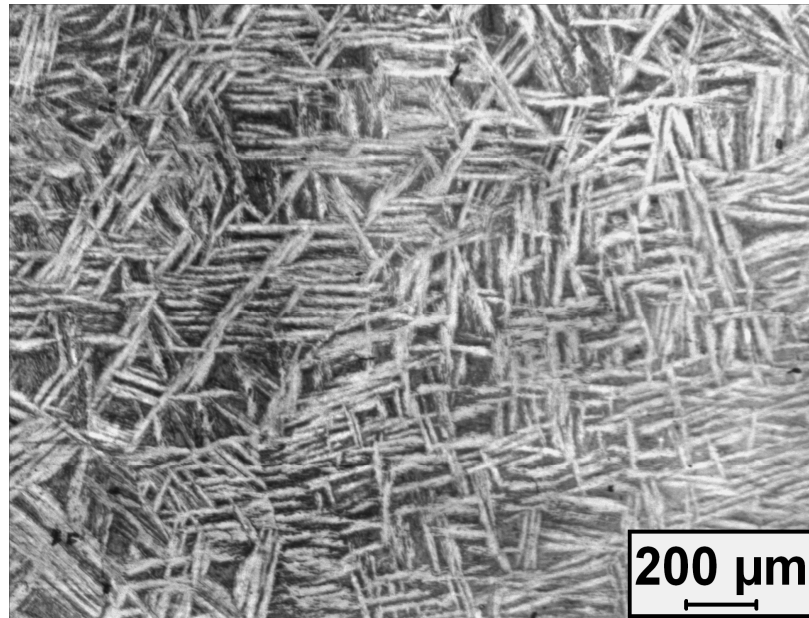


Figure-1.2 Optical micrograph showing the basket weave morphology

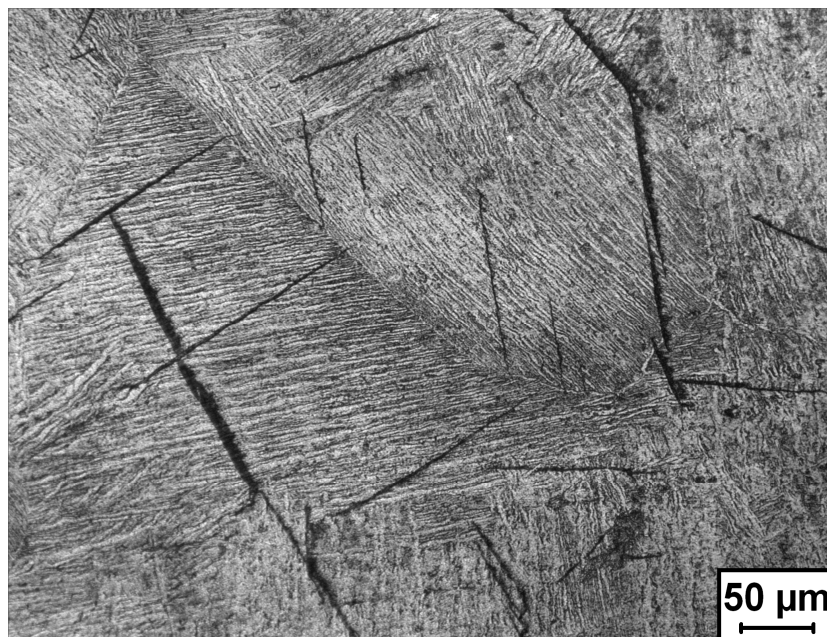


Figure 1.3 Optical micrograph showing the cooling induced cracks in the microstructure

In **Fig. 1.3**, an example of such cooling induced cracks is shown. The reason for highlighting these two extreme cases is to emphasize the role of thermal history in governing microstructural integrity.

As is well known in ferrous metallurgy, the polymorphic structural transformations in titanium too, are highly sensitive to composition, especially minor alloying additions or impurities like oxygen [1, 2]. Different alloying additions have different bearing on the relative thermodynamic stabilities of α and β phases. Besides they also affect considerably the atomic mobilities of different species and interfaces [26]. Accordingly, one can have α -titanium alloys containing predominantly α -phase stabilizing additions, which essentially opens up the domain of stability of α phase, by exhibiting a high degree of solubility in the hcp phase. These alloys following hcp-titanium, are known for their good ductility, moderate strength, but a high degree of plasticity anisotropy, besides good hydrogen pickup. Generally, the elements Al, Ga, C, O, N etc., are known for their α -stabilizing potential; the major reason being they do not distort appreciably the Fermi surface–Brillouin zone interactions that are inherent to the electronic structure and stability of pure hcp titanium [2]. There are also compound or intermetallic forming α -alloys such as Ti-Al, wherein the high intermetallic stability of γ -TiAl ($L1_0$ – face centred tetragonal structure) derives from special considerations arising from opening up of pseudo Fermi Gap in the electronic band structure due to significant Ti-d and Al-sp hybridization [27]. This additional metallic covalency introduces an enhancement of strength, but at the cost of tensile ductility.

The β -bcc stabilizers on the other hand serve to enhance the stability of high temperature bcc phase, which is plastically isotropic. β -stabilizers normally depress the $\alpha \rightarrow \beta$ solvus of titanium through strong *chemical* interaction effects. Quite a few of the

β -stabilizing transition element solutes like V, Nb, Ta, Mo etc., do exhibit appreciable solubility in α -structure, but because of their strong thermodynamic clustering tendency in the β bcc phase, they exhibit often metastable or at times (with Nb as the example) stable miscibility gaps in the β -phase domain. These alloys depending upon the thermodynamic nature of the β -phase miscibility gap, can be of isomorphous type (complete solubility in bcc phase) or monotectoid ones ($\beta \rightarrow \beta_1 + \beta_2$). It is the usual practice that in commercially important Ti-alloys, there will be a purposeful mix of both α and β stabilizing additions that resulting phase diagram will have many interesting and intriguing possibilities [1, 8].

In either case, the physical metallurgy of $\alpha+\beta$ alloys containing a mix of α and β stabilizing solutes exhibit a variety of phase diagram features that are significance to the processing of Ti-alloys [8]. The relative thermodynamic stabilities of α and β phases in many of the commercially important $\alpha+\beta$ alloys are only marginally different [28, 29], unlike the case of Fe-base alloys, where the fcc-derived austenitic and bcc-based ferritic grades differ significantly in their electronic and thermodynamic considerations of stability [30]. *This marginal stability of α/β phases in Ti-alloys (especially in $\alpha+\beta$) act in a synchronized manner and can be manipulated by appropriate selection of external processing variables like heating and cooling rates, soaking time at the β -field, thermomechanical processing in β or $\alpha+\beta$ fields.*

In general, the $\alpha \leftrightarrow \beta$ transformation kinetics taking place under slow or intermediate heating/cooling rates is often limited by the solute diffusion in either or both α and β phases. The diffusivities for most of the heavy transition metal solutes are comparatively sluggish, in the α -hcp phase of $\alpha+\beta$ alloys derived from V, Nb, Ta, Zr, Mo, Cr additions. This implies that for a fixed starting composition, a variety of

transformation induced or tailored microstructures can be realized in $\alpha+\beta$ titanium alloys, by fine tuning the extent of time that the alloy spends in $\alpha+\beta$ two phase domain. One outstanding manifestation of the sluggish solutal diffusivity induced phase cum microstructural metastability under rapid cooling conditions is the onset of martensitic and or ω -mode of β -phase decomposition. The Ti-alloy martensites have either hexagonal or orthorhombic structure [1, 8, 31, 32], depending on the type and concentration of solute content. This martensite upon receiving subsequent thermal activation can decompose in a variety of ways to form finally the equilibrium mixture of $\alpha+\beta$ phases, or if the direct decomposition is kinetically demanding, through an intermediate path involving isothermal ω phase formation. This thermally activated diffusional decomposition is again controlled by the solute diffusion as formation of solute rich β from displacively formed α' or α'' martensite requires long range atom migration due to appreciable solute partitioning. The microstructural pathway can also be considerably influenced by the presence of stress, if the thermomechanical processing results in remnant residual stresses being retained in the ingot [33]. This is a very important factor which influences the physical metallurgy of titanium alloy.

It is well known in alloy design that the desired end application can be met by tailoring the microstructure through varying the composition of the alloy, heat treatment and thermo-mechanical processing schedules [34-38], during which different types of phase transformations might have been suppressed or induced in the material. Hence it is very important to understand the nature of phase transformation or **high temperature phase stability** which in turn is controlled by a combination of thermodynamics and kinetics parameters. In a nutshell, it can be said that a thorough understanding of the **thermo-kinetics** of titanium alloys, derived from experimentally measured

thermodynamic and kinetic investigations of phase changes is essential to enable the knowledge driven approach to alloy design.

In the past decade, the interest in Ti-base alloys containing refractory solutes like Ta, Mo, W, Hf, Nb etc., for biomedical applications has increased manifold. Accordingly there has been a spate of research on applied process metallurgical aspects of these novel Ti-base alloys. However, the extent of research output or investigations on basic and fundamental aspects of alloy phase stability is far limited. There are few theoretical simulation studies on advanced Ti-alloys [39], but practically the number of published research reports on high temperature thermo-kinetic investigations on emerging $\alpha+\beta$ and β alloys of titanium is rather small. In **Table 1.1**, a brief itemized list of major research studies on thermo-kinetic and phase diagram related aspects of $\alpha+\beta$ Ti-alloys that are of relevance to the present study are highlighted.

Table 1.1 Review of the work done on thermodynamics and kinetics of phase transformation in pure Ti and Ti – X (X= Nb, Mo, Zr, V) alloys.

Alloy System Concentration of the alloying element (mass %)	Nature of the study	Reference of the Study
Ti	Heat capacity of α -hcp titanium using adiabatic calorimetry.	W.H. Cash et al. J. Chem. Thermo. 14 (1982) 351-355.
Ti	Reviews and discussion on the available data on thermodynamic properties of Ti.	P.D. Desai, Int. J. Thermophys. 8 (1987) 781-794.
Ti	High temperature thermophysical properties measurement using high temperature electrostatic levitator.	P. F. Paradis et al. J. Chem. Thermo. 32 (2000) 123-133.
Ti	Transformation enthalpy and Phase transformation temperature	E. Kashnitz et al. Int. J. Thermophys. 23 (2002) 1339-1345.
Pure Ti and Zr	Heat capacity by electromagnetic levitation.	B. Guo et al. Int. J. Thermophys. 29 (2008) 1997-2005.
Pure Ti and Zr	Enthalpy measurements of high temperature β phase using levitation drop calorimetry	M. R. Kuhn et al. J. Alloys Comp. 316 (2001) 175-178
Ti	Measurement of heat capacity in the temperature range 1500 to 1900 K	E. Kaschnitz et al. J. Thermal Anal. Calor. 64 (2001) 351-356.

Ti	Measurement of low temperature specific heat from 20° to 200° K.	D. L. Burk et al. Z. Physik. Chem. 16 (1958) 183-193.
Ti	Calculation of Debye temperature from elastic moduli.	Q. Chen et al. Acta Mater. 49 (2001) 947-961.
CP-Ti	Measurement of $\beta \rightarrow \alpha$ transformation kinetics during continuous cooling using a fully computer-controlled resistivity-temperature real-time measurement apparatus.	S. K. Kim et al. Metall. Mater. Trans. A, 33 (2002) 1051-1056.
Ti-Mo	Measurement of low temperature specific heat in the temperature range of 1.4 to 4.2 K	A.K. Sinha, J. Phys. Chem. Solids 29 (1968) 749-754.
Ti-12Mo	Thermal analysis of the ω nanophase transformation by electrical resistivity and dilatometry	F. Sun et al. J. Therm. Anal. Calor. 101 (2010) 81-88.
Ti-X (X-Zr, Nb, Al, Sn etc.)	Enthalpy measurement using calvet calorimeter and estimation of specific heat	H. Bros et al. J. Thermal Anal. 41 (1994) 7-24.
Ti-Nb	Calculation of stable and metastable phase equilibria by Calphad method.	D. L. Moffat et al. Metall. Trans. 19A (1988) 2389-2397.
Ti-Nb	Evaluation of atomic mobilities of Ti and Nb in bcc Ti-Nb alloys by CALPHAD	Y. Liu et al. J. Alloys comp. 476 (2009) 429-435.
Ti-Nb, Ti-V, Ti-Fe	Low temperature specific heat, bulk superconductivity and paramagnetic susceptibility in dilute alloys	F. Heiniger et al., Phy. Rev. A 134 (1964) 1407-1409.
Ti-5Ta-1.8Nb	Measurements of enthalpy increment using drop calorimetry	Madhusmita Behera et al. Int. J. Thermophys. 31 (2010) 2246-2263.
Ti-6Al-4V	Measurement of several thermophysical properties using resistive pulse heating device, DSC and laser polarimeter	M. Boiveneau et al. Int. J. Thermophys. 27 (2006) 507-529
Ti-6Al-4V	Specific heat capacity and electrical resistivity measurement using pulse heating techniques	D. Basak et al. Int. J. Thermophys. 24 (2003) 1721-1733.
90Ti-6Al-4V	Measurement of heat capacity and electrical resistivity and the study of changes in phase transition behavior with milli and microsecond pulse heating systems.	E. Kaschnitz et al. Int. J. Thermophys. 23 (2002) 267-275.
Ti-4Nb-4Zr	Measurement of Enthalpy increment and heat capacity using drop and differential scanning calorimetry.	V. Anbarasan et al. J. Alloys Comp. 463 (2008) 160-167.
Ti-Alloys	Phase diagram modeling using CALPHAD	N. Saunders, Titanium '95: Science and Technology, Proceedings of the Eighth World Conference on Titanium, Institute of Materials, London, (1996) 2167-2176.
Ti-8 Al-1 Mo-1 V alloys	Study of kinetics of $\beta \Rightarrow \alpha + \beta$ transformation under isothermal	S. Malinov et al. J. Alloys Comp. 333 (2002) 122-132.

	condition using electrical resistivity technique.	
Ti-5Al-2Sn-4Zr-4Mo-2Cr-1 Fe	Building of CCT diagram by metallography and electrical resistivity.	C. Angelier et al. Metall. Mater. Trans. A 28 (1997) 2467-2475
Ti-6Al-4V & Ti-6Al-2Sn-4Zr-2Mo-0.08Si	Study of kinetics of $\beta \Rightarrow \alpha + \beta$ transformation under isothermal conditions using resistivity technique.	S. Malinov et al. J. Alloys Comp. 314 (2001) 181-192.
$\beta 21s$	Study of thermodynamics and kinetics of $\beta \Rightarrow \alpha + \beta$ phase transformation under isothermal condition	S. Malinov et al. J. Alloys Comp. 348 (2003) 110-118.
Ti alloys	Study of mechanism and kinetics of phase transformation	S. Bein et al. J. Phys. IV 6 (C1) (1996) 99-108.
β -Cez alloy	Calculation of transformation kinetics of Ti-alloys during continuous cooling.	E. Laude et al. Titanium '95: Science and Technology, Proceedings of the Eighth World Conference on Titanium, Institute of Materials, London, (1996) 2330-2337.
Ti-6Al-4V	Study of kinetics of $\beta \Rightarrow \alpha$ phase transformation under continuous cooling conditions using DSC.	S. Malinov et al. Metall. Mater. Trans. A 32 (2001) 879-887.
Ti-6Al-4V	Study of phase evolution during continuous heating using DSC.	W. Sha et al. J. Alloys Comp. 290 (1999) L3-L7.
Ti-alloys	Computer modeling of thermodynamics and kinetics of phase transformation	S. Malinov et al. JOM (2005) 42-45.
Ti alloys	Modeling of phase transformation kinetics-isothermal treatment.	B. Applaire et al. Acta Mater. 53 (2005) 3001-3011.
TB-13 (Ti-7.5Mo-4.8Nb-3.8Ta-3.6Zr-4Cr-2Al)	Investigation of the ω phase transformation kinetics by non-isothermal dilatometry.	Z. Zhou et al. Mater. Sci. Engg. A 527 (2010) 5100-5104.
Ti-Zr, Ti-Zr-Hf	The temperature and enthalpy changes of the hcp to bcc transformation	J. Blacktop et al. J Less Common Met. 109 (1985) 375-380.
Ti-Nb	Evaluation of thermodynamic properties by using a regular solution model to describe the Gibbs energy function for various stable and metastable phases.	Y. Zhang et al. Calphad 25 (2001) 305-317.
Ti-Nb, Ti-V, Nb-V, Ti-Nb-V	Thermodynamic assessment of phase equilibria	K. C. Harikumar et al. Calphad 18 (1994) 71-79.
Ti-25.5Nb	Measurement of thermodynamic properties using drop calorimetry	A.J. Prabha et al. Physica B 406 (2011) 4200-4209.

1.4 Necessity of Basic Research on Phase Stability & Related Issues on Ti-Ta and Ti-Ta-Nb alloys

In the nuclear reprocessing industry, there is an urgent need to develop highly corrosion resistant (to boiling HNO₃) Ti-alloys which are also known for their good fabricability into huge reprocessing vessels and pipes. In this regard, considerable R&D has already been made on developing a special variant of ($\alpha+\beta$) alloy containing Ti, Ta and Nb [40, 41]. In the process of understanding diverse physicochemical issues related to the successful development of Ti-5 mass%Ta-1.8 mass%Nb alloys, it was realized that the existing basic knowledge with regard to binary Ti-Ta and Ti-Nb alloys itself is rather inadequate. In particular, to the best of our knowledge no reports on any recent research attempts on the thermodynamic characterization of Ti-Ta alloys, which in itself is an important Ti-base corrosion resistant binary alloy was available. It is in this background that the present investigation has focused on generating reliable calorimetry based thermodynamic data on the high temperature phase stability of Ti-xTa alloys (x= 5, 10, 15, 20 mass %) and a Ti-5Ta-1.8Nb ternary alloy. This latter ternary alloy is a candidate structural material for nuclear radwaste reprocessing vessels developed in house at Indira Gandhi Centre for Atomic Research (IGCAR) [42-46]. This research study which originated with a ternary Ti-Ta-Nb alloy as its study material has turned its focus to investigating the binary Ti-Ta system in some depth, since this happens to be the first such comprehensive calorimetry based investigation on this system, to the best of the knowledge of the investigator(s). Although bulk of the study focuses on calorimetry, also adequate emphasis is given to metallographic and electron microscopy investigations to substantiate the major deductions of calorimetry investigations. The microscopy characterization of transformation microstructures using electron microscopy has been done in detail for ternary Ti-5Ta-1.8Nb alloy; similar work on Ti-Ta binary is however scheduled for further study (*Chapter 6*).

It is also realized that more work remains to be done on integrating the data obtained in this study with detailed microscopy and modelling studies. A similar study on Ti-Nb is also warranted and this is concurrently being taken up at present [47, 48], which is beyond the purview of this thesis.

The principal scope of this study is therefore:

CALORIMETRY INVESTIGATION OF HIGH TEMPERATURE PHASE STABILITY AND $\alpha \leftrightarrow \beta$ PHASE TRANSFORMATION KINETICS in select Ti-Ta and a Ti-Ta-Nb alloys.

But before proceeding further with describing the work in detail, a brief account of the necessary metallurgical base on Ti-alloys is provided in the remaining part of this introductory chapter.

1.5 Phase Equilibria of Ti alloys: Further details

Based on nature of alloying element, the titanium alloys are classified as “ α ”, “ β ” and “ $\alpha + \beta$ ” alloys [2, 8]. The fundamental factor that govern the stabilization of the α and β phases in titanium alloys is the electronic structure which is represented by the **e/a** parameter. The **e/a** ratio of Ti metal is taken as 4. The alloying elements with **e/a** ratio less than 4 are considered as α - stabilizers. The elements with **e/a** ratio of 4 are neutral and **e/a** ratio greater than 4 are β stabilizers [8]. Among the interstitial elements C, N, O stabilize the α phase, while H is a strong β stabilizer.

1.5.1 α -Alloys

Unalloyed Ti and alloys with one or more α stabilizers that are stable with α - hcp structure at room temperature are known as α alloys. Commercially pure Ti and its alloys with addition of Al, Ga, Sn and O fall under this category. It is important to note that in α alloys Al is restricted to 5-6 wt% due to their tendency to form brittle α_2

(Ti₃Al) phase [49]. The single phase α alloys exhibit good workability, low to medium strength, good toughness and are not heat treatable. α alloys have higher creep resistance as compared to $\alpha + \beta$ and β alloys, hence are preferred for high temperature applications. The absence of ductile to brittle transformation renders α alloys suitable for cryogenic applications [2].

1.5.2 $\alpha + \beta$ – Alloys

The $\alpha + \beta$ -alloys are that which contain mixture of both α and β stabilizers. Usually these alloys have 4-6 wt% β stabilizers. Ti alloys which contains 10-20 % of retained β along with α phase at room temperature in thermodynamically equilibrium condition can also be considered as $\alpha+\beta$ -alloys [50, 51].

The $\alpha+\beta$ alloys exhibit good fabricability as well as high room temperature strength as compared to single phase α . They are heat-treatable, weldable and possess creep properties in between α and β alloys. The microstructure and the properties of the $\alpha+\beta$ alloys can be varied widely by appropriate heat treatments and/or thermo mechanical treatment such as β or α/β treatment and hence are used for numerous applications. Due to high strength, the two phase $\alpha + \beta$ alloys are used as structural material for many applications. The most commercially important alloy under this category is Ti – 6Al – 4V. This alloy is used for making the forged components for engines like turbine blades and compressor rotor spool. Ti-6Al-4V ELI (Extra Low Interstitial version) is one of the first and most popular bio material used for implantation for long time due to its relatively high strength, low modulus and superior bio compatible characteristics [13, 15]. Other examples under this category are Ti-7Al-4Mo and Ti-3Al-2.5V [2].

1.5.3 β - alloys

The titanium alloys which contain enough β phase stabilizing elements so that β phase is retained in either metastable or stable form at room temperature after cooling to room temperature during heat treatment [8]. Transition metals of the periodic table such as Ta, Nb, Mo, W, V, Fe, Cr, Hf, Mn, Ni, Co, Cu are known as β phase stabilizers [8, 2, 52]. β alloys show good response to heat treatment and have better weldability, ductility, toughness but poor creep resistance [49]. Although they are extremely formable, ductile to brittle transition at low temperature makes them unsuitable for cryogenic applications. The β phase stabilizing elements are further classified as β - isomorphous (Ta, Nb, Mo, W) or β -eutectoid (Fe, Mn, Co, Ni, Cu, Cr) formers depending on their solubility in the β phase. β -isomorphous elements have extensive solubility in the β phase whereas the eutectoid elements have limited solubility and decompose into α and a compound.

The metastable β titanium alloys which are thermodynamically unstable at room temperature may undergo decomposition reaction like α phase precipitation during aging treatment to provide secondary strengthening to the material. Hence, metastable β titanium alloys have higher strength, toughness and improved formability as compared to α and $\alpha+\beta$ alloys. The disadvantage of β titanium alloys include greater possibility of segregation during melting as compared to $\alpha+\beta$ alloys.

However, β titanium alloys find a wide spread use in a variety of application such as aerospace [53] due to high strength and for biomedical devices [54-56] due to their good mechanical, biological and corrosion resistance property. Examples of this type of alloys are Ti-6Al-2Sn-4Zr-6Mo, Ti-5Al-2Sn-2Zr-4Mo-4Cr, Ti-10V-2Fe-3Al, Ti-11.5Mo-6Zr-4.5Sn [8, 1].

In order to compare the effect of α and β stabilizers in a multicomponent alloy system they are expressed in terms of Al and Mo equivalency respectively and can be represented as follows [52, 57].

$$[\text{Al}]_{\text{eq}} = [\text{Al}] + 0.17[\text{Zr}] + 0.33[\text{Sn}] + 10[\text{O}] \quad (1.1)$$

$$[\text{Mo}]_{\text{eq}} = [\text{Mo}] + 0.22[\text{Ta}] + 0.28[\text{Nb}] + 0.4[\text{W}] + 0.67[\text{V}] + 1.25[\text{Cr}] + 1.25[\text{Ni}] + 1.7[\text{Mn}] + 1.7[\text{Co}] + 2.5[\text{Fe}] \quad (1.2)$$

A schematic of equilibrium phase diagram for α , β isomorphous and β eutectoid systems is shown in **Figure 1.4** [49].

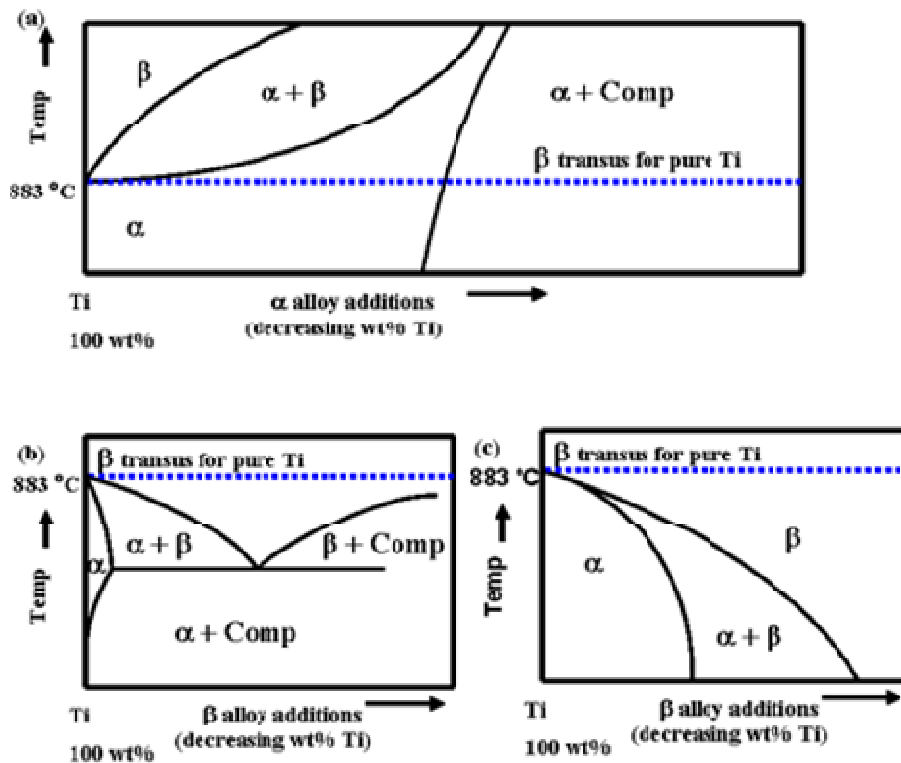


Figure 1.4 Simple equilibrium phase diagram for (a) α , (b) β eutectoid and (c) β isomorphous alloy additions

1.6 Classification of phase transformation in Titanium alloys

According to Buerger, based on mechanism the phase transformation can be classified into two types: (i) Diffusional transformation and (ii) Displacive

transformation [52]. In titanium alloys, both diffusional and displacive transformations or a combination of both are encountered depending on the composition and thermomechanical treatments. The transformation mechanism, which in turn is dependent on the alloy content, nature of phase field and thermomechanical history is the governing factor for the end transformation product resulting in distinct microstructural features. The characteristic features of the above two phase transformations are described below very briefly.

1.6.1 Diffusional transformations

This transformation is a reconstructive transformation, involving both structure and compositional change. In diffusional transformation the atoms of the parent phase move randomly by the process of diffusion to the product lattice sites. This implies that near neighbor bonds are broken at the transformation front and the product structure is reconstructed by the occupation of incoming atoms at the proper positions, which results in the growth of the product lattice. In a diffusional transformation the movement of atoms occurs over a distance longer than the interatomic distances. Some examples of diffusional phase transformation are Widmanstatten transformation, aging of martensite and β phase. In case of α/β or β -Ti alloys, the Widmanstatten $\beta \rightarrow \alpha$ transformation during slow cooling from β phase occurs by diffusional mechanism [58]. Widmanstatten $\beta \rightarrow \alpha$ transformation in titanium alloys is characterized by the formation of lamellar morphology consisting of α platelets with an inter-platelet β phase. The lamellar structure vary from aligned colonies of plate like α at low cooling rate, to basket weave morphology at an intermediate and to a martensitic like structure [59] at very high cooling rates.

The α formed from β phase manifests itself in three different morphologies. The α phase nucleated at the β/β grain boundary, growing along the grain boundary is

termed as the grain boundary α (GB- α plate) [60, 61]. The nucleation of further α on the grain boundary α in a sympathetic manner and grows into the β grain is known as inter-granular α . This process of nucleation is known as sympathetic nucleation, to distinguish from totally un-aided fresh nucleation. During this process the α may nucleate from β phase at same event but grows in different directions which are known as variants. Sometimes α also nucleates and grows inside the β grain, which is also known as intra-granular α .

It is found that the α phase formed within the β grain obeys Burger orientation relationship (BOR): $((110)_{\beta} // (0001)_{\alpha}, [\bar{1}11]_{\beta} // [\bar{2}110]_{\alpha})$ with matrix β phase [62]. This OR is characteristic of Widmanstatten type morphology. The grain boundary α displays Potter OR: $((110)_{\beta} // (0\bar{1}1)_{\alpha}, [\bar{1}\bar{1}1]_{\beta} // [\bar{2}110]_{\alpha})$ with one of the conjugate β grain [62, 63]. Tempering of martensite or isothermal decomposition of martensite is another example of diffusional transformation. In case of solute rich Ti-Nb alloys [64, 65] and Ti-Ta alloys [66-68] the decomposition of metastable orthorhombic α'' martensite or β phase to $\alpha+\beta$ (ω) phases occurs through diffusional mechanism. The formation of isothermal ω phase during aging in β Ti alloys also occurs through diffusional mechanism.

1.6.2 Displacive transformations

In this category of phase transformation the atom movements occur in a cooperative manner by a homogeneous distortion and shuffling of lattice planes. In this type of transformation the atoms may move only through a fraction of an interatomic distance. Displacive transformations initiate by the formation of nuclei of the product phase and the growth of these nuclei occurs by the movement of a shear front at a speed that approaches the speed of sound. In Ti alloys, when the high temperature β bcc phase

is cooled at faster rate martensitic transformations and athermal omega phase formation takes place through displacive mechanism.

Titanium alloys containing β -bcc phase stabilizing elements like Nb, Mo, Ta, V etc. form two different types of martensite: α' -hcp and α'' -orthorhombic structures. Also, metastable retention of β and/or formation of ω phase on quenching from high temperature also take place. The type of β -decomposition product depends on the concentration of the alloying elements and the cooling rate. In pure Ti and the solute lean β alloys, the α' -hcp martensite forms, whereas at higher concentration of β stabilizing elements orthorhombic α'' martensite forms. At very high concentration of β stabilizing elements, on fast cooling it does not undergo any transformation and is retained as such at room temperature.

As mentioned before, there are two types of ω phase is found to form in titanium alloys [69]. The *athermal* ω phase is formed on rapid quenching from the β -bcc phase by displacive mechanism. The *isothermal* ω is formed after prolonged aging at low temperature by a diffusional transformation and it is accompanied by finite scale yet, non equilibrium redistribution of solute elements [24, 70]. The ω phase formed in titanium alloys has hexagonal structure and is formed by the collapse of a pair of $(111)_\beta$ planes [24, 70]. The metastable ω phase formed in titanium alloys has received considerable interest due to its influence on the mechanical and physical properties like strength, ductility and superconducting properties of the alloys [69].

Ti alloys containing refractory elements like Ta, Nb, Mo, V, W etc. attracted the attention of most of the researchers at early stage because of their excellent forming characteristics expected from the body centered cubic structure. In present days, these alloys are widely used in biomedical field because of high corrosion resistance and

lower elastic modulus. The occurrence of different types of phase transformation in Ti-TM (TM = Ta, Nb, Mo, V, W) alloys allows to tailor the microstructure to obtain desired properties for any application. In these alloys when the high temperature β bcc phase cooled from β phase form either equilibrium or non-equilibrium phases depending on the cooling rate which implies the importance of kinetics of phase formation.

These β -isomorphous titanium alloys containing refractory elements like Nb, Mo, Ta, V etc. when cooled from high temperature β -bcc phase form stable α phase and metastable phases (α' , α'' retained β and ω) depending on the composition and thermal history. Due to the slow diffusivity of the above elements in the Ti matrix, the β phase may undergo martensitic transformation on cooling to form non-equilibrium products (α' , α'' retained β and ω). A study on Ti-20 Nb alloy showed a $\alpha+\beta$ two phase microstructure on furnace cooling but when the cooling rate increases the martensites along with some amount of retained β phase is found to form [71]. Extensive literature is available on the effect of cooling rate and alloy composition on phase transformations in Ti-TM (TM= Mo, Nb, etc.) alloys [31, 32 72-79]. Athermal ω phase also forms in these systems are formed during cooling from β -bcc phase field.

1.7 Ti-Ta binary system

Ti-Ta binary alloy is a member of β -isomorphous class of Ti alloys and constitute one of the promising corrosion resistant and bio-compatible candidates among $\alpha+\beta$ or β titanium alloys meant for biomedical applications [80]. **Fig. 1.5** represents the equilibrium phase diagram of Ti-Ta binary system. It exhibits complete mutual solubility in both liquid and in high temperature β -bcc phase, however on the Ti-rich side, Ta shows limited solubility in α -hcp phase and the solubility in α -hcp phase

decreases with decrease in temperature. The $\alpha+\beta/\beta$ phase boundary exhibits a broad plateau signifying an extensive domain of β -bcc phase stability. Due to sluggish diffusion of Ta atoms both in α -hcp and β -bcc phases [81-83], there is possibility of formation of metastable phases even at moderate cooling rate by suppressing the equilibrium $\beta \rightarrow \alpha$ phase transformation. In Ti-Ta alloys, the high temperature β -bcc phase transforms to equilibrium α -hcp phase and to α'/α'' -martensites or β phase is retained depending on the composition and cooling rate [84-89]. Extensive research has been carried out to find out the compositional limit for the formation of non-equilibrium phases [31, 86, 88, 89]. *A detailed survey of various research carried out in Ti-Ta alloys is presented in Table-1.2.*

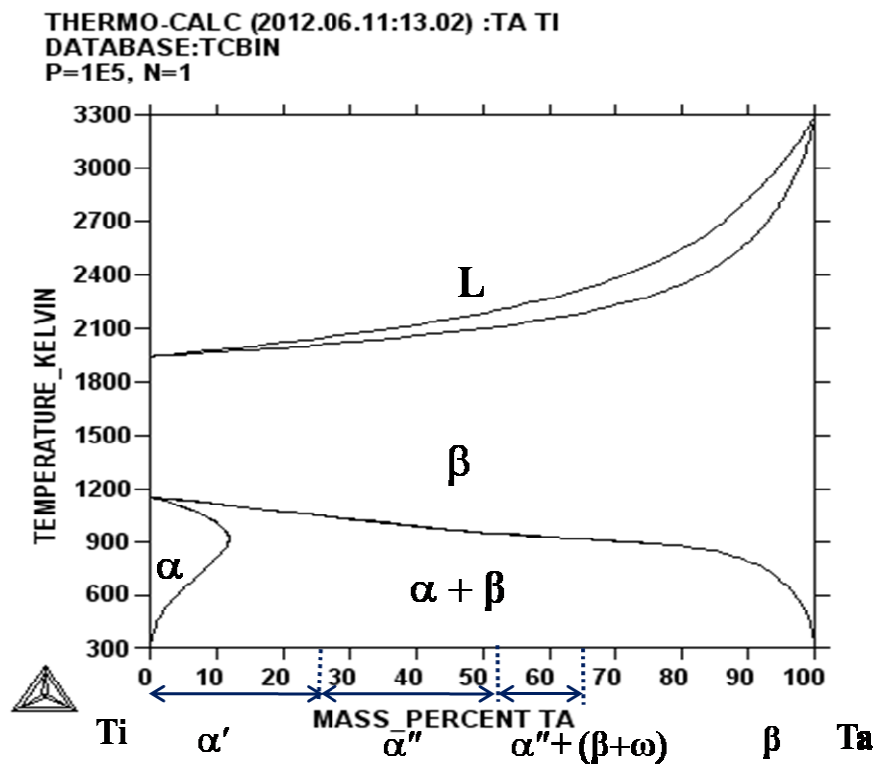


Figure 1.5 Equilibrium phase diagram of Ti-Ta binary system obtained using the ThermoCalc[®] program is shown. The approximate compositional range for formation of α' , α'' and metastable β phases are marked in this figure [86].

In the concentration range of 0-26 mass% Ta α' -hcp martensite, 26-52 mass% α'' - orthorhombic martensite and 52-65 mass% Ta α'' + β phase form. Above 65 mass% Ta the high temperature β phase is retained at room temperature [86]. Unlike Ti-Nb, Ti-Mo alloys, the formation of athermal ω is not reported in Ti-Ta alloys. Instead, isothermal ω phase is formed during aging of quenched Ti-xTa alloy at 673 K. [88]. The formation of ω phase has influence on mechanical properties for ex: the existence of ω phase increases young's modulus [90], hence the formation of ω phase must be avoided to realize low young's modulus to suit biomedical application. The phase transformations [86, 88], evaluation of mechanical properties either experimentally or by first principle calculation [90, 91] and corrosion resistance properties [80] have been characterized in a comprehensive manner for Ti-Ta alloy.

Table-1.2 Review of the work done on Ti – Ta alloys

Alloy System (Concentration of the alloying element are in mass%)	Nature of the study	Reference of the Study
Ti-Ta	Determination of Phase diagram of Ti – Ta system by metallography.	D. J. Maykuth et al. JOM (Trans. AIME) Feb. (1953) 231-237.
Ti-Ta	Transmission Electron Microscopic observation of martensitic transformation in a Ti – 9 wt% Ta alloy.	T. Yamane et al. Acta Metall. 14 (1966) 438-439.
Ti-Ta	Precipitation reactions of α' , α'' martensite and retained β phase during tempering at 400 °C and 600 °C.	K. A. Bywater et al. Philos. Mag. 25 (1972) 1275-1289.
Ti-Ta	Martensitic transformations during quenching from the equilibrium β phase.	K. A. Bywater et al. Philos. Mag. 25 (1972) 1249 -1273.
Ti-Ta	Phase diagram of Ti-Ta alloys	J. L. Murray Bull. Alloy Phase Diagram 2 (1981) 62-66.
Ti-Ta	Investigation of phase structure on quenching the alloys, the direct M_s	S.G. Fedotov et al. Phys. Met. Metall. 60 (1985) 139-143.

	and reverse A_s martensitic transformation temperatures and variation of elastic moduli.	
Ti-Ta	Phase transformation during heating metastable alloys.	S.G. Fedotov et al. Phys. Met. Metall. 62 (1986) 109-113.
Ti-40Ta	Investigation of microstructure and mechanical properties	J. D. Cotton et al. Metall. Mater. Trans. A 25 (1994) 461-472.
Ti-Ta	Kinetics and mechanisms of oxidation of Ti – Ta alloys is studied	R. J. Hanrahan, Jr. et al. Oxid. Metals 47 (1997) 317-353.
Ti-Ta	Interdiffusion of Ta in β -phase Ti-Ta alloys.	D. Ansel et al. Acta Mater. 46 (1998) 423-430.
Ti-60Ta	Influence of processing variables on mechanical properties and phase transformation is studied	R. W. Margevicius, Metall. Mater. Trans. A 29 (1998) 139-147.
Ti-Ta	Kinetics and mechanism thermal oxidation in Ti – Ta alloys with respect to concentration of Ta has been studied	Y. S. Park et al. Oxid. Metal 51 (1999) 383-402.
β -Ti alloys	First principle calculation of effect of alloying element on strength and modulus of β type bio – Ti alloys	Y. Song et al. Mater. Sci. Engg. A 260 (1999) 269-274.
Ti-Ta	Alloying of Ti and Ta by CCLM furnace in a single melting process	A. Morita et al. Mater. Sci. Engg. A 280 (2000) 208-213.
Ti-X Alloys (X=Ta, Nb, Mo, V etc.)	Study of phase constitution of binary Ti - base alloys with d block metals and establishment of the correlation between the M_s curves for these alloys and position of alloying elements in the periodic table.	A.V. Dobromyslov et al. Scr. Mater. 44 (2001) 905-910.
Ti-Ta	Effect of Ta concentration on the phase formation and aging behavior is studied.	M. Ikeda et al. Mater. Trans. 43 (2002) 2984 -2990.
Ti-Ta	Preparation and characterization of Ti – Ta alloys for corrosion application	K. A. de Souza et al. Mater. Lett. 57 (2003) 3010-3016.
Ti-X Alloys (X = Nb, Zr, Ta)	First Principle calculation of elastic moduli.	H.W. Jeong et al. Mater. Sci. Forum 449-452 (2004) 865-868.
Ti-Ta	Effect of Ta concentration on microstructures, Young's modulus and tensile properties of quenched alloys is investigated for biomedical application.	Y. L. Zhou et al. Mater. Sci. Engg. A 371 (2004) 283-290.
Ti-Ta	Study of effect of Ta content and aging temperature on the decomposition of orthorhombic martensite (α'').	Y. L. Zhou et al. Mater. Sci. Engg. A 384 (2004) 92-101.
Ti-Ta	Effect of Ta content on the mechanical properties of the quenched alloys.	Y. L. Zhou et al. Mater. Sci. Forum, 449-452 (2004) 1089-1092.
Ti – X (X = V, Nb, Mo, Ta and W)	First - principles calculation of the young's moduli.	H. Ikehata et al. Phys. Rev. B 70 (2004) 174113-1 – 174113-8.

Ti-Ta	Corrosion resistance and biocompatibility are studied	Y. L. Zhou et al. Mater. Sci. Engg. A 398 (2005) 28-36.
Ti-X Alloys (X= V, Cr, Mn, Fe, Ta, Nb, Mo etc.)	Investigation of the condition for the formation of α'' phase in binary Ti alloys.	A.V. Dobromyslov et al. Mater. Sci. Engg. A 438-440 (2006) 324-326.
Ti-Ta	Determination of interdiffusivity of alloys processed at 1473 K.	J. C. Dibbern, Bachelor of Sci. Thesis Dept.of MS&E, MIT (2007) .
Ti-Ta	Comparison of various properties between Ti-Ta alloys and pure Ti for biomedical applications.	Y. L. Zhou et al. Mater. Trans. 48 (2007) 380-384.
Ti-Ta	Effect of processing on microstructure and properties of Ti – Ta alloys	B. Gortikov, Bachelor of Sci. Thesis submitted to Dept. of MS&E, MIT (2008)
Ti-X Alloys (X= V, Cr, Mn, Fe, Ta, Nb, Mo, Zr etc.)	Investigation of the conditions for formation of non-equilibrium and metastable phase formation in binary Ti- base alloys with d-metals of V- VIII groups.	A.V. Dobromyslov Adv. Mater. Sci. 8 (2008) 37-42.
Ti-Ta (10-80 mass %)	Synthesis of Ti – Ta alloy using CCLM furnace, structural and microstructural characterization using XRD, optical microscopy, determination of β transus temperature by electrical resistivity measurement and comparison of β transus temperature with previously existing literatures.	D. M. Gordin et al. Adv. Eng. Mater. 10 (2008) 714 -719.
Ti-50Ta	Investigation of microstructures and resulting mechanical properties for biomedical applications.	Y. L. Zhou et al. J. Alloys Comp. 466 (2008) 535-542.
Ti-25Ta	Investigation of microstructure, dynamic elastic modulus and mechanical properties for biomedical applications.	Y. L. Zhou et al. Mater. Sci. Engg. C 29 (2009) 1061-1065.
Ti-Ta	Study of corrosion behavior for dental applications.	D. Mareci et al. Acta Biomater. 5 (2009) 3625-3639.
Ti-Ta	Study of phase and structural transformation Ti – Ta alloys in a wide range of Ta concentration.	A.V. Dobromyslov et al. Phys. Met. Metallogr. 107 (2009) 502-510
Ti-Ta	Effect of Ta content on shape memory behavior.	P. John et al. Acta Mater. 57 (2009) 1068-1077.
Ti-(40-65) Ta	Study of microstructure, shape memory behaviors and the effect of heat treatment on shape memory behavior.	Y. Ma et al. Mater. Sci. Forum 610-613 (2009) 1382-1386.
Ti-Ta	First principle calculation of the effect of Ta content on the phase stability and elastic properties of Ti – Ta alloys with BCC crystal structure are studied.	C.Y. Wu et al. Solid State Sci. 12 (2010) 2120-2124.
Ti-Ta	Study of atomic mobilities of Ti, Ta	Y. Liu et al. CALPHAD 34

	using DICTRA software	(2010) 310-316
Ti-Ta	Effect of manufacturing process on the biocompatibility of Ti – 30 Ta alloy is investigated.	P. Gill et al. J. Mater. Engg. Performance 20 (2011) 819-823.

The present study therefore presents a comprehensive description of the thermodynamics and kinetics aspects of Ti-Ta and Ti-Ta-Nb system with emphasis on three main objectives:

- Evaluation of thermodynamic properties of Ti-xTa (x=5, 10, 15, 20 mass %) alloys using drop calorimetry
- Study of phase transformation characteristics and kinetics of Ti-xTa (x=5, 10, 15, 20 mass %) alloys using differential scanning calorimetry.
- Thermodynamics, kinetics and mechanism of phase transformation in Ti-5Ta-1.8Nb alloy

1.8 Organization of the Thesis

This thesis is divided into six chapters which are organized in the following manner.

In this introductory *Chapter 1*, the physical metallurgy of titanium alloys is briefly described. It contains the review of the work carried out on phase stability and kinetics of phase transformation in α + β or β titanium alloys. It also summarizes the work carried out in Ti-Ta alloys till date.

Chapter 2 describes the experimental methods adopted in this investigation. The details with respect to melting of alloys, basic compositional characterization and sample preparation for calorimetry and microscopy investigations, including the details of compositional homogenization treatment and room temperature phase characterization by x-ray diffraction are presented in this chapter. However, the major portion of chapter 2 deals with the detailed descriptions including the calibration

procedures of the static drop and dynamic differential scanning calorimetry techniques. The method of data analysis of the static and dynamic calorimetry is also discussed in this chapter.

Chapter 3 presents and discusses in full perspective of the drop calorimetry measurements of enthalpy increment ($H_T - H_{298.15}$) for four Ti-xTa ($x = 5, 10, 15, 20$ mass %) alloys in the temperature range of 463-1257 K. This temperature range of measurements involve $\alpha+\beta$ two phase field and also the $\alpha+\beta \rightarrow \beta$ phase change. The measured enthalpy variation in the transformation domain is used to obtain the energetic quantities of $\alpha+\beta \rightarrow \beta$ phase change and this is accomplished by invoking an appropriate description of the diffusional kinetics involved. This chapter also discusses the theoretical estimation of low temperature (0 K to 298.15 K) specific heat and the derivation of entropy (S) and Gibbs free energy (G) as a function of temperature.

Chapter 4 presents the results on kinetics of $\alpha \leftrightarrow \beta$ phase transformation in Ti-5, 10, 15, 20 Ta alloys. Most importantly, this chapter brings out the subtle differences involved in the kinetics of thermally activated $\alpha \rightarrow \beta$ and $\beta \rightarrow \alpha$ transformation, probed using dynamic Differential Scanning calorimetry as a function of scan rate in the range 3-99 K min⁻¹. The kinetic modeling has been done by adopting a suitable version of Kolmogorov-Johnson-Mehl-Avrami (KJMA) formalism and the estimated kinetic parameters are discussed in the light of available diffusivity data for transition metals in titanium. Useful data on continuous heating transformation (CHT) and continuous cooling transformation (CCT) have been generated for all the alloys. An extensive post calorimetry microscopic investigation of transformed microstructures has also been discussed in detail in this chapter.

Chapter 5 presents the results of calorimetry-cum modeling investigation of Ti-5Ta-1.8Nb alloy. The scope of the investigation on Ti-5Ta-1.8Nb is along the same

lines of that on Ti-Ta alloys. It is necessary to mention here, that the difficulties encountered in interpreting the results of Ti-5Ta-1.8Nb alloy, an alloy developed for a high corrosion resistance application in this laboratory provided the motivation to undertake a systematic investigation on Ti-Ta and Ti-Nb binaries, of which the results on Ti-Ta forms the core of this thesis. Chapter 5 also contains the results of electron microscopy characterization of transformation microstructures, to identify the transformation mechanisms of Ti-5 Ta-1.8 Nb ternary alloy.

Chapter 6 summarizes the results of chapter 3-5 and is devoted to explore the further avenues of research which can be profitably continued from what limited data has been accrued in this study.

References:

- [1] G. Lutjering and J. C. Williams, *Titanium*, 2nd ed., Springer-Verlag, Berlin, Heidelberg, New York, 2007.
- [2] R. Boyer, G. Welsch and E. W. Collings, *Materials Properties Handbook: Titanium Alloys*, ASM International Materials Park OH, 1994
- [3] J. D. Destefani, in: *Metals Handbook, Properties and Selection: Nonferrous Alloys and Special-Purpose Materials*, ASM International Materials Park, Ohio 10th ed. Vol.2, 1992.
- [4] B. H. Hanson, *Mater. Design* 7 (1986) 301-307.
- [5] R.I. Jaffee and N.E. Promisel, *The Science, Technology and Application of Titanium*, Pergamon Press, Oxford, 1970.
- [6] D. M. Stefanescu and R. Ruxanda, *Metallography and Microstructures*, G. F. Vander Voort (eds.) ASM Handbook, Vol. 9, 116-126.
- [7] R. R. Boyer, *Mater. Sci. Engg. A* 213 (1996) 103-114.
- [8] I. J. Polmear, *Light Alloys: From traditional Alloys to Nano crystals*, 4th ed., Elsevier, Amsterdam, 2006.
- [9] I. V. Gorinin, *Mater. Sci. Engg. A* 263 (1999) 112-116.
- [10] J. W. Davis, M. A. Ulrickson and R. A. Causey, *J. Nucl. Mater.* 212-215 (1994) 813-817.
- [11] K. Wang, *Mater. Sci. Engg. A* 213 (1996) 134-137.
- [12] L. M. Elias, S.G. Schneider, S. Schneider, H. M. Silva and F. Malvisi, *Mater. Sci. Engg. A* 432 (2006) 108-112.
- [13] M. Semlitsch, *Clinical Mater.* 2 (1987) 1-13.
- [14] M. Niinomi, *J. Mech. Behavior Biomedical Mater.* 1 (2008) 30-42.
- [15] H. J. Rack and J. I. Qazi, *Mater. Sci. Engg. C* 26 (2006) 1269-1277.
- [16] C. Zhaoa, X. Zhanga and P. Caob, *J Alloys Comp.* 509 (2011) 8235-8238.
- [17] E. Vasilescu, P. Drob, C. Vasilescu, S. I. Drob, E. Bertrand, D. M. Gordin and T. Gloriant, *Mater. Corros.* 61 (2010) 947-954.
- [18] R.W. Schutz and H. B. Watkins, *Mater. Sci. Engg. A* 243 (1998) 305-315.
- [19] M. Ishii, M. Kaneko and T. Oda, *Nippon Steel Technical Report No. 87*, January 2003, 49-56.
- [20] J. R. Davis, *Alloying: understanding the basics*, ASM international, Materials park, OH, USA, 2001.

- [21] A. M. Russell and K. L. Lee, Structure-Property relations in nonferrous metals, Wiley - Interscience, New Jersey, 2005.
- [22] Z. Nishiyama, M. Oka and H. Nakagawa, Trans JIM 7 (1966) 168-173.
- [23] Y. K. Vohra, E. S. K. Menon, S. K. Sikka and R. Krishnan, Acta Metall. 29 (1981) 457-470.
- [24] D. de Fontaine, Metall. Trans. A 19 (1988) 169-175.
- [25] S. K. Sikka, Y. K. Vohra and R. Chidambaram, Prog. Mater. Sci., 27 (1982) 245-310.
- [26] G. Gottstein and L. S. Shvindlerman, *Grain boundary migration in metals: thermodynamics, kinetics, applications*, 2nd ed., Taylor Francis, London 2009.
- [27] C. Woodward, J. M. MacLaren and S. Rao, J. Mater. Res. 7 No. 7 (1992) 1735-1750.
- [28] W. Sha and S. Malinov, in: *Titanium Alloys: Modelling of microstructure, properties and applications*, CRC Press, Boca Raton (2009).
- [29] J. F. Breedis and L. Kaufman, Metall. Trans. B 2 (1971) 2359-2371.
- [30] A. A. Ogwu and T. J. Davies, Mater. Sci. Tech. 10 (1994) 1026-1030.
- [31] A. V. Dobromyslov and V. A. Elkin, Scripta Mater. 44 (2001) 905-910.
- [32] A. V. Dobromyslov, Adv. Mater. Sci. 8 (2008) 37-42.
- [33] R. W. Margevicius, J. D. Cotton, Metall. Mater. Trans. A 29 (1998) 139-147.
- [34] S. Malinov, Z. Guo, W. Sha and A. Wilson. Metall Mater. Trans. A 32 (2001) 879-887.
- [35] B. Gortikov, "Effect of processing on microstructure and properties of Ti-Ta alloys", Bachelor of Sci. Thesis submitted to Massachusetts Institute of Technology, (2008).
- [36] G. Lutjering, Mater. Sci. Engg. A 243 (1998) 32-45.
- [37] S. Malinov and W. Sha, JOM, September (2005) 42-45.
- [38] N. Saunders, Titanium '95: Science and Technology, in: P. A. Blenkinsop, W. J. Evans, H. M. Flower (Eds.), Proceedings of the Eighth World Conference on Titanium, The Institute of Materials, London, (1996) 2167-2176.
- [39] V. S. Raghunathan, A. L. E. Terrance and S. Raju, in: *Metastable Microstructures, Principles, Design and Applications*,: D. Banerjee and L. A. Jacobson (eds.), Oxford and IBH Publishing Pvt. Ltd., New Delhi (1993) 161-183.

- [40] T. Karthikeyan, R. Mythili, S. Saroja and M. Vijayalakshmi, *Metals Mater. Processes*. 18 (2006) 269-282.
- [41] K. Kapoor, V. Kain, T. Gopalkrishna, T. Sanyal and P. K. De, *J. Nucl. Mater.* 322 (2003) 36-44.
- [42] S. Saroja, M. Vijayalakshmi and Baldev Raj, *Trans. Indian Inst. Metals* 61 (2008) 389-398.
- [43] R. Mythili, S. Saroja, M. Vijayalakshmi and V. S. Raghunathan, *J. Nucl. Mater.* 345 (2005) 167-183.
- [44] R. Mythili, A. Ravi Shankar, S. Saroja, V. R. Raju, M. Vijayalakshmi, R.K. Dayal, V. S. Raghunathan and R. Balasubramaniam, *J. Mater. Sci.* 42 (2007) 5924-5935.
- [45] R. Mythili, S. Saroja and M. Vijayalakshmi, *Mater. Sci. Engg. A* 454-455 (2007) 43-51.
- [46] T. Karthikeyan, Arup Dasgupta, S. Saroja, R. Khatirkar, M. Vijayalakshmi and I. Samajdar, *Mater. Sci. Engg. A* 485 (2008) 581-588.
- [47] A. J. Prabha et al. unpublished research.
- [48] A. J. Prabha, S. Raju, B. Jeyaganesh, Arun Kumar Rai, Madhusmita Behera, M. Vijayalakshmi, G. Paneerselvam and I. Johnson, *Physica B* 406 (2011) 4200-4209.
- [49] Soumya Nag, "Influence of beta instabilities on the early stages of nucleation and growth of alpha in beta titanium alloys", Ph. D. thesis submitted to the Ohio state university.
- [50] R. Mythili, V. Thomas Paul, S. Saroja, M. Vijayalakshmi and V. S. Raghunathan, *Mater. Sci. Engg. A* 390 (2005) 299-312.
- [51] S. L. Semiatin, V. Seetharaman and I. Weiss, *J Metals* June (1997) 33-39.
- [52] S. Banerjee and P. Mukhopadhyay, *Phase transformation Examples from Titanium and Zirconium Alloys*, Elsevier, Amsterdam, 2007.
- [53] R. R. Boyer and R. D. Briggs, *J. Mater. Engg. Perform.* 14 (2005) 681-685.
- [54] D. Raabe, B. Sander, M. Friak, D. Ma and J. Neugebauer, *Acta Mater.* 55 (2007) 4475-4487.
- [55] H. M. Silva, S. G. Schneiderb and C. Moura Neto, *Mater. Sci. Engg. C* 24 (2004) 679-682.

- [56] M. Geetha, A. K. Singh, R. Asokamani and A. K. Gogia, *Prog. Mater. Sci.* 54 (2009) 397-425.
- [57] H. W. Rosenberg, in: *The science, Technology and Application of Titanium*, Proc. First Int. Conf. Titanium, London, R. I. Jafee and N. E. Promisel (Eds.), Pergamon Press, 1970, p.851.
- [58] F. J. Gil, M. P. Ginbera, J. M. Manero, and J. A. Planell, *J. Alloys Comp.* 329 (2001) 142-152.
- [59] R. Ding, Z. X. Guo, and A. Wilson, *Mater. Sci. Engg. A* 327 (2002) 233-245.
- [60] D. Bhattacharya, G. B. Viswanathan, R. Denkuberger, D. Furre and H. L. Fraser, *Acta Mater.* 51 (2003) 4679-4691.
- [61] H. M. Flower, *Mater. Sci. Techno.* 6 (1990) 1082-1092.
- [62] N. Miyano, H. Fujiwara, K. Ameyama and G. C. Weatherly, *Mater. Sci. Engg. A* 333 (2002) 85-91.
- [63] D. I. Potter, *J. Less Common Metals* 31 (1973) 299-.
- [64] D. L. Moffat and U. R. Kattner, *Metall. Trans. A* 19 (1988) 2389-2397.
- [65] Y. Mantani and M. Tajima, *Mater. Sci. Engg. A* 438-440, (2006) 315-319.
- [66] K. A. Bywater and J. W. Christian, *Philos. Mag. A* 25 (1972) 1275-1289.
- [67] M. Ikeda, S. Y. Komatsu and Y. Nakamura, *Mater. Trans.* 43 No. 12 (2002) 2984-2990.
- [68] Y. L. Zhou, M. Niinomi and T. Akahori, *Mater. Sci. Engg. A* 384 (2004) 92-101.
- [69] B. S. Hickman, *J. Mater. Sci.* 4 (1969) 554-563.
- [70] S. Banerjee, in: *Mestable Microstructures, Principles, Design and Applications*, D. Banerjee and L. A. Jacobson (eds.), Oxford and IBH Publishing C. Pvt. Ltd., New Delhi, 1993, 127-147.
- [71] C. R. M. Afonso, G. T. Aleixo, A. J. Ramirez and R. Caram, *Mater. Sci. Engg. C* 27 (2007) 908 -913.
- [72] E. Sarath K. Menon and R. Krishnan, *J. Mater. Sci.* 18 (1983) 365-374.
- [73] M. K. Koul and J. F. Breedis, *Acta Metall.* 18 (1970) 579-588.
- [74] T. Ahmed and H. J. Rack, *J. Mater. Sci.* 31 (1996) 4267-4276.
- [75] T. Ahmed and H. J. Rack, *Mater. Sci. Engg. A* 243 (1998) 206-211.
- [76] X. Tang, T. Ahmed and H. J. Rack, *J. Mater. Sci.* 35 (2000) 1805-1811.
- [77] D. L. Moffat and D. C. Larbalestier, *Metall. Trans.* 19A (1988) 1677-1685.

- [78] R. Davis, H. M. Flower and D. R. F. West, *J. Mater. Sci.* 14 (1979) 712-722.
- [79] S. A. Souza, R. B. Manicardi, P.L.Ferrandini, C. R. M. Afonso, A. J. Ramirez and R. Caram, *J. Alloys Comp.* 504 (2010) 330-340.
- [80] Y. L. Zhou, M. Niinomi, T. Akahori, H. Fukui and H. Toda, *Mater. Sci. Engg. A* 398 (2005) 28-36.
- [81] D. Ansel, I. Thibon, M. Boliveau and J. Debuigne, *Acta Mater.* 46 (1998) 423-430.
- [82] Y. Liu, L. Zhang, Y. Du, J. Wang and D. Liang, *CALPHAD Comp. Coupling of Phase Diag. Thermochemi.* 34 (2010) 310-316.
- [83] R. A. Perez, F. Dymont, G. Garcia Bermudez, D. Abriola and M. Behar, *App. Phys. A* 76 (2003) 247-250.
- [84] K. A. de Souza and A. Robin, *Mater. Lett.* 57 (2003) 3010-3016.
- [85] Y. L. Zhou, M. Niinomi and T. Akahori, *Mater. Sci. Engg. A* 371 (2004) 283-290.
- [86] S. G. Fedotov, T. V. Chelidze, Y. K. Kovneristyy and V. V. Sanadze, *Phys. Met. Metall.* 62 (1986) 109-113.
- [87] T. Yamane and J. Ueda, *Acta Metall.* 14 (1966) 438-439.
- [88] K. A. Bywater and J. W. Christian, *Philos. Mag. A* 25 (1972) 1249-1273.
- [89] J. D. Cotton, J. F. Bingert, P. S. Dunn and R. A. Patterson, *Metall. Mater. Trans. A* 25 (1994) 461-472.
- [90] H. Ikehata, N. Nagasako, T. Furuta, A. Fukumoto, K. Miwa and T. Saito, *Phys. Rev. B* 70 (2004) 174113-1-174113-8.
- [91] Y. L. Zhou, M. Niinomi and T. Akahori, *Mater. Sci. Forum* 449-452 (2004) 1089-1092.

Chapter-2

Experimental Methods

2.1 Introduction

As described in Chapter-1, the high temperature phase stability and phase transformation characteristics in Ti-Ta (Nb) binary and ternary alloys is characterized by static drop and dynamic differential scanning calorimetry, which are used as major experimental techniques in the present study. The present studies are aimed at adding some useful input to the existing thermodynamic property database on titanium alloys which is expected to be of use to material scientists for designing advanced titanium base alloys. Hence, in addition to calorimetry, detailed microscopy analysis has also been carried out to study the phase transformation mechanism and microstructural details in Ti-Ta and Ti-5Ta-1.8Nb alloys.

2.2 Organization of the chapter

This chapter describes the experimental methods involved in the study. In section 2.3, the details of the methods of melting the alloys, their chemical composition and the heat treatment are explained. Section 2.4 presents the specimen preparation method adopted for various experimental techniques employed in this study. The following calorimetry techniques have been used extensively in this study, (a) Isothermal inverse drop calorimetry to measure equilibrium thermodynamic properties and (b) Dynamic differential scanning calorimetry (DSC), which involves the measurement of phase transformation temperature and the kinetics of phase transformation. Hence the basic principles of calorimetry have been presented in section 2.5, followed by the detailed description of drop calorimetry and DSC in section 2.6 and 2.7 respectively. The working principle and experimental procedures of the respective calorimeters are discussed in these sections. Microstructural characterization has been carried out using X-Ray Diffraction (XRD), optical microscopy, Scanning Electron Microscopy (SEM), Transmission Electron Microscopy (TEM) and microhardness. The operating condition of these techniques and the analysis procedure are explained briefly in sections 2.8.

2.3 Alloy preparation

Two alloy systems have been taken up in this study namely Ti-Ta and Ti-Ta-Nb. Four different compositions of Ti-xTa (x=5, 10, 15, 20 mass %) alloys were prepared from its constituents pure Ti (99.99 % - sigma Aldrich, U. K.) in rod form and Ta (Good fellow Metals) in the appropriate stoichiometric ratio. Melting was carried out using tungsten electrode tri-arc furnace with water cooled copper hearth under high pure helium gas atmosphere. Prior to melting the arc furnace was evacuated and backfilled with high purity helium gas. A positive back pressure of 1.2 atmospheres was maintained by gently permeating He, so as to minimize the preferential loss of titanium due to evaporation. Before melting the constituents were ground to remove the oxide layers and ultrasonically cleaned with methanol to remove possible surface contaminants. On account of the large difference in melting points (Ti: 1943 K, Ta: 3269 K) and densities (Ti: 4.51 g.cm⁻³, Ta: 16.6 g.cm⁻³) of pure Ti and Ta, the designed alloy was remelted three to four times. At the same time, the ingots were flipped between two melting processes in order to improve the chemical homogeneity. The as melted ingots were in the form of button shape after melting and mass of each alloy button was in the range of 1 to 2 g, as larger mass resulted in appreciable compositional inhomogeneity of the final melted product. The weight loss after melting was found to be less than 1 mass %. All ingots of the Ti-Ta binary alloy were homogenized at 1273 K for 3 h under flowing high pure Ar atmosphere (Iolar grade-I) and furnace cooled to room temperature in order to avoid the formation of non-equilibrium products [1]. The chemical composition of Ti-xTa (x=5, 10, 15, 20 mass %) binary alloys was analyzed by inductively coupled plasma analysis and are listed in **Table 2.1**. The Ti-Ta alloys in this homogenized condition have been used for further studies.

Table 2.1 Chemical compositions of Ti-xTa (x=5, 10, 15, 20 mass %) alloys

<i>Alloy System</i>	Ta	Fe	O	Cu	V	W	Ti
	<i>Concentration (mass %)</i>						
Ti – 5 Ta	4.76±0.05	0.20±0.02	0.008	<0.02	<0.02	<0.05	Balance
Ti – 10 Ta	10.12±0.1	0.41±0.05	0.009	<0.02	<0.02	<0.05	
Ti – 15 Ta	15.10±0.2	0.09±0.03	0.007	<0.02	<0.02	<0.05	
Ti – 20 Ta	20.80±0.2	0.22±0.03	0.008	<0.02	<0.02	<0.05	

Ternary Ti-5 mass% Ta-1.8 mass% Nb alloy was melted by a triple vacuum arc remelting method [2] at Nuclear Fuel Complex (NFC), Hyderabad. The constituents for the alloy were taken from Ti sponge, high pure Ta and Nb sheet. The as cast alloy had been subjected to a series of thermo-mechanical processing and received in the form of rods of 25 mm and 12.5 mm diameter and reduced to 10 mm by cold swaging which was further reduced to 2.5 mm diameter rod in the laboratory. This 2.5 mm diameter rod was stress relieved in the $\alpha+\beta$ phase field by holding at 973 K for about 5 h. The Ti – 5 mass% Ta – 1.8 mass% Nb alloy in the above mentioned condition was used as the starting material for the present study. The chemical composition analysis of Ti-5Ta-1.8 Nb ternary alloy had been performed on as cast ingot using wet chemical analysis at NFC, Hyderabad. The concentration of Ta and Nb were confirmed by Inductively Coupled Plasma Mass Spectrometry and that of Fe by Atomic Absorption Spectrophotometry. The composition of Ti-5 mass% Ta-1.8 mass% Nb ternary alloys are listed in **Table 2.2**.

Table 2.2 Chemical composition of Ti-5Ta-1.8Nb ternary alloy

<i>Element</i>	Ta	Nb	Fe	O	N	H	C	Ti
<i>Concentration</i>	<i>(mass %)</i>		<i>(ppm by mass)</i>					
		4.39	1.85	263	500	47	9	125

2.4 Specimen preparation

This section describes the method for preparing the specimens for calorimetry and microscopy. The samples for calorimetric measurements were cut using diamond coated copper wheel and they were ground to remove the surface contaminants and to make the surface flat for better thermal conduction in case of differential scanning calorimetry experiment. They were cleaned with methanol or acetone and dried prior to weighing them. The mass of the samples used for drop and differential scanning calorimetry (DSC) experiments were in the range of 40-60 and 50-80 mg with an accuracy of ± 0.1 mg respectively.

The specimens for optical microscopy, scanning electron microscopy (SEM) and micro hardness measurement were prepared by conventional mechanical grinding using successive grades of SiC papers and final polishing with silica suspension. The polished samples were etched with Kroll's reagent (2 ml HF, 8 ml HNO₃ & 90 ml H₂O) [3] by swabbing. Samples for transmission electron microscopy (TEM) investigations were prepared by mechanically grinding a 500 μm thick slice of the alloy up to 150 μm thickness, from which disks of 3 mm diameter were punched out and further reduced to 50 μm thickness using a tripod polisher. Final thinning of specimen was carried out by ion milling using a Technoorg Linda IV4 ion miller to electron transparency.

2.5 Primary experimental techniques: Calorimetry

2.5.1 Basic principle of calorimetry

Calorimetry is the measurement of thermal energy changes associated with the change in the state of the material or during a physical and chemical process. The basic principle of calorimeter is based on the law of conservation of thermal energy, i.e. when two bodies at different temperatures are in thermal contact and no heat transfers between the system and the environment, then heat lost by the hotter body will be equal to the heat gained by the colder body. If this heat transfer takes place in a properly

insulated environment, then the amount of heat transferred is directly proportional to the temperature difference between the two bodies and is given by the following expression.

$$Q = K(T) \times \Delta T \quad (2.1)$$

where, $K(T)$ is the temperature dependent proportionality constant. The proportionality constant K corresponds to the apparent heat capacity of the sample along with the heat transfer characteristics of entire calorimeter cell (crucible, temperature sensor) including the gas flow rate and gas pressure. Although calibration constant $K(T)$ can be estimated *ab-initio* [4], it is preferred to estimate the $K(T)$ experimentally using a standard material for which the amount of Q or enthalpy transacted is already known accurately.

2.5.2 Classification of calorimeters

There are three criteria for the classification of calorimeters [4].

1. The principle of measurement

- Heat conduction calorimeter
- Heat accumulation calorimeter
- Heat exchange calorimeter

2. Mode of operation

- Isothermal calorimeter
 - Isoperibol calorimeter
 - Adiabatic calorimeter
- } static mode
- Scanning of surrounding
 - Isoperibol scanning
 - Adiabatic scanning
- } dynamic mode

3. The construction principle

- Single calorimeter

➤ Twin or differential calorimeter

The present study deals with static drop calorimetry and dynamic differential scanning calorimetry. Static drop calorimetry experiments are performed at constant temperature and under close to equilibrium condition which helps to get equilibrium thermodynamic properties of a stable phase as a function of temperature. In dynamic differential scanning calorimetry, the temperature of the furnace as well as the sample is continuously changed with time and the experiments are carried out under non-equilibrium condition [5]. The various phase transition temperatures as a function of heating and cooling rate together with the heat effect involved in the phase transition are determined by this technique. A detailed description of the static drop calorimeter and dynamic differential scanning calorimeter is presented below.

2.6 Drop Calorimeter

2.6.1 General principle

Drop calorimetry is a technique to measure enthalpy and heat capacity. The drop calorimeter experiment involves isothermal measurements. In the conventional drop calorimetry, the sample is heated to a constant predetermined temperature at a constant heating rate and allowed to equilibrate at that temperature for a fixed duration. After equilibration the sample is dropped into a well insulated calorimeter block that is maintained at ambient temperature. Because of temperature differential there is heat transfer from the sample to the calorimeter substance until thermal equilibrium is attained. The measured rise in the temperature is used to obtain the heat content or enthalpy (Q) of the sample by knowing its mass (m) and heat capacity (C_p) of the calorimeter substance which is given by

$$Q = m \times C_p \times \Delta T \quad (2.2)$$

In drop experiment the dropping of the sample of interest is usually followed by the dropping of a reference material with known mass and enthalpy under identical

experimental conditions. The drop calorimeter experiments involve the measurements at closely spaced interval of discrete temperatures with fresh samples at each temperature. Notwithstanding the fact that the successive drop experiment can be performed at reasonably closely spaced temperature intervals, the drop calorimetry experiment results in discrete data points. Hence one does not obtain a continuous data of enthalpy as a function of temperature using drop calorimeter. The output of the drop calorimetry experiment, heat flow (Q) is related to enthalpy by the following equation

$$Q = m \times C(T) \times (H_T - H_{298.15}) \quad (2.3)$$

where $C(T)$ is the calibration constant which is determined by calibration with a reference material like α - Al_2O_3 . By determining $Q(T)$ as a function of temperature T the enthalpy of the sample at various temperatures can be obtained. The enthalpy versus temperature curve or drop curve for a phase transition in a material taking place at constant temperature is shown in **Fig. 2.1** [6].

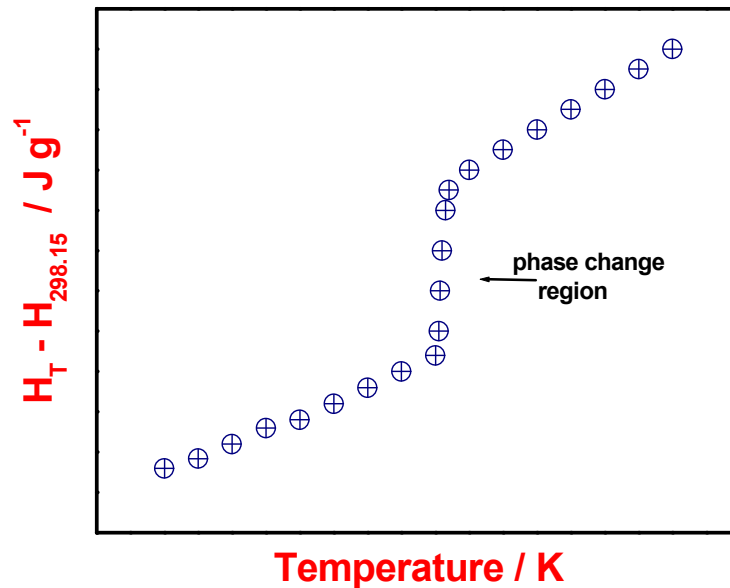


Figure 2.1 Schematic of enthalpy increment variation with temperature. This is referred to as ‘drop curve’ in this thesis.

2.6.2 Inverse Drop Calorimeter

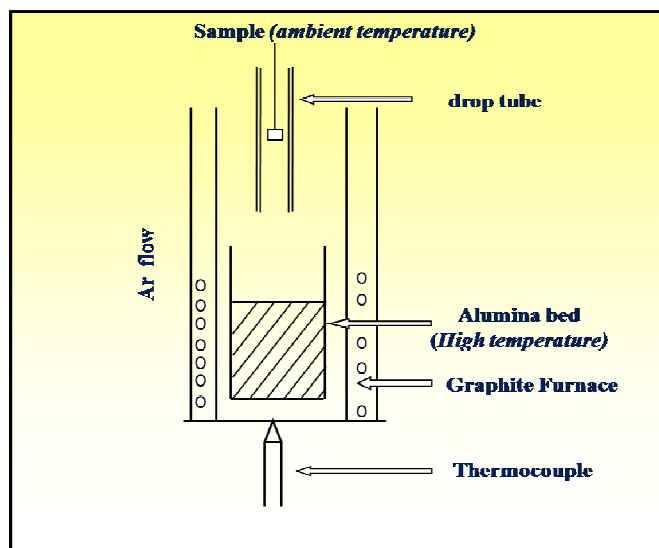


Figure 2.2 Schematic representation of Inverse Drop Calorimeter



Figure 2.3 The experimental set up of drop calorimeter

In the inverse drop calorimetry, the cold sample at room temperature (298.15 K) is dropped into the calorimeter block which is equilibrated at the desired high temperature. The principal advantage of using inverse drop calorimetry is the absence of heat loss during dropping the cold sample to the hot calorimetry block unlike conventional drop calorimeter. There are some more advantages of inverse drop

calorimeter over normal drop calorimeter such as adoption of small sample size, able to study many different types of chemical reactions etc. **Fig. 2.2** represents the schematic of an inverse drop calorimeter. In the present study, the experiments are performed using *Setaram*[®] multi HTC 96 inverse drop calorimeter [7]. The experimental set up of present drop calorimeter is shown in **Fig. 2.3**. The essentials parts of drop calorimeter are described below very briefly [8].

2.6.2.1 High temperature furnace

The high temperature furnace is suspended from the calorimeter cabinet's top plate. The heating element of the furnace is made of graphite tube which surrounds the experimental chamber of the calorimeter and is heated by resistance heating element up to a maximum temperature of 1773 K. A sealed alumina tube crosses the furnace through the centre of the heating element and insulates the experiment chamber from the furnace atmosphere. The line diagram of the high temperature furnace is shown in **Fig. 2.2**.

2.6.2.2 Multi-sample introducer and the drop Tube

The multi sample introducer is equipped at the top portion of the experimental chamber which provides 23 slots to load samples into it. Normally four to six samples are loaded for each measurement. For each sample, a reference sample is also loaded in the adjacent slot. The samples are dropped into the calorimeter block through a guiding alumina tube called drop tube (**Fig. 2.2**) so that the sample falls exactly into the sample crucible during the course of the experiment.

2.6.2.3 Measurement head

Measurement head is an integrated structure made of a cylindrical re-crystallized alumina tube in which two grooves are cut at its bottom to accommodate the sample crucible. The sample crucible used in the present drop calorimeter experiment is made of recrystallized alumina and it contains high pure alumina powder called as calorimeter

substance onto which the samples are dropped during the experiment and in each experiment the filling level of alumina powder in the sample crucible is nearly the same. The sample crucible along with alumina powder is referred as the alumina bed in the present thesis. The sample crucible has a working volume of 6.25 cm^3 with diameter of 16.20 mm and height 44.50 mm. The temperature of the sample crucible is monitored by a thermocell made up of 28 B-type thermocouples distributed over the bottom and side surface of the crucibles. Also a reference crucible having an identical thermocell arrangement is kept underneath the sample crucible and both the sample and reference crucible is placed in the uniform temperature zone of the graphite furnace. The temperature of the furnace and the sample is monitored by two thermocouples of B type (PtRh-6% / PtRh-20%).

2.6.2.4 Gas, Vacuum, Chill-water Circuit and Controller

The equipment contains two separate gas circuits, one for the furnace and another for the analysis chamber to maintain the required inert gas atmosphere. An external rotary vacuum pump (EDWARDS) supplied by *Setaram* is used for evacuating both the experimental and furnace chambers before starting the experiment. An external chill water supply with controlled flow (CWC 4500) is provided for the furnace cooling. The heating schedule programming, the data acquisition and storage are performed through the CS 32 controller interfaced with the personal computer.

The procedure for performing inverse drop calorimetry experiment is discussed in the following section.

2.6.2.5 Experimental procedure

The samples for drop calorimetry measurements were loaded in to the specimen slots of the multi sample introducer of *Setaram* multi HTC 96 inverse drop calorimeter. The standard or reference $\alpha - \text{Al}_2\text{O}_3$ samples, supplied by *Setaram* drop were also loaded adjacent to the sample used for the experiment. The sample crucible or the

working crucible was filled with high pure alumina powder to 3/4th of its capacity and loaded in to the measurement head. After loading the samples and placing the working crucible in its position, the furnace and experimental chamber were evacuated using rotary pump. This was followed by purging both the experimental chamber and furnace with high purity argon gas (Iolar grade II) for few times and continuing with further evacuation. Once the evacuation process was completed both the chambers were allowed to fill with argon gas until the gas pressure level reaches one atmosphere pressure. An inert atmosphere was maintained throughout the experiment in order to prevent the evaporation of carbon from the graphite furnace at high temperature and also to avoid the oxidation of sample. The chill water supply was switched on before the furnace is started to heat. The furnace was gradually heated from 298.15 K to a desired temperature at the rate of 10 K min⁻¹. The surrounding graphite furnace heats the alumina bed. Once the pre-set value of the alumina bed temperature was reached within the accuracy of ± 0.1 K, the samples were dropped from the respective slot to the hot alumina bed through drop tube. The heat absorbed by the sample upon its drop from the ambient temperature into the hot alumina bed can be quantified by monitoring the change in temperature as a function of time t . The integrated output of the drop experiment ΔV vs time for one experimental run is shown in **Fig. 2.4**. The net heat Q flow from the hot alumina bed to the cold sample was measured as area under ΔV vs time t curve [9] and can be represented by the following expression.

$$Q = C(T) \times \Delta V \times \Delta t \quad (2.4)$$

The dropping of the sample at a particular temperature was followed by the dropping of a standard or reference sample like α -Al₂O₃ with known enthalpy and mass at the same temperature in order to determine the calibration constant $C(T)$. Both dropping of the sample and reference were performed under identical conditions. The whole experiment other than the dropping of sample was controlled through a computer that is connected

to the calorimeter by a proprietary interface module. The signals from the calorimeter are digitized and transferred to a computer via an RS 232 series interface. The data acquisition period for each drop was maintained for about 20-25 minutes in the present study. Once the data acquisition was completed for one experiment, a gap of about 20 minutes was kept before dropping the next sample so that the alumina bed regain its thermal equilibrium. Fresh samples were used for each drop experiment. In the present study, the drop experiments for Ti-xTa (x=5, 10, 15, 20 mass %) alloys were performed in the temperature range of 463-1260 K and for Ti-5mass %Ta-1.8mass %Nb alloy in the temperature range of 463-1457 K. After the experiment, the samples were weighed to check any loss or gain due to reaction or due to oxidation. The weight change was found to be less than 1 mg. The isothermal drop experiment is performed at successively higher temperatures with approximate temperature step of 25 K and in the high temperature region with a temperature interval of 10 K due to the large scatter in the data.

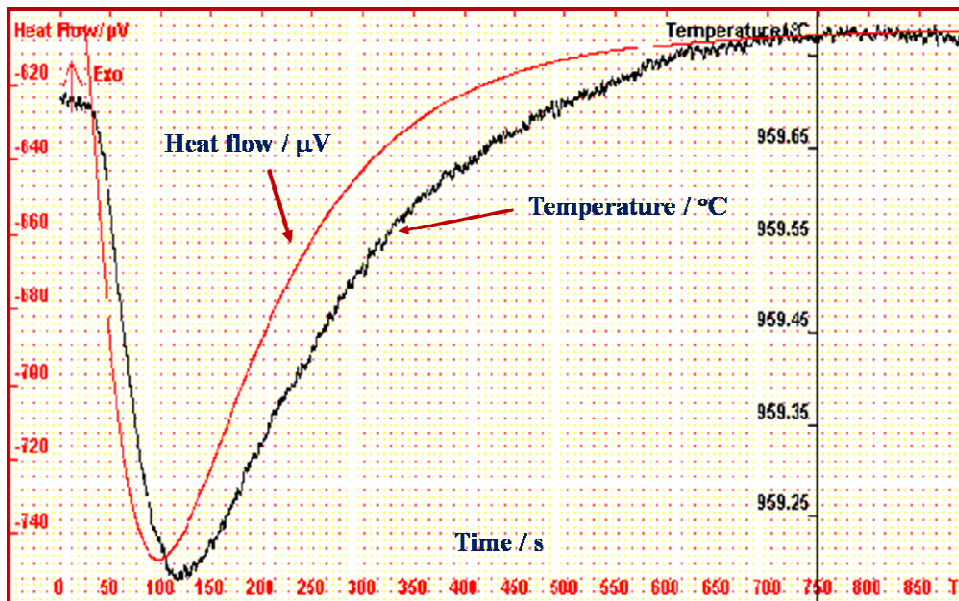


Figure 2.4 Snapshot of the drop experiment output ΔV vs t obtained in this study

2.6.3 Calibration of the drop experiment

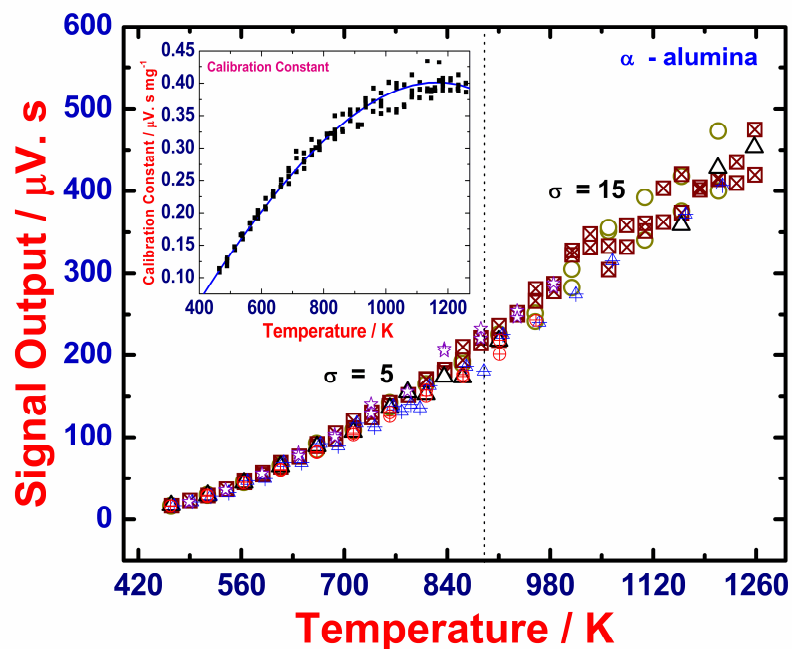


Figure 2.5 Illustration of the temperature variation of Q for a typical experimental schedule and calibration constant (inset)

Prior to the experiment the calorimeter has been calibrated for temperature and the peak area which is referred as heat flow (Q) [6]. The temperature calibration has been carried out with melting points of pure element such as In, Sn, Al, Ag, Au and Cu. The resulting error in the measured temperature was found to be ± 2 K. The heat flow (Q) has been calibrated by dropping α - Al_2O_3 , the reference material into the hot alumina bed set at different temperature during enthalpy measurement of unknown samples. The temperature variation of heat flow Q is shown in **Fig. 2.5**. The individual data points of Q shown in **Fig. 2.5** were taken from different experimental runs (more than 5 experiments) and were compared in the temperature range of 460 to 1373 K. It is observed that the standard deviation of Q is less than 5 upto 910K and is less than 15 for higher temperature. A typical sensitivity calibration curve used for enthalpy evaluation is shown as an inset in **Fig. 2.5**. The calibration constant data obtained as a function of temperature was fitted to four parameter polynomial expression $a+bT+cT^2+dT^3$ and the

fit coefficients obtained were : $a=0.248\pm0.078$, $b=7.84\pm2\times10^{-4}$, $c=8.795\pm3\times10^{-8}$, $d=-2.5\pm1\times10^{-10}$. The high scatter above 910 K is due to the radiation heat loss.

2.6.4 Estimation of Enthalpy

The heat flow Q ($\mu\text{V}\cdot\text{s}$) transferred between the sample or reference and alumina bed which is the raw signal of the drop experiment are measured under identical conditions. Assuming negligible heat loss due to radiation and quasi adiabatic condition in the experimental chamber, $Q_s(T)$, the heat energy transported from the bed to the sample may be written as follows [11,12]

$$Q_s(T) = C(T) \times (m_s/M_s) \times (H_T - H_{298.15})_s \quad (2.5)$$

In the above expression, m_s is the mass of the sample, M_s its molecular weight and $H_T - H_{298.15}$ is the measured enthalpy increment with respect to 298.15 K (25 °C) which is the reference temperature and $C(T)$ is a temperature dependent calorimeter constant. The calibration constant can be obtained from the heat change measured for the standard alumina reference (Q_R) and from the knowledge of its assessed enthalpy increment data [13]. Thus

$$Q_R(T) = C(T) \times (m_R/M_R) \times (H_T - H_{298.15})_R \quad (2.6)$$

In the above equation m_R is the mass of the reference sample and M_R is its molecular weight which is taken to be 101.96 kg m^{-3} [13]. Once the calibration constant $C(T)$ is obtained as a function of temperature from Eq. (2.6), the enthalpy for the unknown sample can be calculated using Eq. (2.5) as a function of temperature.

The measured enthalpy increment as a function of temperature is used to derive the specific heat of the material by fitting the enthalpy increment data to a suitable analytical expression.

2.6.5 Limitation of drop calorimeter

The discrete nature of measurement is the major limitation of drop calorimetry. The drop calorimetry experiments are isothermal measurements and need to be performed at very closely spaced temperature interval. Each experimental run at a given temperature takes about an hour. Hence conducting the drop experiment at every one degree interval is practically difficult. However, the cumulation of drop data points at 20 to 25 K intervals is practically possible. In addition, even if a close temperature step is taken to generate the enthalpy vs temperature curve, a continuous curve cannot be generated using drop calorimetry unlike differential scanning calorimetry. Hence, a precise measurement of transformation temperatures is not generally realized in the drop calorimetry. Also, as drop calorimetry technique involves the measurements under equilibrium conditions, the energetics of metastable phases like martensites cannot be studied by this technique which forms under nonequilibrium conditions during rapid cooling.

2.7 Differential Scanning Calorimetry (DSC)

2.7.1 General principle

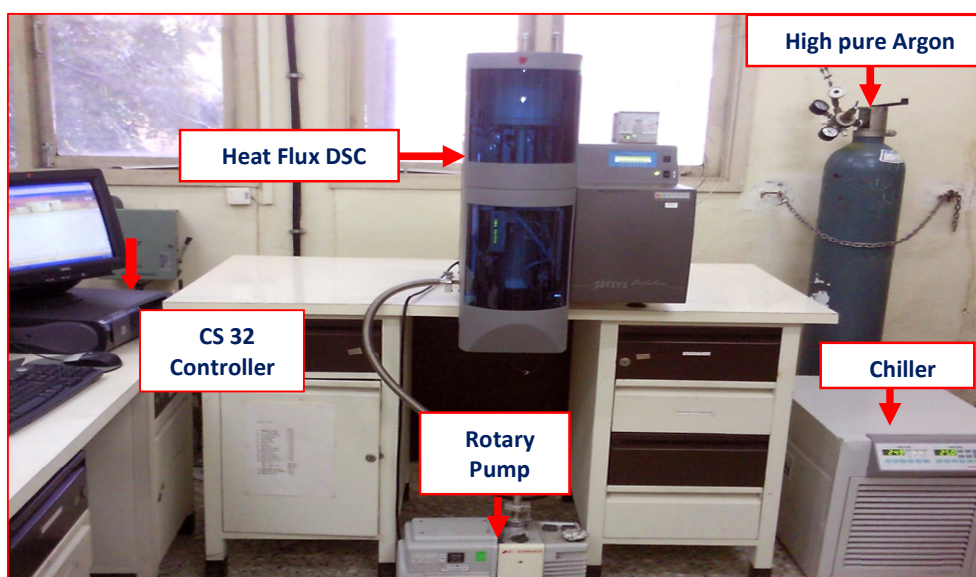


Figure 2.6 The experimental set up of heat flux DSC [6]

Differential Scanning Calorimetry (DSC) is a technique which measures the difference in heat flow between the sample and a reference material when both are heated or cooled at a preset heating or cooling rate. A DSC has two pans; one is kept empty while the other one is loaded with sample. In heat flux DSC, the two pans are housed in a single furnace, which is electrically heated through a programmable temperature controller. In the power compensation DSC, the pans are heated by two separate furnaces. The advantage of heat flux DSC over power compensation DSC is that, it compensates the heat leakage and temperature disturbances, which are common to both the crucibles. In DSC, the absorption and evolution of heat due to phase change in the material induce a commensurate change in the differential heat flow between sample and reference, which in turn appears as an uncompensated temperature differential ΔT . Hence, the basic output of the DSC is the time dependent variation of ΔT . In the present study, the experiments are carried out using Setaram[®] Setsys 1600 heat flux DSC, employing plate type DSC transducer [14] which is shown in **Fig. 2.6** [6]. The essential components of this DSC are as follows [15].

2.7.2 High temperature furnace

The high temperature furnace is shown in **Fig. 2.7 (a)**. It is cylindrical in shape and its heating element is made up of a graphite tube which is heated by resistance heating element. It can be heated upto a maximum temperature of 1873 K. It is separated out from the experimental chamber by an alumina tube. An inert atmosphere is always maintained in the furnace chamber to avoid carbon evaporation at higher temperature. The temperature of the furnace chamber is measured by a B – type (PtRh6% / PtRh30%) thermocouple.

2.7.3 DSC probe

The DSC probe consists of the DSC plate, sample and reference crucibles, thermocouples and guiding alumina tube. The DSC plate is also called as the

measurement head of the calorimeter and is shown in **Fig. 2.7 (b)**. The DSC plate is a thin platinum rectangular strip which is suspended vertically from the top through a guiding annular alumina tube. This plate houses identical recrystallised alumina crucible (one is sample crucible and other one is reference crucible) having mass of about 240-250 mg and volume 100 μL on its either side. One of these crucibles is kept empty (reference crucible), while the sample is placed on the other crucible during the experiment. A thin conducting metallic strip which is made up of platinum connects these two crucibles through which heat is conducted between the sample and reference crucible. The differential thermocouple of B-type (PtRh6% / PtRh30%) is placed exactly underneath the DSC plate to measure the differential temperature ΔT . There is also a B – type thermocouple in the central section of the DSC plate which measures the sample temperature directly. The DSC probe is always housed inside a uniform temperature zone of the water cooled graphite furnace.

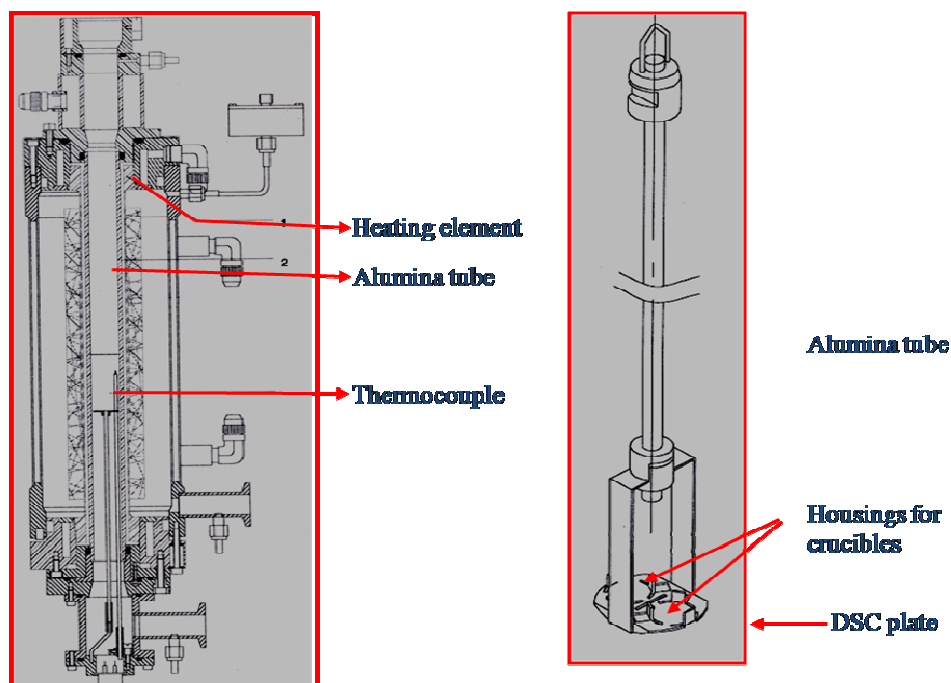


Figure 2.7 (a)Setaram high temperature DSC furnace (b)Heat flux DSC plate-rod [6]

2.7.4 Vacuum pump, Gas Circuit, Chill water Cooling circuit

After loading the sample both the analysis and furnace chamber are evacuated to a vacuum level of 10^{-2} torr using rotary pump. Once the chambers are evacuated they are filled with high pure Ar gas. This inert atmosphere is maintained inside both the chamber throughout the experiment, to avoid any contamination. There are separate ports to carry protective gas and carrier gas. The conductivity of the gas also plays a major role in the heat flow transported. Hence gas used should be as conductive as possible to have a better output. An external chill water supply is provided by the Julabo FC 1600 unit for the furnace. Evacuation, gas filling of analysis and furnace chamber and water supply operations are done through an electro valve command option. The control of the equipment is done through the proprietary software CS32 controller that is interfaced with the equipment.

2.7.5 Mass Flow Controller (MFC)

Mass flow controller plays an important role in the experiment. It controls the flow rate of the gas; say 50 ml / min during the experiment. The improper functioning of the mass flow controller makes the gas flow rate irregular which disturbs the stability of the crucible which is hanging like a balance, and would result in increased noise peaks in the thermogram. The functioning of MFC depends on various parameters such as purity of the gas, humidity of the external atmosphere, temperature maintained in the atmosphere etc.

2.7.6 Experimental procedure

Samples having mass in the range of $40-70 \pm 0.1$ mg was placed in the sample crucible while the reference crucible was kept empty. After loading the samples, the experimental chamber or the analyzer chamber consisting of DSC probe and furnace chamber were evacuated and filled with high pure argon gas (Iolar grade II). A steady argon flow of about 50 ml / min was maintained throughout the experiment and argon

pressure of about 1300 mbar was maintained in the furnace chamber to avoid any evaporation of graphite at high temperature. Once the inert atmosphere was maintained in the furnace as well as the experimental chamber the furnace was allowed to heat. An external and continuous water supply was provided for the furnace.

In the present study the DSC experiment involves the following heating and cooling programme.

(a) Initially the furnace temperature was gradually increased from ambient temperature to 473 K at the rate 10 K min^{-1} and was allowed to stabilize at that temperature for about 10 minutes. This helps in the attainment of thermal equilibrium of the system and it is necessary before starting any measurement. Also this preconditioning results in the formation of smooth and non-wavy baseline.

(b) In the actual experimental run, the sample was heated at a pre determined rate from 473 to 1273 K for Ti-5 mass% Ta-1.8 mass% Nb alloy and 1473 K for Ti – Ta alloys and was equilibrated at this temperature for about 15 minutes and then cooled from this temperature to 473 K at the same rate at which it is heated. Again it is held for about 10 minutes at 473 K before cooling to room temperature. The scanning rate employed in this experiment was varied between 3 to 99 K min^{-1} . Fresh samples were used for each run. The selection of the scan rate is dependent on the nature of the study.

In general, DSC is employed for the following studies:

- a) Determination of phase transformation temperatures
- b) Measurement of heat effects or energy accompanying phase transformations
- c) Estimation of the kinetic parameters of the phase transformations
- d) Measurement of heat capacity

The present study deal with the *determination of phase transformation temperatures, the measurement of heat effects or the enthalpy involved in the phase transformation and its kinetics as a function of varying heating and cooling rate for*

various $Ti-xTa$ ($x= 5, 10, 15$ and 20 mass %) alloys and $Ti-5$ mass% $Ta-1.8$ mass% Nb alloy using DSC.

2.7.7 Determination of phase transformation temperature

When the furnace is heated, heat flows into the sample and reference equally and the basic DSC signal is a smooth and flat baseline. When the sample experiences any phase change, there is difference in the heat flow to the sample and reference due to the latent heat of transformation of the sample and results in a differential signal in the baseline. A DSC thermogram is shown in **Fig. 2.8**, where Y-axis represents the difference in heat flow (μV) which is the output of the instrument and X-axis represents the temperature or time. The phase transformation start (T_s) and transformation finish (T_f) temperatures are determined by drawing tangent to the baseline and from the inflection point of the peak and their intersection point is taken as the transformation temperature. T_s and T_f marked in **Fig. 2.8** represent the phase transformation start and finish temperatures respectively.

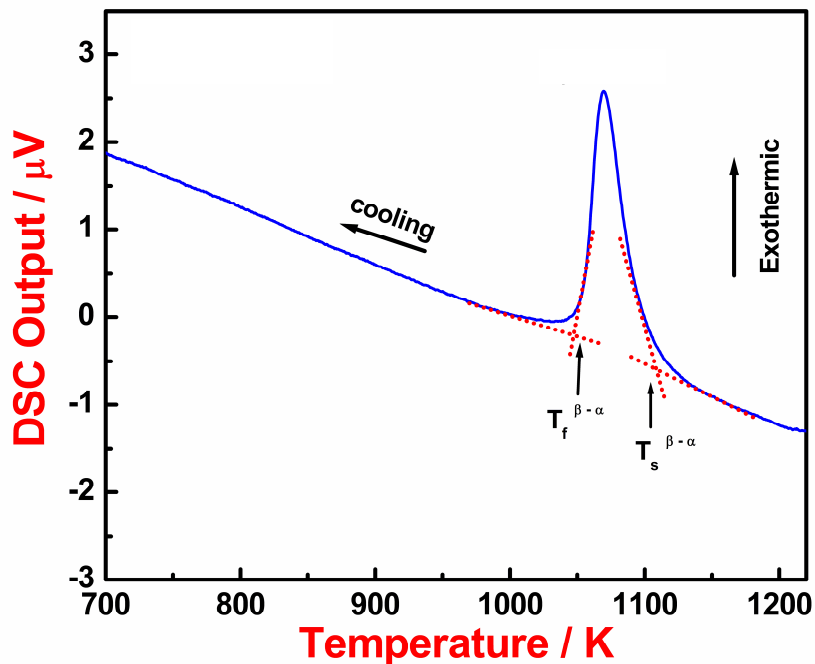


Figure 2.8 Typical DSC thermogram showing start (T_s) and finish (T_f) temperatures of phase transformation on cooling.

2.7.8 Determination of phase transformation enthalpy

In non-isothermal DSC scan, an exothermic or endothermic peak is observed during phase transition. The measured area of the endotherm or exotherm is assumed to be directly proportional to the heat of phase transformation or the enthalpy change. Thus,

$$\Delta H_{tr} = k(T) \times \text{Peak Area} \quad (2.7)$$

where, ΔH_{tr} is the enthalpy change accompanying phase transformation, $k(T)$ is the temperature dependent calibration constant. Peak area is the total area under the endothermic or exothermic peak as the case may be, which is readily obtained by the data processing software after appropriate baseline construction [16-19]. The calibration constant $k(T)$ is obtained by measuring the peak area recorded with the melting or fusion reactions of primary or secondary standards like pure aluminium, zinc, tin, copper and iron of known enthalpy [16-19]. The sensitivity of calibration constant $k(T)$ is influenced by many factors like the heating or cooling rate, the hydrodynamic nature of the ambience and the nature of calibrant which introduces error in the measurement. Most preferably, the melting or solidification reactions of pure metals are employed for calibrating the heat effects of unknown transformation events. In case of metals that solidify with large undercoolings, the actually measured enthalpy will exhibit a deviation from the literature value which pertains to equilibrium solidification. It is for this reason the calibration constants are quite reliably estimated for low heating rates. In addition, it is also desirable to employ a calibrant that has similar thermophysical characteristics with the alloy under investigation so that spurious effects arising from the disparate conduction characteristics are generally avoided. Hence, pure titanium has been used as the calibrant for accurately characterizing the enthalpy effects of Ti-Ta and Ti-Ta-Nb alloys of the present study.

Another source of error in the estimation of the enthalpy arises from the uncertainty associated with the measured peak area, in cases where there is difficulty in unambiguously fixing the transformation start and finish temperatures. In such cases, the measured area might not correspond to 100% of phase change or else, it could be an overestimate as well by the selection of wrong baseline. Hence, in the present study this impertinent source of error has been minimized by going in for accurate baseline calibration by subtracting a nil sample empty run signal from the actual run recorded with the sample in position. Also, identical pair of crucibles, gas flow rate and scanning rate conditions etc., are employed to minimize spurious factors from affecting the accuracy.

2.7.9 Temperature calibration in DSC

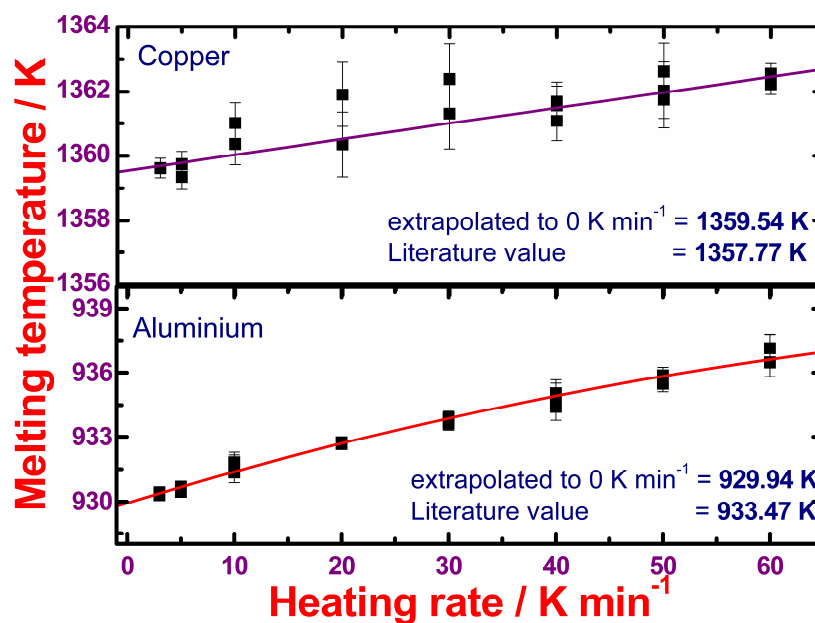


Figure 2.9 Temperature calibrations with Al and Cu

The temperature calibration [6], which is very important in DSC has been carried out using the melting points of pure aluminium, zinc, tin, copper, silver, gold, and iron standards [20]. The start temperature (T_s) of the melting has been determined, based on the procedure explained in Fig. 2.8. These start temperatures are determined for various

heating rates such as 1, 3, 5, 7, 10, 15, 20, 30 K min⁻¹ etc., and is extrapolated to hypothetical 0 K min⁻¹ limit which represents the equilibrium onset temperature [16, 21]. These values are compared with the literature values in order to estimate the correction to be employed for obtaining the true transformation temperature. The temperature calibration procedure for aluminum and copper is illustrated in **Fig. 2.9**. The extrapolated melting temperature of Cu and Al is compared with literature values and the deviation is found to be within ± 4 K. The temperature accuracy in case of low heating rate experiments (1-30 K min⁻¹) is found to be ± 2 K for samples of mass up to 50–100 mg; while, it is ± 4 K for high heating rates (99 K min⁻¹). The temperature calibration of DSC for the cooling cycle is comparatively difficult because of varying degree of undercooling associated with the phase change. Hence, the temperature calibration is only performed for heating cycle of DSC experiments.

2.8 Microstructural characterization and analysis of microstructural parameters

In the present study microstructural characterization has been carried out using X-ray diffraction, optical microscopy, Scanning Electron Microscopy, Transmission Electron Microscopy and microhardness.

2.8.1 X-ray diffraction (XRD) study: Identification of phases

In the present study the X-ray diffraction study has been carried out at room temperature. The X-ray characterization was performed using Philips X'pert powder diffraction system operating in θ - 2θ geometry, and employing Ni-filtered Cu-K α ($\lambda=0.15406$ nm) radiation, with a $\Delta\theta$ step of 0.02° and in the 2θ range of 20 - 85° . Pure silicon powder was used for θ -calibration prior to acquisition of spectra for the specimen. XRD study had been carried out on thin and flat samples. The samples were ground using 1200 grit emery paper and to make the surface flat and cleaned with acetone before spectrum acquisition. The diffraction pattern for each sample is recorded

for 1 h duration. Phase identification in XRD was carried out by comparison with JCPDS file nos.44-1294 for α -Ti, 44-1288 for β -Ti and 04-0788 for Ta.

2.8.2 Optical Microscopy

Optical metallography studies were carried out using *Leica MeF4A* optical microscope fitted with a Leica digital camera along with Leica Qwin software for image acquisition. The magnification calibration of the microscope was carried out for magnification of objective lenses using a standard micrometer stage insert with 1000 lines / mm.

2.8.3 Scanning Electron Microscopy (SEM)

SEM studies were carried out using *Philips XL30 Environmental Scanning Electron Microscopy (ESEM)*. The microstructures are recorded in the Secondary Electron (SE) and Back Scattered Electron (BSE) imaging modes. In all the SEM experiments, the accelerating voltage was maintained in the range of 20-30 kV and spot size in the range of 100 to 1000A°. Standard cross grating samples of 20 lines / mm and 2160 lines / mm were used for magnification calibration. The high resolution test was carried out using a carbon film embedded with gold nano particles, where the spacing between these nano particles is $\sim 20 \text{ \AA}$. Energy Dispersive X-ray analysis was carried out using EDAX X-ray detector attached to the SEM for elemental identity and to establish relative changes in the concentration of any element across different regions. Energy calibration was carried out using pure elements with a detector resolution of 132 eV at Mn-K α .

2.8.4 Transmission Electron Microscopy

TEM studies were carried out using a CM200 Analytical Transmission Electron microscope equipped with Inca X-max with SDD detector for microstructural and microchemical analysis. The experiment was carried out at voltage of 200 kV. Magnification calibration was carried out with a cross grating of 2160 lines/mm with a

separation of 469 nm between two lines. Camera length was calibrated with standard nanocrystalline oriented gold in holey carbon film at different accelerating voltages. The high resolution test with a line resolution of 2.3 Å is performed by using same standard sample. Analysis of selected area (SAD) or micro-diffraction patterns and dark field microscopy were carried out to identify the presence of different phases. An aperture of 10 µm size was used for obtaining the SAD pattern and dark field images. Trace analysis was carried out after applying correction for rotation of SAD pattern w.r.t magnification using MoO₃ crystals. A spot size of ~50 nm was used to collect the characteristic X-rays from the constituent phases for determining the composition. A low background single tilt holder was used to reduce the noise due to spurious X-rays. In-hole spectra were collected periodically to ensure the absence of spurious X-ray sources in the column of the microscope. The conditions for acquisition of the EDS spectra are listed in **Table 2.3** [22]. A large number of spectra were acquired from several regions of the specimen for a statistically meaningful analysis of the composition.

Table 2.3 Conditions adopted for quantification of EDS spectra

Parameter	Value
Operating voltage	200 kV
Angle of tilt	30°
Beam diameter	50 nm
Thickness of the specimen	100 nm
Density	5.1 g/cc
Collection time	50 s

2.8.5 Analysis of microstructural parameters

In this study, important microstructural parameters such as grain size and volume fraction of the constituent phases are measured. The grain size was measured using the

intercept method [23]. The volume fraction of the constituent phases was determined by estimating the area fraction of the phases. This quantification has been done by an automated image analysis using Image J[®] software [3, 24]. Volume fraction analysis has been performed on as collected SEM back scattered electron image using threshold option provided in Image J[®] software. This thresholding procedure converts the grayscale image to binary images and delineates the contrast between features.

2.8.6 Phase Analysis using electron diffraction pattern

The indexing of electron diffraction patterns involves phase identification thus the assignment of specific (hkl) indices to the individual spots and the determination of the beam direction which corresponds to the zone axis of the reflecting planes. To identify the (hkl) planes, the distance (d-spacings) from the diffracted spot to the transmitted spot and the angle between the diffracted spots and the transmitted spot are measured. The matched angles and d-spacings were attained with an error of <1° and 0.2 Å respectively.

2.8.7 Analysis of composition

The composition of α and β phases were determined using Analytical TEM. This method involved acquisition of EDS spectra from the respective phases from many regions in one or two samples. Composition analysis was carried out assuming the thin foil criterion based on the observation that the intensity difference was less than 10% between the in-hole spectrum and that on the specimen. For quantification purposes, only Ti K α , Ta L α and Nb L α peaks were chosen as the Region of Interest (ROI) and quantified using the Cliff-Lorimer method [25]. The following Cliff-Lorimer equation was used for quantification of the spectra using the library values of Cliff – Lorimer constants, (i-e) K_{AB} 's, which were generated theoretically by the software [26].

$$\frac{C_A}{C_B} = K_{AB} \frac{I_A}{I_B} \quad (2.8)$$

where C_A and C_B refer to the concentration of elements A and B in the region of interest and I_A and I_B refer to their respective intensities in the X-ray spectrum. The composition of the alloy determined was verified with that of a β quenched sample with a uniform microstructure and composition. One of the main sources of error in the determination of composition is the acquisition time, which can be minimized by increasing the collection time. Therefore, a collection time of ~50s 'live time' was used. It is assumed that collection of the spectra is from within the beam size and volume of the sample encloses only the region of interest without overlapping of phases, though in some cases it was difficult to ensure this condition. The statistical error for 99% confidence limit ($\pm 2\sigma$) in the compositional analysis from about ten spectra was within ± 2 mass%. During quantification of the spectra, presence of 0.003 mass% Fe, was ignored which is an impurity in the alloy.

2.8.8 Microhardness measurement

Hardness is a measure of the resistance of the material to deformation. In the present study, the hardness measurement was carried out using Leitz Vickers micro hardness tester. A constant load of 100 g was used for all the measurements. About eight to ten measurements were taken for each sample and average of the measurements is reported here. Before loading the sample for measurement a standard sample of known hardness with prescribed load of 100 g is used for calibration. The Vickers hardness number is given by the following equation

$$\text{VHN} = 1.854 \times (L/d^2) \quad (2.9)$$

where L is the load applied during measurements (measured in kilograms - force) and d^2 is the area of the indentation (measured in square millimeters).

References

- [1] S. A. Souza, R. B. Manicardi, P. L. Ferrandini, C. R. M. Afonso, A. J. Ramirez and R. Caram, *J. Alloys Comp.* 504 (2010) 330-340.
- [2] K. Kapoor, V. Kain, T. Gopalkrishna, T. Sanyal and P. K. De, *J. Nucl. Mater.* 322 (2003) 36-44.
- [3] Madhusmita Behera, S. Raju, B. Jeya Ganesh, R. Mythili and S. Saroja, *Int. J. Thermophys.* 31 (2010) 2246-2263.
- [4] W. Hemminger and G. W. H. Höhne, *Calorimetry — Fundamentals and Practice*, Weinheim, Verlag Chemie, 1984.
- [5] P. K. Gallagher, *Handbook of Thermal Analysis and Calorimetry*, 1 (Ed. M. E. Brown), Elsevier, Amsterdam, 1998.
- [6] B. Jeya Ganesh, “Calorimetric investigation of phase stability, energetics and kinetics of phase transformations in 9Cr based ferritic steels”, A Ph. D thesis submitted to University of Madras, 2011.
- [7] <http://www.setaram.com/MHTC-96-Accessories.htm>.
- [8] Multi HTC-96, Setaram Installation Guide and Manual (1997).
- [9] Yoichi Takahashi and Yuji Kohsaka, *J. Nucl. Mater.* 130 (1985) 109-114.
- [10] M. Nevriya, D. Sedimidubsky and J. Leitner, *Thermochim. Acta* 347 (2000) 123-128.
- [11] J. Leitner, A. Strejc, D. Sedimidubsky, and K. Ruzicka, *Thermochim. Acta* 401 (2003) 169-173.
- [12] S. Raju, B. Jeya Ganesh, Aritra Banerjee and E. Mohandas, *Mater. Sci. Engg. A* 465 (2007) 29-37.
- [13] D. G. Archer, *J. Phys. Chem. Ref. Data* 22 (1993) 1441-1453.
- [14] B. Jeya Ganesh, S. Raju, Arun Kumar Rai, E. Mohandas, M. Vijayalakshmi, K. B. S. Rao and Baldev Raj, *Mater. Sci. Tech.* 27 No. 2 (2011) 500-512.
- [15] <http://www.setaram.com/SETSYS-Evolution-DTA-DSC.htm>.
- [16] E. Gmelin and St. M. Sarge, *Pure Appl. Chem.* 67 (1995) 1789-1800.
- [17] B. Wunderlich, *Thermal Analysis*, San Diego, CA, Academic Press, 1990.
- [18] M. Brown, *Introduction to Thermal Analysis*, London, Chapman and Hall, 1988.
- [19] G.W. H. Höhne, W. Hemminger, and H. J. Flammersheim, *Differential Scanning Calorimetry: An Introduction for Practitioners*, Berlin, Springer-Verlag, 1996.
- [20] R. Sabbah, An Xu-wu, J. S. Chickos, M. L. Planas Leitão, M. V. Roux and L. A. Torres, *Thermochim. Acta* 331 (1999) 93-204.

- [21] L. Richardson, E. L. Charsley; "Calibration and Standardisation in DSC", in *Handbook of Thermal Analysis and Calorimetry. Vol. 1: Principles and Practice*, (Ed. M. E. Brown), Elsevier Science B.V. (1998).
- [22] R. Mythili, "Study of a Ti-5%Ta-1.8% Nb alloy: Microstructure and its influence on corrosion and mechanical properties", A Ph. D thesis submitted to University of Madras, 2009.
- [23] G. F. Vander Voort, *Metallography Principles and Practice*, Mc-Graw- Hill book Company, 1984.
- [24] <http://rsb.info.nih.gov/ij/>
- [25] G. Cliff and G. W. Lorimer, in: *Quantitative Microanalysis with high spatial resolution*, M. H. Jacobs, G.W. Lorimer and P. Daig (Eds.), The Metals Society, London, 1981.
- [26] David B. Williams, *Practical Analytical Electron Microscopy in Material Science*, 85 McKee Drive, Mahwah, New Jersey 07430, 1984.

Chapter-3

*Measurement of Thermodynamic
Properties of Ti-xTa (x = 5, 10,
15, 20 mass %) alloys using Drop
Calorimetry*

3.1 Introduction

The phase stability of a material is determined from the knowledge of the variation of the Gibbs free energies of the various phases as a function of composition (x), temperature (T) and pressure (P). If the Gibbs free energy $G(T, P, x)$ is known for possible phases of a given material then the phase diagram can be determined. Hence, the generation of an accurate and reliable $G(T, P, x)$ database is very much essential for any material developed for a particular engineering application.

There has been very limited research carried out on thermodynamic properties, both experimental and theoretical for Ti – TM (TM = Ta, Nb, Zr, Mo, V etc. which are bcc β phase stabilizing elements) binary or multicomponent alloys [1-8]. For the Ti – Ta alloys, which constitute one of the important binaries of the highly corrosion resistant Ti-Ta-Nb and Ti-Ta-Nb-Zr multicomponent systems, there is no published data available in open literature on both high and low temperature thermodynamic properties. In view of this relative scarcity of fundamental thermodynamic properties, an attempt has been made to measure high temperature enthalpy of a series of binary Ti- x Ta ($x = 5, 10, 15, 20$ mass %) alloys. Using the experimentally measured enthalpy increment, other thermodynamic properties such as specific heat (C_p), entropy and Gibbs free energy (G) are estimated for binary Ti- x Ta ($x = 5, 10, 15, 20$ mass %) alloys. The present chapter describes and discusses the results of drop calorimetry measurements performed on binary Ti- x Ta ($x = 5, 10, 15, 20$ mass %) alloys.

3.2 Organization of the chapter

The organization of this chapter is as follows. Section 3.3 describes briefly about the phase diagram of the Ti – Ta binary system. The microstructural characterization of the starting microstructure of the alloy is described in section 3.4. In section 3.5 the enthalpy increment data as a function of temperature is presented in the range 463-1257 K. Microstructural characterization of post drop calorimetry specimens are discussed in

section 3.6. The analysis of experimentally measured enthalpy data for Ti – 5 Ta alloy forms section 3.7. Section 3.8 presents the analysis of enthalpy data for Ti-10, 15, 20 Ta alloys. Theoretical estimation of C_P in the low temperature region is described in section 3.9. Section 3.10 presents the estimation of thermodynamic functions. Section 3.11 summarizes the results of this study.

3.3 Brief description of Ti-Ta binary system

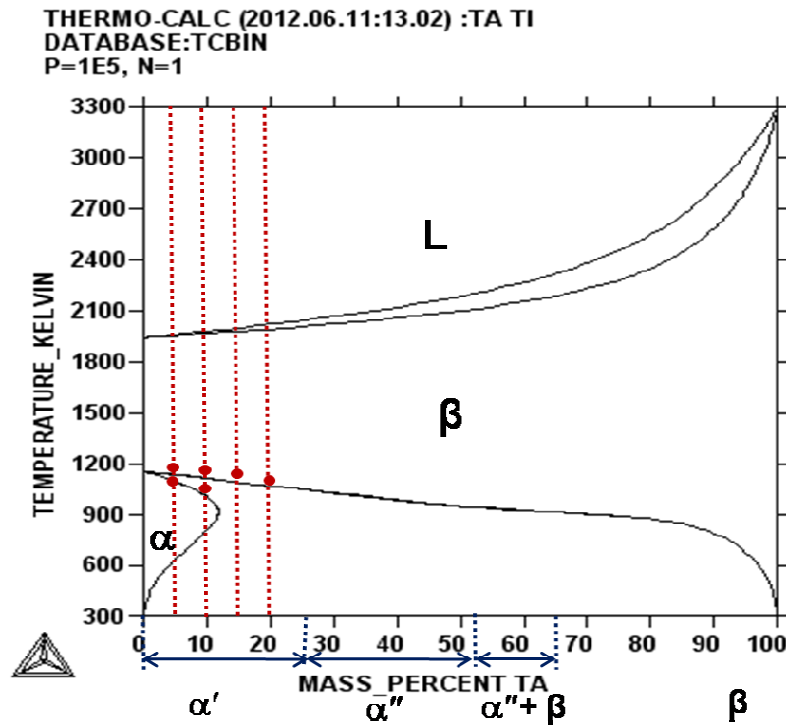


Figure 3.1 Equilibrium phase diagram of Ti-Ta binary system obtained using the Thermo Calc[®] program is shown. The dotted lines stand for the compositions investigated in this study. The circles represent the experimental $\alpha/\alpha+\beta$, $\alpha+\beta/\beta$ solvus temperatures obtained in this study. The approximate compositional domains of α' , α'' , and metastable β phases are also marked in the figure [12,13]

Fig. 3.1 portrays the assessed equilibrium diagram of Ti-Ta binary system, which is typical of binary isomorphous β -titanium alloys exhibiting complete mutual solubility in both liquid and high temperature β -bcc phase fields. On the Ti-rich side, the α -hcp solid solution exhibits considerable solubility for Ta; however, the $\alpha/\alpha+\beta$ solvus is fairly steep for temperatures below about 873 K, suggesting thereby a sharp reduction in

low temperature solubility in the α phase. The $\alpha+\beta/\beta$ phase boundary exhibits a broad plateau signifying an extensive domain of β -bcc phase stability. It is generally well known that in the case of β -titanium alloys, the diffusion of refractory transition metal solutes is sluggish both in β -bcc and specifically in α -hcp phase fields [9, 10]. As a result, it is possible to obtain a variety of metastable phases, by suppressing rather easily the equilibrium $\beta\rightarrow\alpha$ diffusional transformation through even moderate cooling from the high temperature β -phase [11]. The practical implication of this situation is that it is extremely difficult to realize equilibrium distribution of α and β phases in the final microstructure that is obtained after standard thermomechanical processing of the high temperature β phase. The metastable phases that form in Ti-Ta alloys include: (i) hexagonal martensite α' (ii) orthorhombic martensite α'' and (iii) untransformed or retained β phase [12, 13]. The formation of athermal ω -phase upon cooling from β , which is observed in other titanium alloys like Ti-Mo and Ti-Nb has not been reported so far in binary Ti-Ta alloys [12-15]. In **Fig. 3.1**, the probable compositional domains of different metastable phases in Ti-Ta system are delineated [12, 13].

3.4 Structural and Microstructural Characterization of Starting Material

The room temperature X-ray diffraction profiles of homogenized Ti- x Ta ($x=5, 10, 15, 20$ mass %) alloys are stacked in **Fig. 3.2**. As can be seen, the major phase in all the four compositions is the equilibrium α -hcp phase. The Ti-20Ta alloy shows weak reflections of β -bcc phase. According to the equilibrium diagram shown in **Fig. 3.1**, all the alloys except Ti-5Ta should exist as $\alpha+\beta$ two phase mixture, although the XRD profiles in **Fig. 3.2** do not show distinct β -phase reflections. The explicit absence of β reflection is common in many cast/annealed Ti-alloys and this arises due to strong texture effects of α -grains. Nevertheless, the presence of β can still be inferred by the

shoulder like feature appearing in $(00.2)_\alpha$ reflection [16]. The processed XRD data and the calculated lattice parameters following standard procedures are listed in **Table 3.1**.

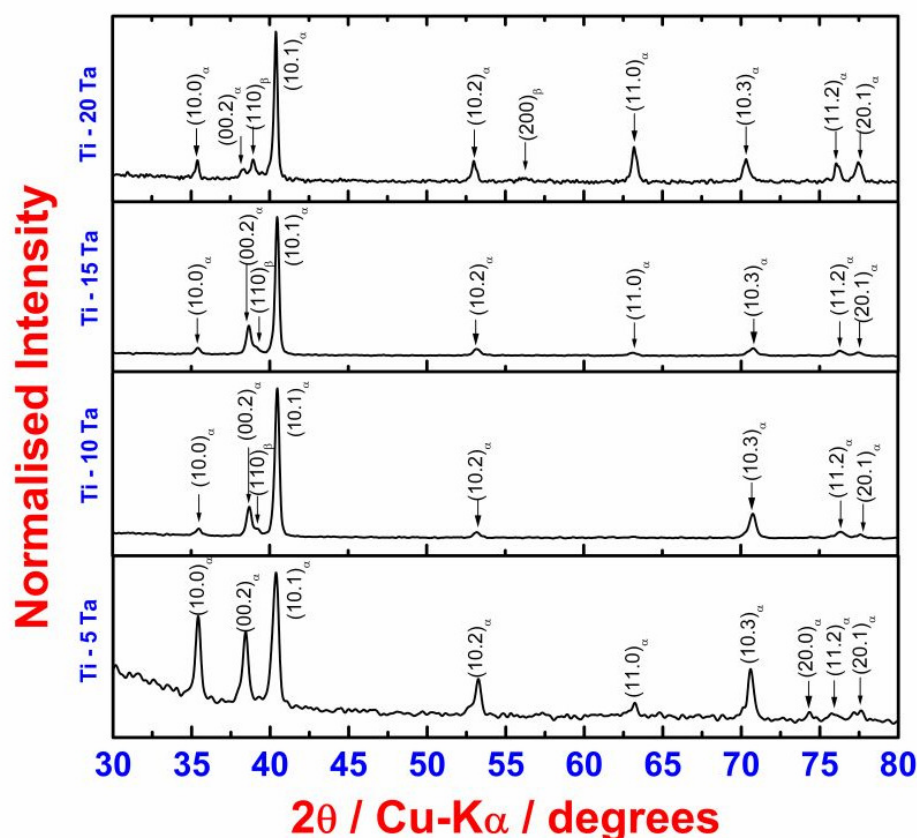


Figure 3.2 Room temperature X-ray diffraction profiles of Ti – xTa ($x = 5, 10, 15, 20$ mass %) alloys. The shoulder like feature adjacent to $(00.2)_\alpha$ indicates the presence of β -bcc phase.

It is found that the lattice parameter of the α -hcp phase does not vary with composition for the alloys studied here (**Fig. 3.3**). This is in line with the fact that in the $\alpha+\beta$ two phase region, the composition of equilibrium phases is expected to remain unaltered. The lattice dimensions of β -bcc phase could not be estimated due to the absence of distinct β reflections except for Ti-20Ta alloy where the $(110)_\beta$ and $(200)_\beta$ could be identified clearly. In **Fig. 3.4**, the lattice parameters of Ti – Ta alloys measured in this study are compared with literature data for similar titanium base alloys. It is evident that

present measurements are in excellent agreement with the general trend exhibited by many related titanium alloys [4, 5, 13, 17-21].

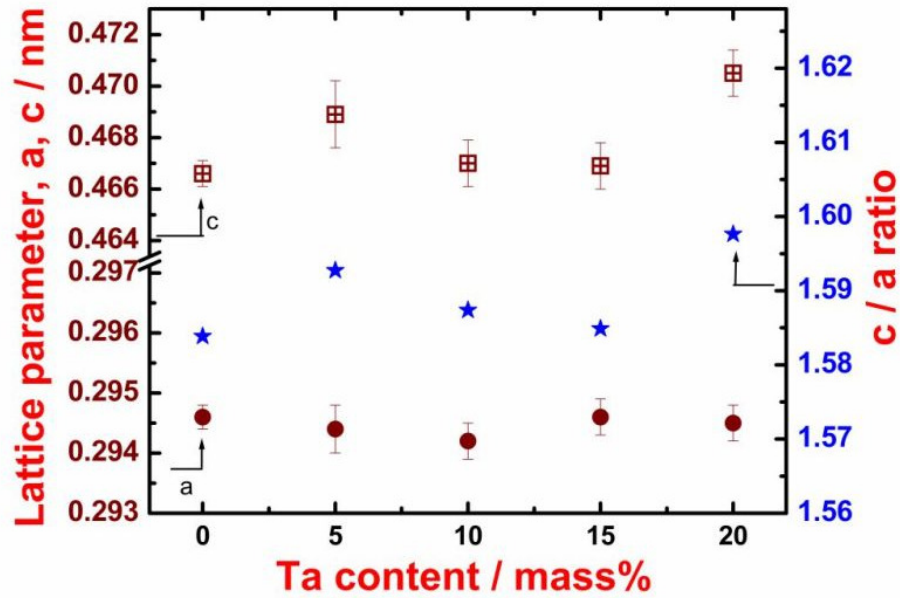


Figure 3.3 Lattice parameter variation with Ta-content.

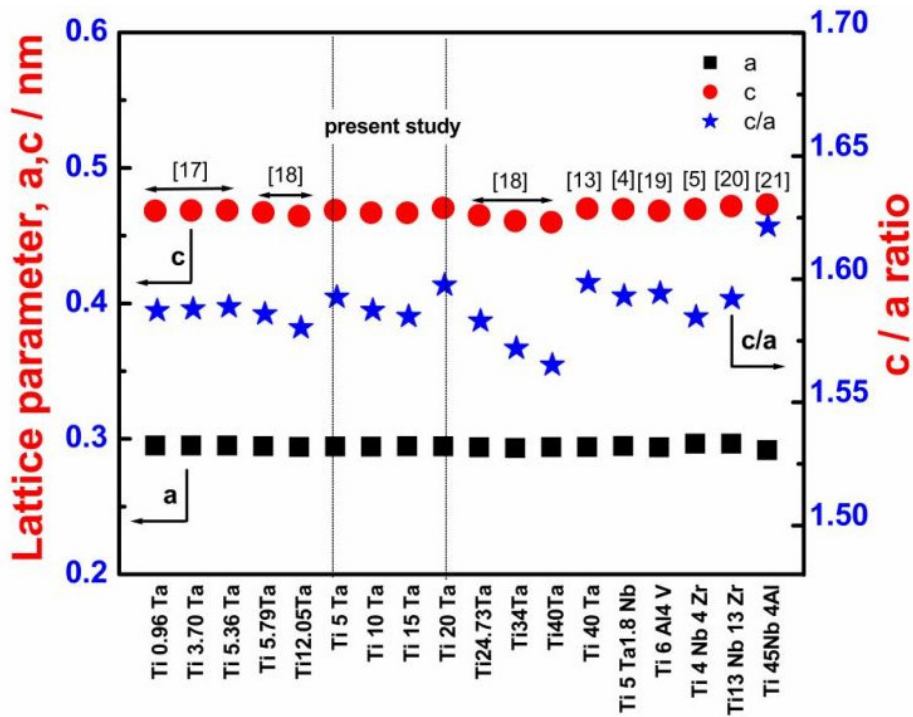


Figure 3.4 A comparison of the lattice parameters of Ti – Ta alloys obtained in this study is made with the literature data on related Ti-base alloys. The numbers given in the square bracket stand for the respective references.

Table 3.1 Room temperature X-ray diffraction data and estimated lattice parameters of Ti-xTa (x = 5, 10, 15, 20 mass %) alloys.

2 θ -CuK α (Degrees)	Normalised Intensity (%)	d _{hkl} (nm)	(hkl) indices	Lattice parameter (nm)
Ti – 5 mass% Ta				
35.41	73.56	0.2533	(10.0) _{α}	a = 0.2944 \pm 0.0004 c = 0.4689 \pm 0.0013 c/a = 1.593 β -phase could not be detected
38.43	63.94	0.2341	(00.2) _{α}	
40.37	100	0.2232	(10.1) _{α}	
53.25	35.53	0.1719	(10.2) _{α}	
63.15	21.00	0.1471	(11.0) _{α}	
70.61	41.53	0.1333	(10.3) _{α}	
74.37	15.46	0.1275	(20.0) _{α}	
75.89	14.58	0.1253	(11.2) _{α}	
77.65	16.39	0.1229	(20.1) _{α}	
Ti – 10 mass% Ta				
35.49	7.80	0.2527	(10.0) _{α}	a = 0.2942 \pm 0.0003 c = 0.4670 \pm 0.0009 c/a = 1.587 β -phase could not be detected
38.71	22.15	0.2324	(00.2) _{α}	
40.49	100	0.2226	(10.1) _{α}	
53.19	5.44	0.1721	(10.2) _{α}	
63.21	2.52	0.1470	(11.0) _{α}	
70.77	17.61	0.1330	(10.3) _{α}	
76.35	5.73	0.1246	(11.2) _{α}	
77.61	3.99	0.1229	(20.1) _{α}	
Ti – 15 mass% Ta				
35.42	6.90	0.2532	(10.0) _{α}	a = 0.2946 \pm 0.0003 c = 0.4669 \pm 0.0009 c/a = 1.585 β -phase could not be detected
38.67	22.68	0.2327	(00.2) _{α}	
40.47	100	0.2227	(10.1) _{α}	
53.15	6.11	0.1722	(10.2) _{α}	
63.13	3.44	0.1472	(11.0) _{α}	
70.77	6.61	0.1330	(10.3) _{α}	
76.27	4.87	0.1247	(11.2) _{α}	
77.45	3.69	0.1231	(20.1) _{α}	
Ti – 20 mass% Ta				
35.39	16.77	0.2534	(10.0) _{α}	a = 0.2945 \pm 0.0003 c = 0.4705 \pm 0.0009 c/a = 1.598 a _{β} = 0.3272
38.35	11.12	0.2345	(00.2) _{α}	
38.95	17.25	0.2311	(110) _{β}	
40.39	100	0.2231	(10.1) _{α}	
52.99	16.37	0.1727	(10.2) _{α}	
56.11	5.26	0.1638	(200) _{β}	
63.19	25.35	0.1470	(11.0) _{α}	
70.33	17.49	0.1338	(10.3) _{α}	
76.05	14.79	0.1251	(11.2) _{α}	
77.47	15.48	0.1231	(20.1) _{α}	

In **Fig. 3.5(a-d)**, the collage of backscattered electron images of the homogenized microstructure for all the four alloy compositions is presented. The back scattered imaging mode is adopted, as it distinctly brings out the contrast difference between Ta rich β -bcc and Ti-rich α -hcp phases. The α -phase due to its growth rate anisotropy forms as thin needles and adopts two crystallographically equivalent variants in mutually intersecting directions that gives rise to the typical morphology seen in **Fig. 3.5**.

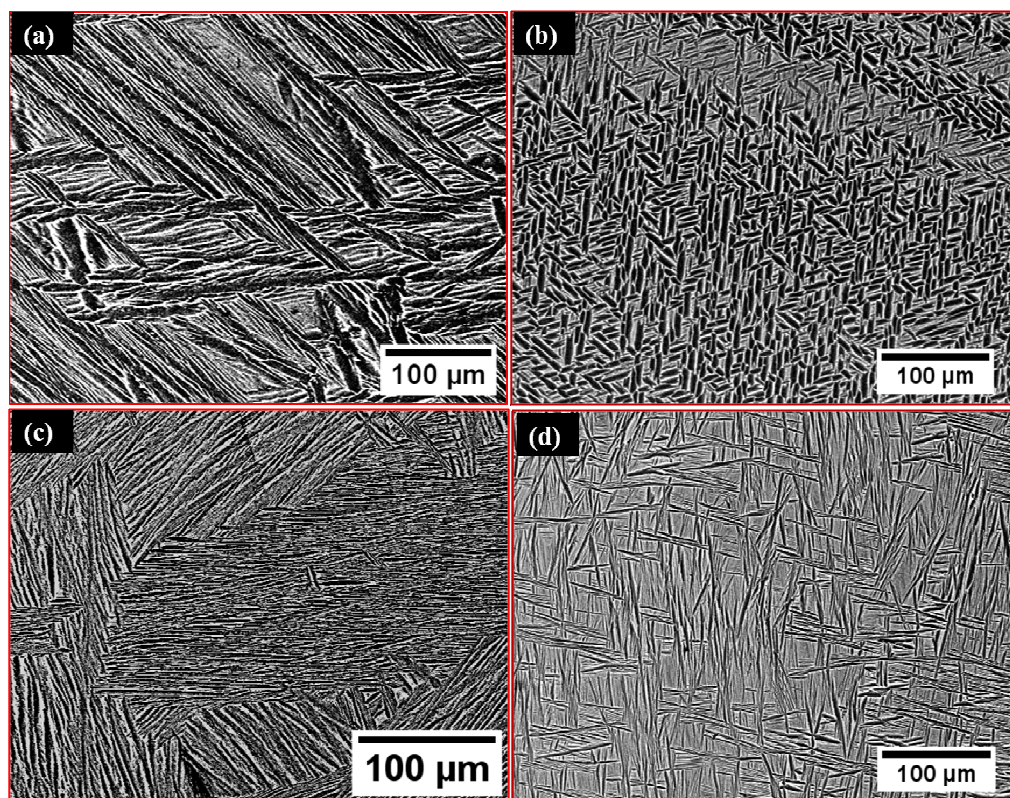


Figure 3.5 Back Scattered Electron images of solution annealed Ti-Ta alloys corresponding to (a) 5 Ta, (b) 10 Ta, (c) 15 Ta, (d) 20 Ta.

With increasing Ta content, the volume fraction of retained β -phase increases; however, the sluggishness of the solid state diffusion renders the formation and growth of α phase difficult. As a result, the width of α -needles in the final microstructure becomes more fine or refined with increasing Ta concentration. Since this study is primarily focused towards thermal property characterization, a detailed study on

microstructural development is not attempted here. The volume fraction of β -phase has been estimated using *Image J* software analysis [4] of the solution annealed microstructure, which is given in **Fig. 3.6**. This is compared with the equilibrium phase diagram estimate at 773 K. It is observed that with increasing Ta content, the volume fraction of retained β in the present samples is found to be somewhat larger than what is dictated by thermodynamic equilibrium conditions. The excess fraction of β obviously arises due to non-equilibrium conditions prevailing during the $\beta \rightarrow \alpha$ phase change upon cooling.

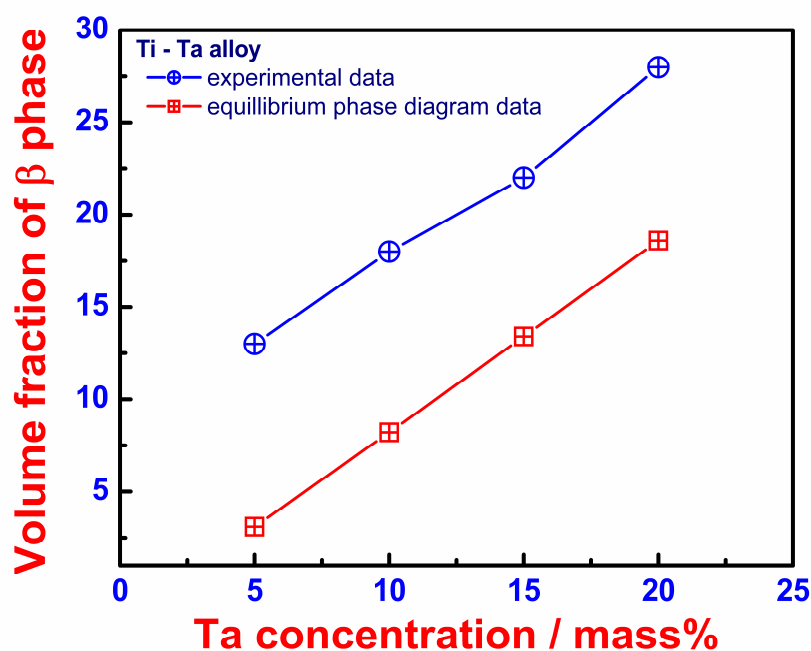


Figure 3.6 Volume fraction of β measured in present study is compared with the equilibrium phase diagram estimate.

In **Fig. 3.7**, the energy dispersive X-ray (EDX) spectra obtained from α and β phases of Ti-xTa ($x = 5, 10, 15, 20$ mass %) alloy is shown. It is seen that the β phase is relatively enriched in Ta, as expected from the equilibrium diagram. The variation of Vickers microhardness with composition is presented in **Fig. 3.8**. It is observed that with increasing Ta content, the hardness exhibits a steady increase, both due to the increased fineness of α colony and also due to increased volume fraction of β -bcc phase.

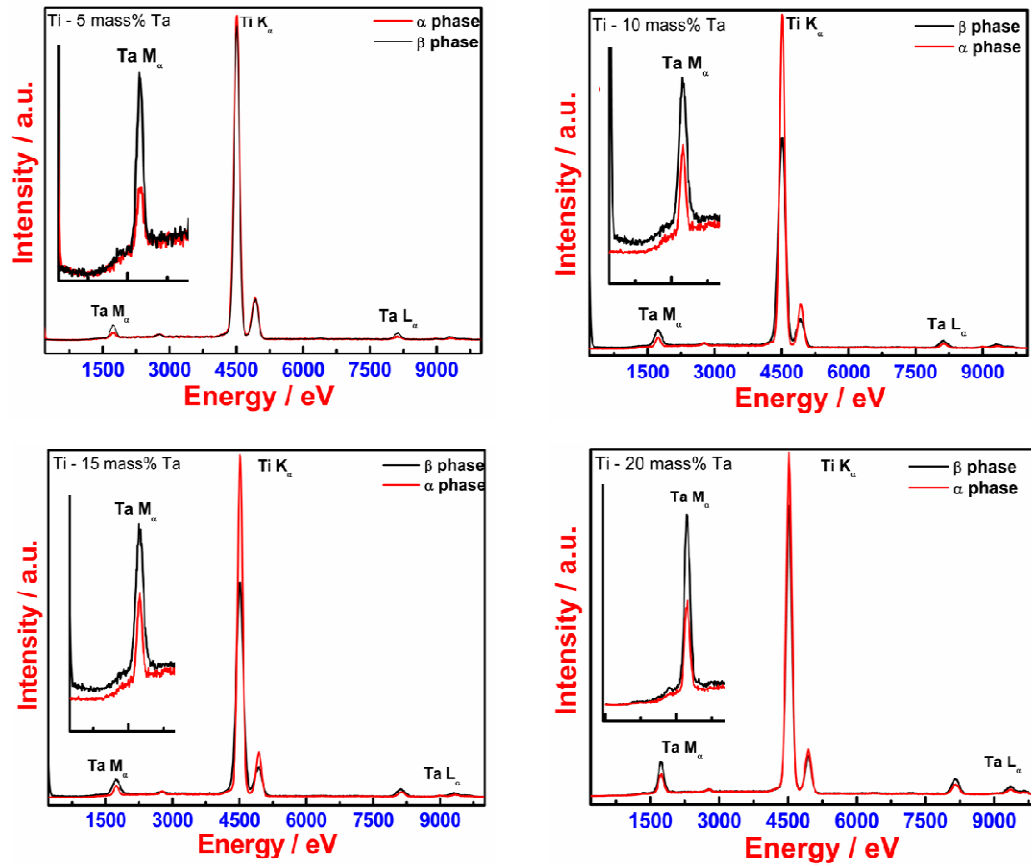


Figure 3.7 EDX spectra showing the relative enrichment of Ta in the β phase of Ti-Ta alloy.

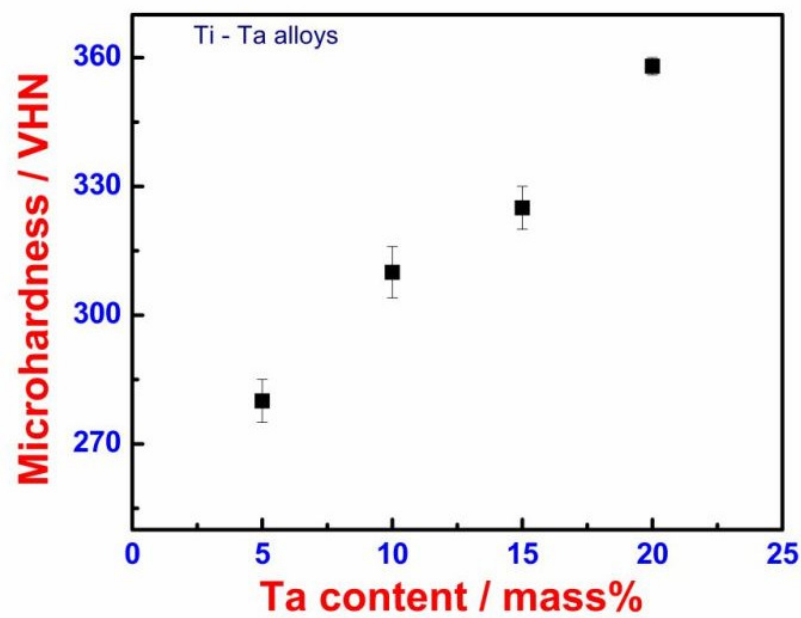


Figure 3.8 Variation of microhardness with Ta content is shown for the solution annealed alloys

3.5 Enthalpy Increment ($H_T - H_{298.15}$) measurement

3.5.1 Enthalpy increment data for Ti – 5 mass% Ta alloy

In Fig. 3.9, the variation in measured enthalpy increment ($H_T - H_{298.15}$) with temperature T in the range ($463 \leq T \leq 1257$ K) is presented for Ti-5Ta alloy. This composition is taken as the typical case study for discussing the salient features of enthalpy increment versus temperature plot.

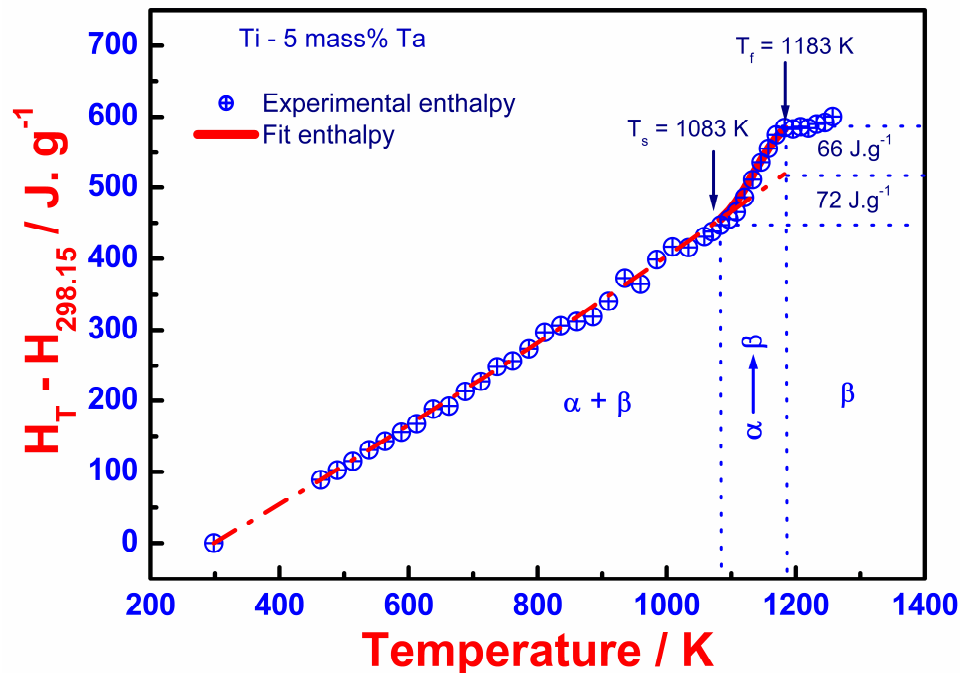


Figure 3.9 Enthalpy increment variation with temperature for Ti–5Ta alloy is graphically illustrated. T_s and T_f represent $\alpha \rightarrow \beta$ transformation start and finish temperature respectively.

In the above figure the crossed circles represent the actual experimental data points and the line joining them serves to delineate the observed temperature dependence of the enthalpy variation. It is readily seen from this figure that the enthalpy exhibits a fairly smooth and continuous increase with temperature in the stability domain of the α phase. The smoothly increasing nature is however altered in the temperature interval ($1083 \leq T \leq 1183$ K) which represents the $\alpha \rightarrow \beta$ phase transformation domain in this alloy. Accordingly, 1083 ± 2 K may be taken as the start temperature (T_s), while 1183 ± 2 K as

the finish temperature (T_f) of $\alpha \rightarrow \beta$ diffusional phase change in Ti-5Ta alloy. Since the drop measurements are carried out under near thermal equilibrium conditions, it is instructive to compare the transition temperatures with the equilibrium phase diagram. In **Fig. 3.1**, the measured transition temperatures by drop calorimetry for different alloy compositions are superposed over the equilibrium diagram. A good agreement between calorimetry based transus values and that of equilibrium $\alpha+\beta/\beta$ phase boundary is evident. However, in order to confirm the definite occurrence of a phase transformation in this domain, a slow heating differential scanning calorimetry experiment (*Setaram DSC Setsys Evolution 1600*) has been run on this alloy. The resulting DSC thermogram is displayed in **Fig. 3.10**.

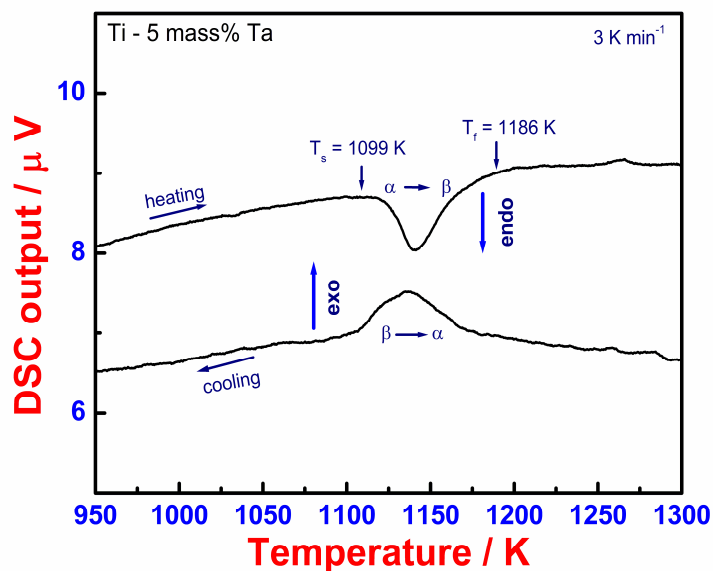


Figure 3.10 Slow scan DSC on-heating and cooling profile obtained for Ti – 5Ta alloy.

It is evident from this figure that in the temperature interval $1099 \leq T \leq 1186$ K, a clear endothermic thermal arrest is observed. This observation lends support to the occurrence of a slope change in the drop enthalpy data, as due to the possible phase change in the system. The small mismatch in the transformation temperature values obtained with DSC and by drop calorimetry technique arises from the finite heating rate

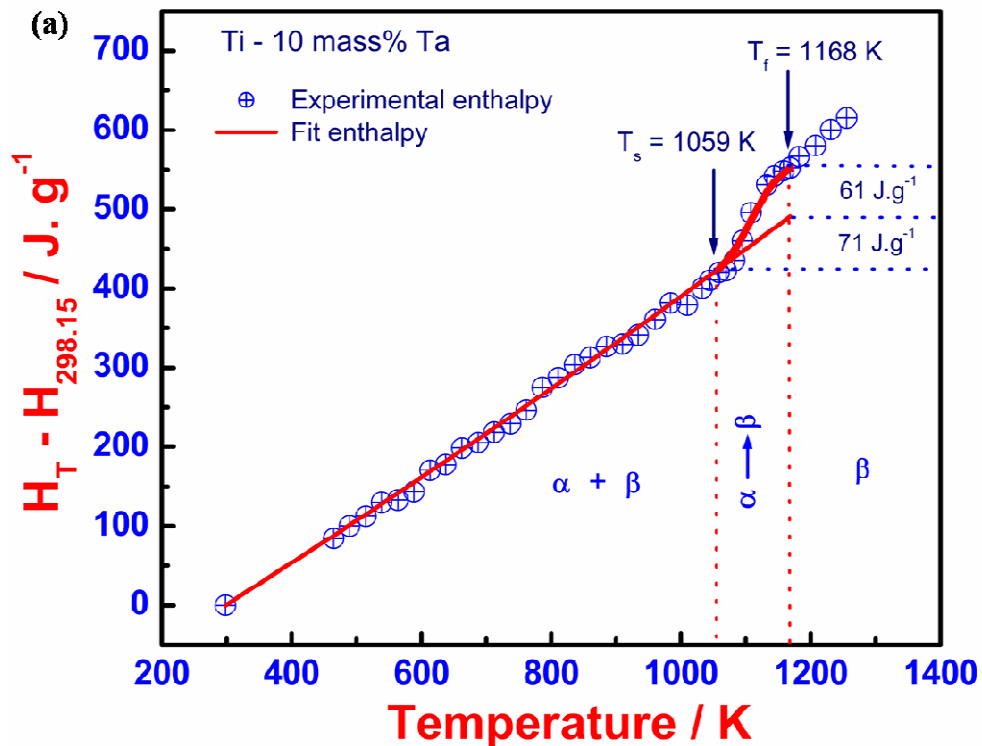
effects of DSC experiments [22]. In isothermal drop calorimetry measurements performed under close to equilibrium conditions, the nearly equilibrium transformation onset and finish temperatures are usually recorded [22], whereas in dynamic calorimetry experiments, the ubiquitous kinetic lag introduces a finite offset of the measured transformation temperature.

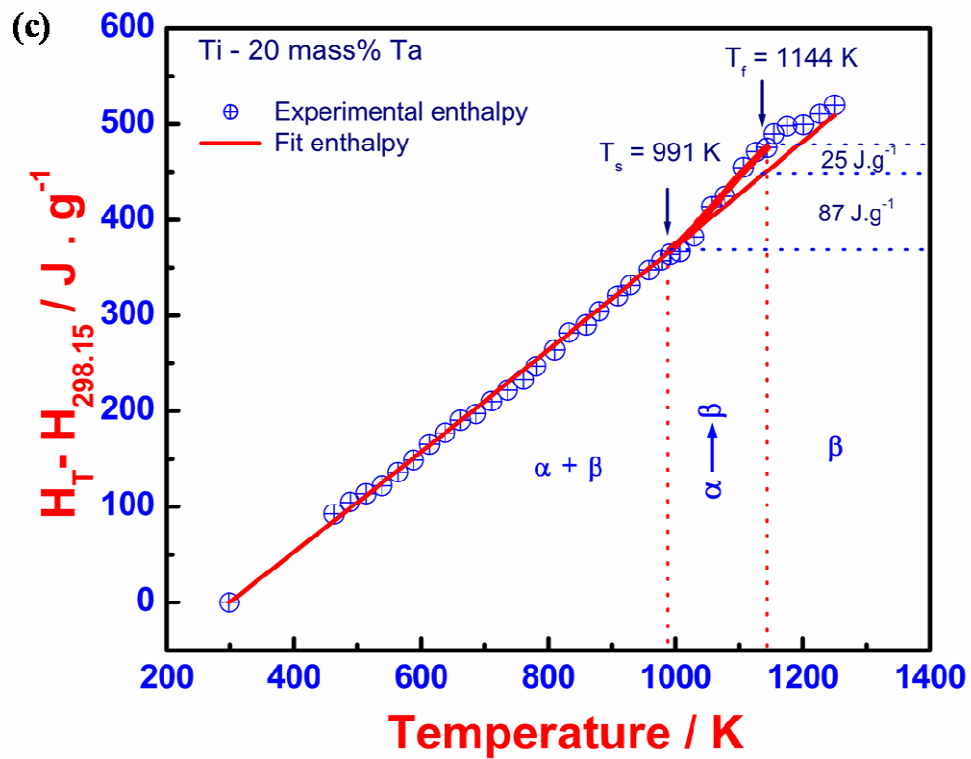
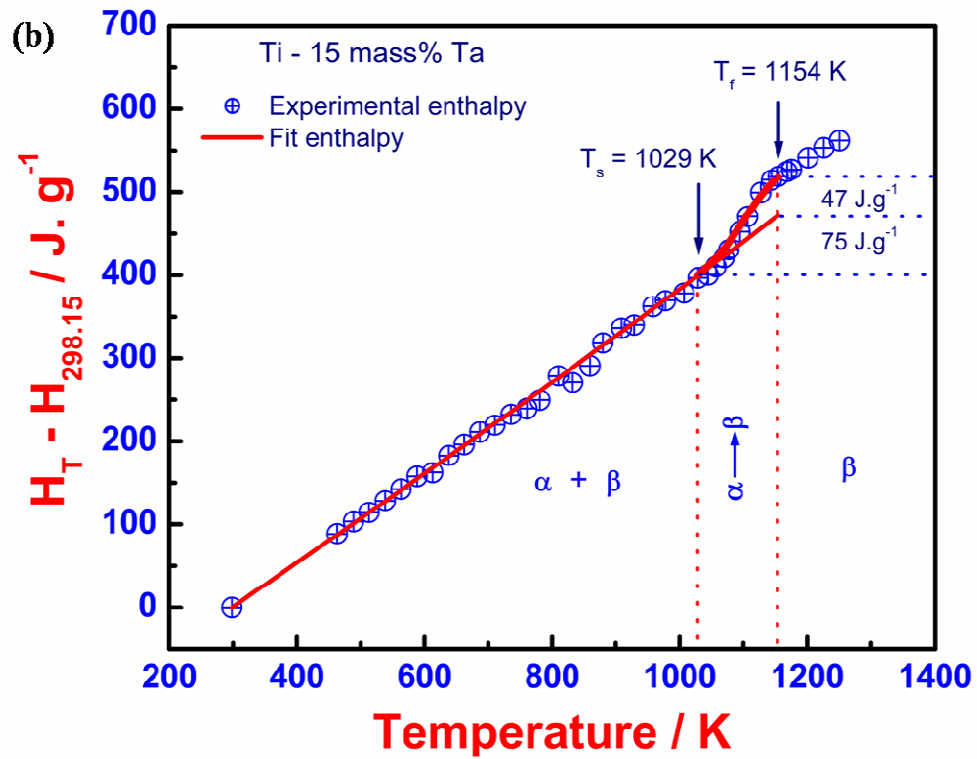
From **Fig. 3.9**, it can be observed that the total increase in enthalpy in the $\alpha \rightarrow \beta$ transformation domain namely 1083–1183 K, is $138 \pm 12 \text{ J g}^{-1}$. It can be mentioned here that the entire quantum of this 138 J g^{-1} could not be attributed to the enthalpy change associated with $\alpha \rightarrow \beta$ phase transformation [2, 4, 22]. This is because of the fact that in the temperature domain $T_s \leq T \leq T_f$, the alloy always exists as the $\alpha + \beta$ two phase mixture, with volume fractions of both α and β phases changing continuously with increasing temperature. In such case, a part of the contribution to total measured enthalpy must also come from the weighted average of the enthalpy due to untransformed α -hcp and the freshly formed β phase. This background or matrix contribution needs to be subtracted from the total measured change in enthalpy namely 138 J g^{-1} , to get the net enthalpy change that derives *only* from $\alpha \rightarrow \beta$ phase transformation. This aspect although graphically depicted in **Fig.3.9**, is addressed in detail in **section 3.8**.

3.5.2 Enthalpy Increment data for Ti – 10, 15, 20 mass% Ta alloy

In **Fig. 3.11 (a-c)**, the temperature dependencies of measured $H_T - H_{298.15}$ data for other compositions namely, Ti-10, 15, 20 Ta are collated together. It is seen that the observed temperature variation of enthalpy with increasing Ta content is similar to that of Ti-5Ta alloy. The $\alpha \rightarrow \beta$ transformation start (T_s) and finish (T_f) temperatures for Ti-10, 15, 20 Ta alloys are listed in **Table 3.2**. It is observed that the measured $\alpha \rightarrow \beta$ transformation start and finish temperatures are becoming progressively lower with increasing Ta content (1083 K/5Ta; 1059 K/10Ta; 1029 K/15Ta; 991K/20Ta), which is in perfect

accord with the β -bcc stabilizing character of tantalum as an alloying addition in titanium. On the other hand, the width of the $\alpha \rightarrow \beta$ transformation domain $\Delta^{\circ}T_{tr}$, that is $(T_f - T_s)$, shows an increase with Ta content – 100 K for 5Ta; 109 K for 10Ta; 125 K for 15Ta; 153 K for 20Ta. This implies the fact that β formation and hence its completion is becoming more sluggish with increasing Ta content. This is despite the fact that the driving force for the $\alpha \rightarrow \beta$ phase change increases with Ta. It is therefore clear that bulk diffusional kinetics of Ta in β assumes considerable importance in influencing the $\alpha \rightarrow \beta$ phase change in high Ta content alloys. It is worth noting here that with increasing Ta content of the alloy, the net jump in the enthalpy content between T_s and T_f , that is $(H^{\circ}_{T_f} - H^{\circ}_{T_s})$ also exhibits a remarkable decrease. Thus we get values of 138, 132, 122, and 112 J g⁻¹ for 5, 10, 15 and 20Ta alloys respectively (**Fig. 3.11 (a-c)**). In **Fig. 3.11 (d)**, the measured enthalpy data in the α -stability regime are compared for the four compositions studied here.





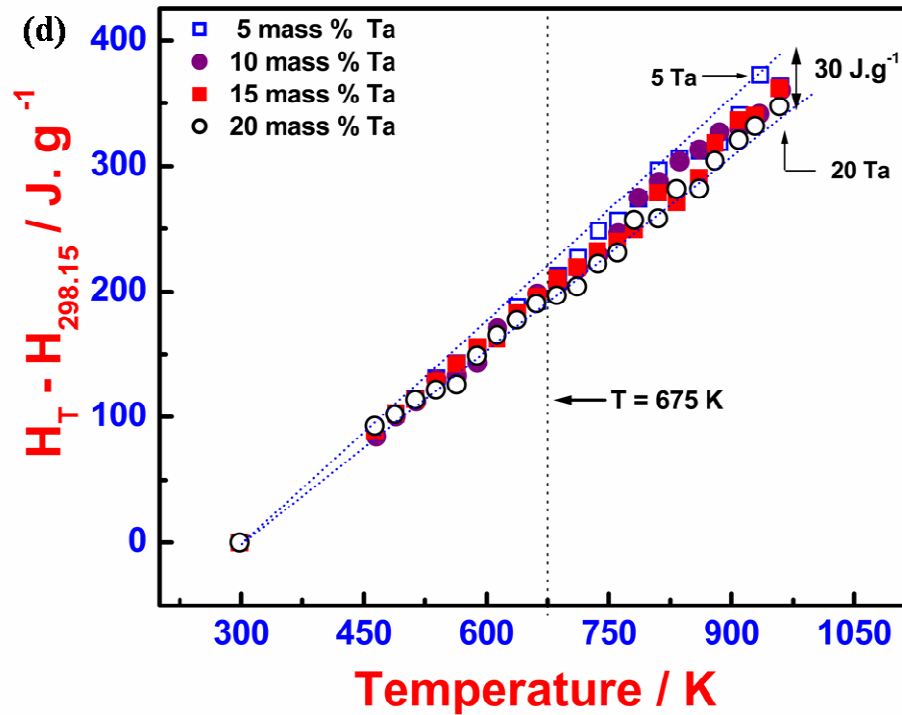


Figure 3.11 Variation of enthalpy increment with temperature is plotted for (a) Ti–10 Ta, (b). Ti–15 Ta (c). Ti–20 Ta alloys. In (d) the data for all the compositions are compared for the $\alpha + \beta$ domain.

It is interesting to observe that the data for all the alloys exhibit a narrow spread of about 30 J.g^{-1} even at the highest temperature. This spread is really not high, considering especially the $\pm 10\%$ uncertainty in the measured enthalpy values. The important deduction from **Fig. 3.11 (d)** is that there seems to be present an underlying homologous character in the fundamental thermodynamic properties of Ti-rich Ti-Ta alloys. This observation will be of use in estimating the thermal property of Ti-Ta alloys using quasi-harmonic theoretical framework.

3.6 Microstructural evolution in $\alpha \rightarrow \beta$ transformation zone

3.6.1 Microstructural characterization of post drop samples of Ti-5 Ta alloy

As seen before (**Fig. 3.5**), the starting microstructure for the homogenized alloys at room temperature consists of a mixture of α and β phases. During heating, when the temperature reaches close to T_s , the equilibrium $\alpha + \beta \rightarrow \beta$ transformation start

temperature, the α phase begins to transform to bcc- β . In the temperature interval $T_s \leq T \leq T_f$, the phase transformation occurs by the gradual time dependent growth of β phase into α region, which is facilitated by the diffusional transfer of Ta atoms, away from the α/β interface and into the growing β phase [2]. At T_f , the transformation finish temperature, $\alpha \rightarrow \beta$ conversion is almost complete. In the current drop calorimetry measurements, each alloy sample spends about 30 minutes at each drop temperature. Hence, it can be assumed that the diffusional $\alpha \rightarrow \beta$ phase change proceeds to near completion under fairly close to equilibrium conditions. Therefore, it is clear that, samples which have been equilibrated at different temperatures in the transformation zone, $T_s \leq T \leq T_f$ would have transformed to only partially. In other words, f_β , the fraction of bcc- β phase formed is a function of temperature in the interval $T_s \leq T \leq T_f$. These partially transformed samples upon cooling will produce a microstructure that will be distinctly reflective of the *relative* extent of $\alpha \rightarrow \beta$ phase change. Incidentally, the β phase formed out of isothermal $\alpha \rightarrow \beta$ reaction at high temperature re-transforms back to α -hcp during slow cooling. In **Fig. 3.12**, a collage of such typical quenched-in transformation zone microstructures for Ti-5Ta alloy is presented. Each micrograph in this collage corresponds to a structure attained by cooling from a different temperature in the transformation zone $T_s \leq T \leq T_f$. A change in the morphology is clearly observed. However, a detailed study on the mechanistic aspects of microstructural evolution in the transformation zone is beyond the scope of the present work. Further, microhardness measurements have also been made on samples drawn from pre-transformation zone, the transformation zone and the post transformation zone temperatures and the results are displayed in **Fig. 3.13**. It can be seen that hardness variation with temperature is indicative of the final microstructure as a consequence of the $\alpha \rightarrow \beta$ transformational effects.

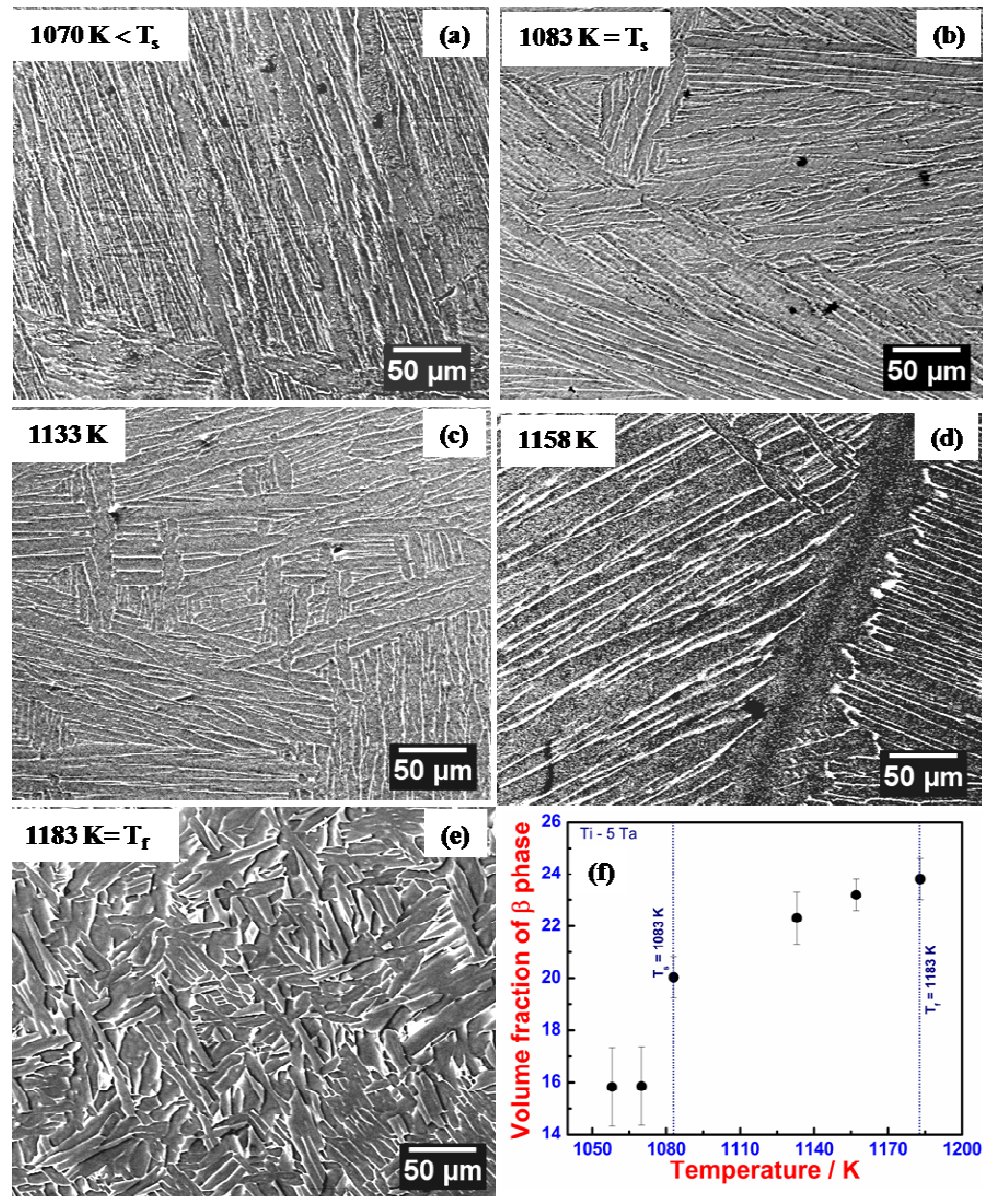


Figure 3.12 Collage of transformation microstructures (a-e) obtained for Ti-5Ta alloy. Each micrograph corresponds to different temperature T in the transformation zone, $T_s \leq T \leq T_f$, and hence exhibit different extents of α : β phase fraction as shown in (f)

In the pre- transformation zone, that is $T \leq T_s$, as a consequence of the general softening of the α - lattice with temperature, the hardness shows a decreasing trend, which persists right up to 1070 K, a temperature just below the T_s . In the transformation domain, the hardness exhibits a gradual increase, which is also corroborated by the change in microstructural features seen in **Fig. 3.12**. The increasing hardness behavior is due to

the increasing volume fraction of fresh and fine α that forms from β during cooling. More importantly, with each successive incremental increase in drop temperature in the transformation zone $T_s \leq T \leq T_f$, the β -phase that forms as a result of isothermal transformation is becoming progressively rich in Ta. This also serves to enhance the hardness of the transformation zone microstructure. In the post transformation zone, the hardness of the quenched-in microstructure exhibits a sharp rise with increasing drop temperature. In the post transformation zone, there is almost 100% β -phase at high temperatures, which transforms back to $\alpha + \beta$ two phase structure upon cooling (see also DSC profile in **Fig. 3.10**). The observed change in the hardness of the post transformation zone quenched microstructure is due to the fine nature of the α -colony and large fraction of β phase (see, **Fig. 3.12(f)**).

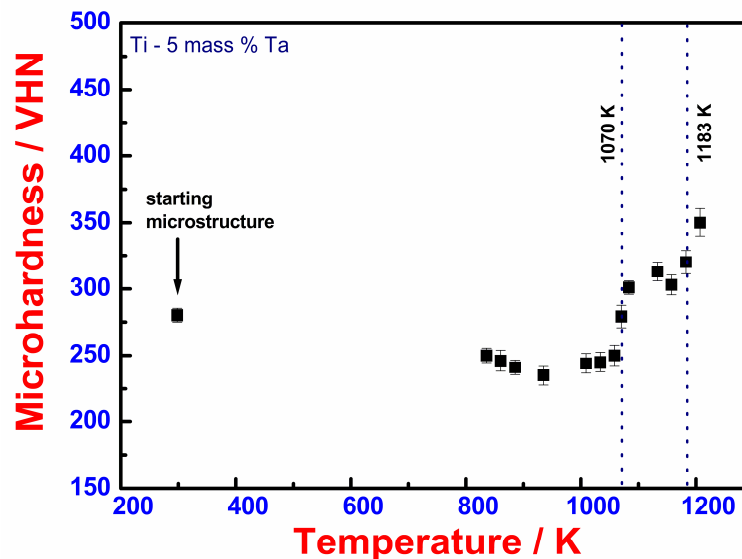


Figure 3.13 Variation of microhardness of the quenched-in microstructure with temperature in the transformation zone for Ti-5 Ta.

3.6.2. Microstructural characterization of post drop samples of Ti-15 Ta alloy

In **Fig. 3.14 (a-e)**, collage of optical micrographs of the samples dropped from various temperatures in the transformation zone $T_s \leq T \leq T_f$ for Ti-15Ta alloy is presented.

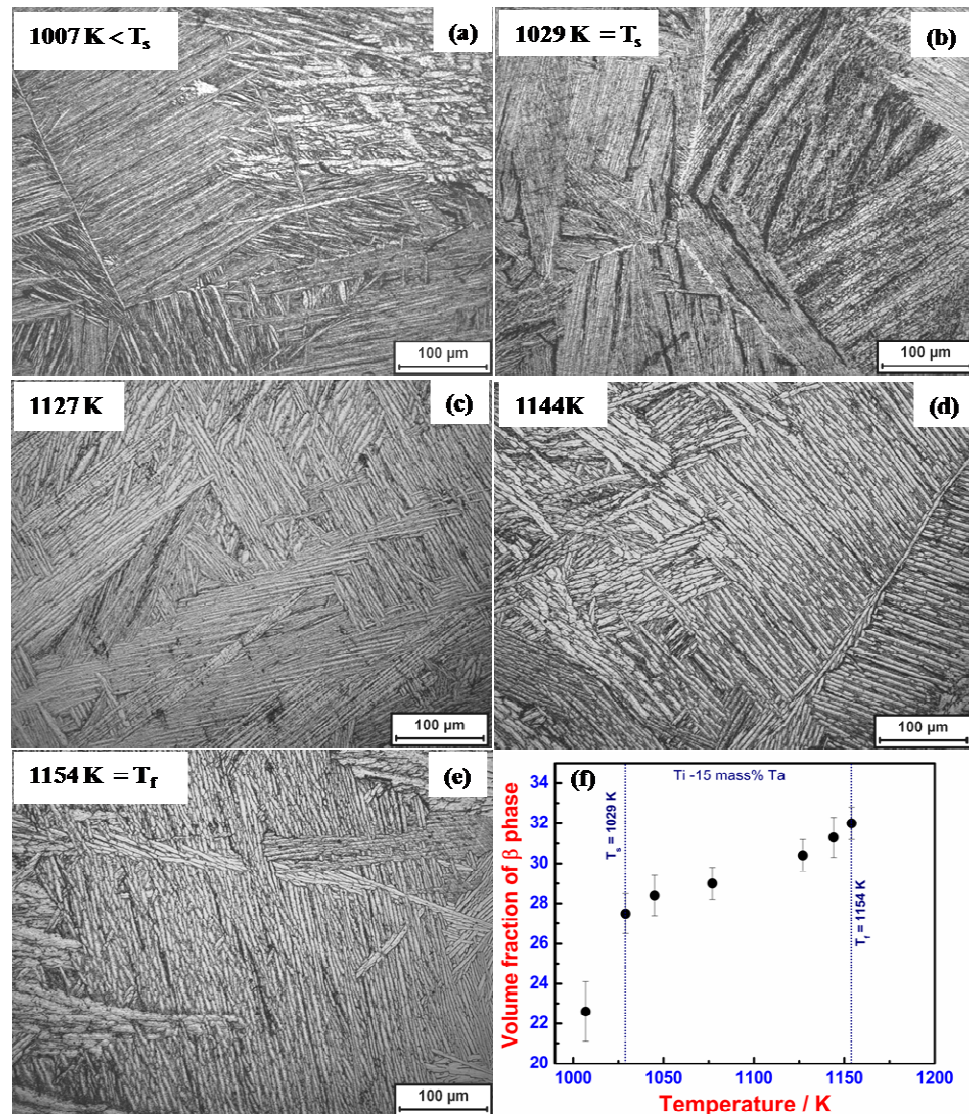


Figure 3.14 Collage of transformation microstructures (a-e) obtained for Ti-15Ta alloy. Each micrograph corresponds to different temperature T in the transformation zone, $T_s \leq T \leq T_f$, and hence exhibit different extents of α : β phase fraction as shown in (f).

As explained in the previous section, during heating when the temperature reaches the transformation start temperature T_s , the α phase begins to transform to bcc- β and at T_f , the transformation finish temperature, $\alpha \rightarrow \beta$ conversion is almost complete. The fraction of β – bcc phase (f_β), formed is a function of temperature T in the interval $T_s \leq T \leq T_f$. The increased volume fraction of β – bcc phase as a function of temperature T is shown in Fig. 3.14 (f).

Microhardness measurements have also been performed on samples of Ti-15Ta alloy drawn from pre-transformation zone, the transformation zone and the post transformation zone temperatures which is displayed in **Fig. 3.15**. It can be seen that hardness variation with temperature shows the similar behavior as in case of Ti-5Ta alloy. There is gentle drop in the hardness value upto transformation start temperature (T_s) due to softening of α -lattice. In the transformation zone $T_s \leq T \leq T_f$, an increasing trend in the hardness value is observed that is due to the increasing volume fraction of β -bcc phase formed during isothermal holding and also the increasing volume fraction of fresh and fine α that forms from β during cooling. In the post transformation zone the hardness value exhibits a sharp rise with increasing drop temperature.

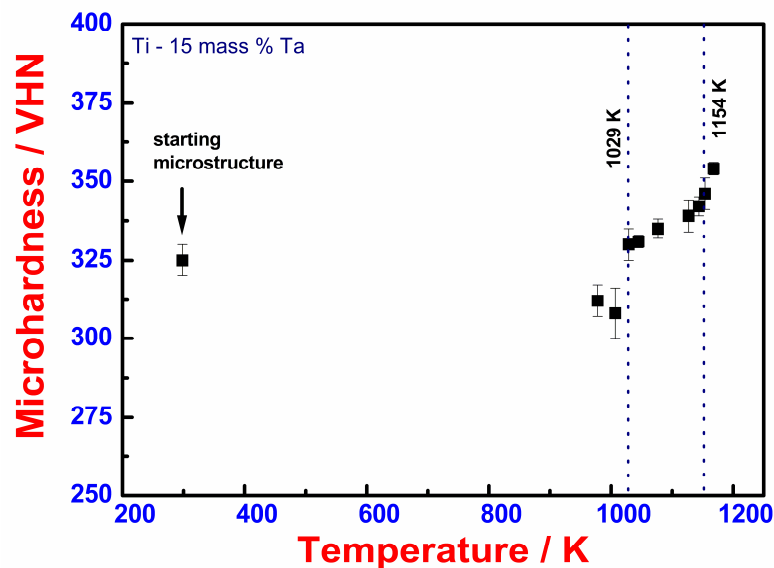


Figure 3.15 Variation of microhardness of the quenched-in microstructure with the temperature in the transformation zone for Ti-15 Ta.

3.7. Analytical representation of enthalpy increment $\Delta^0H(T)$ data for Ti-5Ta alloy

In the temperature span of measurement in the present study, the enthalpy increment variation with temperature is non-linear and exhibits a discontinuous change associated with $\alpha \rightarrow \beta$ phase transformation. Hence, it is not possible to fit $\Delta^0H(T)$ data in the

entire temperature span of measurement by a single functional form. In view of this, the data has been treated separately in two distinct regions that characterize stability domains of $\alpha+\beta$ and $\alpha\rightarrow\beta$ phase transformation respectively.

3.7.1 $\alpha+\beta$ domain: $463 \leq T \leq 1083$ K

The enthalpy increment data in the whole of $\alpha+\beta$ region are fitted by the method of nonlinear least square regression to the following expression [2, 5]

$$\Delta^{\circ}H_T^{\alpha+\beta} / \text{J g}^{-1} = [H_T - H_{298.15}] = a (T-298.15) + b (T^2-298.15^2) + c (T^{-1}-298.15^{-1}) \quad (3.1)$$

The values for the fit coefficients obtained for Ti-5Ta alloy are: $a = 0.50092 \pm 0 \text{ J g}^{-1} \text{ K}^{-1}$; $b = 6 \times 10^{-5} \pm 5.8 \times 10^{-6} \text{ J g}^{-1} \text{ K}^{-2}$; $c = 1.095 \times 10^3 \pm 1.8 \times 10^2 \text{ J g}^{-1} \text{ K}$; and $R^2 (\text{Fit}) = 0.9976$. In the above expression, $\Delta^{\circ}H_T$ is given in J g^{-1} and T in K. Eq. (3.1) ensures that enthalpy increment $\Delta^{\circ}H_T$ at $T = 298.15$ K takes the value of zero and that C_P at 298.15 K = $524 \text{ J kg}^{-1} \text{ K}^{-1}$. At present there are no measured low temperature C_P estimates available for Ti-Ta alloys. Hence, it is not possible to constrain the fit given in Eq. (3.1) to reproduce the measured C_P at 298.15 K. Nevertheless, the estimated C_P value of $524 \text{ J kg}^{-1} \text{ K}^{-1}$ appears realistic, especially with a simple calculation attempted using Debye model with a suitably assessed value for θ_D , the Debye temperature. This aspect will be discussed in **section 3.9**. Following Eq. (3.1), the specific heat C_P is given by the following expression

$$C_P / \text{J kg}^{-1} \text{ K}^{-1} = 500.92 + 12 \times 10^{-2} T - 1.095 \times 10^6 T^{-2} \quad (3.2)$$

3.7.2 $\alpha\rightarrow\beta$ transformation region: $1083 \leq T \leq 1183$ K

3.7.2.1 Estimation of $\alpha\rightarrow\beta$ transformation enthalpy

As can be seen from the enthalpy curve (**Fig. 3.9**), the $\alpha\rightarrow\beta$ transformation occurs in the temperature interval 1083 to 1183 K. Further, as discussed in section 3.5,

the enthalpy increment in the transformation domain is comprised of two components. They are: (i) the sum of enthalpy due to α -hcp and β -bcc phases and (ii) the latent heat contribution associated with $\alpha \rightarrow \beta$ phase change. This second contribution is designated as the transformation enthalpy ($\Delta^\circ H_{tr}$). Keeping in line with this reasoning, the following expression may be used to represent the total enthalpy variation with temperature in the transformation zone, $T_s \leq T \leq T_f$.

$$\Delta^\circ H_T^{\alpha \rightarrow \beta} = [f_\alpha \Delta^\circ H_T^\alpha + f_\beta \Delta^\circ H_T^\beta] + \Delta^\circ H_{tr}(T) \quad (3.3)$$

Further, it is also clear that

$$f_\alpha(T) + f_\beta(T) = 1. \quad (3.4)$$

In the above expression $f_\alpha(T)$ and $f_\beta(T)$ represent the fraction of untransformed α and β phase respectively at temperature T . $\Delta^\circ H_T^\alpha$ and $\Delta^\circ H_T^\beta$ are the respective enthalpy increments of α and β phases at T and $\Delta^\circ H_{tr}$ is the $\alpha \rightarrow \beta$ transformation enthalpy. In the transformation domain $T_s \leq T \leq T_f$, finite fractions of α and β phases always co-exist. Thus at any temperature T in the domain $T_s \leq T \leq T_f$, we have a progressively increasing contribution to the total enthalpy coming from $\alpha \rightarrow \beta$ phase change. Accordingly it is clear that at $T = T_s$, $\Delta^\circ H_{tr}(T) = 0$ and that at $T = T_f$, $\Delta^\circ H_{tr} = \Delta^\circ H_{tr}$ (maximum). It is therefore evident that any attempt to model total enthalpy variation with temperature in the transformation zone in terms of Eq. (3.3) and (3.4) is possible, only when $\Delta^\circ H_T^\alpha$, $\Delta^\circ H_T^\beta$, $\Delta^\circ H_{tr}$, f_α and f_β are known as explicit functions of temperature. It can also be said that the individual enthalpy contributions from α and β phases can not be estimated *a priori* in the transformation region. In such a situation, the values for $\Delta^\circ H_T^\alpha$ and $\Delta^\circ H_T^\beta$ in the phase transformation domain have to be obtained only as extrapolations of their respective trends in the corresponding low temperature $\alpha + \beta$ and high temperature β phase regions [2, 22]. This procedure is graphically illustrated in **Fig. 3.16**, wherein, the dotted line emanating from T_s indicates the extrapolated enthalpy behavior of the $\alpha + \beta$

phase mixture into the transformation domain. This extrapolation, although has no rigorous theoretical basis is taken to be valid up to the transformation end point, T_f . At T_f , the extrapolated enthalpy $\Delta^{\circ}H_T^{\alpha+\beta}(T_f)$ pertains to the hypothetical case of fully *untransformed* α phase plus the original amount of β that was present at the beginning. In other words, the extrapolation of the observed enthalpy behavior right up to T_f implies that no transformation is effectively realized until the transformation end temperature is reached.

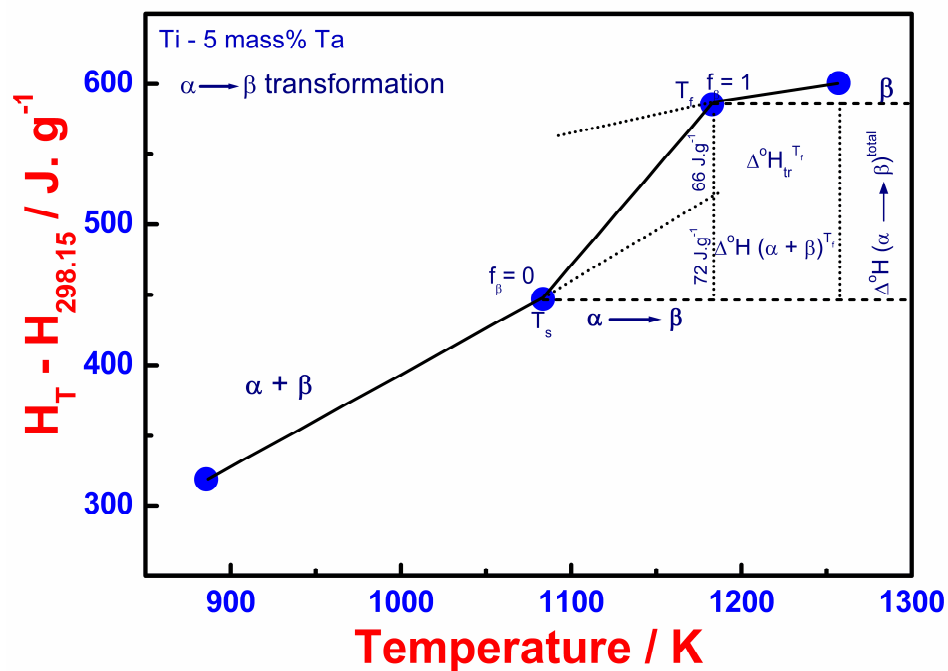


Figure 3.16 Graphical description of the method employed for estimating the $\alpha \rightarrow \beta$ transformation enthalpy, $\Delta^{\circ}H_{tr}$

In the second step, at T_f , the $\alpha \rightarrow \beta$ phase change is allowed to take place *isothermally* till it reaches completion. Thus, the continuous $\alpha \rightarrow \beta$ phase change in the domain $T_s \leq T \leq T_f$ is split into two sequential hypothetical unit processes and the net enthalpy change is also treated as a superposition of the two contributions. Of these, the baseline contribution which represents the weighted average enthalpy of untransformed $\alpha + \beta$ two phase mixture is given by the first term included within the square braces on the right

hand side of Eq. (3.3). This contribution is graphically estimated as 72 J g^{-1} , as indicated in the drop curve given in **Fig. 3.9**. The other contribution, namely the transformation enthalpy, which is shown as the difference component is estimated to be 66 J g^{-1} . This value of $\alpha \rightarrow \beta$ transformation enthalpy obtained for Ti-5Ta in this study compares fairly well with similar estimates obtained in the case of Ti-4 wt.%Nb-4wt.%Zr [5], Ti-5wt%Ta-1.8wt%Nb [4] and Ti-25.5 wt.% Nb [2] alloy systems. It should be remembered however, that in the actual process of $\alpha \rightarrow \beta$ phase change which occurs in a continuous fashion upon heating, the total transformation enthalpy value of 66 J g^{-1} is distributed over the entire transformation domain $T_s \leq T \leq T_f$. In other words,

$$\Delta^{\circ}H_{\text{tr}} (\text{total}) = \int_{T_s}^{T_f} [\Delta^{\circ}H_{\text{tr}}(T) dT]. \quad (3.5)$$

The evaluation of the integral on the right hand side necessitates that a suitable functional representation of the temperature variation of the transformation enthalpy be known a priori. This is a difficult problem to address on a rigorous basis, but a simpler alternative would be to approximate $\Delta^{\circ}H_{\text{tr}}$ in the following manner [2].

$$\Delta^{\circ}H_{\text{tr}} (T) \approx f_{\beta}^{\text{tr}}(T) \times \Delta^{\circ}H_{\text{tr}}(T_f). \quad (3.6)$$

where, $f_{\beta}^{\text{tr}}(T)$ is the fraction of β phase formed as a result of $\alpha \rightarrow \beta$ phase change in the transformation domain and $\Delta^{\circ}H_{\text{tr}}(T_f)$ is the total or full value of the transformation enthalpy measured at T_f . Eq.(3.6) predicts that at $T=T_s$, $f_{\beta}^{\text{tr}} = 0$; $\Delta^{\circ}H_{\text{tr}} = 0$ and at $T = T_f$, $f_{\beta}^{\text{tr}} = 1$; $\Delta^{\circ}H_{\text{tr}} = 66 \text{ J g}^{-1}$. In view of the above model, it now remains to devise a simple method for estimating $f_{\beta}^{\text{tr}}(T)$, so that $\Delta^{\circ}H_{\text{tr}} (T)$ may be calculated using Eq. (3.6). This aspect is addressed in the following section.

3.7.2.2 Model for temperature driven $\alpha \rightarrow \beta$ transformation kinetics

The fractional extent of $\alpha \rightarrow \beta$ transformation as a function of temperature in the transformation domain, namely $f_{\beta}^{\text{tr}}(T)$ is expressed in terms of a simple empirical model

for the diffusional transformation kinetics. The governing expression for the non-isothermal, site saturation approximation of the diffusional Kolmogorov-Johnson-Mehl-Avrami (KJMA) model is given below [23].

$$f_{\beta}^{\text{tr}}(T) = 1 - \exp(-k_0^n \exp\{-nQ_{\text{eff}}/(RT)\} (R(T-T_s)^2/\phi Q_{\text{eff}})^n) \quad (3.7)$$

In the above expression, Q_{eff} is the apparent activation energy for the overall transformation process, n is an empirical transformation exponent, k_0 is the frequency factor, ϕ is the heating rate in K s^{-1} (in the present study it nearly corresponds to slow heating rates such as 1 K s^{-1} , so that at each temperature T in the transformation domain, the equilibrium extent of $\alpha \rightarrow \beta$ transformation is realized) and R is the universal gas constant. It should be noted that Eq. (3.7) is a simple empirical model for the transformation kinetics, which is valid only under special conditions imposed on nucleation and growth mechanisms. But in the present study, we use this expression for the sole purpose of fitting empirically the observed temperature variation of the transformation extent. In the present study, since we allow for 30 minutes to elapse at each drop experiment and further only samples of about 40-60 mg are used, it is presumed that f_{β}^{tr} (experiment) corresponds to f_{β}^{tr} (equilibrium). Thus combining Eq. (3.3), (3.6) and (3.7), the enthalpy variation in the transformation domain can be analytically fitted to a simple physically based description of transformation kinetics. The fitting exercise yielded the following values for the kinetic quantities: $n = 0.68 \pm 0.03$; $Q_{\text{eff}} = 284 \pm 10 \text{ kJ mol}^{-1}$ and $k_0 = 1.4 \times 10^{12} \pm 3.4 \times 10^{10} \text{ s}^{-1}$. Thus in the final analysis, the total enthalpy increment in $\alpha \rightarrow \beta$ transformation domain $T_s \leq T \leq T_f$ may be represented by the following expression.

$$\Delta^{\circ}H_T^{\alpha \rightarrow \beta} / \text{J g}^{-1} = \{0.50092(T-298.15) + 6 \times 10^{-5}(T^2 - 298.15^2) + 1.095 \times 10^3 (1/T - 1/298.15)\} + f_{\beta}^{\text{tr}}(T) \times \Delta^{\circ}H_{\text{tr}}(T_f) \quad (3.8)$$

The first contribution included inside the curved braces is the baseline contribution and is akin to the first term in the square braces of Eq. (3.3). The second term gives the temperature dependent transformation enthalpy. In **Fig. 3.17**, the experimental and fit enthalpy increment values are compared for Ti-5Ta alloy in the $\alpha \rightarrow \beta$ transformation domain. As can be seen, the present method of treating the transformation energetics in conjunction with KJMA model for diffusional transformation kinetics, gives a fairly good analytical description of the experimental data. The C_p expression for the transformation region is obtained by taking the temperature derivative of Eq. (3.8).

$$\Delta^{\circ}C_p^{\alpha \rightarrow \beta} / \text{J kg}^{-1} \text{ K}^{-1} = 500.92 + 12 \times 10^{-2} T - 1.095 \times 10^6 T^{-2} + f_{\beta}^{\text{tr}} \times \Delta^{\circ}C_p^{\text{tr}} + df_{\beta}^{\text{tr}} / dT \times \Delta^{\circ}H_{\text{tr}}(T_f) \quad (3.9)$$

where,

$$df_{\beta}^{\text{tr}} / dT = -n(1 - f_{\beta}^{\text{tr}}) \ln(1 - f_{\beta}^{\text{tr}}) [(2/T) + Q_{\text{eff}} / (RT^2)] \quad (3.10)$$

$\Delta^{\circ}C_p^{\text{tr}}$ is the change in C_p associated with the net $\alpha \rightarrow \beta$ transformation enthalpy, which in the present study is estimated in the following manner.

$$\Delta^{\circ}C_p^{\text{tr}} = \Delta^{\circ}H_{\text{tr}}^{\alpha \rightarrow \beta} / \Delta T = \Delta^{\circ}H_{\text{tr}}^{\alpha \rightarrow \beta} / (T_f - T_s) = 667 \text{ J kg}^{-1} \text{ K}^{-1} \quad (3.11)$$

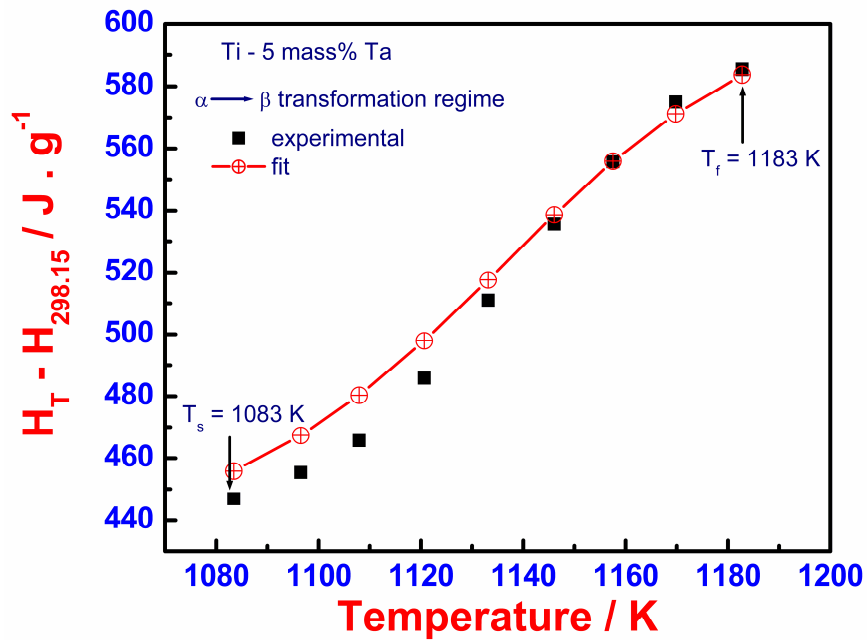


Figure 3.17 Comparison of the model and experimental values of enthalpy increment in the transformation domain for Ti-5 Ta alloy

The total change in specific heat in the entire $\alpha \rightarrow \beta$ transformation domain $\Delta^{\circ}C_p$, which is also inclusive of the baseline contribution from untransformed α phase is given by the change in *total* enthalpy increment per unit temperature rise between transformation start and finish temperature interval. This is given as,

$$\begin{aligned}\Delta^{\circ}C_p (\text{total}) &= (\Delta^{\circ}H_{T_f} - \Delta^{\circ}H_{T_s}) / (T_f - T_s) \\ &= (585.2 - 446.9) \times 1000 \text{ J kg}^{-1} / (1182.9 - 1083.4) \text{ K} = 1393 \text{ J kg}^{-1} \text{ K}^{-1}\end{aligned}\quad (3.12)$$

In the above expression, $\Delta^{\circ}H_{T_s}$ and $\Delta^{\circ}H_{T_f}$ are the measured enthalpy increment values at T_s and T_f respectively. It should be clear that $\Delta^{\circ}C_p^{\text{tr}}$ and $\Delta^{\circ}C_p (\text{total})$ are two different physical quantities.

3.8 Analytical representation of enthalpy increment $\Delta^{\circ}H(T)$ data for Ti-10, 15, 20 Ta alloy

The method of data analysis of enthalpy increment outlined above has been applied for other compositions as well. In **Table 3.2**, the fit parameters of Eq. (3.1) for the enthalpy increment data are listed. In **Table 3.3, 3.4, 3.5 and 3.6**, the experimental values of enthalpy increment and specific heat are presented for Ti-5Ta, 10Ta, 15 Ta and 20Ta respectively. The estimated parameters related to $\alpha \rightarrow \beta$ transformation energetics and kinetics are listed in **Table 3.7**. It is observed from **Table 3.7** that with increasing Ta content, the transformational enthalpy component $\Delta^{\circ}H_T^{\alpha \rightarrow \beta}$ exhibits a clear decrease: 66 J g⁻¹/5Ta; 61 J g⁻¹/10Ta; 47/ J g⁻¹/15Ta; 25 J g⁻¹/20Ta. On the other hand, the baseline or matrix contribution to total measured enthalpy exhibits a steady increase: 72 J g⁻¹/5Ta; 71 J g⁻¹/10Ta; 75/ J g⁻¹/15Ta; 87 J g⁻¹/20Ta. This latter trend reflects the role of increasing volume fraction of β phase retained in final annealed microstructure. This also accounts for the decreasing trend in the transformation enthalpy component with Ta, as progressively lesser amounts of α phase is allowed to undergo transformation to high temperature β . Besides it is also understood that with

increasing Ta, the $\alpha \rightarrow \beta$ transformation is kinetically retarded due to sluggish diffusion of Ta. Thus for example, the estimated values of apparent activation energy for the overall kinetics of the $\alpha \rightarrow \beta$ phase transformation increases with Ta concentration (**Table 3.7**). Although it is difficult to attribute a definite physical significance to the estimated Q_{eff} , it is observed that the estimated values are in reasonable agreement with the diffusional activation energy of Ta in hcp-titanium matrix [10]. It requires considerable superheating above the $\alpha + \beta/\beta$ solvus and long annealing durations for realising the full extent of $\alpha \rightarrow \beta$ transformation. The $\Delta^\circ C_p^{\text{tr}}$ values also exhibit a decrease with Ta content, for the reasons discussed above. In the present study, however, we have not attempted elaborate measurements in the full β -bcc region of the phase diagram. The effect of Ta concentration on the $\alpha \rightarrow \beta$ transformation start (T_s), finish (T_f) temperatures and the latent heat or the enthalpy need for the transformation is shown graphically in **Fig. 3.18 & 3.19** respectively.

Table 3.2 The $\alpha \rightarrow \beta$ transformation temperatures & the fit parameters of Eq. 2 for the enthalpy increment data for all Ti-Ta alloys.

S. No.	Ti-5 Ta	Ti-10 Ta	Ti-15 Ta	Ti-20 Ta
T_s (K)	1083	1059	1029	991
T_f (K)	1183	1168	1154	1144
Fit parameters				
a ($\text{J g}^{-1} \text{K}^{-1}$)	0.50092 ± 0.009	0.49178 ± 0.009	0.5081 ± 0.009	0.5047 ± 0.009
b ($\text{J g}^{-1} \text{K}^{-2}$)	$6 \times 10^{-5} \pm 5.8 \times 10^{-6}$	$5 \times 10^{-5} \pm 6.6 \times 10^{-6}$	$3 \times 10^{-5} \pm 6.8 \times 10^{-6}$	$2 \times 10^{-5} \pm 5.0 \times 10^{-6}$
C ($\text{J g}^{-1} \text{K}$)	$1.095 \times 10^3 \pm 1.8 \times 10^2$	$0.279 \times 10^3 \pm 2 \times 10^1$	$0.232 \times 10^3 \pm 1.9 \times 10^1$	$0.118 \times 10^3 \pm 1.3 \times 10^1$
R² (fit)	0.9976	0.9969	0.9972	0.99852

Table 3.3 Experimental and derived thermodynamic properties for Ti-5Ta alloys

T (K)	$H^{\circ}_T - H^{\circ}_{298.15}$ Experimental (J g ⁻¹)	$H^{\circ}_T - H^{\circ}_{298.15}$ Fit (J g ⁻¹)	Deviation (%)	C°_P (J kg ⁻¹ K ⁻¹)	S°_T (J kg ⁻¹ K ⁻¹)	G°_T (kJ kg ⁻¹)
$\alpha + \beta$ region						
298	0	0	-	524	566	-83
464	89	89	0	551	804	-197
490	102	103	1.0	555	834	-219
514	115	117	1.7	558	860	-239
539	131	131	0	562	887	-261
564	143	145	1.4	565	913	-283
589	156	159	1.9	568	938	-307
613	167	173	3.5	572	960	-329
638	188	187	-0.5	575	983	-354
663	192	201	4.5	578	1005	-378
688	213	216	1.4	581	1027	-404
712	227	230	1.3	584	1047	-429
737	248	245	-1.2	587	1067	-456
761	256	259	1.2	590	1086	-482
786	274	274	0	594	1105	-509
811	297	289	-2.8	597	1124	-536
835	306	304	-0.7	600	1142	-565
860	312	318	1.9	603	1159	-593
910	340	348	2.3	609	1193	-651
935	373	364	-2.5	612	1210	-681
959	364	378	3.7	615	1225	-711
984	399	394	-1.3	618	1241	-742
1009	417	409	-2.0	621	1257	-773
1034	416	425	2.1	624	1272	-804
1058	431	440	2.0	627	1286	-835
1070	438	448	2.2	628	1293	-851
1083	447	456	2.0	630	1301	-868
$\alpha \rightarrow \beta$ transformation region						
1096	455	467	2.6	729	-	-
1108	466	480	2.9	892	-	-
1121	486	498	2.4	1129	-	-
1133	511	517	1.2	1363	-	-
1146	536	539	0.5	1530	-	-
1157	556	556	0	1567	-	-
1170	575	571	-0.7	1504	-	-
1183	585	583	-0.3	1401	-	-

Table 3.4 Experimental and derived thermodynamic properties of Ti–10 Ta alloys

T (K)	$H^{\circ}_T - H^{\circ}_{298.15}$ Experimental (J g ⁻¹)	$H^{\circ}_T - H^{\circ}_{298.15}$ Fit (J g ⁻¹)	Deviation (%)	C°_P (J kg ⁻¹ K ⁻¹)	S°_T (J kg ⁻¹ K ⁻¹)	G°_T (kJ kg ⁻¹)
$\alpha + \beta$ region						
298	0 (set)	0	-	518	539	-79
465	84	88	4.5	537	773	-189
490	100	101	1	540	801	-209
514	113	115	1.7	542	828	-229
539	130	128	-1.6	545	853	-250
564	133	142	6.3	547	878	-271
589	143	155	7.7	550	902	-293
614	171	169	-1.2	552	924	-316
637	178	182	2.2	555	946	-339
662	199	196	-1.5	557	967	-362
687	206	210	1.9	560	988	-387
712	219	224	2.2	562	1008	-411
737	229	238	3.8	565	1027	-437
762	246	252	2.4	567	1046	-462
786	275	266	-3.4	570	1064	-489
811	288	280	-2.9	572	1081	-515
836	304	294	-3.4	575	1099	-542
860	313	308	-1.6	577	1115	-569
885	327	323	-1.2	580	1132	-597
910	330	337	2.1	582	1148	-625
934	341	351	2.8	585	1163	-653
960	361	367	1.6	587	1179	-684
984	382	380	-0.5	590	1194	-712
1010	379	396	4.3	592	1209	-743
1033	400	409	2.2	595	1222	-771
1045	410	417	1.7	596	1229	-786
1059	420	425	1.2	597	1237	-803
$\alpha \rightarrow \beta$ transformation region						
1070	422	434	2.8	684	-	-
1083	435	449	3.1	875	-	-
1095	460	465	1.1	1104	-	-
1108	496	486	-2.1	1335	-	-
1132	531	522	-1.7	1421	-	-
1144	542	534	-1.5	1323	-	-
1158	549	546	-0.5	1216	-	-
1168	552	552	0	1182	-	-

Table 3.5 Experimental and derived thermodynamic properties of Ti–15 Ta alloys

T (K)	H ^o _T -H ^o _{298.15} Experimental (J g ⁻¹)	H ^o _T -H ^o _{298.15} Fit (J g ⁻¹)	Deviation (%)	C ^o _p (J kg ⁻¹ K ⁻¹)	S ^o _T (J kg ⁻¹ K ⁻¹)	G ^o _T (kJ kg ⁻¹)
α + β region						
298	0 (set)	0	-	523	531	-78
463	89	87	-2.3	535	764	-186
490	103	101	-2.0	536	793	-206
513	114	114	0	538	819	-226
538	128	128	0	540	845	-247
563	143	141	-1.4	541	869	-268
589	156	155	-0.6	543	893	-290
638	183	182	-0.5	546	937	-336
662	196	195	-0.5	547	957	-358
687	211	209	-1.0	549	977	-382
711	220	222	0.9	550	996	-406
736	232	235	1.3	552	1015	-431
761	240	249	3.6	553	1033	-456
781	250	260	3.8	555	1048	-477
810	279	277	-0.7	556	1068	-508
833	271	289	6.2	558	1084	--533
860	291	304	4.3	559	1101	-562
880	318	316	-0.6	561	1114	-584
909	336	332	-1.2	562	1133	-617
929	340	343	0.9	564	1145	-640
958	362	360	-0.6	565	1163	-674
978	369	371	0.5	567	1174	-697
1007	378	387	2.3	568	1191	-731
1029	397	400	0.8	570	1203	-758
α → β transformation region						
1045	400	411	2.7	628	-	-
1057	410	421	2.6	708	-	-
1070	421	432	2.5	820	-	-
1077	431	440	2.0	894	-	-
1095	452	459	1.5	1070	-	-
1107	471	473	0.4	1153	-	-
1127	499	496	-0.6	1157	-	-
1144	515	511	-0.8	1065	-	-
1154	519	518	-0.2	1009		

Table 3.6 Experimental and derived thermodynamic properties of Ti-20 Ta alloys

T (K)	$H_T^0 - H_{298.15}^0$ Experimental (J g ⁻¹)	$H_T^0 - H_{298.15}^0$ Fit (J g ⁻¹)	Deviation (%)	C_P^0 (J kg ⁻¹ K ⁻¹)	S_T^0 (J kg ⁻¹ K ⁻¹)	G_T^0 (kJ kg ⁻¹)
$\alpha + \beta$ region						
298	0 (set)	0	-	515	524	-77
463	93	86	-8.1	523	752	-183
488	105	99	-6.1	524	780	-202
513	114	112	-1.8	525	806	-223
538	122	125	2.4	526	831	-243
563	136	138	1.4	527	855	-264
588	149	151	1.3	528	878	-286
613	165	164	-0.6	529	900	-308
638	177	177	0	530	921	-330
661	191	190	-0.5	531	940	-352
686	197	203	2.9	532	959	-376
711	210	216	2.8	533	978	-399
736	222	230	3.5	534	997	-424
761	233	243	4.1	535	1015	-449
781	247	254	2.8	536	1029	-470
810	264	269	1.9	537	1048	-500
832	282	281	-0.4	538	1063	-524
860	290	296	2.0	539	1080	-553
880	304	307	0.9	540	1093	-575
909	321	323	0.6	541	1110	-607
929	332	333	0.3	542	1122	-629
958	348	350	0.6	543	1139	-663
978	358	360	0.6	544	1150	-685
991	364	367	0.8	544	1157	-701
$\alpha \rightarrow \beta$ transformation region						
1007	367	377	2.6	580	-	-
1029	383	392	2.3	643	-	-
1057	414	413	-0.2	737	-	-
1077	425	429	0.9	789	-	-
1107	455	451	-0.9	798	-	-
1127	471	465	-1.4	765	-	-
1144	476	475	-0.2	736	-	-

Table 3.7 Thermodynamic and kinetics parameters pertaining to $\alpha \rightarrow \beta$ phase transformation are tabulated for all the alloy compositions investigated in this study.

Parameters	Ti-5Ta	Ti-10Ta	Ti-15Ta	Ti-20Ta
$\Delta^\circ H_{tr}$ (J g ⁻¹)	66	61	47	25
$\Delta^\circ C_p^{tr}$ (J kg ⁻¹ K ⁻¹)	667	561	376	161
$\Delta^\circ C_p(\text{total})$ (J kg ⁻¹ K ⁻¹)	1393	1208	975	731
$H^\circ_{298.15}$ (J g ⁻¹)	86	82	80	79
$S^\circ_{298.15}$ (J kg ⁻¹ K ⁻¹)	566	539	531	524
Kinetic parameters				
n	0.68 ± 0.03	0.66 ± 0.05	0.59 ± 0.01	0.45 ± 0.03
Q_{eff} (kJ mol ⁻¹)	284 ± 14	301 ± 15	325 ± 16	336 ± 12
k₀ (s ⁻¹)	1.4 × 10 ¹² ± 3.4 × 10 ¹⁰	2.29 × 10 ¹³ ± 2.1 × 10 ¹²	2.19 × 10 ¹⁴ ± 6.9 × 10 ¹²	1.28 × 10 ¹⁵ ± 1.6 × 10 ¹⁴
R²	0.99889	0.99497	0.99913	0.99405

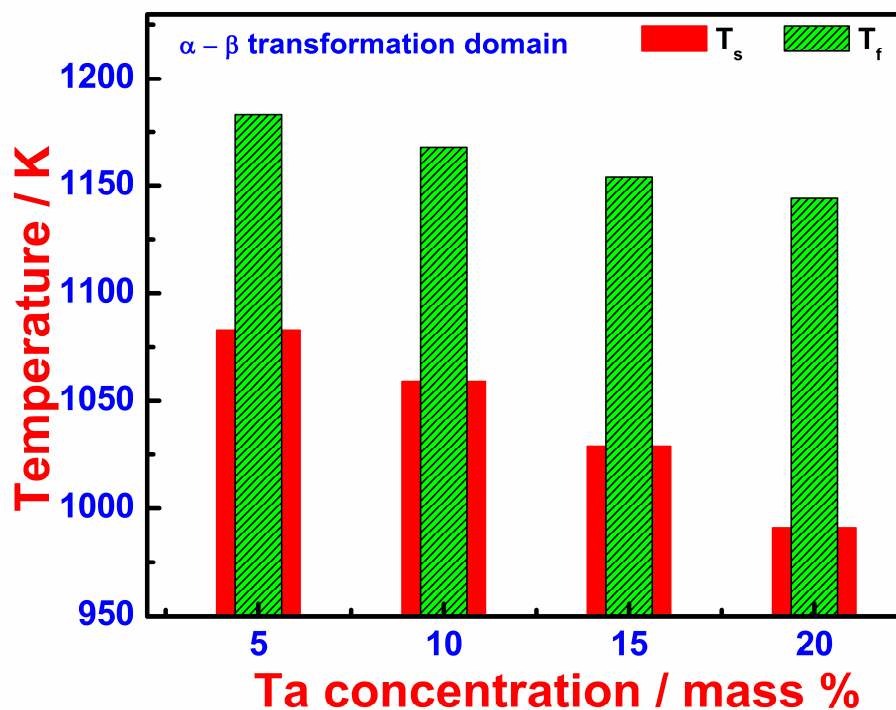


Figure 3.18 Effect of Ta concentration on the $\alpha \rightarrow \beta$ transformation start (T_s) and finish (T_f) temperatures.

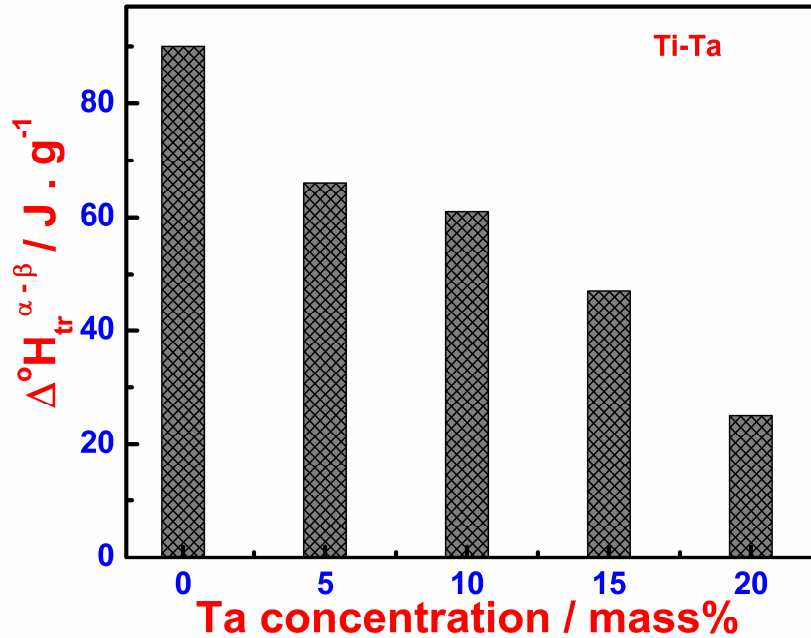


Figure 3.19 Effect of Ta concentration on the $\alpha \rightarrow \beta$ transformation enthalpy ($\Delta H_{tr}^{\alpha-\beta}$)

3.9 Theoretical estimate of C_p in low temperature region

As summarized quite elaborately by Collings [24], data on low temperature specific heat measurements and hence on calorimetric Debye temperatures (θ_D) are available for many compositions in titanium alloys, like Ti-Nb and Ti-Mo systems. However, there is no published data available in open literature on both high temperature and low temperature thermodynamic properties of Ti-Ta alloys. Some recent information on the variation of bulk modulus with Ta concentration is available for the β -bcc phase in published literature [25, 26]. Apart from these, no ab-initio or semi empirical density functional theory based physical property estimates are available for $\alpha+\beta$ two phase Ti-Ta alloys. It appears that most of the theoretical interest in Ti-Ta system is directed towards the high temperature bcc phase [27]. Nevertheless, with the knowledge of the lattice dimensions of α - phase obtained from the present X-ray diffraction results and the average atomic mass of the alloy, it is possible to estimate a reasonable value for θ_D elastic from the expression suggested by Moruzzi and Janak

[28] or the one modified by Chen and Sundman for hcp metals [29].

$$\theta_D (\text{K}) = 47.236 \times \{B_T \times r_o / M_{av}\}^{1/2} \quad (3.13)$$

In the above expression, B_T is the isothermal bulk modulus in kbar, r_o is the nearest neighbor separation in a.u and M_{av} is the average atomic mass of the alloy. In **Table 3.8**, the input values used for calculating θ_D in Ti-Ta alloys are listed. The values of θ_D estimated turn out to be, 366 K, 370 K, 360 K, 348 K for the α phase in Ti-5, 10, 15 and 20 Ta alloys respectively. In the present study, the lattice contribution to the specific heat at low temperatures has been approximated using Einstein model of specific heat, with $\theta_E \approx 0.77\theta_D$ [2, 30]. The electronic contribution to specific heat, C_v^e is given as $\gamma_e T$, with γ_e representing the coefficient of electronic specific heat, given in $\text{J kg}^{-1} \text{K}^{-2}$. An estimate of γ_e is obtained from the theoretical values of $N(E_F)$, the electronic density of states at the Fermi level on per atom basis [31] using the following expression.

$$\gamma_e = (2\pi^2/3) \times N(E_F) \times k_B^2 \quad (3.14)$$

In Eq. (3.14) k_B is the Boltzmann constant. The available theoretical estimates of $N(E_F)$ pertains to high Ta alloys, exceeding about 55 mass percent [26]. In view of this fact, an empirical extrapolation is attempted for low Ta compositions, with the $N(E_F)$ value for pure hcp Ti serving as the reference point. The low temperature C_V including the electronic contribution has been estimated for the α phase region of the four compositions studied here. It may be mentioned at this juncture that the dilatational contribution to heat capacity, given by the relation $C_p = C_v (1 + \gamma_G \alpha_V T)$ is not included in the present analysis, as data on thermal expansion coefficient α_V and Grüneisen parameter γ_G for Ti-Ta alloys are currently lacking. However, the volume coefficient of thermal expansion (α_V) and the Grüneisen parameter (γ_G) are calculated at room temperature (298.15 K) for all compositions of Ti-Ta alloys studied here using the following expressions.

$$\alpha_V = (C_P - C_V / V B_T T)^{1/2} \quad (3.15)$$

$$\gamma_G = (\alpha_V V B_T) / C_V \quad (3.16)$$

In the above expression, B_T is the isothermal bulk modulus in k bar, C_P and C_V are the experimentally derived and theoretically calculated heat capacity respectively at 298.15K and V is the volume in m^3/kg . The calculated values of α_V and γ_G at 298.15 K are listed in **Table 3.8**. In **Fig. 3.20 (a)**, the calculated low temperature C_V is shown for Ti-5Ta alloy, along with the experimental heat capacity data obtained by drop calorimetry for the $\alpha+\beta$ region.

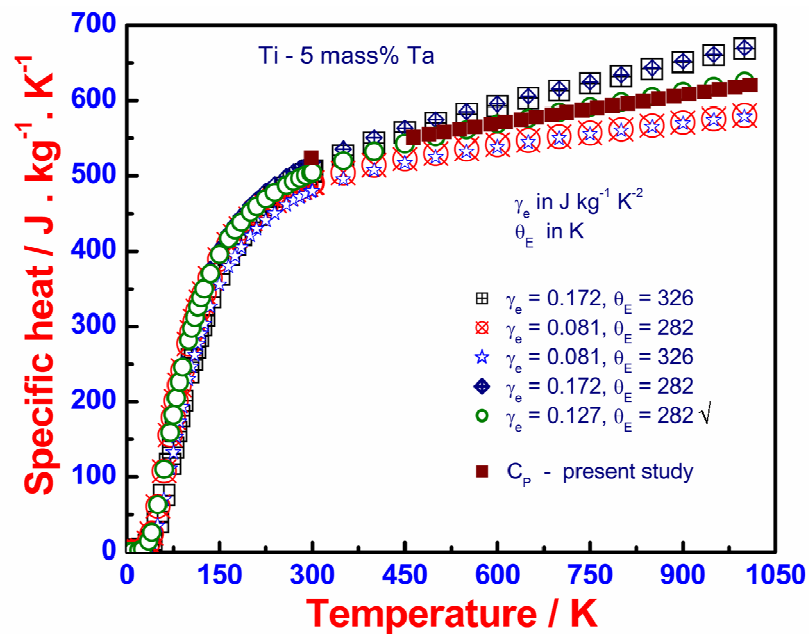


Figure 3.20 (a) Selection of γ_e and θ_E to obtain a good agreement between the experimental high temperature C_p and the simulated low temperature C_v data

This figure illustrates the crucial balance of the proper choices of values for θ_E and γ_e , in obtaining a good agreement between the experimental drop calorimetry based high temperature C_p data and the low temperature simulated ones using Einstein model, with due inclusion of electronic contribution. In the present study, we have adopted $\theta_E=282\text{K}$ and $\gamma_e=0.127 \text{ J kg}^{-1} \text{ K}^{-2}$ for Ti-5Ta alloy. The values for other compositions are listed in **Table 3.8**. In **Fig. 3.20 (b)** the heat capacity variation with temperature in the

temperature range of 0 – 1257 K is presented for Ti-5 Ta alloy.

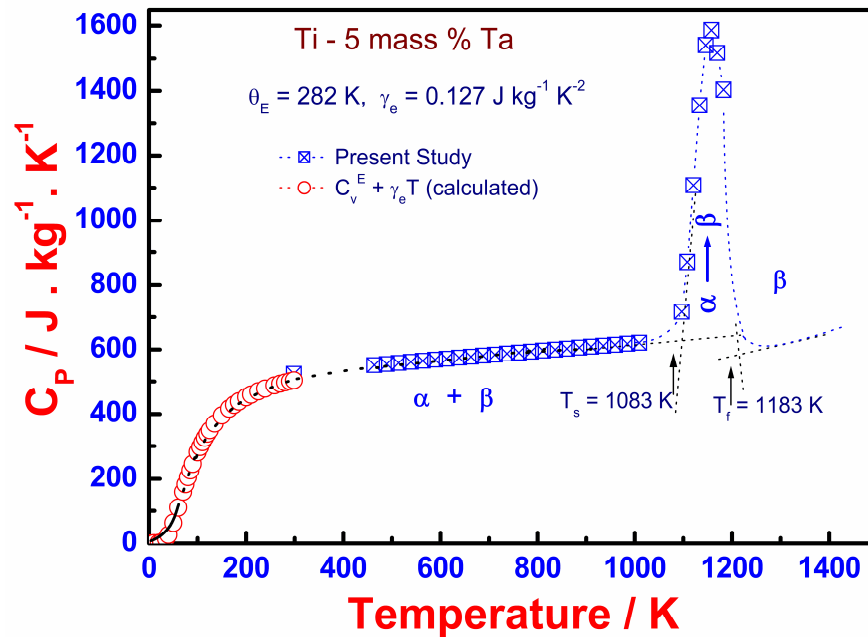


Figure 3.20(b) The calculated low temperature C_v for Ti-5Ta alloy is presented together with the experimental high temperature C_p obtained in the present study.

In **Fig. 3.21 (a-c)** the heat capacity variations with temperature for the entire range, 0-1257 K are summarized for the other three compositions namely Ti-10, 15, 20 Ta alloy studied here. In **Fig. 3.21 (d)**, the heat capacity variation with temperature in the $\alpha+\beta$ two phase domain, is portrayed. It can be seen that with increasing Ta, the experimental heat capacity exhibits a general decrease, although in a nonlinear fashion. The present experimental measurements of high temperature heat capacity together with theoretical estimates for the low temperature region offers a comprehensive set of thermodynamic data available for Ti-Ta alloys. The absence of other supporting physical property information like the basic equation of state parameters such as, isothermal compressibility, its pressure derivative, the thermal Grüneisen parameter etc., in addition to information on phonon properties makes the situation truly difficult for attempting even a semi-empirical integrated analysis of thermal properties [31]. It suggested that a detailed first principles based theoretical analysis of cohesive and

thermal properties of two phase Ti-Ta alloys may help considerably in interpreting the experimental results obtained which is beyond the scope of the present study.

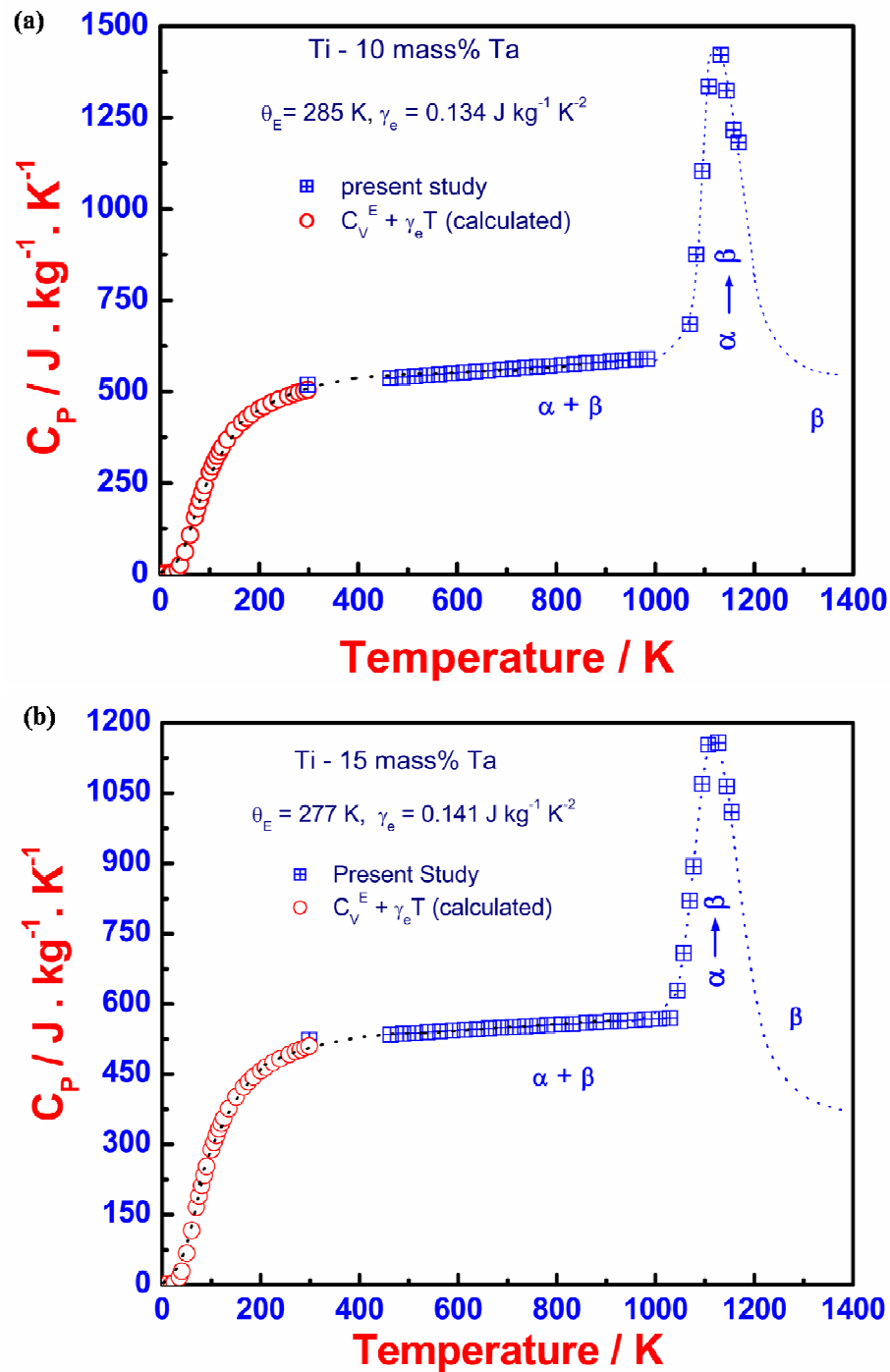
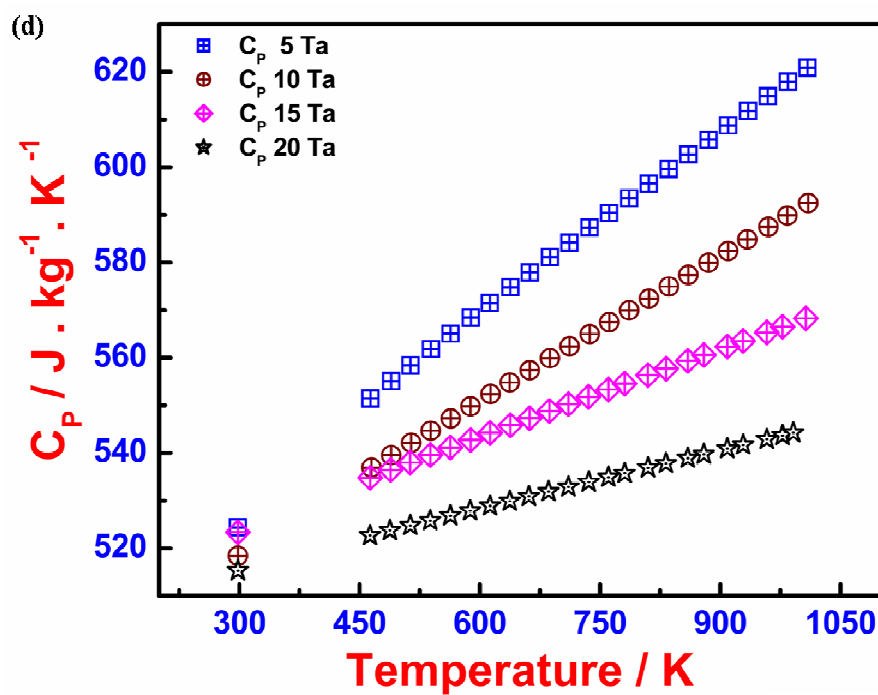
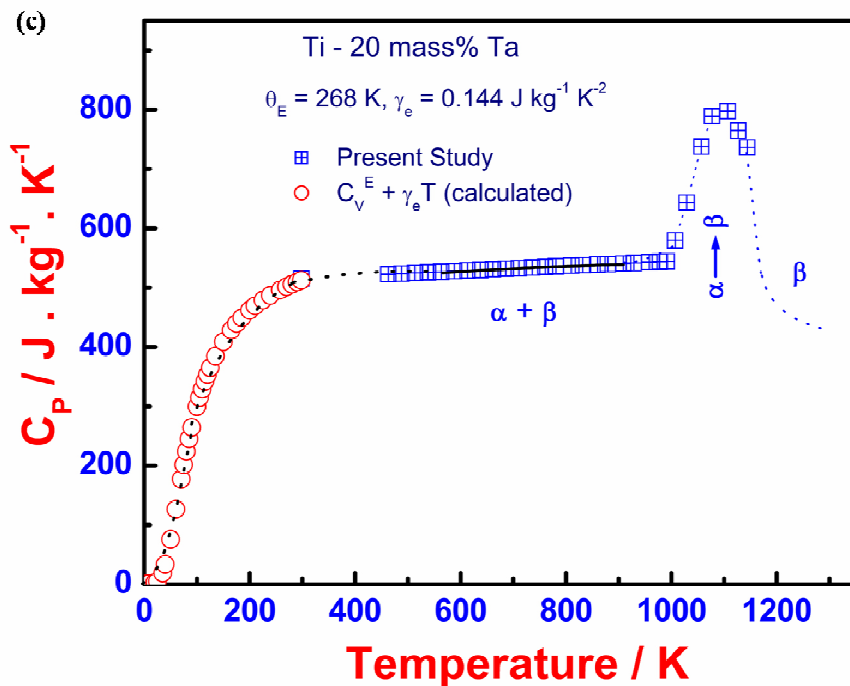


Figure 3.21 The C_p data for Ti-Ta alloys estimated in this study are summarized. (a) 10 Ta, (b) 15 Ta, (c) 20 Ta. In (d) comparison of C_p for all compositions in the $\alpha + \beta$ region is shown.



Contd.

3.10 Estimation of Thermodynamic Functions

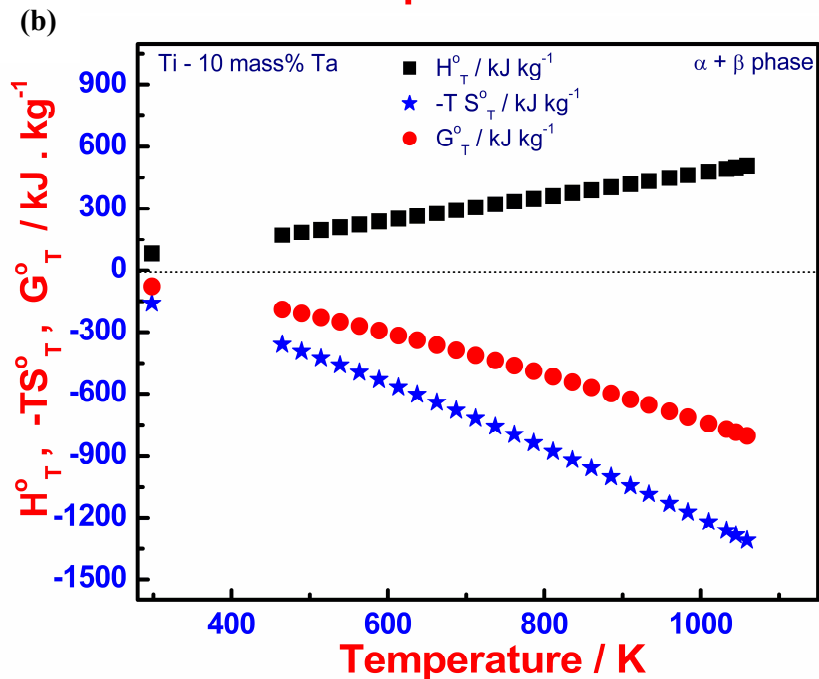
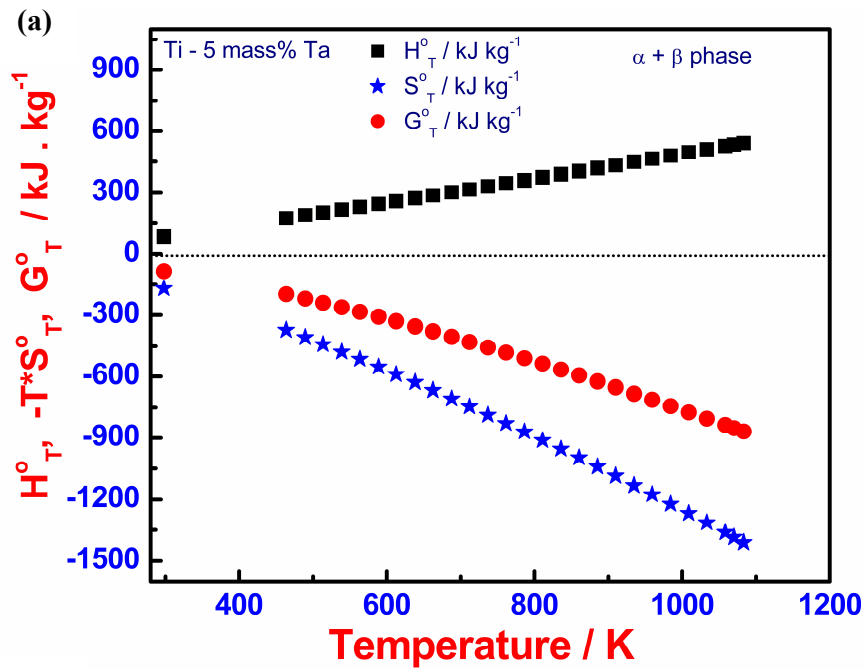
The vibrational entropy S_T^0 as a function of temperature has been calculated using the relation

$$S^{\circ}_T = S^{\circ}_{298.15} + 298.15 \int^T C_P d \ln T \quad (3.17)$$

In the absence of actual experimental value for $S^{\circ}_{298.15}$, the entropy at 298.15 K is taken as the corresponding Debye approximation limit which is given as [31].

$$S^{\circ}_{298.15} = 3R \{4/3 + \ln (298.15/\theta_D)\} \quad (3.18)$$

In the above expression, R is the gas constant. The values of $S^{\circ}_{298.15}$, estimated in this manner are: 566, 539, 531, 524 J kg⁻¹ K⁻¹ respectively for Ti-5, 10, 15, 20 Ta alloys (Table 3.7).



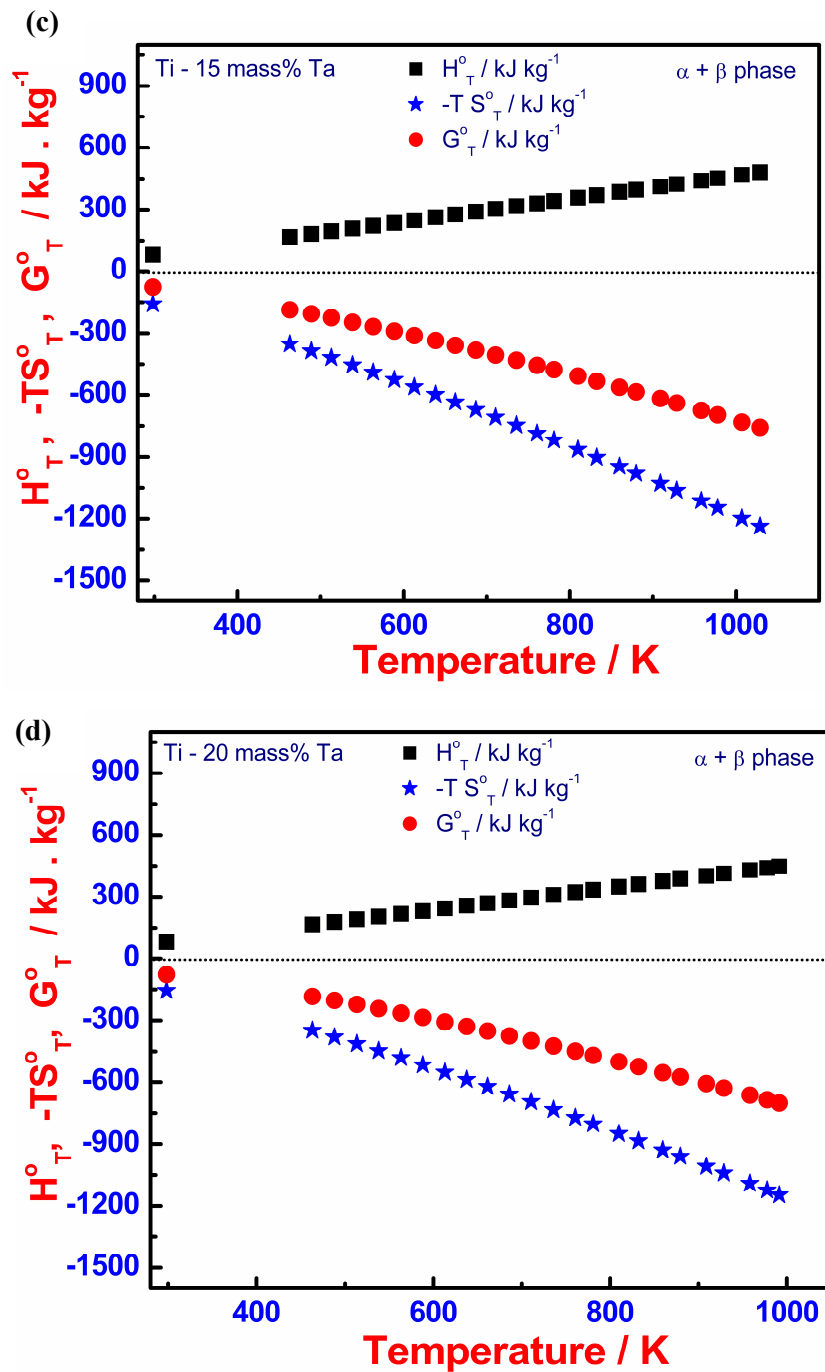


Figure 3.22 The variation of H_T^o , $-TS_T^o$ and G_T^o with temperature T in the $\alpha+\beta$ region of Ti-Ta alloys (a) 5 Ta, (b) 10 Ta, (c) 15 Ta, (d) 20 Ta

Again owing to the lack of actual experimental data on $H_{298.15}^o$, the following empirical relation connecting standard entropy and enthalpy of many inorganic and organic solids has been employed [32].

$$S^{\circ}_{298.15} / H^{\circ}_{298.15} = 0.0066 \text{ K}^{-1} \quad (3.19)$$

Having obtained an estimate of both $S^{\circ}_{298.15}$ and $H^{\circ}_{298.15}$, it is now possible to calculate G°_T , the Gibbs energy as a function of temperature for all the four compositions studied here. This computed quantities for the $\alpha+\beta$ region are listed in **Tables 3.3, 3.4, 3.5, 3.6** for Ti -5, 10, 15, 20 Ta alloys respectively. The variation of H°_T , $-TS^{\circ}_T$ and G°_T as a function of temperature for all Ti-Ta alloys is shown in **Fig.3.22**. It may be added that the present data appear to be the first experimental estimates of thermodynamic quantities of Ti-Ta alloys.

3.11 Conclusions

- i. The enthalpy increment as a function of temperature ($463 \leq T \leq 1257$ K) has been measured for the Ti-xTa ($x= 5, 10, 15, 20$ mass %) alloys using inverse drop calorimetry technique. It involves the measurement of enthalpy increment as a function of temperature at closely spaced interval (15-25 K). The measured enthalpy increment are used to calculate specific heat by treating the same by a suitable functional form.
- ii. The occurrence of $\alpha \rightarrow \beta$ phase formation during heating has been detected for all the alloys. The measured transformation temperatures exhibited good agreement with the current assessed equilibrium diagram.
- iii. The thermodynamics of $\alpha \rightarrow \beta$ diffusional transformation and the enthalpy variation in the two phase transformation zone have been modelled using KJMA model description of diffusional transformation kinetics. Values of apparent activation energy for the $\alpha \rightarrow \beta$ phase transformation have been estimated for all the four compositions.

- iv. The specific heat capacity at 298.15 K is found to decrease with increasing content, although there is a homologous character present in the temperature variation of heat content among four compositions.
- v. The $\alpha \rightarrow \beta$ transformation enthalpy exhibited a decrease with increasing content; however, the width of the transformation zone increased with Ta content of the alloy.
- vi. A consistent thermodynamic dataset in the temperature range 0-1257 K have been obtained by combining the experimental data with simulated values for the low temperature region.

Table 3.8 Elastic and Thermodynamic properties of $Ti_{1-x}Ta_x$ ($x = 5, 10, 15, 20$ mass %) alloys at 298.15 K.

Ta content (mass %)	$B \times 10^9$ (N/m ²)	M_{av} (g)	r_o (a.u.)	θ_D^{***} est. (K)	θ_E (0.77* θ_D) (K)	γ_e est. (J kg ⁻¹ K ⁻²)	C_V est. (J kg ⁻¹ K ⁻¹)	C_P measured (J kg ⁻¹ K ⁻¹)	$V \times 10^{-4}$ est. (m ³)	$\alpha_v 10^{-5}$ est. (K ⁻¹)	γ_G
5	109*	49.69	2.74	366	282	0.127	504	524	0.1058	5.42	2.49
10	116**	51.67	2.73	370	285	0.134	518	518	0.1052	4.31	2.02
15	115*	53.8	2.73	360	277	0.141	523	523	0.106	4.55	2.02
20	111**	56.13	2.74	348	268	0.144	515	515	0.107	4.75	1.97

Note:

* Bulk modulus estimated from experimentally measured Young's modulus and poisson's ratio [25]

**Bulk modulus are evaluated by acoustic wave velocity measurement [25]

*** θ_D is estimated from bulk modulus using the expression suggested by Moruzzi *et al.*[28] with the scaling constant (k^{hex}) for hexagonal structure determined by Chen *et al.*[29]

References:

- [1] H. Bros, M. L. Michel and R. Castanet, *J. Therm. Anal.* 41 (1994) 7-24.
- [2] A. J. Prabha, S. Raju, B. Jeyaganesh, Arun Kumar Rai, Madhusmita Behera, M. Vijayalakshmi, G. Paneerselvam and I. Johnson, *Physica B* 406 (2011) 4200-4209.
- [3] A. K. Sinha, *J Phys. Chem. Solids* 29 (1968) 749-754.
- [4] Madhusmita Behera, S. Raju, B. Jeyaganesh, R. Mythili and S. Saroja, *Int. J. Thermophys.* 31 (2010) 2246-2263.
- [5] V. Anbarsan, B. Jeyaganesh, S. Raju, S. Murugesan, E. Mohandas, U. Kamachi Mudali and G. Manivasagan, *J. Alloys Comp.* 463 (2008) 160-167.
- [6] A. Kostov and D. Zivkovic, *J. Alloys Comp.* 460 (2008) 164-171
- [7] M. Hoch and R. Viswanathan, *Metall. Trans.* 2 (1971) 2765-2767.
- [8] C. Cagran, B. Wilthan, G. Pottlacher, B. Roebuck, M. Wickins and R. A. Harding, *Intermetallics* 11 (2003) 1327-1334.
- [9] D. Ansel, I. Thibon, M. Boliveau and J. Debuigne, *Acta Mater.* 46 No.2 (1998) 423-430.
- [10] R. A. Perez, F. Dymont, G. Garcia Bermudez, D. Abriola and M. Behar, *Appl. Phys. A* 76 (2003) 247-250.
- [11] S. A. Souza, R. B. Manicardi, P. L. Ferrandini, C. R. M. Afonso, A. J. Ramirez and R. Caram, *J. Alloys Comp.* 504 (2010) 330-340.
- [12] S. G. Fedetov, T. V. Chelidze, Y. K. Kovneristy and V. V. Sanadze, *Phys. Met. Metall.* 62 (1986) 109-113.
- [13] J. D. Cotton, J. F. Bingert, P. S. Dunn and R. A. Patterson, *Metall. Mater. Trans. A* 25 (1994) 461-472.
- [14] A. V. Dobromyslov and V. A. Elkin, *Scripta Mater.* 44 (2001) 905-910.
- [15] K. A. Bywater and J. W. Christian, *Philos. Mag. A* 25 (1972) 1249-1273
- [16] K. A. De Souza and A. Robin, *Mater. Lett.* 57 (2003) 3010-3016.
- [17] D. J. Maykuth, H. R. Ogden and R. I. Jaffee, *Trans. AIME, J Metals Feb.*, (1953) 231-237.
- [18] J. L. Murray, *Bull. of alloy phase diagram* 2, No. 1 (1981) 62-66.
- [19] S. Malinov, W. Sha, Z. Guo, C. C. Tang and A. E. Long, *Mater. Chara.* 48 (2002) 279-295.

- [20] M. Geetha, A. K. Singh, K. Muraleedharan, A. K. Gogia and R. Ashokamani, *J. Alloys Comp.* 329 (2001) 264-271.
- [21] B. Dutta, T. Keller, M. Rettenmayr, U. Jantsch and D. F. Lupton, *Mater. Sci. Engg A* 382 (2004) 57-63.
- [22] S. Raju, B. Jeyaganesh, A. Banerjee and E. Mohandas, *Mater. Sci. Engg. A* 465 (2007) 29-37.
- [23] F. Liu, F. Sommer and E. J. Mittemeijer, *Int. Mater. Rev.* 52 (2007) 193-212.
- [24] E. W. Collings, *Applied Superconductivity: Metallurgy and physics of Titanium alloys*; Plenum Press: New York 1 (1986) 307-332.
- [25] H. W. Jeong, Y. S. Kim, S. E. Kim, Y.T. Hyun, Y. T. Lee and J. K. Park, *Mater. Sci. Forum* 449–452 (2004) 865 – 868.
- [26] C. Y. Wu, Y.H. Xin, X.F. Wang and J. G. Lin, *Solid State Sci.* 12 (2010) 2120-2124.
- [27] H. Ikehata, N. Nagasako, T. Furuta, A. Fukumoto, K.Miwa and T. Saito, *Phys. Rev. B* 70 (2004) 174113-1-174113-8.
- [28] V. L. Moruzzi, J. F. Janak and K. Schwarz, *Phys. Rev. B* 37 (1988) 790-799.
- [29] Q. Chen and B. Sundman, *Acta Mater.* 49 (2001) 947-961.
- [30] H. L. Ledbetter, *Phys. Status Solidi B* 181 (1994) 81-85.
- [31] G. Grimvall, *Thermophysical Properties of Materials*, 1st edition, North Holland, Amsterdam, 1999, P 167.
- [32] F. L. Lambert and H. S. Leff, *J. Chem. Edu.* 86 (2009) 94-98.

Chapter-4

Study of phase transformation kinetics in Ti- xTa (x = 5, 10, 15, 20 mass %) alloys using Differential Scanning Calorimetry

4.1 Introduction

The end application of any alloy with desired properties can be obtained by tailoring the microstructure through phase transformation. The kinetics of phase transformation is the governing factor which regulates the microstructure at the end of heat treatment schedule. Extensive literatures elucidating the transformation behavior of $\alpha+\beta$ or near β titanium alloys using experimental as well as theoretical and modeling techniques [1-7] are available. However, there are only few studies on the kinetics aspect of $\alpha\leftrightarrow\beta$ phase change in titanium alloys using calorimetry techniques are available [5-7]. This statement is quite true for Ti-Ta binary alloys which are promising corrosion resistant and biocompatible candidates among $\alpha+\beta$ or β titanium alloys [8]. Hence, the scope of this chapter is to measure the $\alpha\leftrightarrow\beta$ phase transformation temperatures and the transformation enthalpy of Ti-x Ta (x= 5, 10, 15, 20 mass %) alloys as a function of various heating and cooling rates using high resolution differential scanning calorimetry.

Differential Scanning Calorimetry has been used as a powerful tool to study the phase transformation in titanium alloys [5, 6]. In the present study, the DSC experiments are followed by metallography characterization of post DSC samples. The results of this thermal analysis study are modeled using Kolmogorov-Johnson-Mehl-Avrami (hereafter called KJMA) formalism to describe the kinetics of phase transformation. The kinetic quantities for $\alpha\leftrightarrow\beta$ diffusional transformation have been evaluated as a function of heating and cooling rate. Using the results of DSC measurements, the continuous heating transformation and continuous cooling transformation diagrams are generated for Ti-x Ta (x= 5, 10, 15, 20 mass %) alloys. In addition, a comparative discussion of present results, in the light of available information on other related Ti-base systems has also been presented.

4.2 Organization of Chapter

The organization of this chapter is as follows. In section 4.3 the structural and microstructural characterization of starting material is discussed very briefly. In section 4.4 and 4.5 the raw output of DSC experiments such as the transformation temperatures and the transformation peak profile are described. Section 4.6 discusses the comparison of measured $\alpha+\beta/\beta$ transformation temperatures and the enthalpy needed for the transformation in the present study with the available literature data. Section 4.7 deals with the discussion of kinetics of $\alpha\leftrightarrow\beta$ phase transformation in Ti-Ta alloys. Section 4.8 summarizes the results of this study.

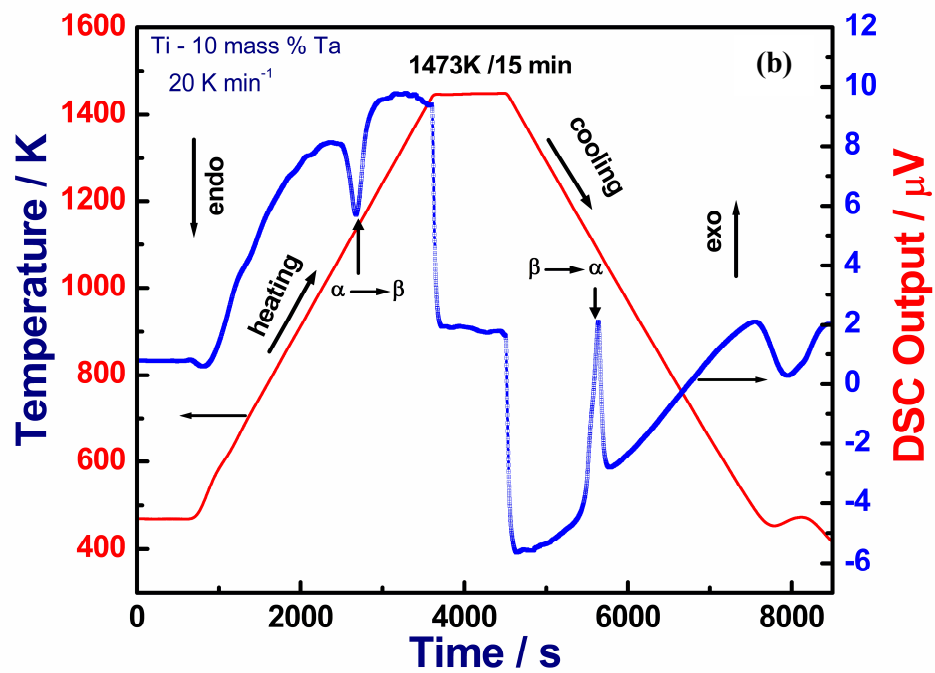
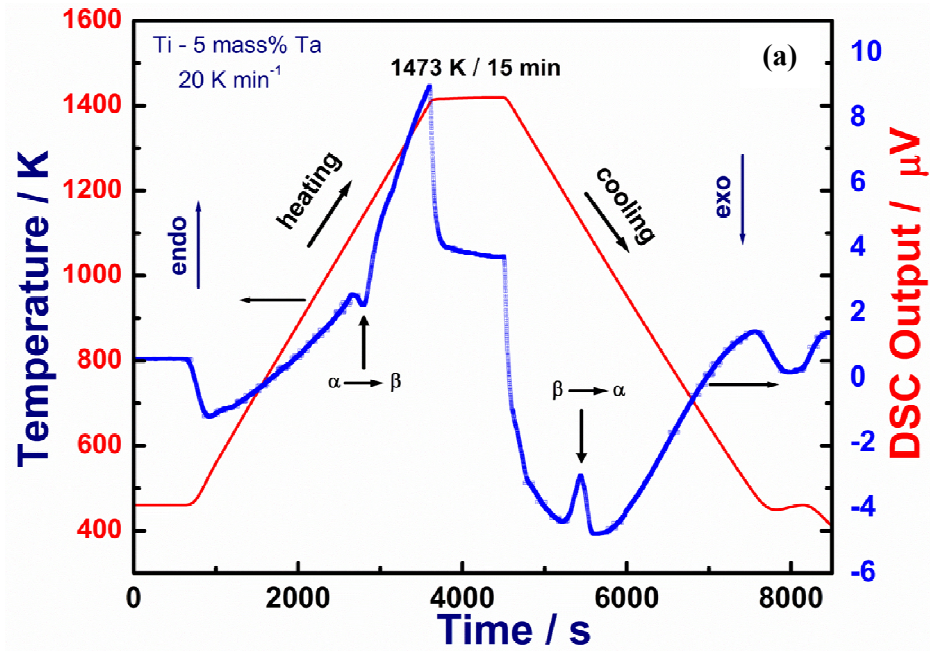
4.3 Structural and microstructural characterization of initial alloy

The starting material used for the DSC experiments is same as that of the material used for the drop experiment (**Chapter 3**). The initial structural and microstructural characterization of this alloy is discussed in **section 3.4** of **chapter 3**. The room temperature X-ray diffraction pattern of solutionized Ti-xTa ($x=5, 10, 15, 20$ mass %) alloys is already discussed in **chapter 3 (Fig. 3.2)**. It shows the presence of α and β phases in all the alloys except Ti-5Ta at room temperature. In case of Ti-10 and 15 mass% Ta the β -bcc phase peak is observed as a shoulder of $(00.2)_{\alpha}$ reflection but for Ti-20 mass% Ta a clear $(110)_{\beta}$ bcc peak is observed. The microstructure of the starting material shows basket weave morphology (**Fig. 3.5, chapter 3**).

4.4 DSC results: Transformation temperatures and transformation peak profiles

In **Fig. 4.1 (a-d)**, the on-heating and cooling DSC thermogram for Ti-xTa ($x = 5, 10, 15, 20$ mass %) alloy recorded at 20 K min^{-1} is presented. The maximum temperature up to which the sample heated is 1473 K and the sample is isothermally

held for about 15 minutes before cooling to room temperature. The same heat treatment condition is maintained for all the alloys in this study.



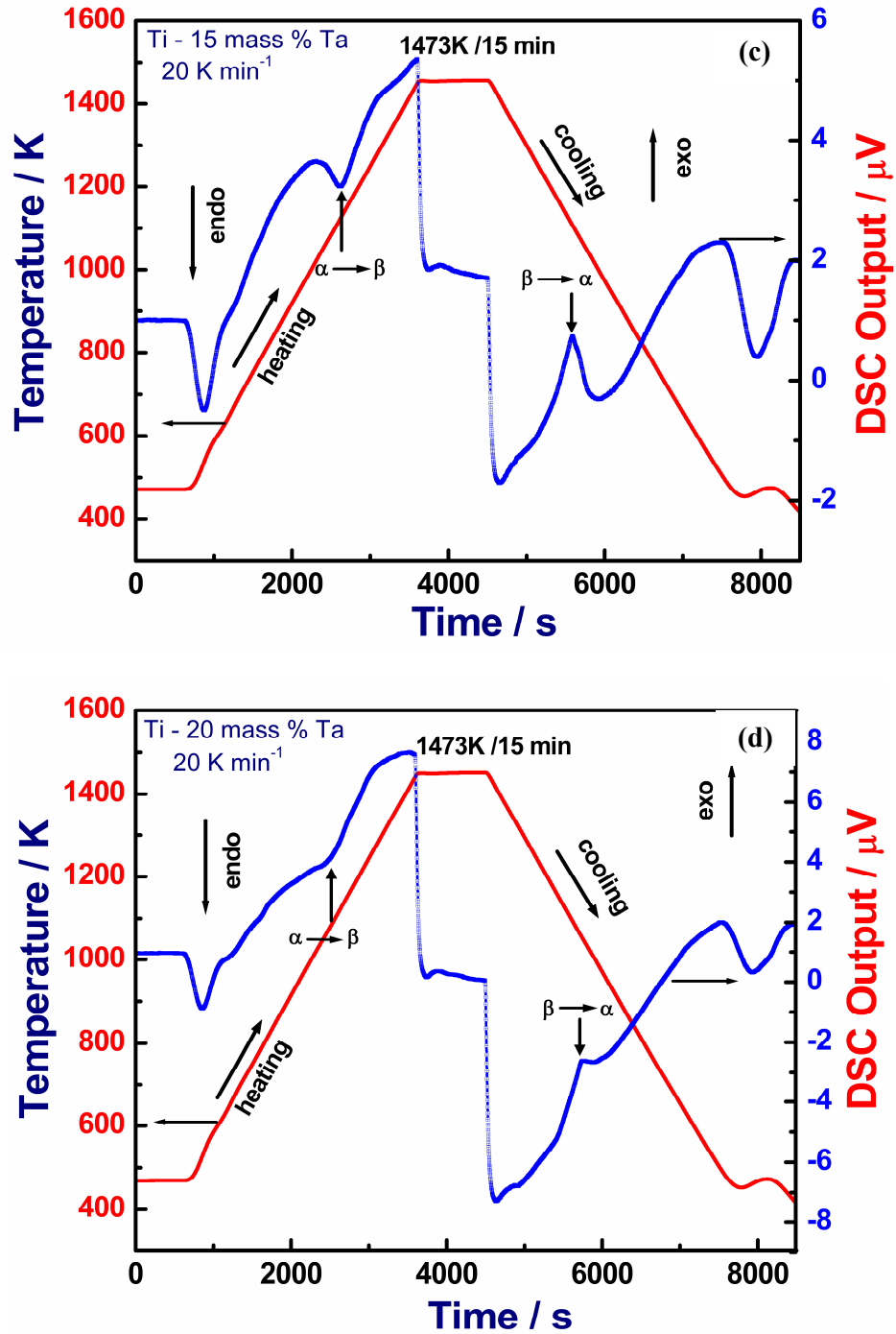


Figure 4.1 The on-heating and cooling DSC profiles for (a) Ti-5Ta, (b) Ti-10Ta, (c) Ti-15Ta & (d) Ti-20Ta alloys, recorded at 20 K min⁻¹.

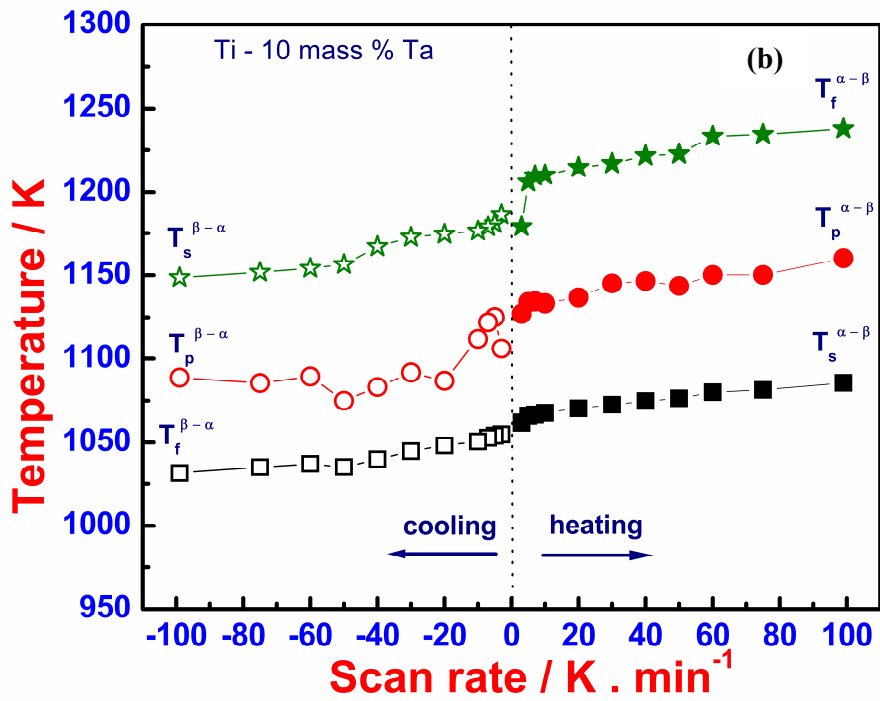
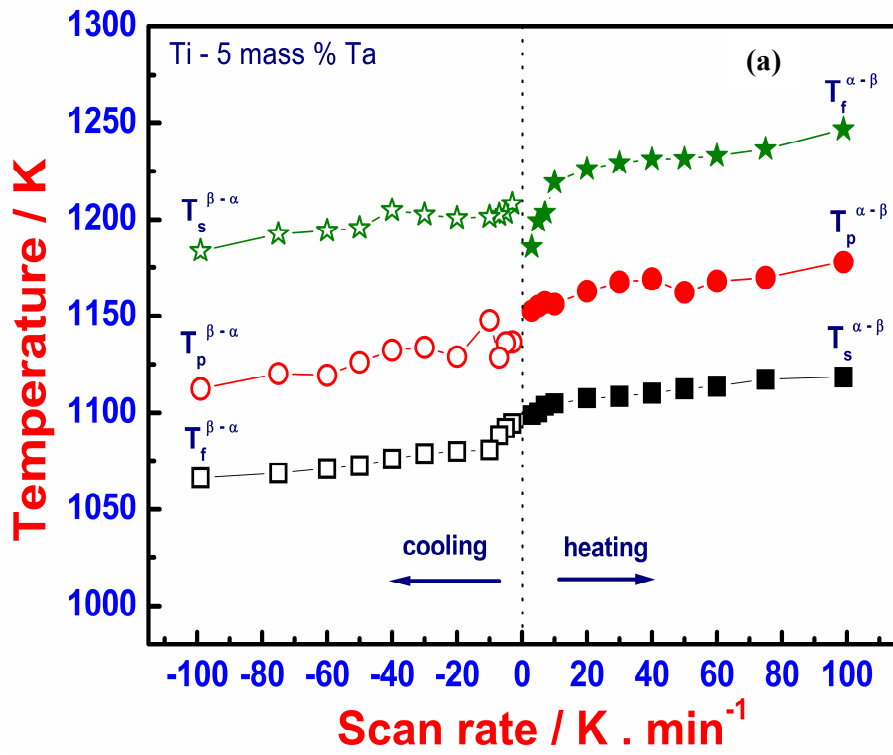
It is observed from **Fig. 4.1 (a)** that the on-heating $\alpha \rightarrow \beta$ phase change while exhibiting a sharp transformation onset temperature ($T_s^{\alpha \rightarrow \beta}$), presents a diffuse tail for the transformation finish ($T_f^{\alpha \rightarrow \beta}$) temperature, which as can be seen, extends well up to

1200 K or slightly upwards thereof. This suggests that despite the fact that $\alpha \rightarrow \beta$ transformation takes place with increasing temperature; the progress of the 100% β formation is only gradual, since it is mainly decided by the diffusion of less mobile Ta atoms. This will be further discussed at a later section of this chapter. At faster rates of heating, it is also possible that Ta-diffusion away from the $\alpha + \beta / \beta$ interface and into the growing β nodule is unable to keep pace with the physical advancement of the actual transformation front due to temperature gradient. This leads to the natural building-up of solute enrichment locally in the vicinity of the freshly formed β and further acts as a drag force on the transformation front, which leads eventually to the slowing down of the further progress of $\alpha \rightarrow \beta$ transformation. This solute drag is expected to be more pronounced for concentrated alloys and also with increasing severity of the heating rate. This will induce considerable fine scale compositional inhomogeneity in the β -phase that is obtained upon fast heating [9]. The other important consequence of this diffusional lag is the considerable superheating of the dynamically measured $\alpha + \beta / \beta$ solvus above the equilibrium phase boundary. This fact is important while comparing the solvus temperatures estimated by dynamic calorimetry with the calculated values that assume full thermodynamic equilibrium to prevail at the α / β interface.

The $\beta \rightarrow \alpha$ thermal arrest obtained during cooling on the other hand is reasonably sharp with clearly delineated transformation start ($T_s^{\beta \rightarrow \alpha}$) and finish temperatures ($T_f^{\beta \rightarrow \alpha}$) (**Fig. 4.1 (a) & (b)**). It must however be mentioned that an undercooling of about 25 K has often been observed for the initiation of $\beta \rightarrow \alpha$ transformation. Another important observation in **Fig. 4.1** is with regard to the total peak area associated with the forward and reverse phase changes; in the present study, it is generally observed that the peak area associated with $\beta \rightarrow \alpha$ phase change is somewhat larger than the corresponding on-heating $\alpha \rightarrow \beta$ thermal arrest peak area (**Table 4.1-4.4**). In order to see this clearly, it

is necessary to fix appropriately the $T_f^{\alpha \rightarrow \beta}$ temperature by selecting the derivative of the heat flow signal, as the transformation finish temperature is not sharply defined in the heating cycle trace. Further, the peak area difference is found to be little higher, for higher cooling rates and also for increasing Ta concentrations of the alloy. Although the present DSC experiments have not been calibrated for the cooling cycle, it is possible to infer that the $\beta \rightarrow \alpha$ transformation occurring at kinetic undercooling has slightly larger enthalpy effects, as compared to the on-heating $\alpha \rightarrow \beta$ transformation. This kinetics induced forward and reverse reaction asymmetry is typical of measurements of phase transformation using scanning calorimetry, since the $\Delta^{\circ}C_p^{\beta \rightarrow \alpha}$, the heat capacity difference between participating phases increases slightly with undercooling. The other practical implication of $\beta \rightarrow \alpha$ transformation taking place with finite undercooling is that some excess or non equilibrium β is always retained in the post DSC cooled samples due to the incomplete nature of $\beta \rightarrow \alpha$ transformation under non-isothermal conditions, especially at low temperatures. This non equilibrium or excess β may undergo further decomposition upon subsequent thermal aging in $\alpha + \beta$ two phase field [10, 11]. This aspect has however not been investigated in this study.

In **Fig. 4.2 (a-d)**, the observed heating and cooling rate dependencies of the start, finish and peak transformation temperatures is presented in graphical form for both $\alpha \rightarrow \beta$ and $\beta \rightarrow \alpha$ phase changes for Ti-5, 10, 15, 20 mass% Ta alloys. It is clear from **Fig. 4.2** that the transformation temperatures exhibit a non-linear variation with scan rate and this nonlinearity is more pronounced for the transformation finish temperatures. As a result the width of the transformation domain ($\Delta T = T_f - T_s$) becomes more for high heating and cooling rates, especially in the case of high Ta alloys.



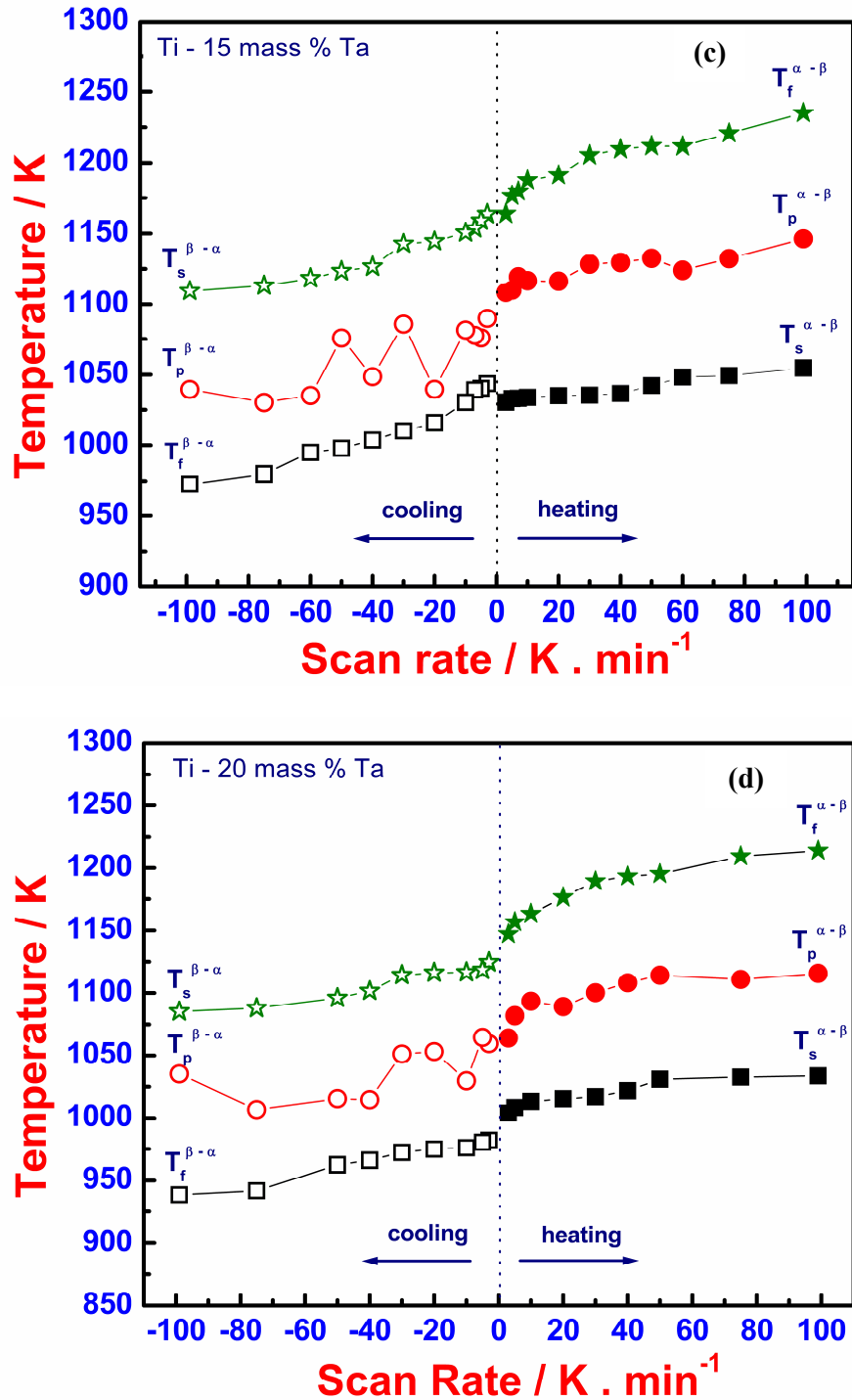


Figure 4.2 Graphical representation of heating and cooling rate variation of transformation start (T_s), peak (T_p) and finish (T_f) temperatures for (a) Ti-5Ta, (b) Ti-10Ta, (c) Ti-15Ta and (d) Ti-20Ta alloys

Fig. 4.3 (a) presents the variation of width of the transformation domain ($\Delta T_{tr}=T_f-T_s$) with Ta concentration for $\alpha \rightarrow \beta$ phase change, which brings out the above point well. Similarly the extent of undercooling for $\beta \rightarrow \alpha$ phase change (**Fig. 4.3 (b)**) has also been found to be somewhat more for high Ta-alloys, and in particular for high cooling rates. In Table 4.1-4.4, the scan rate dependence of $\alpha \leftrightarrow \beta$ transformation arrest temperatures are listed for Ti-xTa (x=5, 10, 15, 20 mass %) alloys. Besides, the $\alpha \leftrightarrow \beta$ transformation enthalpy ($\Delta^{\circ}H_{tr}^{\alpha \leftrightarrow \beta}$) values are listed for all the alloys. These values of transformation enthalpy were obtained based on the calibrating run performed with pure Ti under identical conditions. The accuracy involved in the measured temperatures is ± 2 K and enthalpy is 8 %.

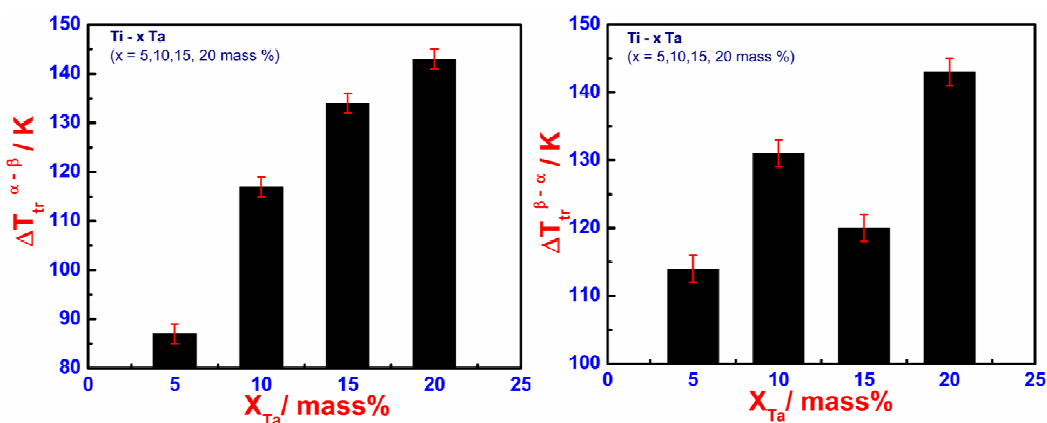


Figure 4.3 The composition dependence of the width ($\Delta T_{tr}^{\alpha \leftrightarrow \beta}$) of the (a) $\alpha \rightarrow \beta$ transformation and (b) $\beta \rightarrow \alpha$ transformation domain measured at 3 K min^{-1} . The vertical bars denote the typical spread of the measurement data.

Table 4.1 $\alpha \leftrightarrow \beta$ transformation temperatures for Ti-5 mass% Ta alloy

Scan rate (K / min)	T_s (K)	T_p (K)	T_f (K)	Area ($\mu\text{V.s/mg}$)	Enthalpy (J/g)
<i>$\alpha \rightarrow \beta$ transformation (heating)</i>					
3	1099	1153	1186	8.6913	60.35
5	1100	1155	1199	9.077	62.64
7	1104	1157	1204	9.217	71.99
10	1105	1156	1220	5.7635	43.75
20	1108	1163	1226	6.0593	55.31
30	1109	1168	1229	5.6121	49.35
40	1110	1169	1231	5.4346	55.25

50	1113	1162	1232	6.6728	64.14
60	1114	1168	1233	6.4872	64.99
75	1117	1170	1237	6.2943	62.19
99	1118	1178	1247	6.5947	65.87
$\beta \rightarrow \alpha$ transformation (cooling)					
3	1208	1137	1094	-7.2012	72.35
5	1204	1136	1092	-6.1502	58.25
7	1203	1129	1088	-7.4008	67.26
10	1202	1148	1081	-7.1731	51.19
20	1201	1129	1080	-7.2824	58.66
30	1203	1134	1079	-6.8059	52.83
40	1205	1132	1076	-9.1316	80.23
50	1196	1126	1072	-10.1257	78.47
60	1194	1119	1071	-9.7681	78.94
75	1193	1120	1069	-10.0956	78.74
99	1184	1113	1066	-9.815	76.31

Table 4.2 $\alpha \leftrightarrow \beta$ transformation temperatures for Ti-10 mass% Ta alloy

Scan rate (K / min)	Ts (K)	Tp (K)	Tf (K)	Area ($\mu\text{V.s/ mg}$)	Enthalpy (J/g)
$\alpha \rightarrow \beta$ transformation (heating)					
3	1062	1127	1179	6.37	66.00
5	1066	1134	1206	4.09	40.62
7	1067	1134	1210	5.90	57.58
10	1068	1133	1210	7.92	60.11
20	1070	1137	1215	5.41	49.40
30	1072	1145	1217	3.86	33.94
40	1075	1147	1222	4.74	48.20
50	1076	1144	1223	5.91	56.84
60	1080	1150	1233	5.04	50.49
75	1081	1150	1235	6.78	66.94
99	1086	1160	1238	7.03	70.22
$\beta \rightarrow \alpha$ transformation (cooling)					
3	1186	1106	1055	-8.2847	83.24
5	1181	1125	1054	-4.8298	45.74
7	1179	1122	1053	-6.7664	61.49
10	1176	1112	1051	-8.7399	62.37
20	1174	1087	1048	-7.248	58.38
30	1173	1092	1045	-5.5388	42.99
40	1167	1083	1040	-6.0479	53.14
50	1157	1075	1035	-7.7215	59.84
60	1154	1089	1037	-4.4589	36.03
75	1152	1086	1035	-9.3365	72.82
99	1149	1089	1032	-8.5091	66.15

Table 4.3 $\alpha \leftrightarrow \beta$ transformation temperatures for Ti-15 mass% Ta alloy

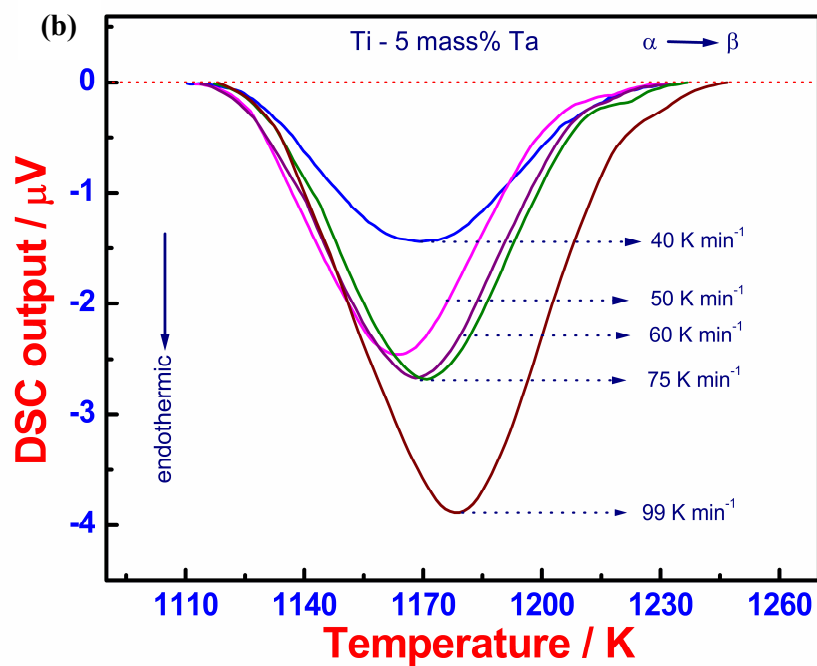
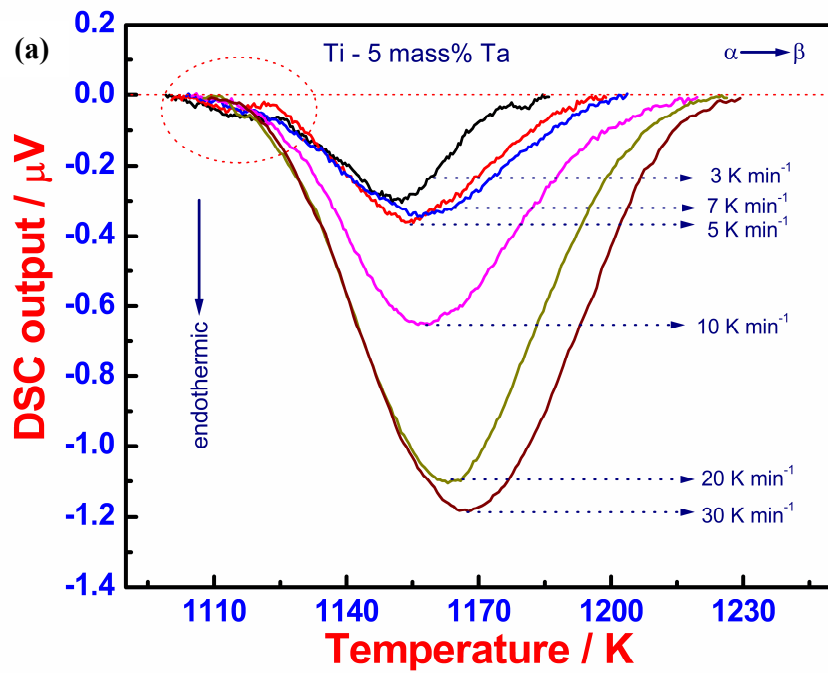
Scan rate (K / min)	T _s (K)	T _p (K)	T _f (K)	Area ($\mu\text{V.s/mg}$)	Enthalpy (J/g)
<i>$\alpha \rightarrow \beta$ transformation (heating)</i>					
3	1030	1108	1164	5.0804	52.61
5	1033	1110	1176	5.9414	58.91
7	1033	1119	1180	5.2023	50.80
10	1034	1117	1187	6.0266	45.75
20	1035	1116	1191	5.3739	49.05
30	1035	1128	1205	3.011	26.48
40	1037	1129	1209	6.4101	65.17
50	1042	1132	1212	2.1576	20.74
60	1048	1124	1211	5.5607	55.71
75	1049	1132	1221	6.092	60.19
99	1055	1146	1235	6.6804	66.79
<i>$\beta \rightarrow \alpha$ transformation (cooling)</i>					
3	1164	1090	1044	-5.5963	56.23
5	1159	1076	1040	-4.9879	47.24
7	1154	1078	1039	-5.3928	49.01
10	1151	1081	1030	-3.7769	26.95
20	1144	1040	1016	-6.7775	54.59
30	1143	1086	1010	-5.3621	41.62
40	1126	1049	1004	-8.9609	78.73
50	1123	1076	998	-5.0787	39.36
60	1118	1035	995	-7.3884	59.71
75	1113	1030	980	-7.5649	59.0
99	1109	1039	973	-10.2044	79.33

Table 4.4 $\alpha \leftrightarrow \beta$ transformation temperatures for Ti-20 mass% Ta alloy

Scan rate (K / min)	T _s (K)	T _p (K)	T _f (K)	Area ($\mu\text{V.s/mg}$)	Enthalpy (J/g)
<i>$\alpha \rightarrow \beta$ transformation (heating)</i>					
3	1004	1064	1147	1.6013	16.58
5	1008	1082	1157	1.8756	18.60
10	1013	1093	1163	2.9706	22.55
20	1015	1089	1176	1.6943	15.46
30	1017	1100	1189	2.2802	20.05
40	1022	1108	1193	4.6508	47.28
50	1031	1114	1195	2.3842	22.92
75	1033	1111	1209	5.7143	56.45
99	1034	1116	1214	2.8039	28.00
<i>$\beta \rightarrow \alpha$ transformation (cooling)</i>					
3	1125	1060	982	-3.1966	32.12
5	1118	1065	980	-3.5711	33.82

10	1117	1030	976	-4.4106	31.47
20	1116	1053	975	-2.4421	19.67
30	1114	1051	972	-2.9058	22.55
40	1101	1015	966	-7.5054	65.94
50	1096	1016	962	-3.4253	26.55
75	1088	1007	942	-7.6989	60.04
99	1085	1035	938	-4.6323	36.01

4.5. Composite nature of transformation peak profiles



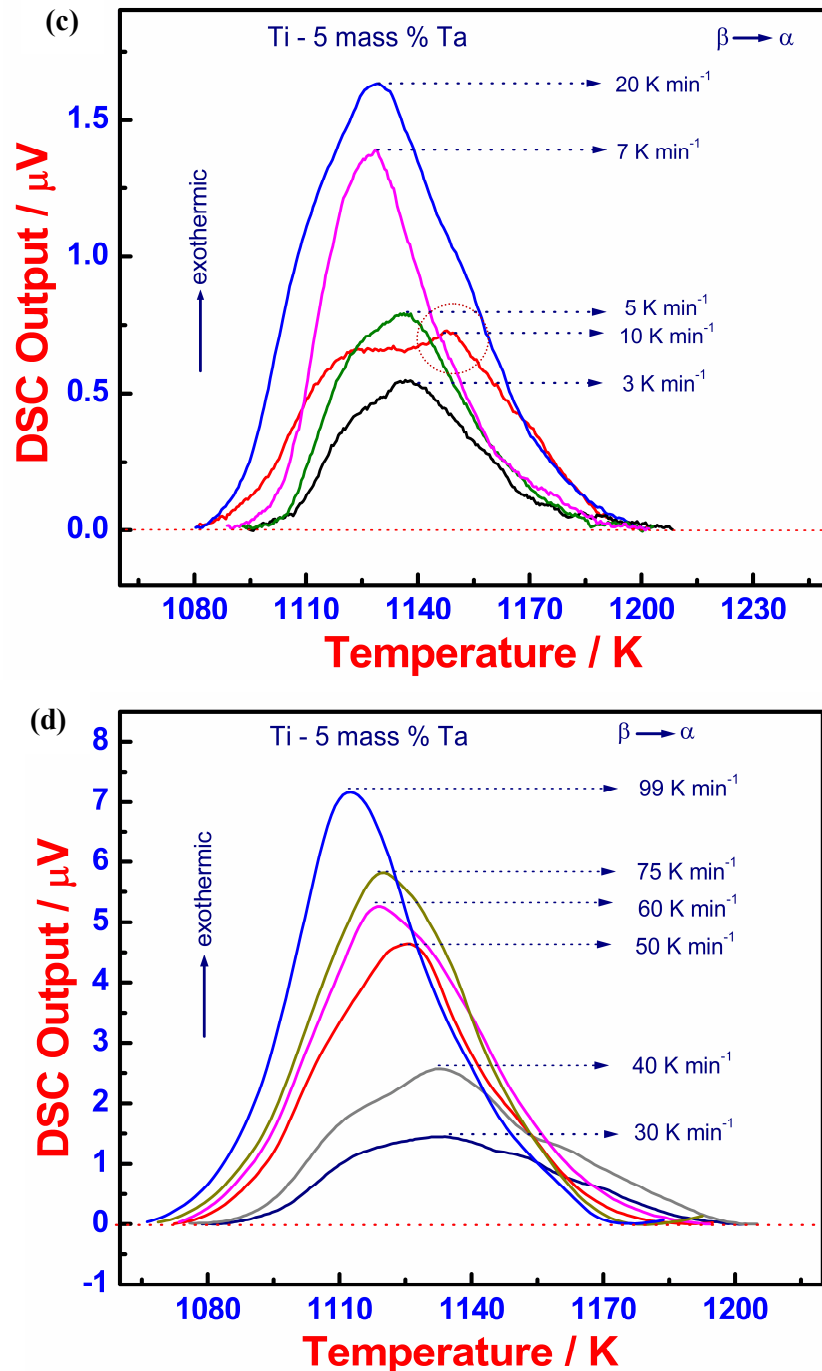


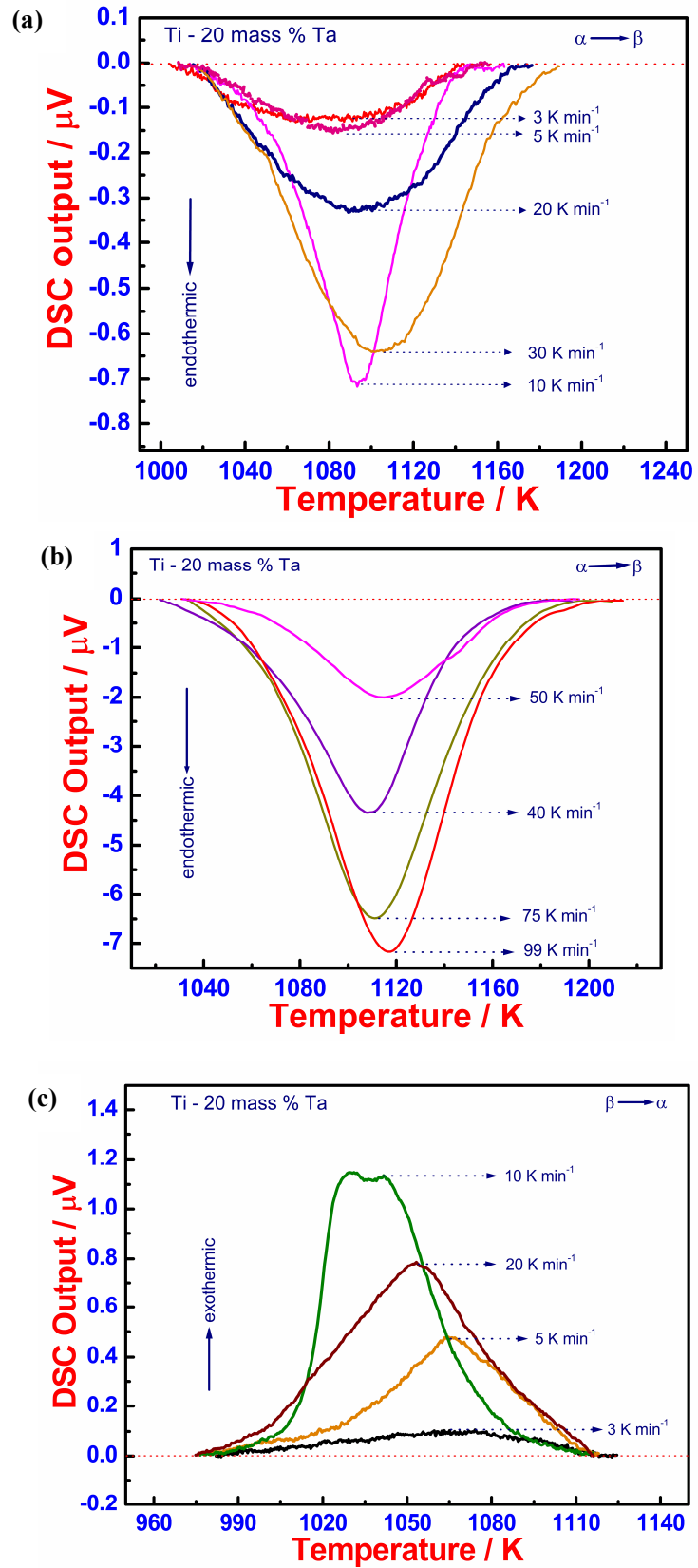
Figure 4.4 (a) & (b) The $\alpha \rightarrow \beta$ transformation and **(c) & (d)** The $\beta \rightarrow \alpha$ transformation peak profiles for Ti-5Ta alloy. The dotted ellipse outlines the shallow peak seen at the start of the $\alpha \rightarrow \beta$ thermal arrest for low heating rates.

In **Fig. 4.4 & 4.5**, the $\alpha \leftrightarrow \beta$ transformation peak profiles obtained under successively increasing scan rates are shown for Ti-5Ta and Ti-20Ta alloys respectively. For convenience, the profiles obtained at lower scan rates are separated

from their higher scan rate counterparts. One important point that emerges from **Fig. 4.4 (a)** is that for lower heating rates (3, 5 and 7 K min⁻¹), the $\alpha \rightarrow \beta$ transformation profiles appear to be composite ones consisting of two overlapping peaks, of which the first one (circled) is somewhat shallow as compared to the second, which is the dominant one. It is also evident that with increasing heating rates, the first shallow peak is gradually getting diminished in magnitude, shifted to higher temperatures and merges smoothly with the major peak. The split-peak phenomenon has also been observed for $\beta \rightarrow \alpha$ transformation during cooling (**Fig. 4.4 (c)** circled). In thermal analysis studies, the occurrence of split or composite thermal arrest for a phase change can arise due to both sample related artefacts (especially in powder samples due to varying thermal resistance at different parts of sample) and also due to transformation related ones [5]. Thus for an example, if there are two distinct α phase morphologies present, *viz.*, the primary α and transformed β in the starting microstructure, then it is likely that these two phases might not begin their transformation concurrently, but with slightly different incubation times. Hence these simultaneous $\alpha \rightarrow \beta$ events would register as two distinct and overlapping peaks, with different strengths [5]. The dominant one would of course be due to $\alpha_{primary} \rightarrow \beta$, as this constitute larger volume fraction and would therefore sweep the major peak area under fast heating rates.

Going by the above line of reasoning, it is expected that this split peak phenomenon should be operating even more readily in the $\beta \rightarrow \alpha$ transformation upon cooling, as the starting or prior β -grain size is large ($\sim 150\text{--}200\ \mu\text{m}$) after 1473 K/15 min holding. The evidence for this split character of the $\beta \rightarrow \alpha$ peak profiles can be seen very clearly from **Fig. 4.4 and 4.5**. For the cooling induced $\beta \rightarrow \alpha$ transformation, this aspect may be rationalized as follows.

If competitive nucleation of the α -phase from both β -grain boundary (grain edge, grain interface and grain triple points) and grain interior sources with varying degrees of nucleation potencies is assumed [12], then it is plausible that the thermal arrest due to $\beta \rightarrow \alpha$ nucleation and its initial phase of growth may give rise to two overlapping peaks of differing magnitudes [13]. Such an event is hypothesized for the polymorphic transition in pure iron, as well as in uranium [14, 15]. In the case of fine grained starting microstructure, the copious and facilitated availability of grain boundary nucleation sources will dominate the initial transformation kinetics over the grain interior nucleated one, which needs a slightly larger incubation time, due to the lower driving force. The converse holds good for coarse grained starting microstructure. In either case, the simultaneous operation of two potent nucleation sources with differing potencies will result in composite peak. With increasing rates of cooling, these two competing nucleation events with unequal statistical weights shall tend to merge or get biased towards the more prominent nucleation mechanism. In the present case, the β -matrix at 1473 K after 15 minutes solution treatment, has reasonably large grain size and would therefore *not* have abundant potent heterogeneous grain boundary nucleating sources for the α -phase formation. Therefore, the other nucleation contribution to the $\beta \rightarrow \alpha$ thermal arrest, namely the grain interior must also be operative. It is only while slow cooling, there is ample scope for the multiple nucleation possibilities to register their individual presence; otherwise, the predominantly assisted nucleation dominates at fast rates of cooling.



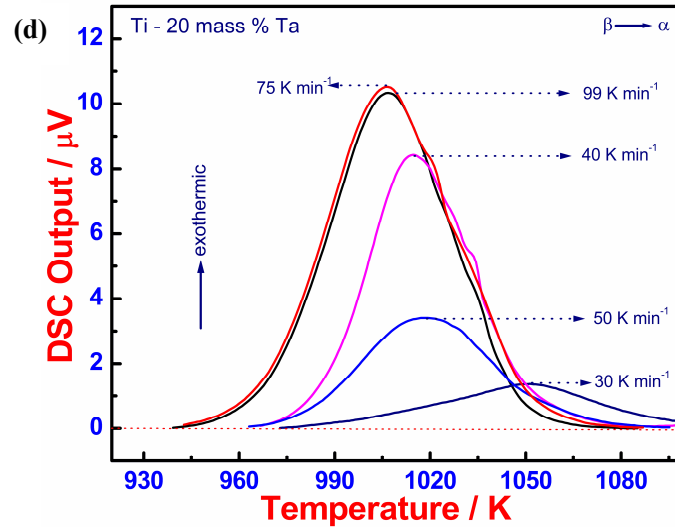


Figure 4.5 (a) & (b) The $\alpha \rightarrow \beta$ transformation and **(c) & (d)** $\beta \rightarrow \alpha$ transformation peak profiles for Ti-20Ta alloy.

Despite the fact that the transformation remains diffusive in character even for the maximum cooling rate of 99 K min^{-1} , there is bound to be some refinement in the final microstructure which is brought about by fast cooling. Hence, the cooling rate dictated change in nucleation mode and its impact on microstructure development has been studied. **Fig. 4.6** presents a collage of microstructures of post DSC samples of Ti-20Ta alloy that have experienced the $\beta \rightarrow \alpha$ phase change at successively increasing cooling rates. It is observed from **Fig. 4.6** that at 5 K min^{-1} cooling, the microstructure contains largely the grain boundary nucleated long α -plates (Widmanstätten like) but the structure indicates no evidence for the copious α nucleation at grain interiors, although there could still be few plates nucleated and grown within the grains. With increasing cooling rates, it is seen that the fine α -lamellae originate in the grain- interior and grow in crisscrossing and orthogonally intersecting habits, which is attributed to strain accommodation. It is known that with increasing cooling rates, α -nucleation occurs at higher undercooling and hence with larger driving force, which is responsible for the fineness of microstructure arising from increased nucleation rate (see the graph in **Fig.**

4.6 (f)). From Fig. 4.6 (f), it is observed that α lamella size decreases with increase in cooling rate and it is also found that the α lamella size become finer with increase in Ta concentration in the alloy.

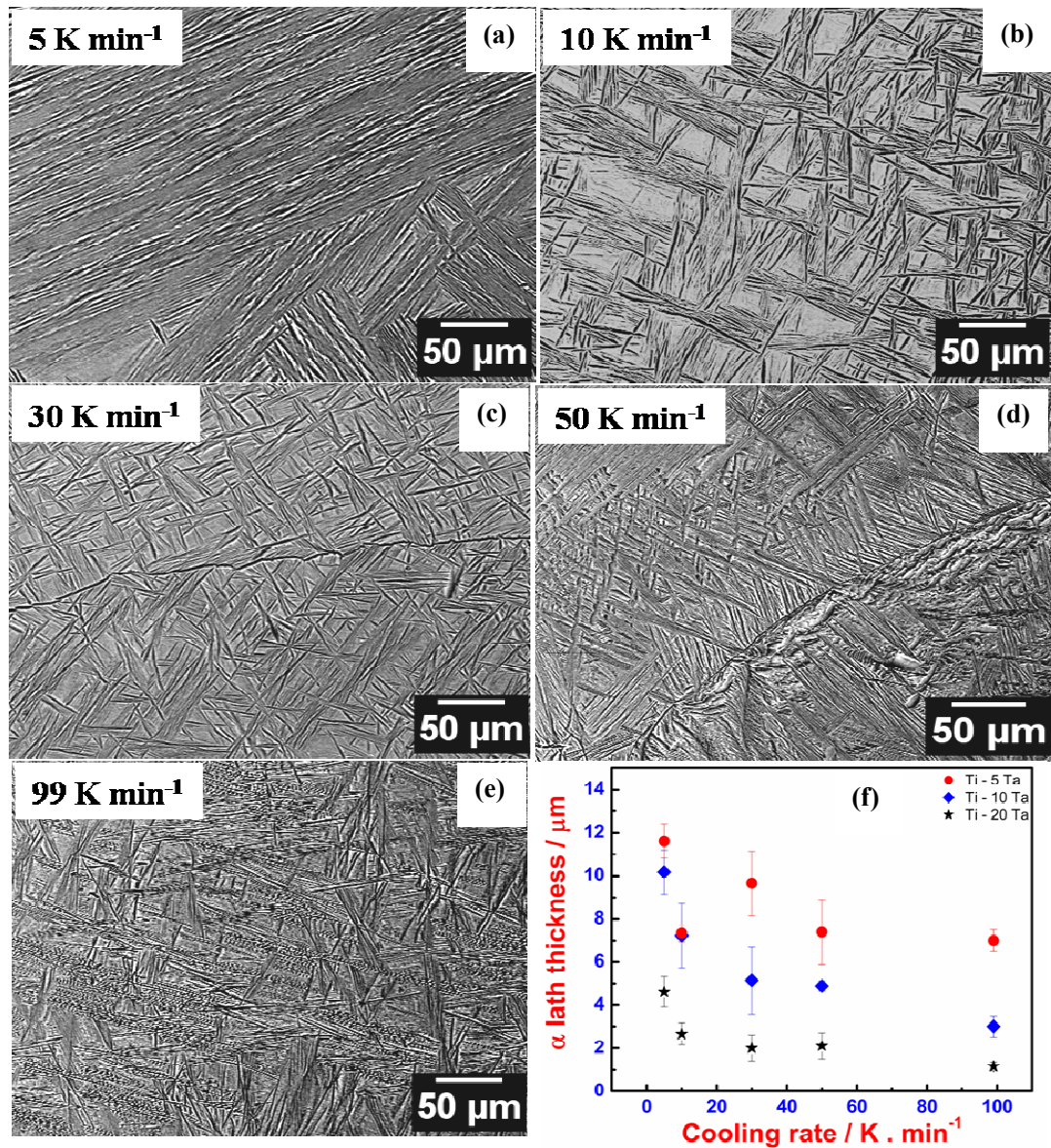


Figure 4.6 Optical microstructures of the post DSC samples of Ti-20Ta alloy showing the effect of cooling rate on microstructures that have undergone $\beta \rightarrow \alpha$ diffusional phase transformation

No α'' -orthorhombic marenite has been detected in any of the alloys studied here, which is also in broad accord with the earlier findings of Bywater and Christian [16] and Cotton et al [17].

Fig. 4.7 shows the variation of hardness as a function of cooling rate and Ta concentration. The microhardness shows a steady increase with cooling rate which is attributed to the cooling induced microstructure refinement. It can also be seen from Fig. 4.7 that the microhardness of transformation microstructure increases with Ta concentration due to fine α lamella formed in high Ta alloy.

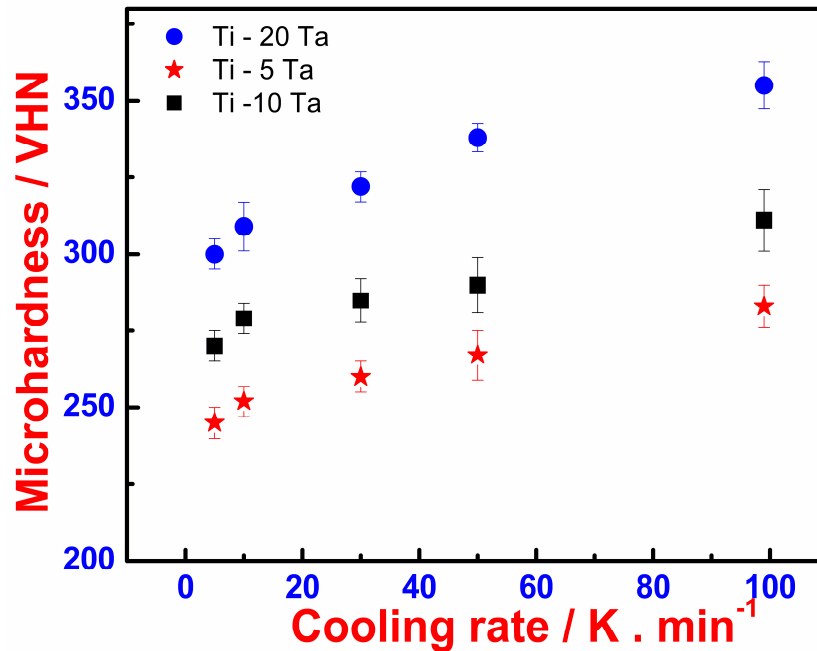


Figure 4.7 Microhardness data from post $\beta \rightarrow \alpha$ transformation microstructures showing the effect of cooling rate and Ta concentration.

4.6 $\alpha + \beta \rightarrow \beta$ transformation temperatures and transformation enthalpy

The on-heating $\alpha + \beta / \beta$ solvus temperatures for Ti-5, 10, 15 and 20 Ta alloys measured at the slowest heating rate of the present study are compared with the currently reported experimental data from diverse sources [18-23] and is shown in Fig. 4.8. The figure also highlights the drastic disparity seen among the β -solvus phase boundary data coming from different studies including one of the earlier thermodynamic assessments, due to Murray [22] and the recent one obtained from *Thermocalc*[®] simulation [23]. It can be noticed at a first glance that present

measurements based on dynamic calorimetry compare rather poorly with the equilibrium assessed estimates of phase boundary. Nevertheless, as discussed in section 4.4, the β -solvus temperatures, determined as the transformation finish temperatures $T_f^{\alpha \rightarrow \beta}$ of the dynamically recorded DSC thermograms, are by their very nature overestimate the actual or equilibrium $\alpha+\beta/\beta$ temperatures. This point is valid, no matter how slow a heating rate is chosen, consistent with experimental feasibility. The 3 K min⁻¹ heating rate has been chosen here as a compromise between the ideal slowest scan desirable from the point of view of maintaining total thermal equilibrium at each temperature, and yet realizing the experiment within a reasonable time frame maintaining thermal stability. As mentioned before, the kinetics of $\alpha \rightarrow \beta$ transformation is sluggish owing to slow volume diffusion of Ta in Ti-Ta alloys [24], and as a result, the completion of $\alpha \rightarrow \beta$ phase change culminating in the formation of *chemically homogeneous* β requires some definite superheating above the equilibrium solvus temperature. Naturally, the extent of this superheating will be more for Ta rich alloy compositions. This is the principal reason as to why dynamic measurements of solvus always overestimate the equilibrium transformation temperatures. Further, it is interesting to note that our measurements are somewhat closer to one of the earlier data of Budberg and Shakova [20], and also that of Summers- Smith [19]; while all others portray a rather steeply falling $\alpha+\beta/\beta$ solvus for high Ta alloys. The results of Gordin especially portray an exaggerated stability of β -phase domain [18]; nevertheless, it is not clear as to whether these different experiments are conducted with full maintenance of thermodynamic equilibrium. In the present study, the starting microstructure for all compositions contained some excess β , which would certainly play a role in affecting the completion of β -phase formation upon heating. However, it is not clear as to how much of such non equilibrium β had been present in the alloy samples of earlier

investigators, in order to make an objective assessment of the different experimental estimates of $\alpha+\beta/\beta$ phase boundary.

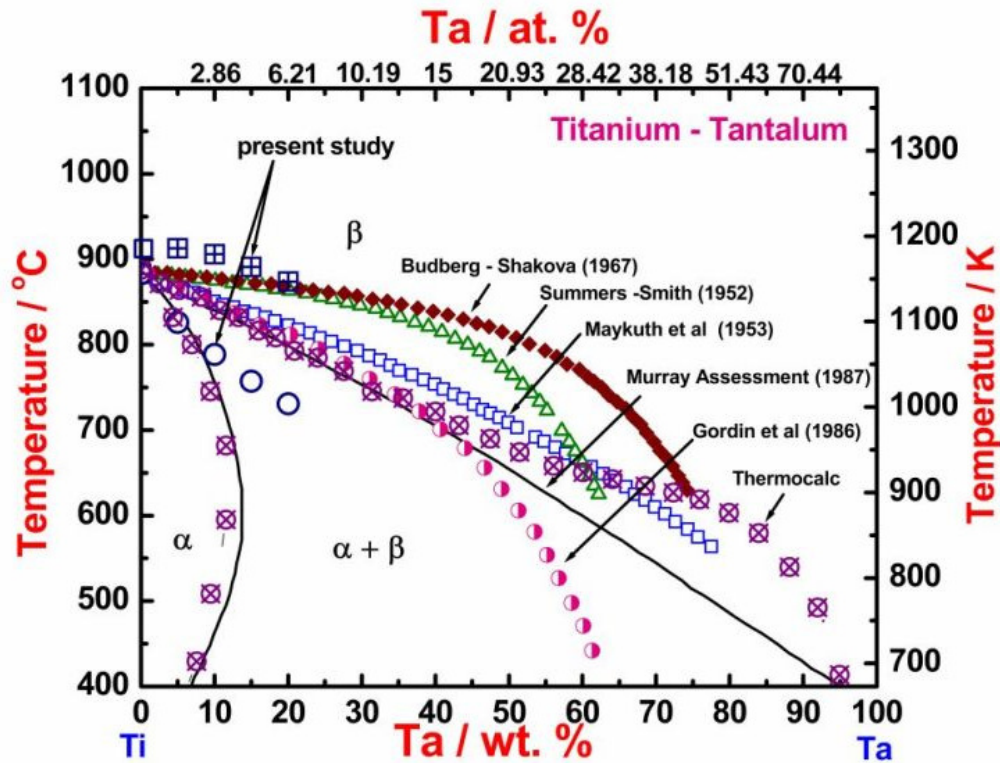


Figure 4.8 A comparison of measured $T_s^{\alpha \rightarrow \beta}$ and $T_f^{\alpha \rightarrow \beta}$ temperatures in the present study with select literature data on phase boundaries is made.

The lower phase boundary namely $\alpha/\alpha+\beta$ can be truly determined only for low Ta-alloys, having less than about 10 mass percent of Ta or so [22, 23]. For all other higher Ta containing compositions, only one thermal arrest representing $\alpha+\beta \rightarrow \beta$ transformation alone is obtained, which is the case in present measurements. In **Fig. 4.8**, we have also plotted the measured $\alpha \rightarrow \beta$ transformation start ($T_s^{\alpha \rightarrow \beta}$) temperatures along with the assessed equilibrium $\alpha/\alpha+\beta$ phase boundary [22, 23]. It is seen that only for Ti-5Ta alloy, which contains a larger fraction of α phase to start with, there is some agreement of the measured $T_s^{\alpha \rightarrow \beta}$ with the equilibrium $\alpha/\alpha+\beta$ solvus temperature; otherwise, the measured $\alpha+\beta \rightarrow \beta$ transformation start temperatures are systematically

higher, again due to dynamic scanning effects. At this juncture, it may be mentioned that a comprehensive fresh measurement of phase boundaries on properly equilibrated high purity samples in conjunction with CALPHAD type thermodynamic assessment could provide an insight into the real nature of phase boundaries in Ti-Ta alloys, which

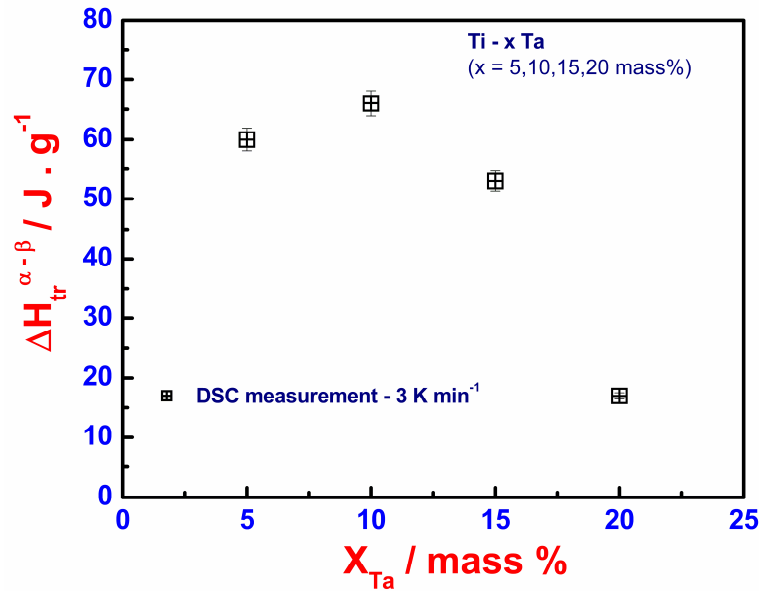


Figure 4.9 Variation of measured $\alpha \rightarrow \beta$ transformation enthalpy ($\Delta H_{tr}^{\alpha \rightarrow \beta}$) with Ta content.

is beyond the scope of the present study.

In **Fig. 4.9**, the measured transformation enthalpy $\Delta^{\circ}H_{tr}^{\alpha \rightarrow \beta}$ at 3 K min^{-1} for the $\alpha \rightarrow \beta$ phase transformation has been presented as a function of Ta concentration. As can be seen the transformation enthalpy exhibits a pronounced non-linear drop with increasing Ta content; a behavior that is on expected lines, since β -bcc phase is getting more and more stabilized with regard to increasing Ta (β -stabilizer) concentration. Further, owing to the fact that the fraction of β -phase retained in the starting microstructure increases with Ta concentration, and as a result the amount of α -hcp that undergoes transformation to β upon heating is also commensurately less, giving rise to low transformation enthalpy values. A similar trend has been noticed in the case of Ti-

Nb and Ti-Zr(Hf) alloys as well [25, 26]. As mentioned in earlier section, the heat flux calibration has not been carried out for the cooling cycle; however, if the calibration constant as obtained with the $\beta \rightarrow \alpha$ phase change of pure titanium is employed for the cooling cycle of Ti-Ta alloys, a similar trend for $\Delta^{\circ}H_{tr}^{\beta \rightarrow \alpha}$ variation with Ta content is obtained.

A general survey of literature revealed that there have been no previous reports of experimentally measured values of transformation enthalpies for Ti-Ta binary alloys. In addition, we could not trace any theoretical estimates for this quantity from first principles calculations as well. In **Fig. 4.10**, the linear systematic relationship noticed between the enthalpy change $\Delta^{\circ}H_{tr}^{\alpha \rightarrow \beta}$ and the entropy change $\Delta^{\circ}S_{tr}^{\alpha \rightarrow \beta}$ due $\alpha \rightarrow \beta$ phase transformation, for few $\alpha + \beta$ -titanium alloys containing Nb, Zr and Ta is illustrated. For comparison purposes, the datum point for pure titanium representing 100% of $\alpha \rightarrow \beta$ energetic quantities is also included.

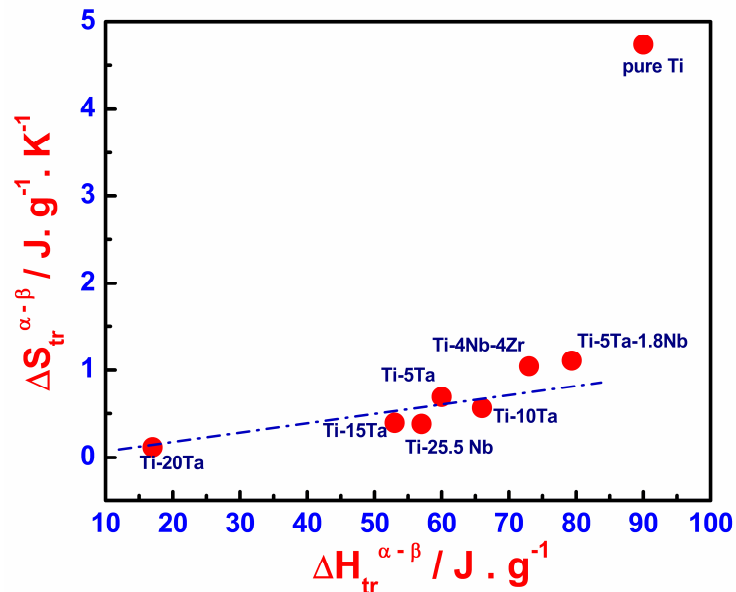


Figure 4.10 Correlation between measured $\alpha \rightarrow \beta$ transformation enthalpy ($\Delta H_{tr}^{\alpha \rightarrow \beta}$) and ($\Delta S_{tr}^{\alpha \rightarrow \beta}$). The value for titanium is taken from reference [27], while for others from our previously published data [28-30]. The dash dotted line indicates the linear relation between these two quantities for few Ti-alloys containing Ta, Zr, and Nb.

4.7 Kinetics of $\alpha \leftrightarrow \beta$ phase transformation

At the outset, it must be mentioned that both $\alpha \rightarrow \beta$ and the reverse $\beta \rightarrow \alpha$ phase transformations are diffusive in character for the complete spectrum of heating and cooling rates (3-99 K min⁻¹) employed in this study. The fractional extent of the transformation as a function of time or temperature at a constant scan rate (ϕ) can be obtained directly as the ratio of partial peak area to the total one, given by the relation [6]:

$$f(T) = \frac{\int_{T_s}^T y(T) dT}{\int_{T_s}^{T_f} y(T) dT} \quad (4.1)$$

$y(T)$ is the baseline compensated heat flux signal, measured as a function of T , in the range, $T_s \leq T \leq T_f$. $\int_{T_s}^T y(T) dT$ is the partial area under the peak upto temperature T and $\int_{T_s}^{T_f} y(T) dT$ is the total peak area. The transformation plots for both $\alpha \rightarrow \beta$ and $\beta \rightarrow \alpha$ phase transformations in Ti-xTa ($x = 5, 10, 15, 20$ mass%) alloys obtained at varying scan rates are presented in **Fig. 4.11 - Fig. 4.14**. As can be seen, the transformation curves are sigmoidal in character, which is supportive of the diffusion assisted nucleation and growth characteristic of transformations.

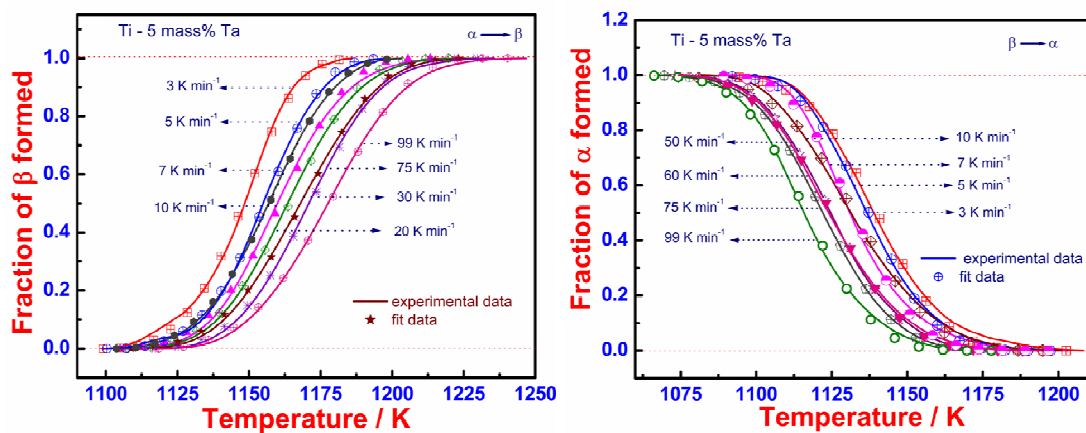


Figure 4.11 Experimentally obtained transformation plots for $\alpha \rightarrow \beta$ (left) and $\beta \rightarrow \alpha$ (right) transformations in Ti-5Ta alloy. The line stands for the experimental data, while the symbols are non-isothermal KJMA fit.

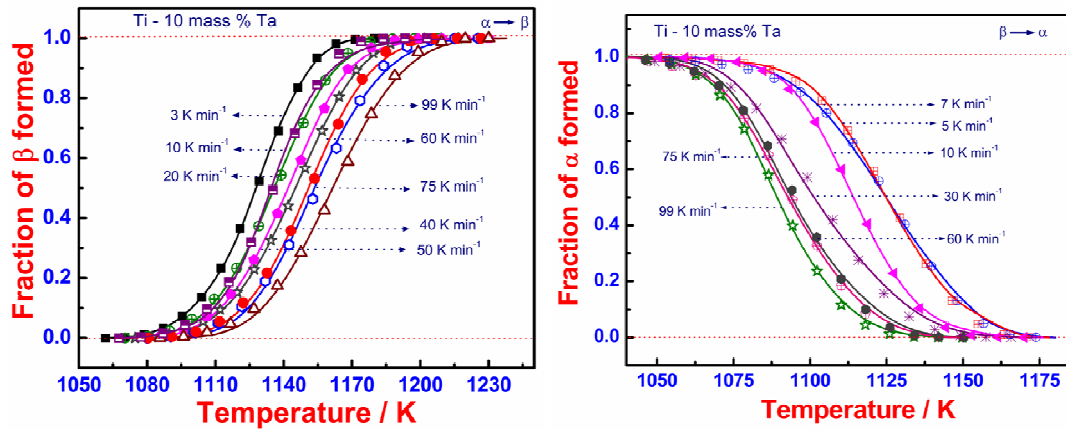


Figure 4.12 Experimentally obtained transformation plots for $\alpha \rightarrow \beta$ (left) and $\beta \rightarrow \alpha$ (right) transformations in Ti-10Ta alloy. The line stands for the experimental data, while the symbols are non-isothermal KJMA fit.

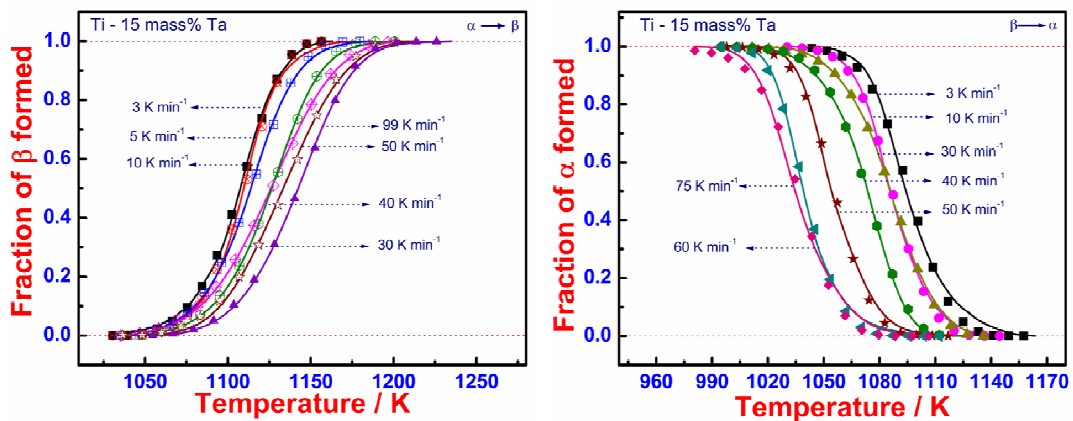


Figure 4.13 Experimentally obtained transformation plots for $\alpha \rightarrow \beta$ (left) and $\beta \rightarrow \alpha$ (right) transformations in Ti-15Ta alloy. The line stands for the experimental data, while the symbols are non-isothermal KJMA fit.

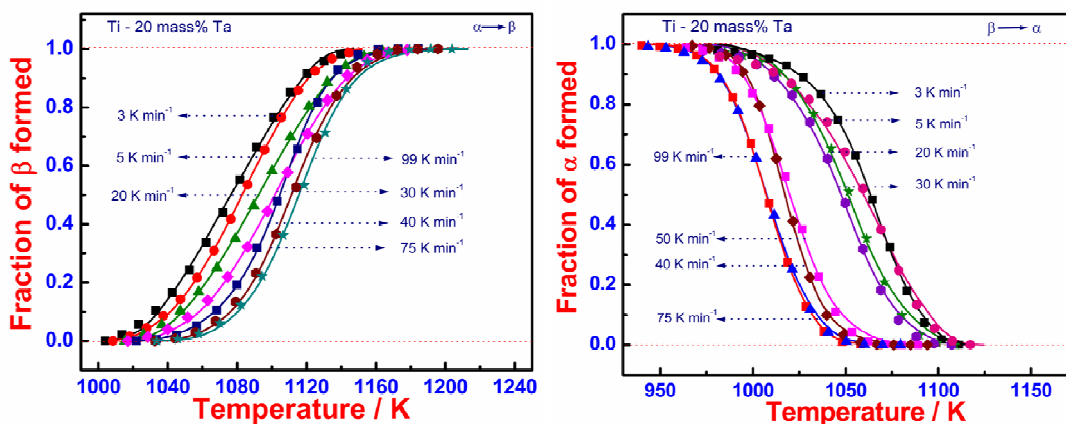


Figure 4.14 Experimentally obtained transformation plots for $\alpha \rightarrow \beta$ (left) and $\beta \rightarrow \alpha$ (right) transformations in Ti-20Ta alloy. The line stands for the experimental data, while the symbols are non-isothermal KJMA fit.

It may also be noticed upon careful scrutiny that with increasing heating rate, the transformation curve for $\alpha \rightarrow \beta$ phase change becomes progressively less steep, although only in a small incremental manner.

4.7.1 Ta diffusion as the rate controlling step

It is well-known that the kinetics of diffusive transitions involving distinct nucleation and growth steps can be satisfactorily analysed by employing the Kolmogorov-Johnson-Mehl-Avrami (KJMA) formalism, with varying degrees of technical sophistication that depends on the complexity of mechanisms assumed for the individual nucleation and growth steps [31-33]. In the case of $\alpha \rightarrow \beta$ or more precisely, the $\alpha + \beta \rightarrow \beta$ phase change, it is rather safe to assume site saturation approximation, in which all β -nucleation sites are effectively pre-present in the starting microstructure. As discussed in chapter 3 (**Fig. 3.5**), the starting microstructure in our case is one of interpenetrating copious and thin α -lamellae, with the interlath boundary being decorated by continuous β network. Thus, the pre-existing α/β interface can serve as potent sites for the nucleation of fresh β , once the temperature exceeds the equilibrium $\alpha + \beta/\beta$ solvus, creating thus a finite driving force. It is very difficult to predict about the general growth characteristics of β at the starting stages of phase change. However, it can be predicted that the nuclei of β formed will have very different composition from the surrounding α -lath mainly with respect to enrichment in Ta. Therefore the growth of β is served, by the transport of Ta away from shrinking or dissolving α and into the nascent and growing β -nuclei. Further, one may also visualize a situation in which the thickening of existing β occurs, again facilitated by the Ta-transport across the α/β interface. The major difference in the later mechanism is that the problem of separate nucleation of β is avoided. For all alloys having a mix of $\alpha + \beta$ phases as the starting microstructure, the slow heating is expected to induce a continuous increase in the phase

fraction of β , if Ta diffusion in α is appreciable. Since this is not the case as the temperature domain of the stability of the α -phase is rather low, the thickening of existing β at the expense of shrinking α can occur only at temperatures approaching that of β -solvus.

As shown in **Fig. 3.12 (chapter 3)**, a collage of quenched-in transformation microstructures obtained from different temperatures in the transformation domain $T_s \leq T \leq T_f$, is assembled. It is strikingly clear that the actual beginning of transformation takes place at some finite temperature T (~ 1070 K) which is only slightly lower than the measured T_s (~ 1083 K). From the sequence of quenched in microstructure shown in **Fig. 3.12 (chapter 3)**, it appears that during the initial stages of $\alpha \rightarrow \beta$ phase change, some lateral expansion of β or effectively shrinking of the α phase does take place; although, the bulk of transformation proceeds by nucleation and growth of β once β -solvus is exceeded. The steep rise in volume fraction of β with temperature as observed from the last graph of **Fig. 3.12 (chapter 3)** supports the nucleation and growth mechanism of β rather than the dissolution of α -phase, which at best serves as a source of Ta that is needed for the growth of β .

If to a first order approximation, the growth of β is treated as being similar to the precipitation of a second phase from supersaturated solid solution, then we may write,

$$S (dr/V_m^\beta) \times \{c^\beta - c^{\alpha/\beta}\} = dC_{Ta}. \quad (4.2)$$

In Eq. (4.2), r is the β particle radius; S is the surface area of the β particle; V_m^β is the molar volume of β ; and dC_{Ta} is the difference in magnitude of Ta transferred across α/β interface. According to Fick's first law, we may write for the time averaged transport of Ta,

$$dC_{Ta}/dt = (D_{Ta}^\alpha S / V_m^\alpha) \times (dc^\alpha/dx). \quad (4.3)$$

D_{Ta}^{α} , is the diffusion coefficient of Ta in α -phase; V_m^{α} is the molar volume of α phase; and x is the distance coordinate. If we approximate (dc^{α}/dx) as

$$dc^{\alpha}/dx \approx \Delta x/r \approx (c^{\alpha}-c^{\alpha/\beta})/r. \quad (4.4)$$

and eliminate S from the above formulation and further approximating, $V_m^{\alpha} \approx V_m^{\beta}$ for convenience, we arrive at the following simplification

$$r.dr = D_{Ta}^{\alpha} \{(c^{\alpha}-c^{\alpha/\beta})/(c^{\beta}-c^{\alpha/\beta})\} dt. \quad (4.5)$$

Integrating from 0 to r , we obtain

$$r(t)^2 = 2D_{Ta}^{\alpha} \{(c^{\alpha}-c^{\alpha/\beta})/(c^{\beta}-c^{\alpha/\beta})\} t. \quad (4.6)$$

Notwithstanding the assumptions involved in setting up Eq. (4.6), it emerges that the growth of β is decided by two factors: (i) the relative super/under saturation of Ta in β and α phases respectively from the equilibrium α/β interfacial concentration, and (ii) the diffusivity of Ta in the α -phase, which serves as the source of Ta atoms. Under non-isothermal conditions with a constant heating rate $\phi = dT/dt$, Eq. (4.6) can be simplified as

$$r(T)^2 = 2D_{Ta}^{\alpha} \{(c^{\alpha}-c^{\alpha/\beta})/(c^{\beta}-c^{\alpha/\beta})\} (T-T_s)/\phi. \quad (4.7)$$

Further, if $D = D_0 \exp(-Q/RT)$ is assumed for the Ta-diffusivity, then,

$$r(T)^2 = 2D_{0Ta}^{\alpha} \exp(-Q/RT) \times \{(c^{\alpha}-c^{\alpha/\beta})/(c^{\beta}-c^{\alpha/\beta})\} (T-T_s)/\phi. \quad (4.8)$$

Regrouping the terms, we get,

$$r(T)^2 = 2D_{0Ta}^{\alpha} \{(c^{\alpha}-c^{\alpha/\beta})/(c^{\beta}-c^{\alpha/\beta})\} \times \exp(-Q/RT) (T-T_s)/\phi. \quad (4.9)$$

Equation (4.9) is probably the simplest physical model of diffusion driven growth of β , under site saturation nucleation. The term $\{(c^{\alpha}-c^{\alpha/\beta})/(c^{\beta}-c^{\alpha/\beta})\}$ stands basically for the driving force for the phase change, given here as dimensionless concentration ratio. At present, we do not have experimentally measured estimates of this driving force for Ti-Ta alloys. In addition, no recent experimental estimates of D_{Ta}^{α} are also available in open literature, save an assessment study by Liu et al. [34]. However, a preliminary

unpublished experimental report on the diffusivity of tantalum in β -phase of Ti-Ta alloys (1473 K) suggests that D_{Ta} could be of the order of $10^{-13} \text{ m}^2 \text{ s}^{-1}$ [35], and based on the trend observed for the ratio of β to α diffusivities in titanium base alloys, a tentative estimate of $\sim 10^{-16} \text{ m}^2 \text{ s}^{-1}$ can be ascribed to the diffusivity of tantalum in α -phase. If $r = 10^{-6} \text{ m}$ ($1 \mu\text{m}$) is arbitrarily assumed as the typical β particle radius, and a value of $\{(c^\alpha - c^{\alpha/\beta})/(c^\beta - c^{\alpha/\beta})\} = \{0.03 - 0.01/0.015 - 0.01\} = 4$ based on a typical data observed for Ti-Nb alloy is invoked for the dimensionless driving force, then $t = (10^{-12}/2 * 10^{-16}) * 4 = 2 * 10^4 \text{ s} = 5.56 \text{ h}$, is required to realise isolated β formation to $1 \mu\text{m}$ size. This is certainly a crude estimate, however, the estimated time reflects the typical order of homogenization anneal required in case of Ti-Ta alloys. The purpose of setting up this simple model is to establish the point that $\alpha \rightarrow \beta$ phase change in Ti-Ta alloys is significantly influenced by Ta-diffusion. Another useful point to note is that Eq. (4.6) after substituting for $D = D_0 \exp(-Q/RT)$ has striking resemblance with Avrami equation for the fractional extent of phase transformed under isothermal conditions. This is further discussed below in the context of modeling of transformation kinetics.

4.7.2 KJMA Modelling of transformation kinetics

It is possible to model $\alpha \leftrightarrow \beta$ phase change by invoking standard nucleation and growth mechanisms, in which the driving force for both nucleation and growth and their dimensionalities are separately taken into consideration. However, as shown in many recent publications, especially that of Sha and co-workers on titanium base systems [2, 3, 6, 36], the simple KJMA formalism of diffusional phase transformation kinetics may also be adopted for getting consistent estimates of the kinetic parameters. The standard KJMA model for the isothermal diffusional transformation kinetics is given by the expression

$$f(t) = 1 - \exp\{(-kt)^n\}. \quad (4.10)$$

$$k = k_0 \exp(-Q^{eff}/RT). \quad (4.11)$$

$k(T)$ is the temperature dependent empirical rate constant, with k_0 as the prefactor, Q^{eff} is the effective or apparent activation energy for the overall transformation and n is the transformation exponent, whose magnitude can be interpreted in terms of the combined dimensionalities of nucleation and growth, if Eq. (4.10) and (4.11) are based on physical descriptions of individual nucleation and growth steps [31-33]. The generalization of isothermal KJMA (Eq. 4.10) to non-isothermal linear heating/cooling conditions has already been elucidated in many works, notably that of Liu et al., [31, 32, 37] and that of Farjas [38, 39]. The non-isothermal version of KJMA model under site-saturation nucleation approximation may be written as follows.

$$f_{\beta}^{tr}(T) = 1 - \exp(-k_0^n \exp\{-nQ_{eff}/RT\} (R(T-T_s)^2/\phi Q_{eff})^n). \quad (4.12)$$

Within the spirit of isoconversional reaction rate formalism, the apparent activation energy Q^{eff} can be estimated from the measured heating or cooling rate (ϕ) dependence of the transformation peak temperature (T_p) by means of the Kissinger linearisation scheme, as given below [40, 41].

$$\ln(\phi/T_p^2) = -Q^{eff}/RT_p + \text{Constant}. \quad (4.13)$$

In **Fig. 4.15**, the Kissinger plot is shown for the $\alpha \rightarrow \beta$ phase change transformation kinetics in Ti-x Ta (x = 5, 10, 15, 20 mass %) alloys. As may be seen, two distinct values are obtained for the low heating and high heating rate regimes. Further, the effective activation energy obtained for lower heating rates turns out to be higher than that obtained for the high heating rates. This inverse correlation between Q^{eff} and ϕ is slightly unusual, but nevertheless had been found earlier by Sha for the $\alpha \rightarrow \beta$ phase change in Ti-6Al-4V alloy [5]. Moreover, what is interesting is the high values of Q^{eff} obtained (1500 and 732 kJ mol⁻¹) by the Kissinger method, which are difficult to rationalize directly based on probable activation barrier values for Ta diffusion in Ti.

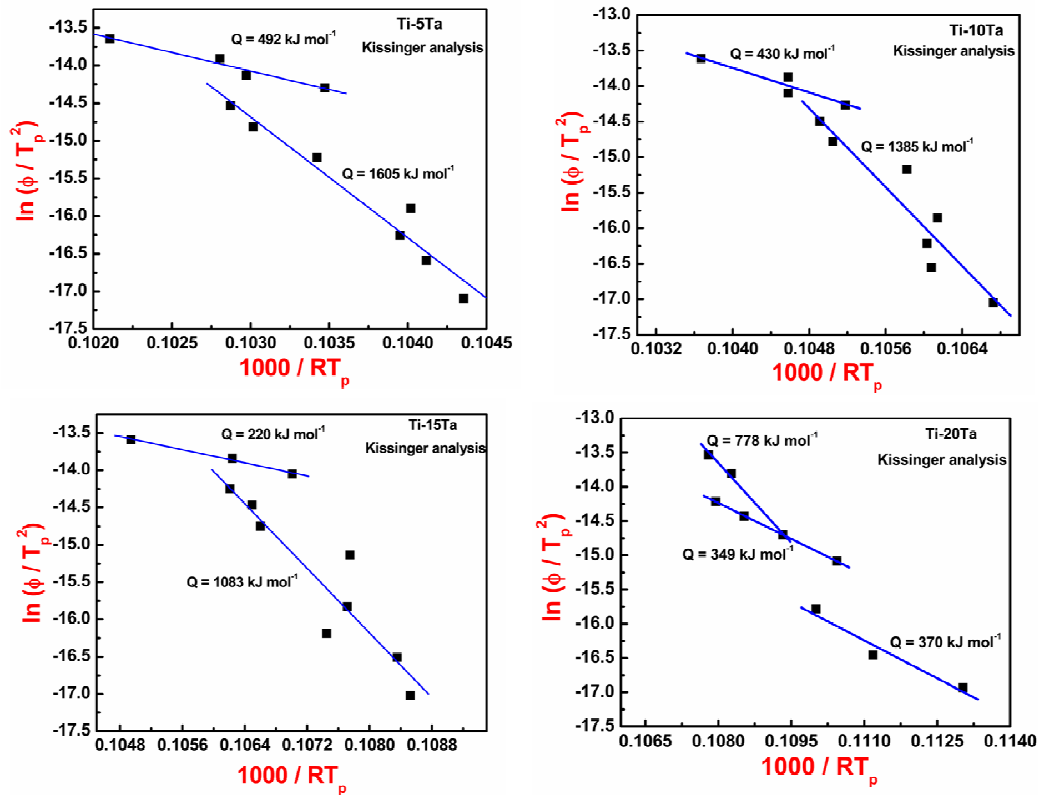


Figure 4.15 Kissinger plot for the $\alpha \rightarrow \beta$ transformation in Ti-x Ta ($x = 5, 10, 15, 20$ mass %) alloys.

A similar scenario with regard to high activation energy values obtained by isoconversional Kissinger method has also been observed by Baumann et al., and a definite resolution of this paradox is lacking as of yet [42]. In our view, the incidence of high values Q^{eff} obtained by any of the isoconversional linearization methods such as due to Kissinger, Ozawa, or their equivalent, is an artefact, although a consistent and valid one, if assessed within the purview of expressing the total transformation rate as a product of a separable functions $f(x_v)$ of x_v , the volume fraction transformed and $k(T)$, the temperature dependent rate constant, for a fixed linear heating rate ϕ .

$$dx_v/dT = f(x_v) \times k(T) \times \phi. \quad (4.14)$$

$f(x_v)$ can take a suitable functional form which characterizes a particular (empirical) reaction model. For the standard, Avrami model $f(x_v)$ may be given as

$$f(x_v) = n(1-x_v)[-ln(1-x_v)]^{n-1/n}. \quad (4.15)$$

In thermal analysis literature, there have been extensive discussions about the validity of the homogeneous reaction model of Kissinger, when applied to solid state transformations, such as polymorphic transformations, glass crystallization, etc. Matusita and Saka, for example have suggested an alternate or modified Kissinger (like) linearization scheme which may be represented as follows [43, 44].

$$dx_v/dT = A \phi^n (1-x_v)^p \exp(-mQ^{eff}/RT). \quad (4.16)$$

A, m, n, and p are again empirical constants, which depending upon the transformation mechanism can assume different values. The linearization scheme of Matusita and Sakka is represented as follows.

$$\ln(\phi^n/T_p^2) = -mQ^{eff}/RT_p + \text{Constant}. \quad (4.17)$$

In arriving at Eq. (4.17), $p = 1$ and the composite term ApR/mQ^{eff} is held constant. Following Matusia and Sakka, if $n=1$ and $m=3$ are assumed, reasonably lower values of Q^{eff} are obtained (500 and 244 kJ mol⁻¹ for low and high heating rate regimes) for Q^{eff} , but still the values are higher than the Q^{eff} for the diffusion of Ta in titanium.

It may be remarked at this juncture that as an empirical fit parameter, higher values of Q^{eff} obtained by model free isoconversional methods are not problematic in themselves, and they can be used together with a suitable reaction model $f(x_v)$ to provide an empirical description of the transformation curve. Such an approach has been adopted by many researchers, especially in conjunction with the rule of additivity for modelling nonisothermal transformation kinetics [45, 46]. On the other hand, Leblond and Devaux have suggested an altogether different scheme based on the non-linear version of the incubation time with thermal history for modelling nonisothermal transformation kinetics [47]. These models have succinctly discussed in recent overview by one of the authors [48]. In the present study, we however have adopted the nonisothermal variant of KJMA (Eq. 4.12) for modelling the $\alpha \rightarrow \beta$ and $\beta \rightarrow \alpha$

transformation kinetics. In **Tables 4.5** and **4.6**, the KJMA fit parameters obtained by fitting the calorimetrically measured transformed fraction data to Eq. (4.12), are tabulated for $\alpha \rightarrow \beta$ and $\beta \rightarrow \alpha$ transformations respectively. In **Fig. 4.16**, the variation of Q^{eff} value obtained at 3 K min^{-1} with Ta-concentration is displayed for both $\alpha \rightarrow \beta$ and reverse transformations. From the data presented in **Table 4.5**, it can be seen that for the on-heating $\alpha \rightarrow \beta$ transformation, the estimated values for the effective activation energy are in the range, 280 to 350 kJ mol^{-1} , the higher values are obtained for Ti-20 Ta alloy. Further, for a given composition, the apparent activation energy exhibits only a marginal increase with heating rate, which is quite unlike the case with Kissinger linearization scheme, that it can be considered effectively constant for the given alloy. The value for the overall transformation exponent n is generally close to unity; but again exhibits a small decrease with increasing Ta-content. The low value for the transformation exponent is due to growth impingement effects strongly operating under site-saturation nucleation conditions. The values of Q^{eff} for the $\beta \rightarrow \alpha$ transformation are substantially lower than their heating counterparts (**Table 4.6**) and besides, it does not vary appreciably with Ta content or with cooling rate as well (**Fig. 4.16(b)**).

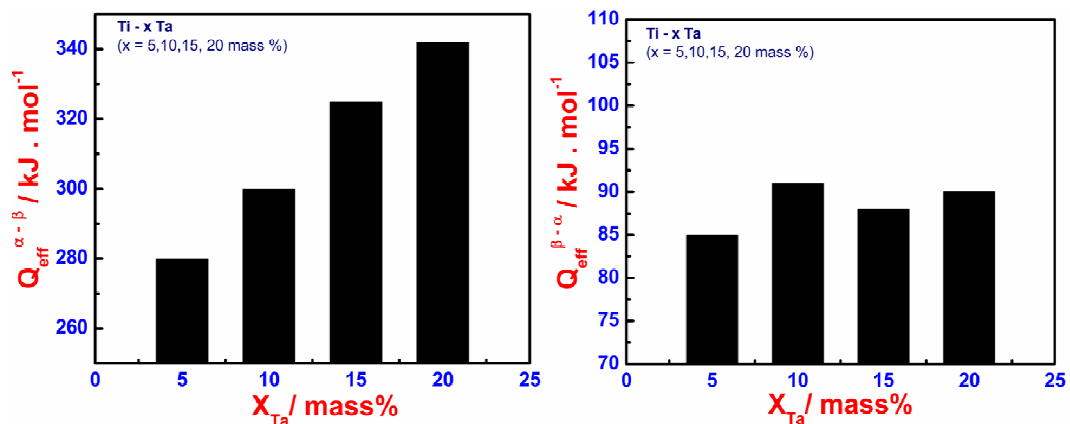


Figure 4.16 The variation of effective activation energy, Q^{eff} , for (a) $\alpha \rightarrow \beta$ and (b) $\beta \rightarrow \alpha$ transformations with Ta concentration.

Table 4.5 Kinetics parameters for $\alpha \rightarrow \beta$ transformation obtained by fitting experimental data to non-isothermal KJMA model

Ti-5 mass% Ta					Ti-10 mass% Ta				
ϕ (K min ⁻¹)	n	Q _{eff} (kJ mol ⁻¹)	k ₀ × 10 ¹³ (s ⁻¹)	R ² for the fit	ϕ (K min ⁻¹)	n	Q _{eff} (kJ mol ⁻¹)	k ₀ × 10 ¹⁴ (s ⁻¹)	R ² for the fit
3	1.09	280	0.28	0.99874	3	0.97	300	0.22	0.99988
5	1.1	282	0.35	0.99932	5	0.83	301	0.25	0.99901
7	0.96	284	0.60	0.99985	7	0.90	305	0.58	0.99821
10	0.95	285	0.84	0.99853	10	0.96	312	2.09	0.99827
20	0.93	289	2.25	0.99922	20	0.87	313	4.47	0.99946
30	0.89	291	3.13	0.99942	30	0.81	314	4.43	0.99931
40	0.89	292	4.45	0.99913	40	0.85	313	6.3	0.99981
50	0.90	293	9.25	0.99909	50	0.85	315	11.38	0.99954
60	0.89	293	10.02	0.99956	60	0.85	316	9.13	0.99837
75	0.89	296	15.65	0.99941	75	0.88	317	15.37	0.99933
99	0.87	298	18.53	0.99956	99	0.84	320	16.98	0.99888
Ti-15 mass% Ta					Ti-20 mass% Ta				
ϕ (K min ⁻¹)	n	Q _{eff} (kJ mol ⁻¹)	k ₀ × 10 ¹⁵ (s ⁻¹)	R ² for the fit	ϕ (K min ⁻¹)	n	Q _{eff} (kJ mol ⁻¹)	k ₀ × 10 ¹⁶ (s ⁻¹)	R ² for the fit
3	0.91	325	0.47	0.99936	3	0.53	342	0.71	0.99894
5	0.99	327	0.92	0.99852	5	0.57	342	0.98	0.99888
7	0.93	327	0.97	0.9997	10	0.84	344	2.12	0.99976
10	0.82	331	2.09	0.9995	20	0.54	345	3.77	0.99953
20	1.11	332	6.2	0.9995	30	0.58	346	3.88	0.99967
30	0.67	332	3.46	0.99976	40	0.75	349	7.77	0.99966
40	0.83	335	6.98	0.99976	50	0.72	349	6.47	0.99924
50	0.71	336	6.96	0.99894	75	0.70	351	1.54	0.99908
60	0.90	338	26.39	0.99939	99	0.73	353	2.00	0.99916
75	0.80	339	22.51	0.99935	-	-	-	-	-
99	0.75	340	19.48	0.99977	-	-	-	-	-

Table 4.6 Kinetics parameters for $\beta \rightarrow \alpha$ transformation obtained by fitting experimental data to non-isothermal KJMA model

Ti-5 mass% Ta					Ti-10 mass% Ta				
ϕ (K min ⁻¹)	n	Q _{eff} (kJ mol ⁻¹)	k ₀ × 10 ³ (s ⁻¹)	R ² for the fit	ϕ (K min ⁻¹)	n	Q _{eff} (kJ mol ⁻¹)	k ₀ × 10 ³ (s ⁻¹)	R ² for the fit
3	2.98	85	0.776	0.99748	3	3.19	91	1.38	0.99496
5	2.97	81	0.853	0.99844	5	1.85	89	3.16	0.99867
7	3.30	75	0.567	0.99735	7	1.94	86	3.38	0.99866
10	1.97	73	0.674	0.99796	10	2.76	87	4.63	0.9996
20	2.45	70	0.851	0.99783	20	3.98	80	3.01	0.99843
30	2.11	61	0.454	0.99772	30	2.46	77	3.71	0.99627
40	2.20	63	0.701	0.99717	40	3.61	80	6.03	0.99644
50	2.82	66	1.328	0.99969	50	3.77	74	4.2	0.99883
60	2.56	62	0.959	0.99915	60	2.35	80	16.07	0.99757
75	2.77	63	1.352	0.99993	75	2.70	76	11.45	0.99936
99	2.81	67	3.683	0.99905	99	2.1	77	20.63	0.99841
Ti-15 mass% Ta					Ti-20 mass% Ta				
ϕ (K min ⁻¹)	n	Q _{eff} (kJ mol ⁻¹)	k ₀ × 10 ³ (s ⁻¹)	R ² for the fit	ϕ (K min ⁻¹)	n	Q _{eff} (kJ mol ⁻¹)	k ₀ × 10 ³ (s ⁻¹)	R ² for the fit
3	2.99	84	1.02	0.99623	3	1.74	90	3.14	0.99626
5	3.95	81	1.02	0.99519	5	1.80	92	8.17	0.99940
7	3.57	80	1.58	0.99635	10	3.78	90	9.24	0.99784
10	3.12	92	11.18	0.99888	20	2.09	83	8.74	0.99716
30	2.14	90	29.14	0.99946	30	2.14	80	9.08	0.99844
40	3.85	91	42.04	0.99776	40	4.71	83	15.3	0.99936
50	2.00	81	25.02	0.99957	50	3.24	79	13.15	0.99858
60	3.98	59	0.907	0.99822	75	3.67	80	24.02	0.99948
75	3.76	84	33.88	0.99730	99	3.74	81	38.11	0.99984
99	3.23	85	58.48	0.99968	-	-	-	-	-

Thus there seems to be an interesting kinetic asymmetry with regard to on-heating $\alpha \rightarrow \beta$ and cooling induced $\beta \rightarrow \alpha$ transformations in Ti-Ta alloys. The low values of Q^{eff} , of the order of 80-90 kJ mol⁻¹ obtained in this study cannot be reconciled with bulk or volume diffusivity of Ta in the high temperature β -bcc phase. On the contrary, it may possibly be taken to imply the crucial role played by grain boundary diffusion in catalysing the nucleation of allotriomorphic or grain boundary α having favourable low energy interface with β . The transformation exponent n for the $\beta \rightarrow \alpha$ transformation also assumes a higher value of nearly 3, which is implying a two dimensional growth habit with 3D nucleation, and with little blocking of the growth front by hard impingement considerations. In literature, Q^{eff} of about 90–92 kJ mol⁻¹ has already been attributed to $\beta \rightarrow \alpha$ transformation in some titanium alloys [49-51]; but its plausible physical interpretation remains yet to be clarified. While discussing the kinetics of $\beta \rightarrow \alpha$ transformation two issues need to be kept in mind: the basic on-cooling thermal arrest does not have a long tail as is the case with on-heating $\alpha \rightarrow \beta$ thermal arrest. Also, the post DSC samples appeared to possess some excess β . The former observation indicates that $\beta \rightarrow \alpha$ transformation after having been initiated at some finite undercooling, does not proceed further into the low temperature domain of $\alpha + \beta$ two phase region with same velocity, due to sluggish solutal diffusion at this temperatures. Hence in all probability, the critical step of $\beta \rightarrow \alpha$ transformation is the heterogeneous nucleation of it at multiple grain boundary sources, with each nuclei advancing fairly independently of each other at the initial stages. The source of Ta for initial β nuclei formation must be supplied through grain boundary sources, whose activation barrier is rather low. This may account for the lower range of Q^{eff} obtained in this study. We however hasten to add that elucidation of $\beta \rightarrow \alpha$ transformation needs further in-depth investigation. In particular, variation of holding time and temperature in the β -phase and

or hot working in the β -domain followed by rapid cooling and electron microscopy investigation of post transformation microstructures are some of the experiments that can shed further insight into the operative mechanism of $\beta \rightarrow \alpha$ transformation.

In **Fig. 4.17-4.20**, the continuous heating transformation (CHT) diagram for the $\alpha \rightarrow \beta$ transformation and continuous cooling transformation (CCT) diagram for the $\beta \rightarrow \alpha$ transformation are presented for Ti-xTa ($x = 5, 10, 15, 20$ mass%) alloys. It is easy to obtain these diagrams from the KJMA model given in Eq.(4.12), which can in principle be solved to give (T, t) coordinate pairs for a chosen temperature and fixed x_v , the fraction transformed, under a set of known kinetic parameters which are in turn obtained by fitting the experimental data to Eq. (4.12). As can be seen, the KJMA model successfully reproduces the experimentally observed CHT and CCT diagrams.

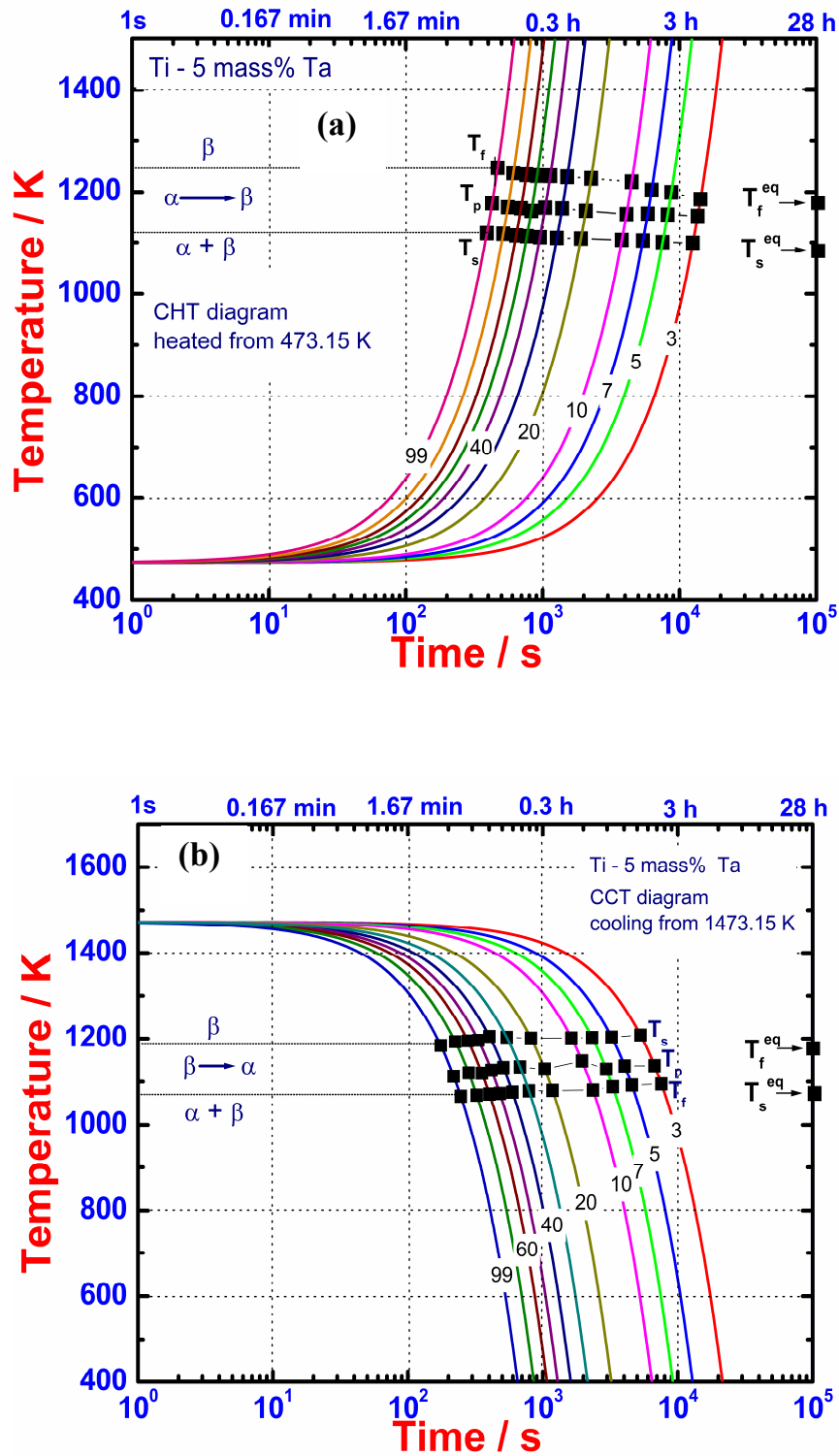


Figure 4.17 (a) The continuous heating transformation (CHT) diagram for $\alpha \rightarrow \beta$ and (b) continuous cooling transformation (CCT) diagram for $\beta \rightarrow \alpha$ transformations obtained in the present study for Ti-5Ta alloy

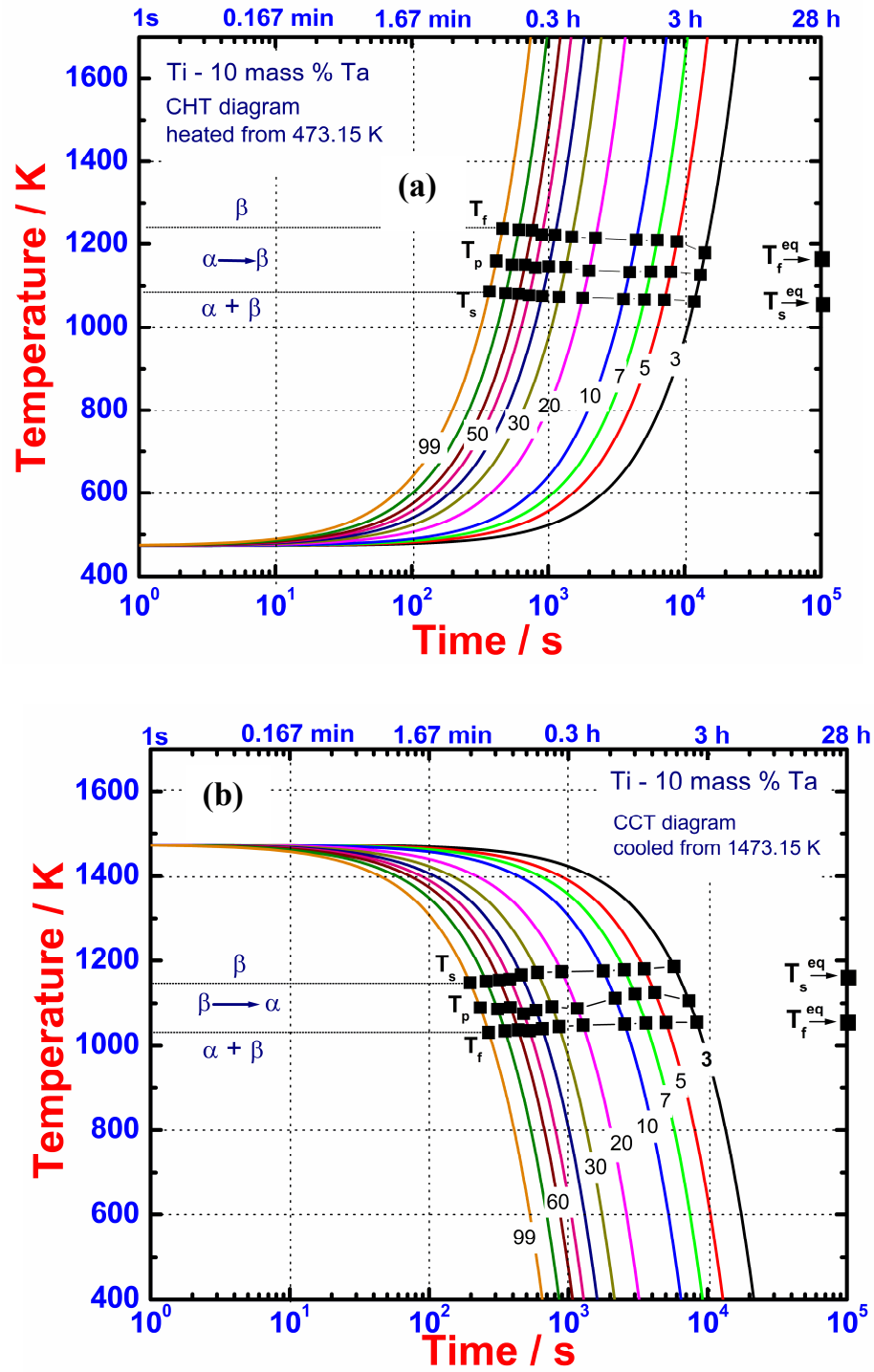


Figure 4.18 (a) The continuous heating transformation (CHT) diagram for $\alpha \rightarrow \beta$ and (b) continuous cooling transformation (CCT) diagram for $\beta \rightarrow \alpha$ transformations obtained in the present study for Ti-10Ta alloy

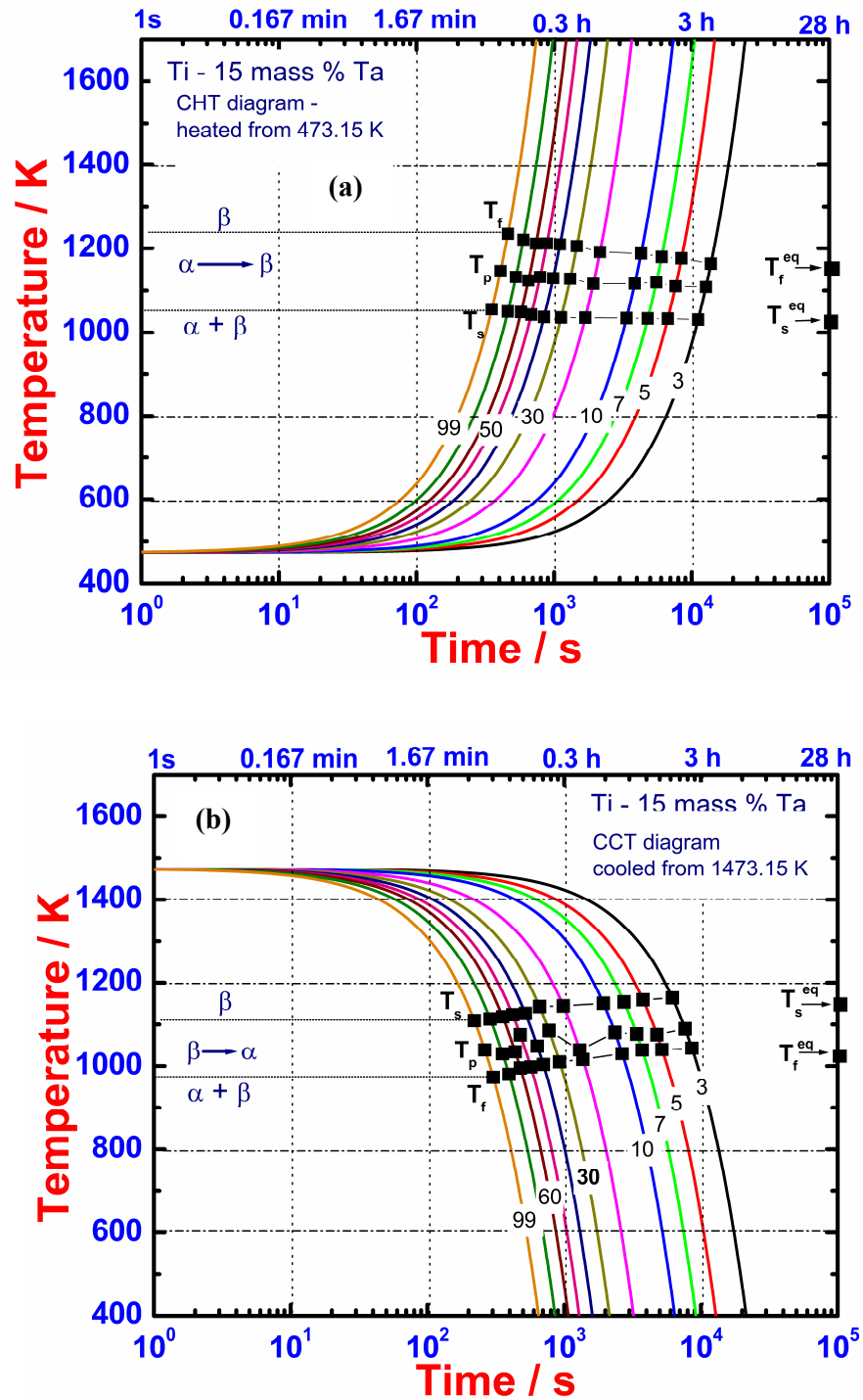


Figure 4.19 (a) The continuous heating transformation (CHT) diagram for $\alpha \rightarrow \beta$ and (b) continuous cooling transformation (CCT) diagram for $\beta \rightarrow \alpha$ transformations obtained in the present study for Ti-15Ta alloy

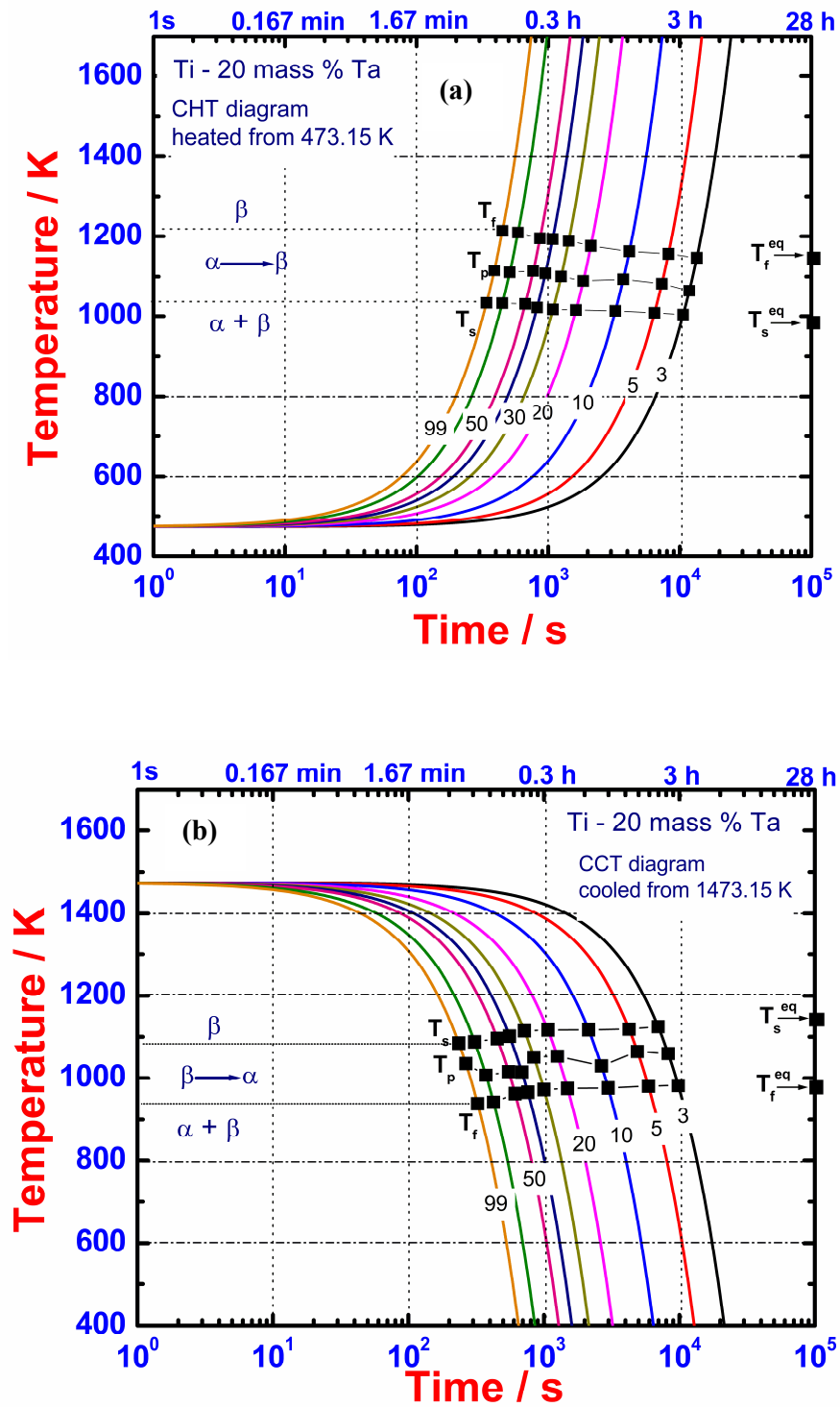


Figure 4.20 (a) The continuous heating transformation (CHT) diagram for $\alpha \rightarrow \beta$ and (b) continuous cooling transformation (CCT) diagram for $\beta \rightarrow \alpha$ transformations obtained in the present study for Ti-20Ta alloy

4.8 Conclusions

- (i) Differential scanning calorimetry investigations of on-heating and cooling transformations have been performed as a function of several heating and cooling rates on Ti-xTa ($x=5, 10, 15, 20$ mass %) alloys.
- (ii) In general, the $\alpha \leftrightarrow \beta$ transformation start and finish temperatures exhibited a nonlinear variation with heating and cooling rate. In particular, the transformation finish temperatures for the $\alpha \rightarrow \beta$ phase change in the case of high tantalum alloys (20 mass %) exhibited a pronounced increase at higher heating rates.
- (iii) It is suggested that bulk diffusion of Ta in α -hcp solid solution phase is the rate controlling step for the $\alpha \rightarrow \beta$ transformation. It is further suggested that owing to the relatively comparative sluggish diffusion of Ta, the attainment of full-chemical homogenisation of β phase in high tantalum alloys require longer annealing times.
- (iv) The dynamically measured $\alpha + \beta \rightarrow \beta$ on-heating solvus temperatures are found to be higher than the currently available assessed equilibrium solvus boundary estimates, which suggest a serious need for fresh thermodynamic assessment of Ti-Ta binary system.
- (v) The enthalpy or heat change due to $\alpha \rightarrow \beta$ phase transformation $\Delta^{\circ}H_{tr}^{\alpha \rightarrow \beta}$, exhibited a decrease with increasing Ta-content of the alloy. Further, an empirical linear correlation has been found between the $\Delta^{\circ}H_{tr}^{\alpha \rightarrow \beta}$ and $\Delta^{\circ}S_{tr}^{\alpha \rightarrow \beta}$, the entropy of phase change, which is also borne by available data on other $\alpha + \beta$ titanium base alloys.
- (vi) The KJMA model fits well the observed transformation curves for both $\alpha \rightarrow \beta$ and $\beta \rightarrow \alpha$ transformations. However a significant kinetic asymmetry has been noticed with regard to the activation energy parameters estimated thereof.

- (vii) The effective activation energy for $\alpha \rightarrow \beta$ transformation has been found to be in the range, 280 to 350 kJ mol⁻¹. Relatively higher values are obtained for Ti-20 Ta alloy. On the other hand, for the reverse $\beta \rightarrow \alpha$ transformation, an almost composition independent value of 80-90 kJ mol⁻¹ has been obtained.
- (viii) It is suggested that $\alpha \rightarrow \beta$ transformation has been governed by volume diffusion of Ta in α phase, while grain boundary diffusion in the β phase contributed to the nucleation of α during cooling.

References

- [1] S. Bein and J. Bechet, *J Phys. IV* 6 (C1) (1996) 99-108.
- [2] S. Malinov, P. Markovsky, W. Sha and Z. Guo, *J Alloys Comp.* 314 (2001) 181-192.
- [3] S. Malinov, W. Sha and P. Markovsky, *J alloys Comp.* 348 (2003) 110-118.
- [4] C. Angelier, S. Bein and J. Bechet, *Metall. Mater. Trans. A* 28 (1997) 2467-2475.
- [5] W. Sha and Z. Guo, *J Alloys Comp.* 290 (1999) L3-L7.
- [6] S. Malinov, Z. Guo, W. Sha and A. Wilson. *Metall Mater. Trans. A* 32 (2001) 879-887.
- [7] W. Szkliniarz and G. Smotka, *J Mater. Proc. Techno.* 53 (1995) 413-422.
- [8] Y. L. Zhou, M. Niinomi, T. Akahori, H. Fukui and H. Toda, *Mater. Sci. Engg. A* 398 (2005) 28-36.
- [9] O. Ivasishin and H. M. Flower, *J Mater. Sci.* 21 (1986) 2519-2524.
- [10] Y. Mantani and M. Tajima, *Mater. Sci. Engg. A* 438-440 (2006) 315-319.
- [11] K. Bywater and J. W. Christian, *Philos. Mag. A* 25 (1972) 1275-1289.
- [12] Y. C. Liu, *J. Mater. Sci.* 39 (2004) 4009-4011.
- [13] G. P. Krielaart and S. Van der Zwaag, *Mater. Sci. Tech.* 14 (1998) 10-18.
- [14] Y. C. Liu, F. Sommer and E. J. Mittemeijer, *Philos. Mag.* 84 (2004) 1853-1876.
- [15] Arun Kumar Rai, S. Raju, B. Jeyaganesh, E. Mohan das, R. Sudha and V. Ganesan, *J. Nucl. Mater.* 383 (2009) 215 -225.
- [16] K. Bywater and J. W. Christian, *Philos. Mag. A* 25 (1972) 1249-1274.
- [17] J. D. Cotton, J. F. Bingert, P. S. Dunn and R. A. Patterson, *Metall. Mater. Trans. A* 25 (1994) 461-472.
- [18] D. M. Gordin, E. Delvat, R. Chelariu, G. Ungureanu, M. Besse, D. Laille and T. Gloriant, *Adv. Engg. Mater.* 10 No.8 (2008) 714-719.
- [19] D. Summers-Smith, *J. Inst. Met.* 81 (1952) 73-76.
- [20] P. B. Budberg and K. I. Shakova, *Izv. Akad. Nauk SSSR, Neorg Mater.* 3 (1967) 656-660.
- [21] D. J. Maykuth, H. R. Ogden and R. I. Jaffee, *Trans. AIME, J Metals Feb.* (1953) 231-237.
- [22] J. L. Murray, *Phase diagram of binary Titanium alloys*, ASM International, Materials Park, OH, 1987.
- [23] Thermo-Calc Software AB, TCW Ver. 5, TCBIN database (2008), Sweden.

- [24] R. A. Perez, F. Dymont, G. Garcia Bermudez, D. Abriola and M. Behar, *Appl. Phys. A* 76 (2003) 247-250.
- [25] A. Josephine Prabha., Unpublished research work on Ti-Nb system, personal communication.
- [26] J. Blacktop, J. Crangle and B. B. Argent, *J. Less-Comm. Metals* 109 (1985) 375-380.
- [27] E. Kaschnitz and P. Reiter, *Int. J Thermophys.* 23 (2002) 1339-1345.
- [28] Madhusmita Behera, S. Raju, B. Jeyaganesh, R. Mythili and S. Saroja, *Int. J. Thermophys.* 31 (2010) 2246-2263.
- [29] A. J. Prabha, S. Raju, B. Jeyaganesh, Arun Kumar Rai, Madhusmita Behera, M. Vijayalakshmi, G. Paneerselvam and I. Johnson, *Physica B* 406 (2011) 4200-4209.
- [30] V. Anbarasan, B. Jeyaganesh, S. Raju, S. Murugesan, E. Mohandas, U. Kamachi Mudali and G. Manivasagan, *J. Alloys Comp.* 463 (2008) 160-167.
- [31] F. Liu, C. Yang, G. Yang and Y. Zhou, *Acta mater.* 55 (2007) 5255-5267.
- [32] F. Liu, F. Sommer, and E.J. Mittemeijer, *J. Mater. Sci.* 39 (2004) 1621-1634.
- [33] F. Liu, F. Sommer, C. Bos and E.J. Mittemeijer, *Int. Mater. Rev.* 52 No. 4 (2007) 193-212.
- [34] Y. Liu, L. Zhang, Y. Du, J. Wang and D. Liang, *CALPHAD: Comp. Coupling of phase diagrams and Thermochem.* 34 (2010) 310-316.
- [35] J.C. Dibbern, Interdiffusivity in Titanium-Tantalum Alloys processed at 1473 K, Bachelor of Science Thesis submitted to Department of Materials Science and Engineering, Massachusetts Institute of Technology, (2007).
- [36] S. Malinov, P. Markovsky and W. Sha, *J Alloys Comp.* 333 (2002) 122-132.
- [37] F. Liu, G. C. Yang and J. N. Liu, *Thermochim. Acta* 438 (2005) 83-89.
- [38] J. Farjas and P. Roura, *Acta Mater.* 54 (2006) 5573-5579.
- [39] J. Farjas and P. Roura, *J. Therm. Anal. Calorim.* 105 (2011) 767-773.
- [40] H. E. Kissinger, *Anal. Chem.* 29 (1957) 1702-1706.
- [41] R. L. Blaine and H. E. Kissinger, *Thermochim. Acta* 540 (2012) 1-6.
- [42] W. Baumann, A. Lieneweber and E. J. Mittemeijer, *J. Mater. Sci.* 45 (2010) 6075-6082.
- [43] K. Matusita, S. Sakka, and Y. Matsui, *J. Mater. Sci.* 10 (1975) 961-966.
- [44] K. Matusita and S. Sakka, *J. Non-Crystal Solids* 38-39 (1980) 741-746.

- [45] E. B. Hawbolt, B. Chau and J. K. Brimacombe, *Metall. Mater. Trans. A* 14 (1983) 1803-1815.
- [46] M. Umemoto, K. Horiuchi and I. Tamura, *Trans. Iron Steel Inst. Jpn.* 22 (1983) 690-695.
- [47] J. B. Leblond and J. Devaux, *Acta Metall.* 31 (1984) 137-146.
- [48] S. Raju and E. Mohandas, *J. Chem. Sci.* 122 (2010) 83-89.
- [49] F.J. Gil and J. A. Planell, *Scripta Metall. Mater.* 25 (1991) 2843-2848.
- [50] F.J. Gil and J. A. Planell, *Mater. Sci. Engg. A* 283 (2000) 17-24.
- [51] W. Gang, Z. De-chang and L. Zhong-wu, *Trans. Nonferrous Met. Soc. China* 22 (2012) 1711-1716.

Chapter-5

*Thermodynamics, kinetics and
mechanism of phase
transformation in Ti-5Ta-1.8Nb
alloy*

5.1 Introduction

Ti-5 mass% Ta-1.8 mass% Nb alloy is an indigenously developed as a structural material for nuclear spent fuel reprocessing application in highly oxidizing and corrosive media [1]. This ternary alloy shows an excellent corrosion resistance as compared to conventional stainless steel and nitric acid grade stainless steel [1]. A comparative study of corrosion rate of Ti alloys shows that the addition of 5 mass% Ta and 1.8 mass% Nb alloy results in lower corrosion rate as compared to other Ti based alloys [2]. It is well understood that the successful tailoring of microstructure to suit the desired end application through carefully structured thermo-mechanical and other processing schedules, depends on the ready availability of reliable and accurate thermo-kinetic database [3-7]. A complete microstructural characterization and its influence on corrosion resistance and mechanical properties have been studied in detail for this alloy [8-15]. However, the investigation of thermodynamics and kinetics aspects of phase stability and phase transformation is also important to understand the system completely. Hence, the present chapter describes the evaluation of thermodynamic properties using static drop calorimetry, the kinetics of phase transformation during heating and cooling at varying rates using differential scanning calorimetry in Ti-5Ta-1.8Nb alloy. This chapter also includes the studies on the mechanism of phase transformation on continuous cooling from high temperature β phase field in this alloy using transmission electron microscopy.

5.2 Organization of the chapter

The organization of the present chapter is as follows. Section 5.3 describes structural and microstructural characterization of the initial alloy. In section 5.4, the enthalpy increment variation as a function of temperature is discussed. In section 5.5, the microstructural changes during $\alpha \rightarrow \beta$ transformation is discussed. The analysis of

experimentally measured enthalpy data forms section 5.6. In section 5.7, the calculation of specific heat using Neumann-Kopp approximation is described. The Differential Scanning Calorimetry results are discussed in section 5.8. Section 5.9 deals with the kinetics of on-heating $\alpha \rightarrow \beta$ and cooling $\beta \rightarrow \alpha$ transformation. In section 5.10, the microstructural characterization of the alloy on continuous cooling from the high temperature β phase is discussed.

5.3 Structural and microstructural characterization of the starting alloy

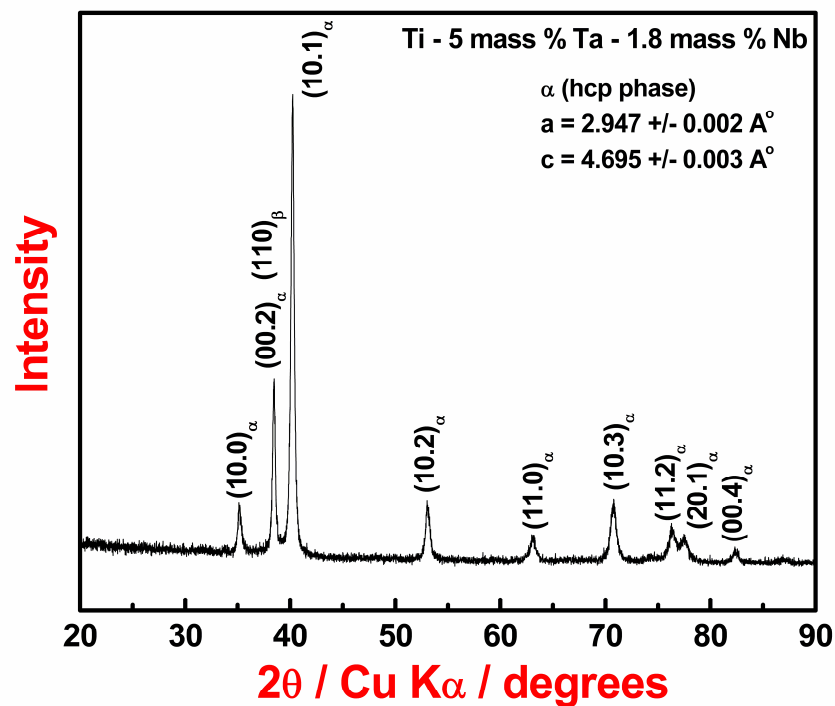


Figure 5.1 The room temperature XRD pattern of the Ti-5 mass% Ta-1.8 mass%Nb alloy showing the presence of α - phase peaks.

Fig. 5.1 shows the room temperature XRD pattern of Ti-5mass%Ta-1.8mass%Nb alloy. The presence of the major α -hcp phase is clearly observed from **Fig. 5.1**. The processed X-ray diffraction results and the calculated lattice parameters are listed in **Table 5.1**.

Table 5.1 Room temperature X-ray diffraction data on Ti-5mass%Ta-1.8 mass% Nb alloy

2 θ -CuK α (Degrees)	Normalised Intensity (%)	(hkil) value	Lattice Parameter (nm)
35.12	13.9	(10.0) $_{\alpha}$	$a = 0.2947 \pm 0.0002$ $c = 0.4695 \pm 0.0003$ $c/a = 1.593$
38.48	40.1	(00.2) $_{\alpha}$, (110) $_{\beta}$	
40.23	100	(10.1) $_{\alpha}$	
53.02	14.4	(10.2) $_{\alpha}$	
62.99	7.3	(11.0) $_{\alpha}$	
70.77	14.7	(10.3) $_{\alpha}$	
76.29	9.6	(11.2) $_{\alpha}$	
77.36	6.9	(20.1) $_{\alpha}$	
82.33	4.7	(00.4) $_{\alpha}$	

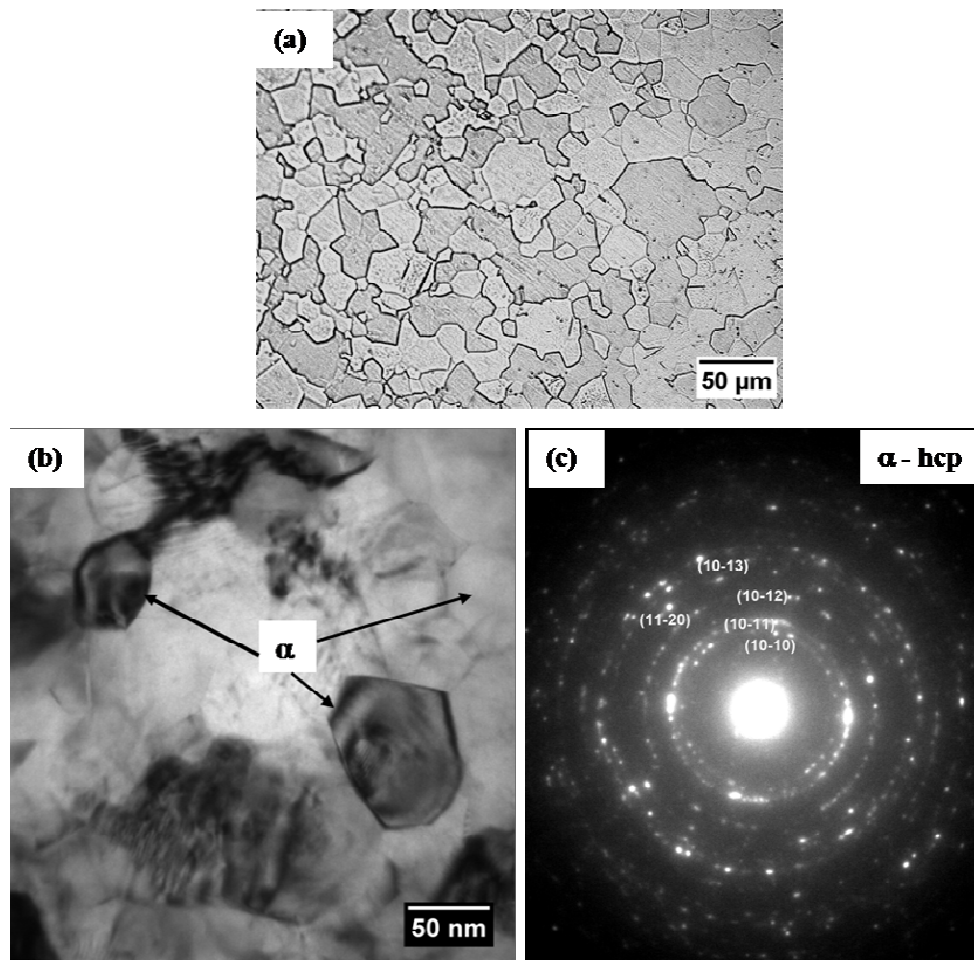


Figure 5.2 (a) Optical and (b) TEM micrograph showing fine equiaxed grains, (c) SAD pattern showing a polycrystalline pattern corresponding to α -hcp phase.

The microstructure of the starting material annealed at 973 K for 5 h is shown in **Fig. 5.2 (a)**. It is observed that the microstructure consists of well-defined equiaxed α -grains, characteristic of an annealed state. **Fig. 5.2 (b)** shows the transmission electron micrograph of the starting material which confirms the presence of equiaxed- α grains. The SAD pattern taken from these grains is shown in **Fig. 5.2 (c)** which confirms that they are α -hcp grains. Based on the chemical composition of this ternary alloy as presented in **Table 1** of **chapter 2**, the present alloy is expected to be a α (hcp)+ β (bcc) two phase alloy. However, the XRD pattern, optical microscopy observations and also the TEM observation did not reveal the presence of β -bcc phase unequivocally. The presence of a small amount of the β -phase in this alloy has been confirmed based on microstructural evidence obtained using electron microscopy [13]. The possible reasons for the β phase not being detected in XRD could be the strong overlap of the major β -phase reflections with the matrix α -lines and further, the volume fraction of β being small to make a distinct registry of its own weak reflections [13]. As it is mentioned in **chapter 2**, the starting material used in the present study has undergone a series of thermo-mechanical processing stages which might have broken the small amount of β already present and hence could not be observed in optical micrograph as well as in TEM micrograph.

5.4 Enthalpy Increment ($H_T - H_{298.15}$) variation with temperature

The temperature variation of enthalpy increment ($H_T - H_{298.15}$) measured in the temperature range of 463-1457 K is shown in **Fig. 5.3**. The scattered data points represent the actual experimental enthalpy and the line joining them serves to delineate the observed temperature dependence of the enthalpy variation. It is observed from **Fig.5.3**, that the enthalpy increment ($H_T - H_{298.15}$) for the low temperature α -phase increases steadily in a non-linear fashion with temperature up to about 1072 K. At this

temperature there is a clear change in the enthalpy variation behavior indicating the possible commencement of $\alpha \rightarrow \beta$ phase transformation [16]. In $\alpha \rightarrow \beta$ transformation region, the enthalpy increment values show a steeply rising character with temperature. This trend persists until about 1156 K and subsequently, another marked change in the enthalpy variation has been observed. This second inflection temperature is taken to mark the approximate completion (T_f) of β -phase formation. Accordingly, 1072 ± 2 K and 1156 ± 2 K are taken as the start (T_s) and finish (T_f) of $\alpha \rightarrow \beta$ diffusional phase transformation for Ti-5Ta-1.8Nb alloy. In the β -phase regime, the enthalpy again shows a continuous, non-linear increase with temperature.

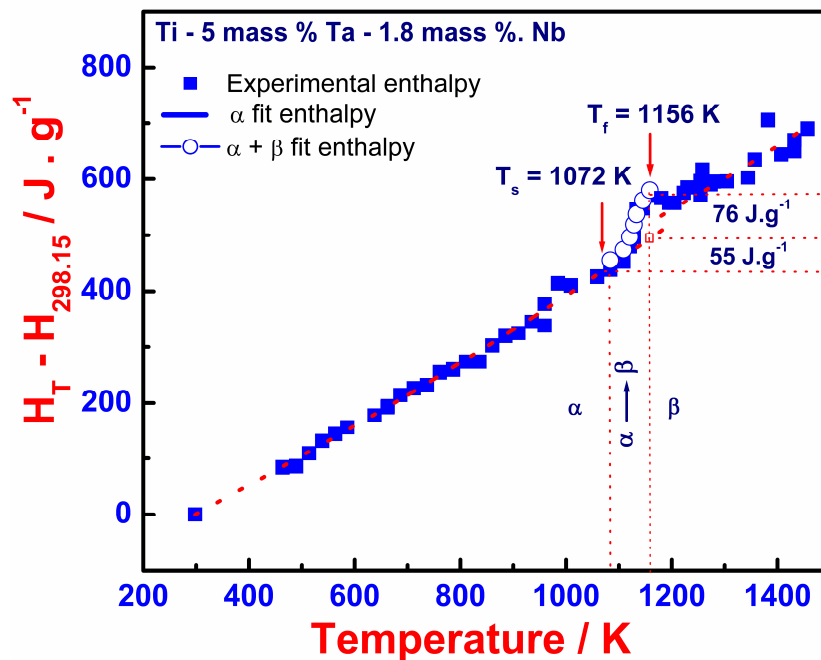


Figure 5.3 Variation of enthalpy increment with temperature for Ti-5 mass%Ta-1.8 mass%Nb alloy.

In order to confirm the occurrence of a phase transformation in this domain, a slow heating differential scanning calorimetry experiment has been run on this alloy. The resulting DSC profile is displayed in **Fig. 5.4**. It is observed from this figure that in the temperature domain of 1077K-1159K there is a clear endothermic peak which

corresponds to the $\alpha \rightarrow \beta$ phase transformation. The reason for the small difference between the measured transformation temperatures by drop calorimetry and DSC has already been discussed in section 3.5 of chapter 3.

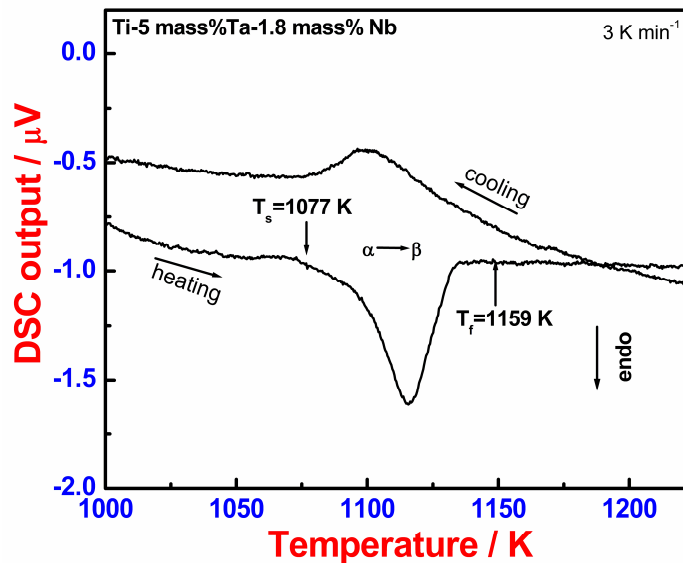


Figure 5.4 Slow scan DSC profile obtained for Ti-5mass%Ta-1.8mass%Nb alloy

5.5 Microstructural changes during $\alpha \rightarrow \beta$ transformation

Although the presence of distinct inflections in the enthalpy curve (**Fig. 5.3**) clearly demonstrated the occurrence of $\alpha \rightarrow \beta$ phase change, it is also confirmed by an independent observation of the microstructural evolution at select temperatures in the transformation zone. This microstructural observation is carried out on samples that are dropped from the $\alpha \rightarrow \beta$ transformation temperature domain. The choice of the temperature is so made that one sample each is drawn from just below the $\alpha \rightarrow \beta$ phase transformation start (T_s), in the actual $\alpha \rightarrow \beta$ transition region and just after the completion of $\alpha \rightarrow \beta$ phase transformation. The microstructure of these alloy samples is shown as a collage in **Fig. 5.5**. It is observed from **Fig.5.5 (a)** that at 1060 K, a temperature that is little lower than the actual $\alpha \rightarrow \beta$ phase transformation start temperature T_s , (*i.e. in α -phase field*), a microstructure with equiaxed α -grains and fine

inter and intragranular β -precipitates is observed. This again confirms the fact that at 1060 K, the matrix is predominantly α phase and the β phase is nucleated at the grain boundary. The relative amount of β phase fraction at this temperature is estimated to be about $3.7 \pm 0.5\%$. **Fig. 5.5 (b)** compares the EDS spectra collected from the equiaxed α -grains and from the β precipitates. It is clearly seen that β phase is slightly enriched in Ta and Nb content as compared to α phase; a fact which suggests that certain solute repartitioning should have taken place during the course of formation of β phase. In **Fig. 5.5 (c)**, the microstructure of the drop sample pertaining to a higher temperature namely, 1083 K is shown. From this figure, a slight coarsening of the β precipitates is noticed; the amount of β phase at this temperature is estimated to be around $6.6 \pm 1.3\%$. At still higher temperatures namely 1120 and 1133 K, the microstructure shown in **Fig. 5.5 (d) and (e)** respectively consisted of a large amount of a transformed β fraction. In **Fig. 5.5 (f)**, corresponding to sample dropped from 1158 K, an almost fully transformed β structure is noticed and this indicates that the $\alpha \rightarrow \beta$ phase transformation is by and large complete at 1158 K. So from the microstructure observation, the temperature 1158 K may be taken as the typical end point of the $\alpha \rightarrow \beta$ transformation. This temperature is in excellent agreement with the inflection point of 1156 K obtained from calorimetry data (**Fig. 5.3**). It can also be stated here that this calorimetric estimate of transformation finish temperature (T_f) is close to the β -transus temperature of 1143 K evaluated in a previous studies [13].

It is to be recalled that in typical drop calorimetry studies, no matter how close the temperature interval is chosen, it is not possible to trace the enthalpy behavior with temperature in a continuous manner. Further, the first detectable evidence of the β -phase formation in drop calorimetry occurs only when the fraction transformed reaches a minimum threshold that is adequate to induce a measurable thermal effect. Thus the true

transformation start temperature is not detected in the drop calorimetry measurements. A similar limitation also exists for the metallographic detection of transformation onset as well. Despite these limitations, it is observed that the drop calorimetry signature of the $\alpha \rightarrow \beta$ transformation domain is in fair accord with the microstructural evidence.

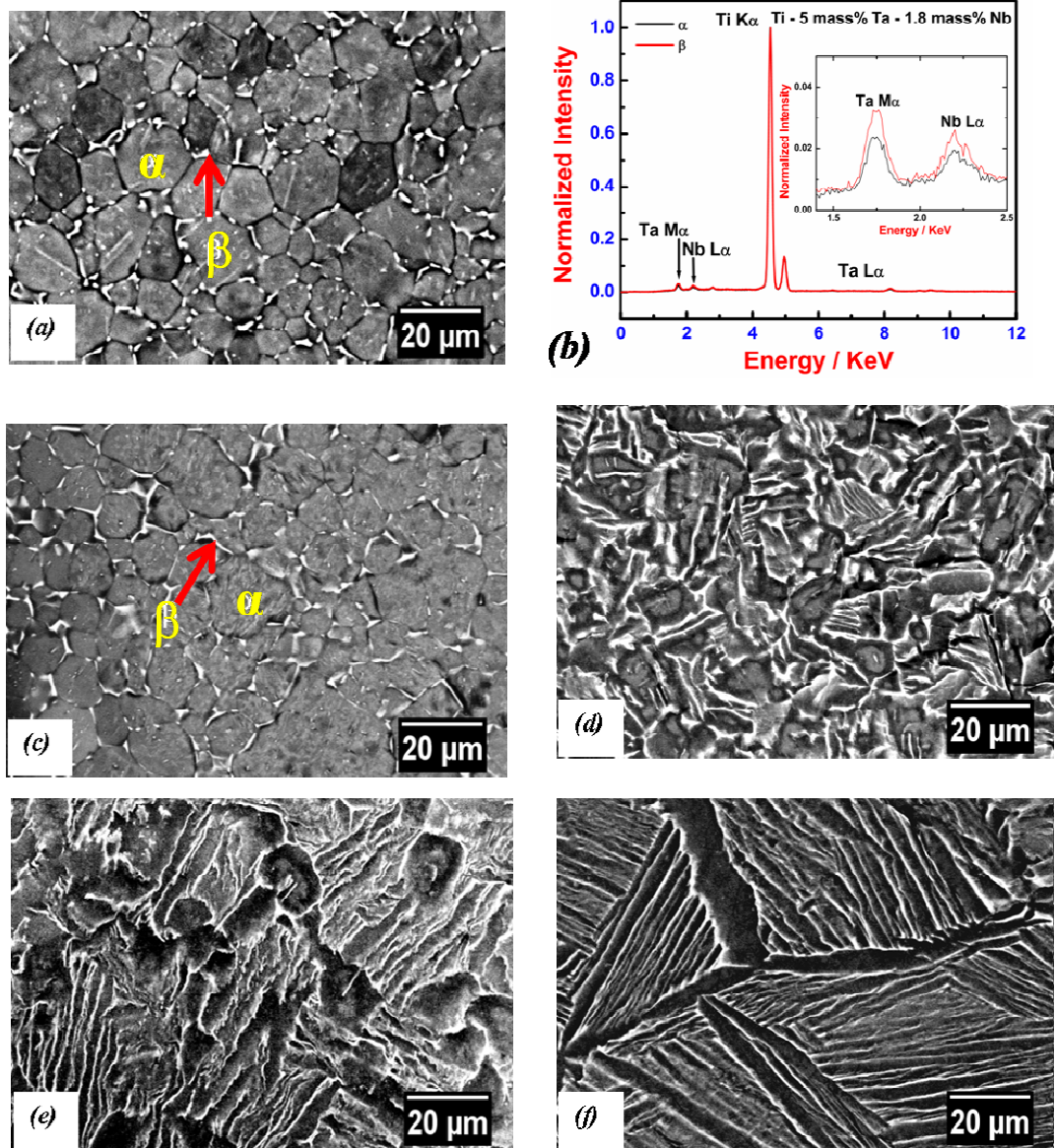


Figure 5.5 (a) Back scattered electron image showing predominately equiaxed primary α phase at 1060 K, (b) EDS spectra obtained from α and β phases, (c-f) Back scattered electron images showing the variation in microstructural features with Temperature; (c) 1083 K, (d) 1120 K, (e) 1133 K and (f) 1158 K.

5.6 Analytical representation of enthalpy increment ($H_T - H_{298.15}$) data

In the present study, the variation of experimental enthalpy increment with temperature in the temperature range of 463-1457 K is non-linear and exhibits a discontinuous change associated with $\alpha \rightarrow \beta$ phase transformation. Hence, the enthalpy increment data in α , $\alpha + \beta$, and β phase regions are fitted to the following expressions and the corresponding specific heat (C_p) values are calculated from these fit expressions.

5.6.1 α phase: $463 \text{ K} \leq T \leq 1072 \text{ K}$

The enthalpy increment data in α phase ($463 \text{ K} \leq T \leq 1072 \text{ K}$) are fitted by non-linear least square regression method to the following expression.

$$\Delta^{\circ}H \text{ (J g}^{-1}\text{)} = [H_T - H_{298.15}] = 0.39964 (T - 298.15) + 1.1 \times 10^{-4} (T^2 - 298.15^2) - 4.825 \times 10^3 (T^{-1} - 298.15^{-1}) \quad (5.1)$$

The above Eq. (5.1) for α phase domain is chosen by fixing $\Delta^{\circ}H_{298.15} = 0$ and the specific heat C_p at 298.15 K is $519 \text{ J kg}^{-1} \text{ K}^{-1}$. The specific heat value in the same range is reported for Ti-4Nb-4Zr alloy [16]. The specific heat in α phase domain can be derived by taking the derivative of the above Eq. (5.1).

$$C_p \text{ (J kg}^{-1} \text{ K}^{-1}\text{)} = d(\Delta^{\circ}H)/dT = 399.64 + 0.22 T + 4.825 \times 10^6 T^{-2} \quad (5.2)$$

5.6.2 $\alpha \rightarrow \beta$ transformation region: $1072 \text{ K} \leq T \leq 1156 \text{ K}$

Unlike the phase transformation in a unary system, the phase transformation in an alloy occurs over a range of temperatures. Hence, in the $\alpha \rightarrow \beta$ transformation region both the α and β phases coexist in finite amount and the amount of α phase continuously change with temperature until it completely transforms to β . Hence, the total enthalpy increment ($\Delta^{\circ}H_T$) at any temperature T in the $\alpha + \beta$ two phase domain is basically a sum of two independent contributions. Of these, the first one comes from the weighted sum of individual enthalpy contributions from α and β phases. The other one,

termed as the phase transformation enthalpy ($\Delta^{\circ}H_{tr}$) arises from the so-called latent heat associated with $\alpha \rightarrow \beta$ phase transformation. Thus to a first approximation the total measured enthalpy increment $\Delta^{\circ}H_T$ in the transformation domain ($1072 \text{ K} \leq T \leq 1156 \text{ K}$) may be written as follows [17-19].

$$\Delta^{\circ}H_T = [f_{\alpha} \Delta^{\circ}H_T^{\alpha} + f_{\beta} \Delta^{\circ}H_T^{\beta}] + \Delta^{\circ}H_{tr}. \quad (5.3)$$

$$\text{Where,} \quad f_{\alpha}(T) + f_{\beta}(T) = 1. \quad (5.4)$$

In the above equations, $f_{\alpha}(T)$ and $f_{\beta}(T)$ denote the fraction of α and β phases respectively present at temperature T , $\Delta^{\circ}H_T^{\alpha}$ and $\Delta^{\circ}H_T^{\beta}$ are the enthalpy increment of α and β phases respectively at temperature T . The latent heat or the enthalpy for the $\alpha \rightarrow \beta$ phase transformation ($\Delta^{\circ}H_{tr}$) for the present alloy is determined by using the above Eq. (5.3). The method of evaluation for the $\alpha \rightarrow \beta$ transformation enthalpy ($\Delta^{\circ}H_{tr}$) for Ti-5 mass% Ta -1.8 mass% Nb alloy is same as the method applied for the evaluation of $\alpha \rightarrow \beta$ transformation enthalpy ($\Delta^{\circ}H_{tr}$) in case of Ti-Ta alloys and is discussed elaborately in **section 3.7.2 of chapter 3**. From **Fig. 5.3**, it can be observed that the total increase in enthalpy in the $\alpha \rightarrow \beta$ transformation domain ($1072 \text{ K} \leq T \leq 1156 \text{ K}$) is $131 \pm 12 \text{ J g}^{-1}$. The entire quantum of this 131 J g^{-1} could not contribute to the enthalpy change associated with $\alpha \rightarrow \beta$ transformation [17-19]. It includes both the enthalpy contribution from the α and β phases and the transformation enthalpy which can be mathematically represented by Eq. (5.3). Hence, the $\alpha \rightarrow \beta$ transformation enthalpy ($\Delta^{\circ}H_{tr}$) calculated by the method described in **section 3.7.2 of chapter 3** for Ti-5 mass% Ta -1.8 mass% Nb alloy is 76 J g^{-1} and the contribution from α and β phases is 55 J g^{-1} which corresponds to the first term inside the square braces on right side of Eq. (5.3) and graphically shown in **Fig. 5.3**. Thus, in the final analysis, the total enthalpy increment ($\Delta^{\circ}H_T$) in the transformation zone is represented by the following expression.

$$\Delta^{\circ}H_T / J g^{-1} = [H_T - H_{298.15}] = \{0.39964 (T-298.15) + 1.1 \times 10^{-4} (T^2 - 298.15^2) - 4.825 \times 10^3 (T^{-1} - 298.15^{-1})\} + f_{\beta} (T) \Delta^{\circ}H_{tr}. \quad (5.5)$$

It is reiterated here that the first term inside the curved braces on the right hand side of Eq. (5.5) denotes the α -phase enthalpy which is extrapolated up to T_f . The second term is the transformation component.

The temperature dependence of the progress of $\alpha \rightarrow \beta$ transformation, namely $f_{\beta}(T)$, is explained in terms of an empirical model for the diffusional phase transformation kinetics name by the Kolmogorov-Johnson-Mehl-Avrami (KJMA) model. According to this model, $f_{\beta}(T)$ is given by the following expression [20],

$$f_{\beta}(T) = 1 - \exp\{-k_0^n \exp\{(-nQ_{eff}/RT)\} (R(T-T_s)^2/\phi Q_{eff})^n\}. \quad (5.6)$$

Here, Q_{eff} represents the apparent activation energy for the overall transformation, n is an empirical transformation exponent, k_0 is the frequency factor, and R is the universal gas constant. It should be noted that Eq. (5.6) is a simple model for the isochronal transformation kinetics that is valid under certain conditions only [21, 22]. In this sense, the parameter ϕ appearing in Eq. (5.6) should correspond ideally to slow rates of heating such that at each temperature T in the transformation zone, the equilibrium limit of $f_{\beta}(T)$ is realised. In the present set of drop calorimetry measurements, we allow for about 20 minutes to elapse between successive drops, and hence it is presumed that $f_{\beta} = f_{\beta}^{eq}$ at each temperature interval in the transformation domain. The experimental enthalpy data corresponding to the transformation temperature zone are fitted to Eq. (5.6) to obtain the following values of the kinetic quantities: $n = 1.1$; $Q_{eff} = 295 \text{ kJ mol}^{-1}$; and $k_0 = 1.06 \times 10^{13} \text{ s}^{-1}$. Substituting Eq. (5.6) in Eq. (5.5) the enthalpy in the transformation domain can be generated. The specific heat C_p expression in the transformation zone is obtained by taking the derivative of equation (5.5) with respect to T .

$$\Delta C_p^{\alpha \rightarrow \beta} / \text{J kg}^{-1} \text{K}^{-1} = 399.64 + 0.22 T + 4.825 \times 10^6 T^{-2} + f_\beta \Delta^\circ C_p + df_\beta/dT (\Delta^\circ H_{tr}). \quad (5.7)$$

Here, $\Delta^\circ C_p$ is the change in C_p associated with $\alpha \rightarrow \beta$ phase transformation. Its value is estimated to be $(\Delta^\circ H_{tr}/\Delta T) = 904 \text{ J Kg}^{-1} \text{K}^{-1}$.

5.6.3 Enthalpy representation in β region: $1156 \text{ K} \leq T \leq 1457 \text{ K}$

In the β -phase region the enthalpy increment values are fitted to the following expression

$$\Delta^\circ H_T / \text{J g}^{-1} = 0.22515 T + 1.5 \times 10^{-4} T^2 + 7.0534 \times 10^4 T^{-1} \quad (5.8)$$

The specific heat C_p in the β -phase can be represented by the following expression.

$$C_p / \text{J kg}^{-1} \text{K}^{-1} = d(\Delta^\circ H_T)/dT = 225.15 + 0.3 T - 7.0534 \times 10^7 T^{-2} \quad (5.9)$$

The variation of C_p with temperature in α -phase, in the $\alpha \rightarrow \beta$ phase transformation region and in β -region are shown in **Fig. 5.6**. In **Table 5.2**, the experimental enthalpy, fit enthalpy and specific heat values are listed for select temperatures in α and β phase regions.

5.7 Neumann-Kopp approximation for C_p evaluation

As not much data is available on thermal properties of advanced titanium alloys containing bcc transition elements, the measured specific heat values for Ti-5Ta-1.8Nb alloy are compared with the reported values for Ti-4Nb-4Zr alloy [16]. Besides, an attempt is also made to compare the present experimental values with the estimated ones using Neumann-Kopp (N-K) approximation which is given by Eq. (5.10) [23] and is shown in **Fig. 5.6**.

$$C_p^{\text{Ti-Ta-Nb}} = x_{\text{Ti}} C_p^{\text{Ti}} + x_{\text{Ta}} C_p^{\text{Ta}} + x_{\text{Nb}} C_p^{\text{Nb}} \quad (5.10)$$

Where x_{Ti} , x_{Ta} , and x_{Nb} are mole fractions of Ti, Ta, Nb in the alloy and C_p^{Ti} , C_p^{Ta} , C_p^{Nb} are heat capacities of Ti, Ta and Nb respectively. The input data for the C_p of pure elements are taken from the standard source [24].

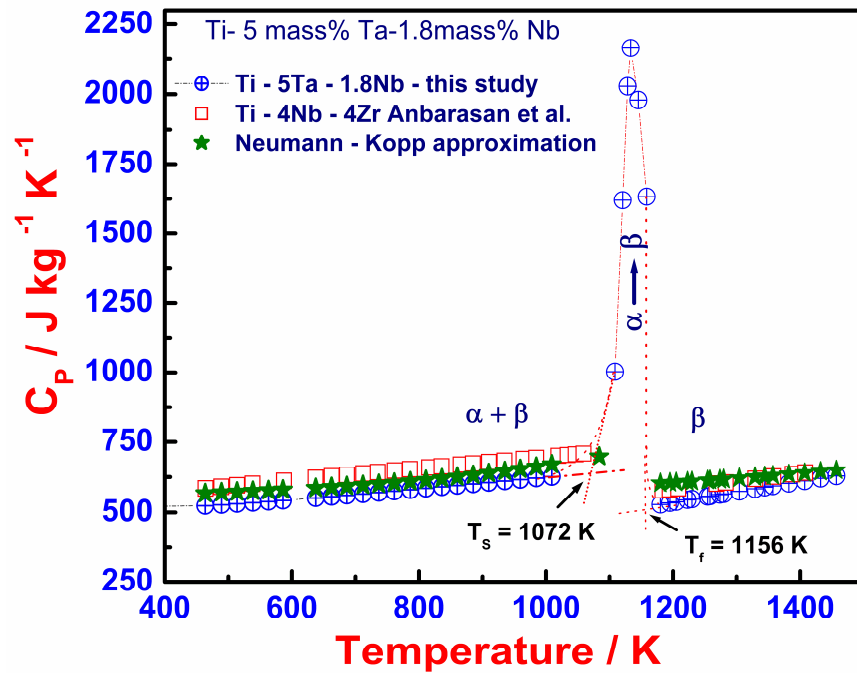


Figure 5.6 Variation of specific heat C_p with temperature for Ti-5 mass%Ta-1.8 mass% Nb alloy and its comparison with Ti-4Nb-4Zr alloy and the estimation using Neumann-Kopp approximation.

It is observed from **Fig. 5.6** that the measured values of specific heat C_p for Ti-5Ta-1.8Nb alloy compare well with the reported specific heat values for Ti-4Nb-4Zr alloy and also the estimated C_p by Neumann-Kopp (N-K) approximation is slightly higher than the experimental one; nevertheless its behavior is quite similar to the experimental trend.

Table 5.2 Experimental enthalpy, fit enthalpy and the derived specific heat data for Ti -5 mass% Ta-1.8 mass% Nb alloy.

T (K)	$\Delta^{\circ}H_T$ experimental (J.g ⁻¹)	$\Delta^{\circ}H_T$ Fit (J.g ⁻¹)	Deviation (%)	C_P° (J.kg ⁻¹ . K ⁻¹)	T (K)	$\Delta^{\circ}H_T$ experimental (J.g ⁻¹)	$\Delta^{\circ}H_T$ Fit (J.g ⁻¹)	Deviation (%)	C_P° (J.kg ⁻¹ . K ⁻¹)
<i>α-phase</i>					<i>$\alpha+\beta$ phase</i>				
298	0 (set)	0	-	520	1109	452	474	4.8	1003
464	84	86	2.4	524	1121	480	496	3.3	1620
514	109	112	2.7	531	1158	569	580	1.9	1633
539	132	126	-4.5	535	<i>β-phase</i>				
563	144	139	-3.5	539	1195	557	542	-2.7	534
586	156	151	-3.2	543	1205	557	548	-1.6	538
638	177	179	1.1	552	1223	575	557	-3.1	545
662	192	193	0.5	556	1230	585	561	-4.1	547
737	232	235	1.3	571	1258	617	577	-6.4	558
761	254	249	-1.96	575	1274	590	585	-0.8	564
811	273	278	1.8	585	1280	595	589	-1.0	566
860	302	307	1.6	595	1304	596	603	1.1	575
885	319	322	0.9	601	1344	603	626	3.8	589
935	345	352	2.0	611	1357	635	634	0	594
959	338	367	8.5	616	1382	705	649	-7.9	603
985	414	383	-7.5	621	1407	644	664	3.1	612
1009	410	398	-2.9	626	1432	670	679	1.3	620
1059	426	429	0.7	637	1457	690	695	0.7	629

The phase transformations that occur in the solid state represent the thermodynamic instabilities of the different phases present explicitly. While the thermodynamic properties decide the stability of the phases present, it is time scale of the transformation processes that attests the rate at which the transformation attains this true thermodynamic equilibrium, which decides the effective usefulness of the material as an engineering material. Hence a detailed investigation has been carried out to study the kinetics of $\alpha \leftrightarrow \beta$ phase transformation using differential scanning calorimetry in Ti-5 mass%Ta-1.8 mass% Nb alloy by varying the heating and cooling rate.

5.8 Differential Scanning Calorimetry result: Transformation peak profile and transformation temperatures

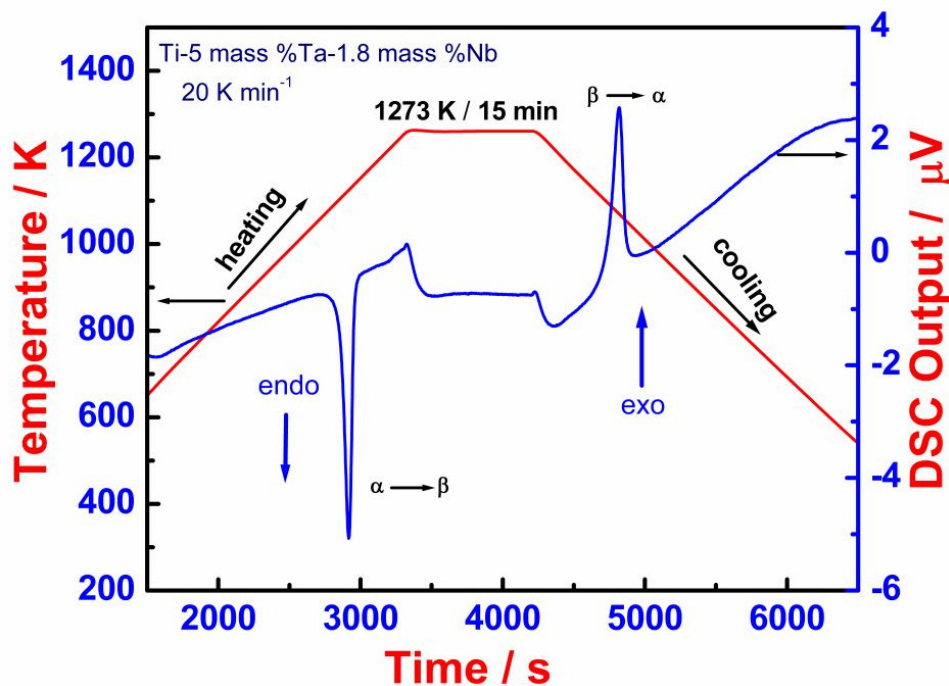


Figure 5.7 On-heating and cooling DSC profile for Ti-5 mass%Ta-1.8 mass%Nb alloy recorded at 20 K min⁻¹.

Fig 5.7 shows the on-heating and cooling DSC profile obtained at a scan rate of 20 K min⁻¹. The maximum temperature up to which the sample is heated is 1273 K and the sample is isothermally held at that temperature for 15 min before cooling to room temperature. In **Fig 5.7**, a clear and reasonably sharp endothermic peak during heating

and exothermic peak during cooling are observed which indicates the heat effect associated with the diffusional $\alpha \rightarrow \beta$ and $\beta \rightarrow \alpha$ phase transformations respectively. The start (T_s) and finish (T_f) temperature of $\alpha \leftrightarrow \beta$ transformation are clearly delineated from the above figure. During cooling, it is observed that the $\beta \rightarrow \alpha$ transformation occurs at kinetic undercooling of 30 K and this undercooling effect is more at higher cooling rate. It is also observed from **Fig 5.7** that the total peak area associated with the forward reaction is larger than the corresponding on-cooling transformation peak area. This kinetics asymmetry between the forward and reverse reaction is typical of measurements of phase transformation using scanning calorimetry, since the heat capacity difference between the participating phases increases reasonably with undercooling.

In **Fig. 5.8 (a-d)**, the DSC profiles in the transformation region alone for $\alpha \leftrightarrow \beta$ transformation for various heating and cooling rates in the range 3-99 K min^{-1} are shown as a collage.

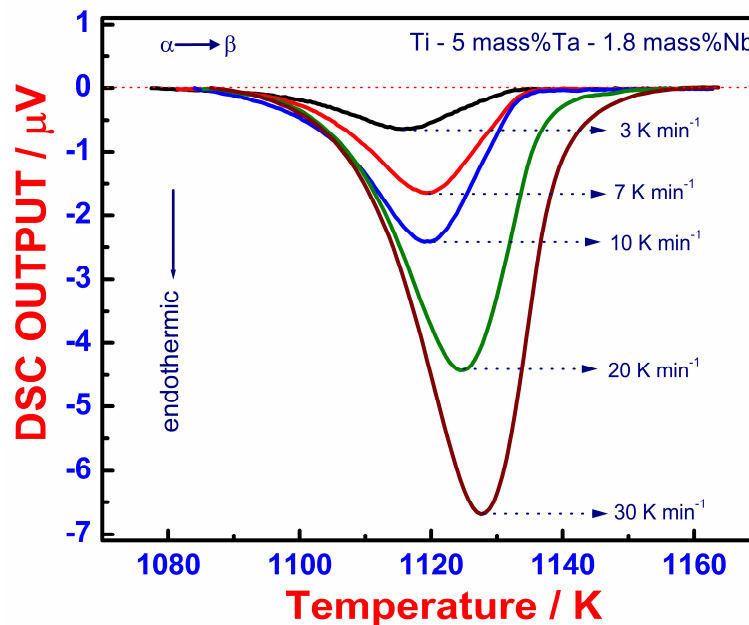


Figure 5.8 (a) The $\alpha \rightarrow \beta$ transformation peak profiles for slow heating rate.

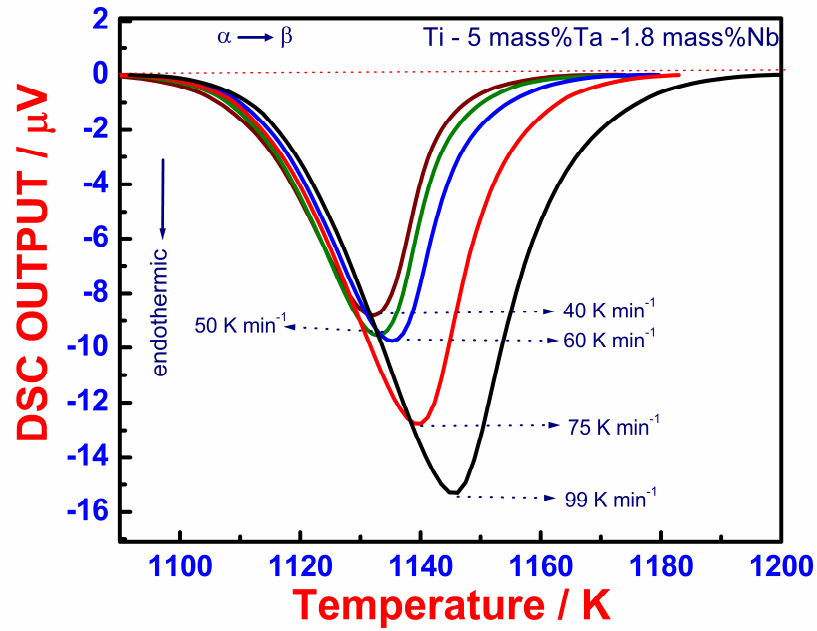


Figure 5.8 (b) The $\alpha \rightarrow \beta$ transformation peak profiles for high heating rate.

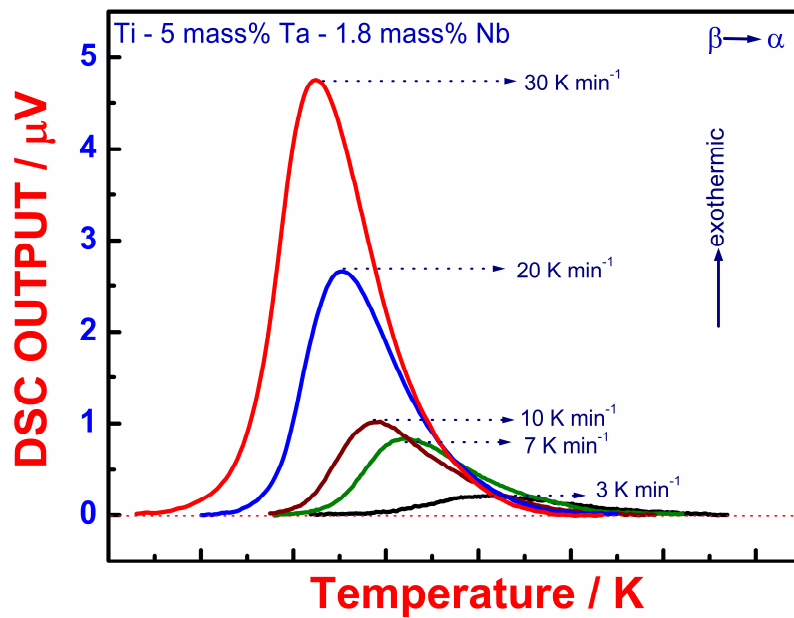


Figure 5.8 (c) The $\beta \rightarrow \alpha$ transformation peak profiles for low cooling rate.

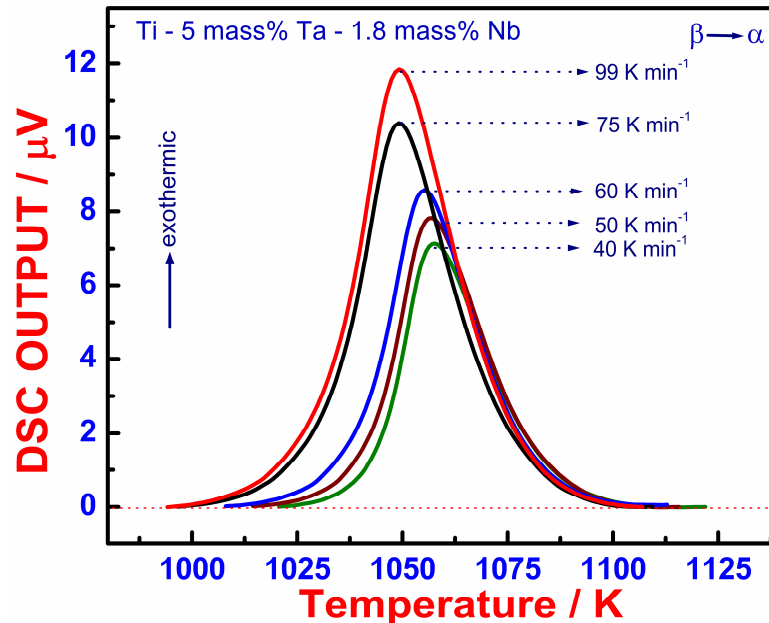


Figure 5.8 (d) The $\beta \rightarrow \alpha$ transformation peak profiles for high cooling rate

For the sake of clarity, the peak profiles at lower scan rate are separated from their higher scan rate counterparts. It is apparent from **Fig. 5.8**, that with increase in heating (or cooling) rates there is general increase (or decrease) in transformation arrest (T_s , T_p , T_f) temperatures. These temperatures and associated peak areas are listed in **Table 5.3**. Besides the latent heat or the enthalpy involved in the $\alpha \leftrightarrow \beta$ transformation ($\Delta^{\circ}H_{tr}^{\alpha \leftrightarrow \beta}$) is also listed in this table. The transformation enthalpy values are obtained by doing calibration with pure Ti under identical conditions. The observed heating and cooling rate dependencies of the start (T_s), peak (T_p) and finish (T_f) transformation temperatures for both $\alpha \rightarrow \beta$ and $\beta \rightarrow \alpha$ transformation is shown graphically in **Fig. 5.9**. It is apparent from the above **Fig. 5.9** that the transformation temperatures exhibit a non-linear variation with scan rate and this non-linearity is more pronounced for the transformation peak and finish temperatures. Consequently, the width of the transformation domain ($\Delta T_{tr} = T_f - T_s$) becomes more which implies kinetics induced expansion of ($\alpha + \beta$) two phase fields for high heating or cooling rates. It has also been observed from **Fig. 5.9**

that there is considerable degree of under cooling during $\beta \rightarrow \alpha$ transformation. This undercooling effect increases with increase in cooling rate.

The observed dependency of transformation arrest temperatures on the heating and cooling rate variation is inherent to the various nucleation and growth mechanism through which the transformation progresses. Since, a minimum time called incubation time is needed for the nucleation of any phase at any temperature that is greater than the equilibrium transformation temperature. Hence, by the time the system completes its incubation, its temperature is increased by the scanning heating rate to higher temperature or decrease by the scanning cooling rate to lower temperature.

Table 5.3 $\alpha \leftrightarrow \beta$ transformation temperatures for Ti-5mass%Ta-1.8mass%Nb alloy

Scan rate (K/min)	T _s (K)	T _P (K)	T _f (K)	Peak area ($\mu\text{V.s/mg}$)	Enthalpy $\Delta^\circ\text{H}_{\text{tr}}^{\alpha \leftrightarrow \beta}$ (J/g)
<i>$\alpha \rightarrow \beta$ transformation (heating)</i>					
3	1077	1116	1159	11.33	86.12
5	1079	1119	1160	11.35	80.18
7	1081	1119	1162	11.37	79.70
10	1084	1119	1163	11.61	76.66
20	1085	1124	1162	12.10	78.86
30	1087	1128	1164	12.60	79.47
40	1087	1132	1174	12.40	76.86
50	1089	1133	1175	12.52	83.28
60	1090	1135	1180	11.99	77.69
75	1090	1140	1183	11.76	77.14
99	1091	1146	1202	11.2	72.62
<i>$\beta \rightarrow \alpha$ transformation (cooling)</i>					
3	1154	1103	1063	-7.50	73.13
5	1150	1086	1060	-7.85	63.14
7	1144	1084	1055	-8.88	76.33
10	1138	1079	1055	-8.58	65.66
20	1130	1070	1040	-10.89	78.28
30	1127	1065	1026	-12.46	81.5
40	1122	1058	1021	-12.48	83.38
50	1116	1057	1014	-12.86	79.06
60	1113	1054	1007	-12.77	72.06
75	1109	1049	997	-12.36	80.32
99	1107	1049	994	-13.07	78.52

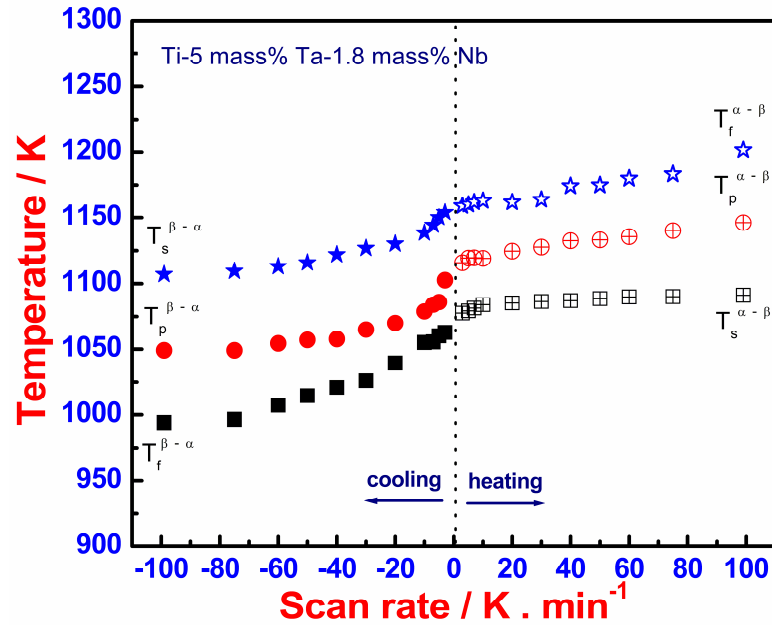


Figure 5.9 Graphical representations of heating and cooling rate variation of transformation start (T_s), peak (T_p) and finish (T_f) temperatures for Ti-5 mass% Ta-1.8 mass% Nb alloy

5.9 Kinetics of $\alpha \leftrightarrow \beta$ transformation

It is known that both $\alpha \rightarrow \beta$ and $\beta \rightarrow \alpha$ transformation are diffusive in nature for the entire range of heating and cooling rates (3-99 K min⁻¹) in the present study. As it is well known that the degree of transformation is equal to the fraction of heat absorbed or released, so the fractional extent of transformation $f(T)$ as a function of time or temperature at a constant scan rate can be calculated from the experimental DSC peak profile using the following relation [25]:

$$f(T) = \frac{\int_{T_s}^T y(T) dT}{\int_{T_s}^{T_f} y(T) dT} \quad (5.11)$$

$y(T)$ is the baseline compensated heat flux signal, measured as a function of T , in the range, $T_s \leq T \leq T_f$. The integral in the numerator stands for the partial area under the peak in the temperature domain $T_s - T$ and the denominator stands for the total peak area covering the entire transformation temperature range ($T_s - T_f$). The estimation of degree of transformation as a function of temperature using Eq. (5.11) is done by assuming that

the transformation is undergoing 100 % completion upon reaching T_f . But this is generally not the case especially in case of higher scan rates. This is due to the well-known kinetic lag.

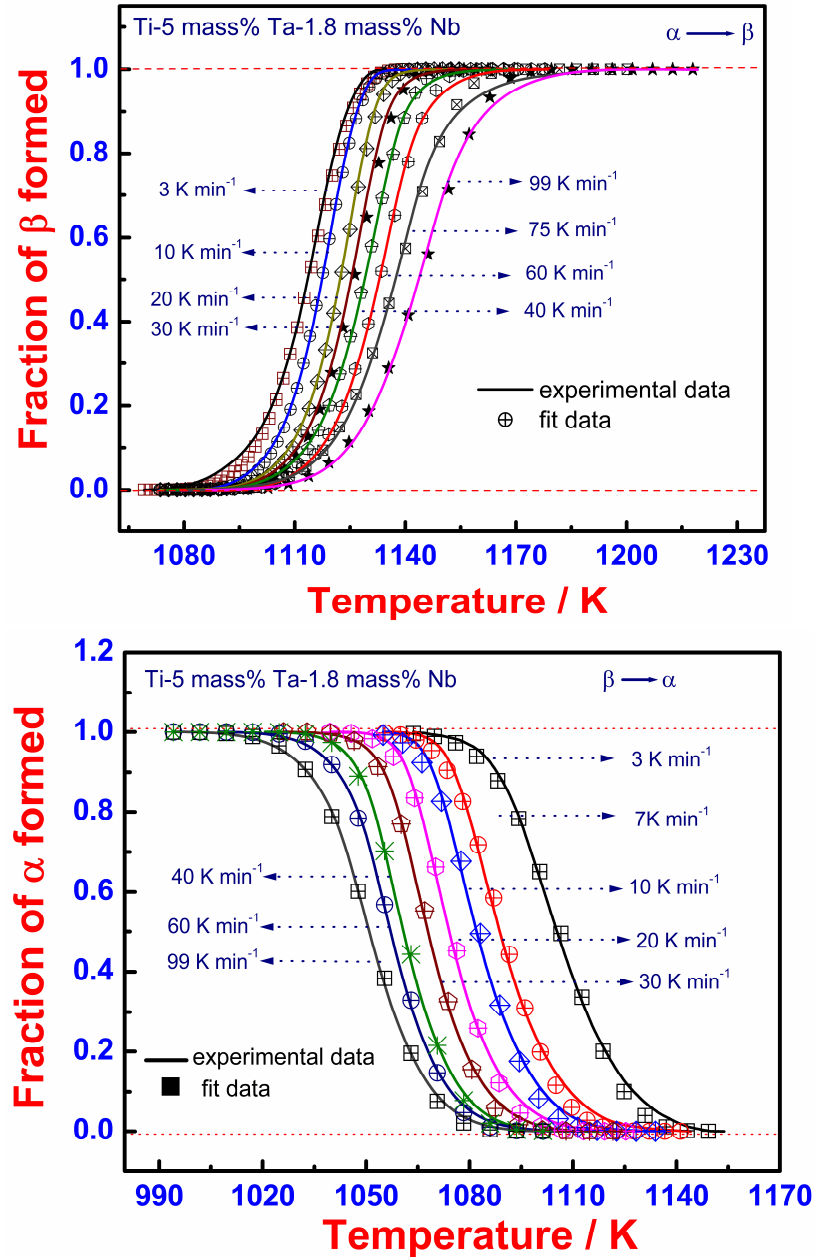


Figure 5.10 Experimentally obtained transformation plot for (a) $\alpha \rightarrow \beta$ transformation, (b) for $\beta \rightarrow \alpha$ transformation. The line stands for the experimental data, while the symbols are the non-isothermal KJMA fit.

The transformation plots for the $\alpha \rightarrow \beta$ and $\beta \rightarrow \alpha$ phase transformation obtained at various scan rates are presented in **Fig. 5.10(a) & (b)** respectively. It is observed from the figure that the fraction transformed curve for heating as well as cooling show sigmoidal behavior for the entire range of heating and cooling rates adopted in this study. In Ti-5Ta-1.8 Nb alloy the transformation takes place by the diffusion of Ta and Nb in titanium as in case of Ta diffusion in Ti-Ta alloys (**Chapter -4**). It is well known that the kinetics of diffusional transformation involving distinct nucleation and growth steps can be analysed by employing the Kolmogorov-Johnson-Mehl-Avrami (KJMA) formalism [26-28]. In many recent publications, especially by Sha and co-workers the kinetics of diffusional phase transformation in titanium base systems is described using simple KJMA formalism [29-32]. Similar to the analysis of kinetics of $\alpha \leftrightarrow \beta$ phase transformation in Ti-Ta alloys as explained in **section 4.7 of chapter-4** using non-isothermal version of KJMA model under site saturation condition, the kinetics of $\alpha \leftrightarrow \beta$ phase transformation in Ti-5Ta-1.8Nb alloy has been modeled using non-isothermal KJMA model. The selection of the above formalism to illustrate the kinetics of transformation is explained elaborately in **section 4.7 of chapter-4**. The non-isothermal version of KJMA model under site saturation condition can be written as follows.

$$f_{\beta}^{\text{tr}}(T) = 1 - \exp(-k_0^n \exp\{-nQ_{\text{eff}}/RT\} (R(T-T_s)^2/\phi Q_{\text{eff}})^n) \quad (5.12)$$

where, Q_{eff} is the effective or apparent activation energy for the overall transformation, k_0 = pre exponential factor and n = the avrami or transformation exponent which gives information on the combined dimensionalities of nucleation and growth. The fitting of experimentally obtained fraction transformed curve using the Eq. (5.12) is done by means of a standard non-linear optimization method. The resulting fit parameters Q_{eff} , n , k_0 are listed in **Table 5.4**.

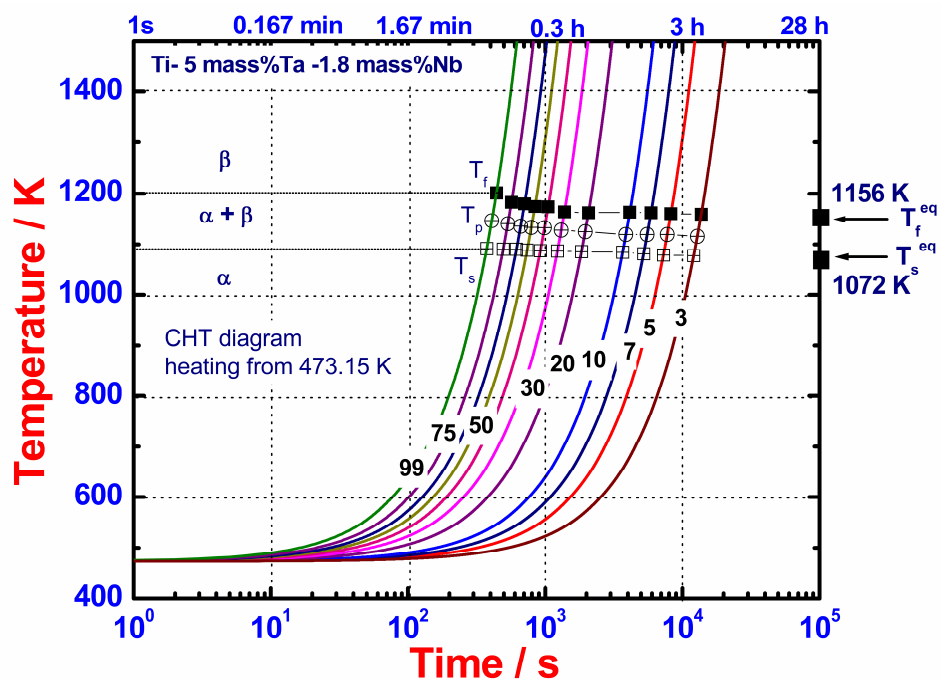
Table 5.4 Kinetics parameters for $\alpha \leftrightarrow \beta$ phase transformation obtained by fitting experimental data to non-isothermal KJMA model.

<i>$\alpha \rightarrow \beta$ transformation</i>				
Heating rate (K min ⁻¹)	n	Q _{eff} (kJ mol ⁻¹)	k ₀ × 10 ¹³ (s ⁻¹)	R ² value for the fit
3	1.51	290	1.81	0.99708
5	1.95	279	1.24	0.99987
7	1.69	278	1.85	0.99956
10	1.79	280	2.93	0.99983
20	1.91	284	6.74	0.99987
30	1.82	281	6.74	0.99982
40	1.72	283	8.05	0.99976
50	1.70	282	8.65	0.99967
60	1.65	281	8.75	0.99944
75	1.38	282	8.93	0.99985
99	1.32	281	8.94	0.99896
<i>$\beta \rightarrow \alpha$ transformation</i>				
Cooling rate (K min ⁻¹)	n	Q _{eff} (kJ mol ⁻¹)	k ₀ × 10 ⁴ (s ⁻¹)	R ² value for the fit
3	2.22	81	0.119	0.99816
7	3.33	91	0.856	0.9971
10	3.63	95	2.28	0.9971
20	3.8	98	7.20	0.99816
30	3.99	90	3.84	0.99928
40	3.99	100	17.0	0.9994
50	3.9	106	50.69	0.99956
60	3.72	106	61.0	0.99956
75	3.61	102	53.7	0.9996
99	3.4	108	140.0	0.9996

It can be seen from **Table 5.4** that the effective activation energy Q_{eff} for on-heating $\alpha \rightarrow \beta$ phase transformation is varying between 280-300 kJ mol⁻¹ which may possibly be due to the volume diffusion of Ta and Nb in the Ti matrix. Also this high value of activation energy is observed in case of Ta diffusion in α -Ti and self diffusion in α -Ti [33, 34]. The Avrami exponent (n) varies between 1.18-1.95. The low value for the transformation exponent is due to the growth impingement effects strongly operating under site-saturation nucleation conditions. The values of Q_{eff} for $\beta \rightarrow \alpha$ phase transformation are lower than their heating counterparts and it varies between 80-110

kJ mol^{-1} which may possibly be attributed to the grain boundary diffusion. In literature, Q_{eff} of about $90\text{-}92 \text{ kJ mol}^{-1}$ has already been attributed to $\beta \rightarrow \alpha$ transformation in some titanium alloys [35-37]. The transformation exponent (n) during $\beta \rightarrow \alpha$ transformation assumes a higher value of nearly 3, which implies a two dimensional growth habit with 3D nucleation, and with little blocking of the growth front by hard impingement considerations.

Based on the experimentally observed transformation temperatures, the continuous heating transformation (CHT) diagram for the $\alpha \rightarrow \beta$ transformation and continuous cooling transformation (CCT) diagram for the $\beta \rightarrow \alpha$ transformation have been constructed and are shown in **Fig. 5.11 (a) & (b)** respectively. The CHT and CCT diagram can be obtained from the KJMA model given in Eq. (5.12) which can in principle be solved to give (T,t) coordinate pairs for a chosen temperature and fixed fraction transformed, under a set of known kinetic parameters which are in turn obtained by fitting the experimental data to Eq. (5.12).



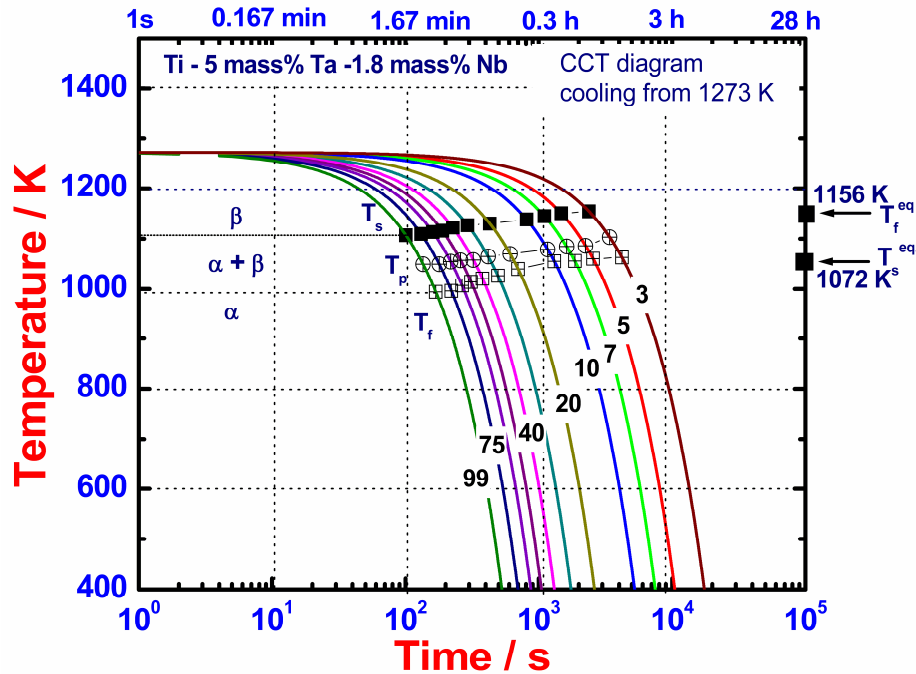


Figure 5.11 (a) The continuous heating transformation (CHT) diagram for $\alpha \rightarrow \beta$ and **(b)** continuous cooling transformation (CCT) diagram for $\beta \rightarrow \alpha$ transformations obtained in the present study for Ti-5mass%Ta-1.8 mass% Nb alloy.

5.10 Microstructural evolution during $\beta \rightarrow \alpha$ transformation

5.10.1 Microstructural changes during cooling from high temperature β - phase field

Microstructural characterization of the alloy has been carried out after the cooling cycle of DSC runs in order to understand the effect of cooling rate on microstructural evolution. **Fig. 5.12** shows the room temperature microstructure of samples of Ti-5 Ta-1.8 Nb alloy after continuous cooling from high temperature β phase field at different rate. It is observed that the microstructure consists of large equiaxed β grains, with continuous layer of α along the β grain boundary known as the grain boundary α (GB α). Also within the prior β grains, a colony microstructure with lamellar morphology termed as transformed β structure is observed at all cooling rates. DSC cooled samples at some selected cooling rates such as 20, 40, 50, 75 and 99 K min^{-1} are characterized by Transmission Electron Microscopy. The TEM micrographs of the alloy cooled at 20, 40,

50, 75 and 99 K min⁻¹ is shown in **Fig. 5.13 (a-e)** respectively. Selected Area Diffraction (SAD) patterns for a sample cooled at 99 K min⁻¹ is shown in **Fig. 5.13 (f & g)** and **Fig. 5.13 (h)** shows the Energy Dispersive Spectra (EDS) collected from alternate lamellae of the alloy cooled at 99 K min⁻¹.

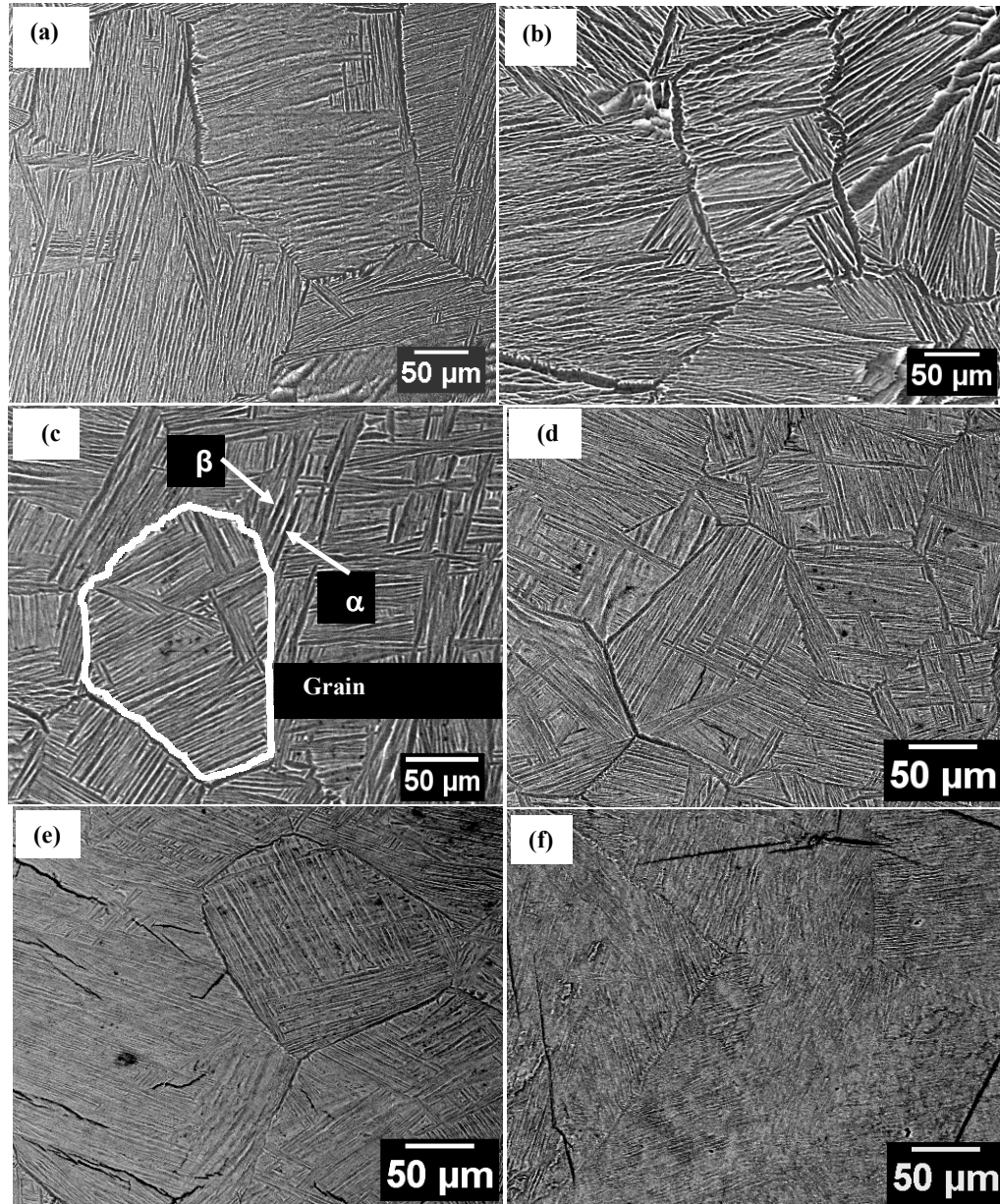
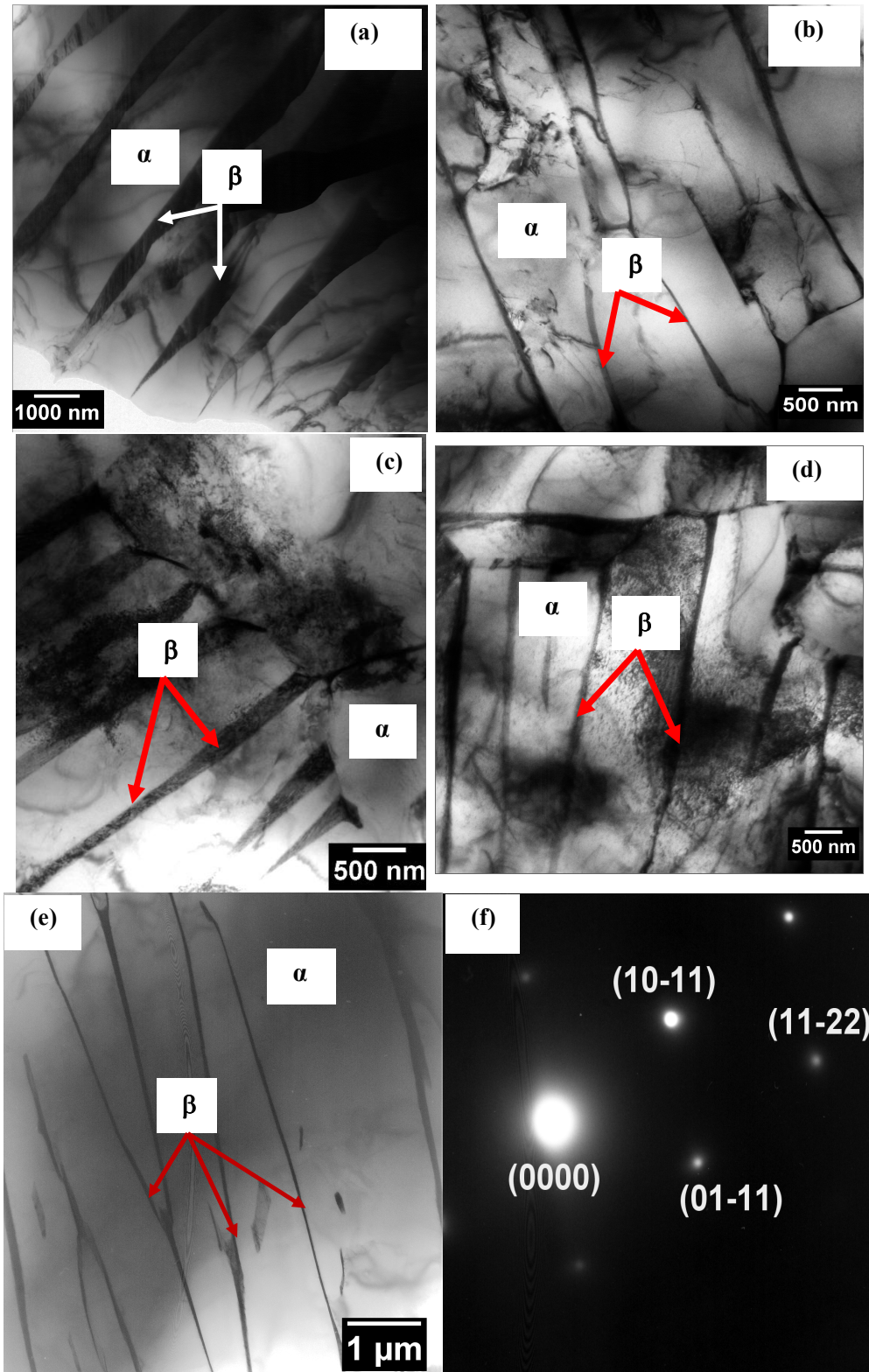


Figure 5.12 SEM micrographs showing lamellar morphology of the products of $\beta \rightarrow \alpha$ transformation at different cooling rates such as (a) 5, (b) 10, (c) 20, (d) 40, (e) 75 and (f) 99 K min⁻¹. Decrease in lamellae size with increase in cooling rate is evident in the micrographs.



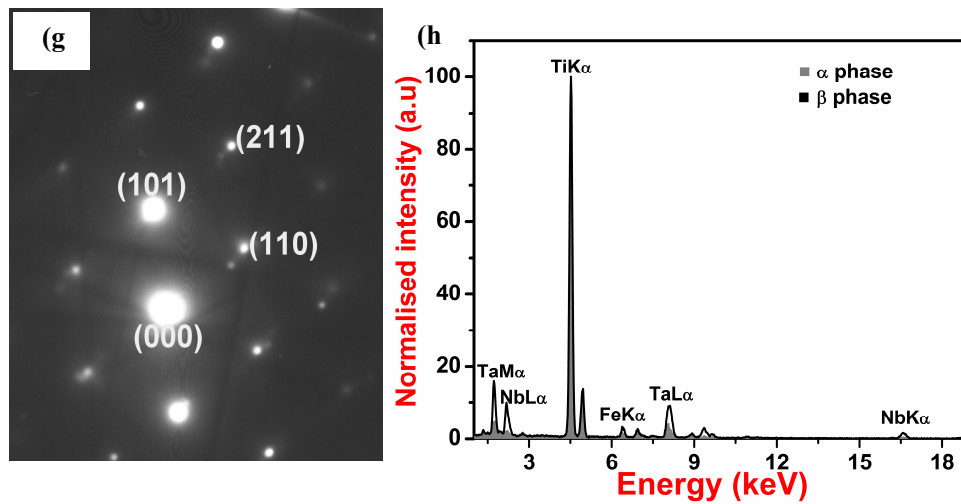


Figure 5.13 (a-e) TEM micrographs of alloy cooled at (a) 20, (b) 40, (c) 50, (d) 75, (e) 99 K min⁻¹ showing alternate lamella of α and β phases, **(f) & (g)** represent the SAD pattern for the sample cooled at 99 K min⁻¹ corresponding to α - hcp and β - bcc phases along $[11\bar{2}3]$ and $[\bar{1}11]$ zone axis respectively, **(h)** represents the EDS spectrum showing the enrichment of Ta and Nb in the β lamella as compared to α lamella.

From **Fig. 5.13 (a-e)**, it is observed that a lamellar morphology is obtained at all the above cooling rates. The SAD pattern (**Fig. 5.13(f) & (g)**) collected from the bright and dark lamellae of the sample cooled at 99 K min⁻¹ confirmed that they are α -hcp and β -bcc phases respectively. The EDS spectra (**Fig. 5.13 (h)**) collected from alternate lamellae of the alloy cooled at 99 K min⁻¹ shows a higher amount of Ta and Nb in β phase compared to α phase. The observed lamellar α + β microstructure (**Fig. 5.12 & 5.13**) at all cooling rates suggests that the cooling rates employed in the present study are rather low thereby promoting primarily a diffusional Widmanstatten transformation of the high temperature β phase.

The effect of cooling rate on evolution of microstructure has been studied systematically through measurements of different microstructural parameters such as size of α and β lamella, α colony, GB α size and volume fraction of α and β phases. The size of α lamellae is measured from SEM micrographs, while that of β lamellae is measured from the TEM micrographs due to their fine size. **Fig. 5.14** shows the

variation of α , β lamella size and grain boundary α thickness as a function of cooling rate.

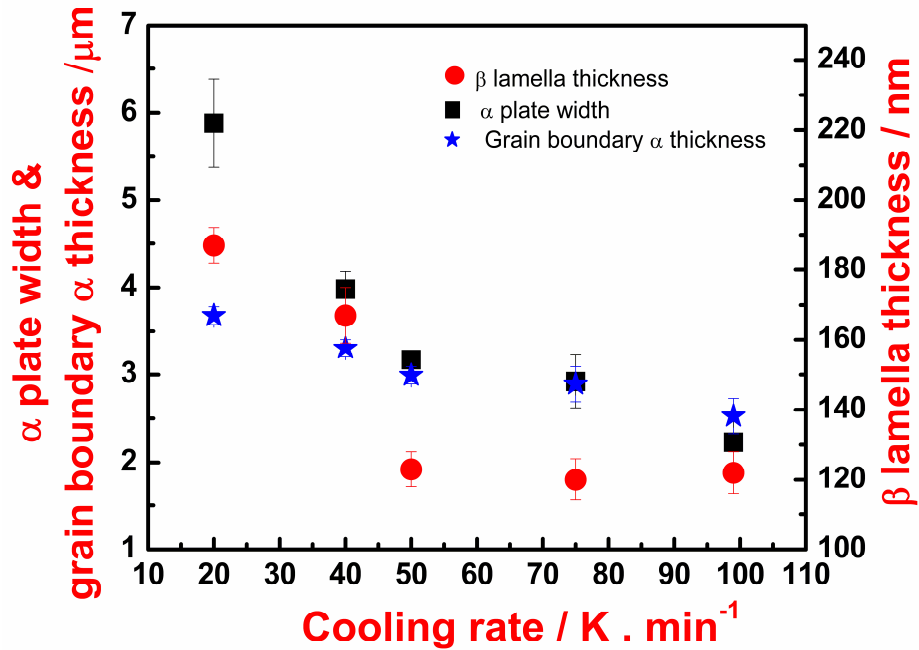


Figure 5.14 Variation of α and β lamella size and grain boundary α thickness as a function of cooling rate.

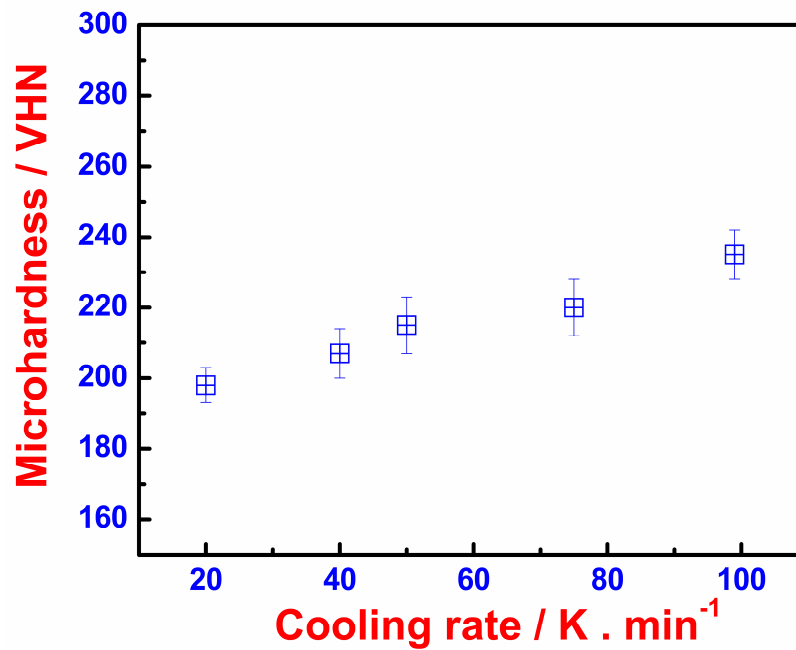


Figure 5.15 Effect of cooling rate on microhardness of $\beta \rightarrow \alpha$ transformation microstructure.

It is observed from the above figure that the width of both α and β lamellae decreases as the cooling rate increases. This is accordance with literature, where it is reported [38, 39] that the lamellar microstructure may vary from aligned α colonies to basket weave α with increase in cooling rate. The decrease in α lamella size is reflected in the microhardness of transformation microstructure which is shown in **Fig. 5.15**. The microhardness value increases with increase in cooling rate. The decrease in lamella size is due to the fact that at higher cooling rates the undercooling effect is more, which increases the nucleation kinetics, rather than the growth kinetics. Also, with increase in cooling rate there is insufficient time for the diffusion controlled thickening of the α and β lamellae. Hence the GB α and α lamellae that nucleate at higher cooling rates are finer. The volume fraction of α and β phases retained in the room temperature microstructure are measured from BSE images of SEM as a function of cooling rate, which is plotted in **Fig. 5.16**.

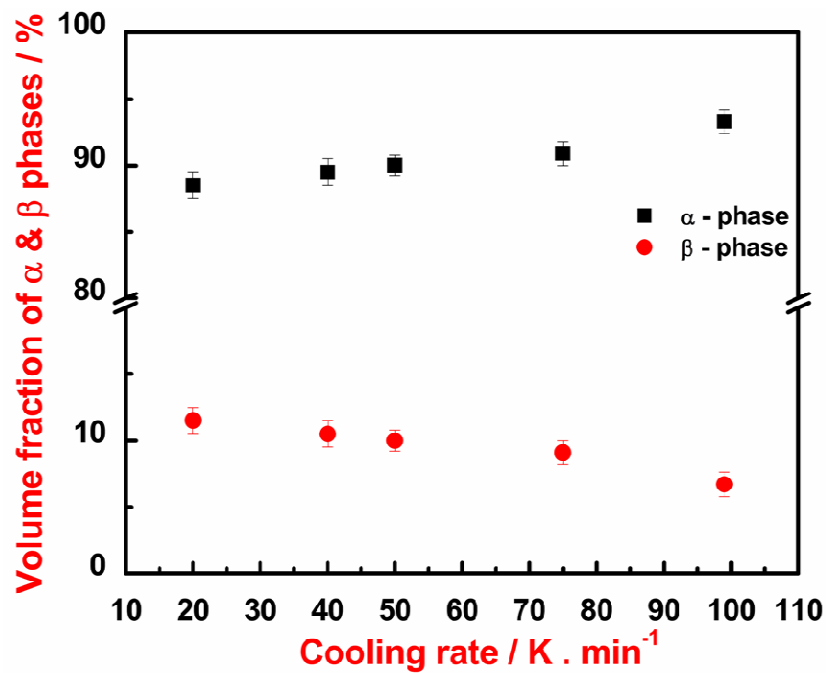


Figure 5.16 Variation of volume fraction of α and β phase as a function of cooling rate.

It is found that the volume fraction of retained β is low at all cooling rates and does not vary significantly. However, within the small variations, it is observed that there is a decreasing trend in the volume fraction of retained β with increase in cooling rate. It should be mentioned here that the calculated volume fraction of α phase corresponds only to the matrix α phase forming due to the primary transformation of β phase on cooling from the β phase field. The concentration of Ta and Nb in α and retained β phases are also analyzed as a function of cooling rate using EDS analysis in TEM. **Fig. 5.17** displays the variation of Ta equivalent of α and retained β phases as a function of cooling rate.

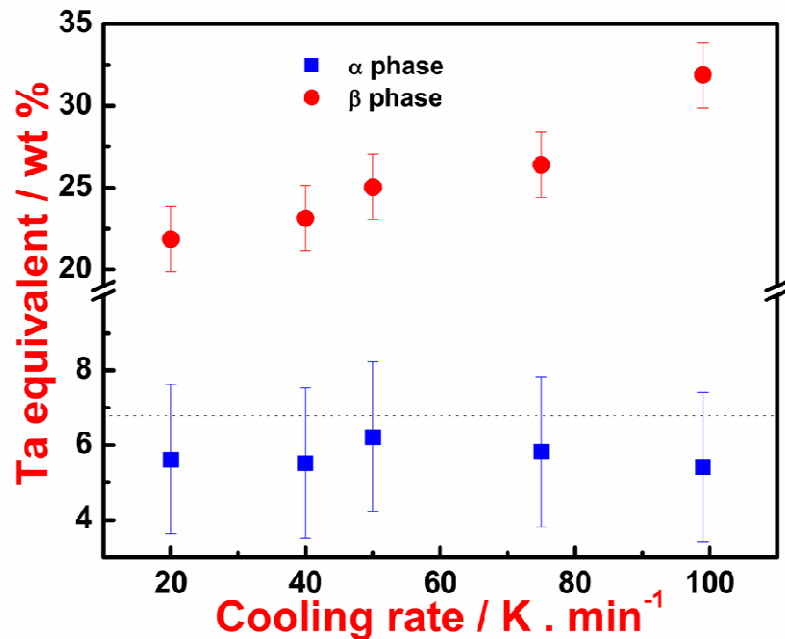


Figure 5.17 Variation of Ta equivalent of α and β phases as a function of cooling rate and the dotted line parallel to X-axis represents the alloy composition.

In the above figure, the concentrations of Ta and Nb in α and β phases has been expressed in terms of Ta equivalent, as both Ta and Nb are isomorphous β phase stabilizers. The Ta equivalent can be calculated based on the β_c (the minimum critical β stabilizer concentration for retention of 100 % β at room temperature) value of Ta and

Nb. The β_c value for Ta and Nb are 45.45 wt% and 35.71 wt% respectively. Hence the Ta equivalent can be expressed by the following expression.

$$\begin{aligned} \text{Ta equivalent} &= \text{wt\% Ta} + \{\beta_c(\text{Ta}) / \beta_c(\text{Nb})\} * \text{wt\% (Nb)} \\ &= \text{wt\% Ta} + 1.27 * \text{wt\% (Nb)} \end{aligned} \quad (5.13)$$

In general as the cooling rate increases, the time available for the repartitioning of solutes between the constituent phases decreases and the concentration of Ta and Nb in retained β phase is expected to decrease. However in the present study, it is observed that the concentration of Ta and Nb (expressed in terms of Ta *equivalent*) in the retained β phase increases with cooling rate. At the same time the concentrations of Ta and Nb in the α phase is within the limits of experimental scatter and hence does not show any significant variation with cooling rate. The error in the estimation of composition of the constituent phases is ~2%.

It should be mentioned that the β phase always shows an enrichment of the β stabilizers not only Ta and Nb but also Fe which is an impurity in the alloy. However, due to the low level of Fe (~300ppm) in the alloy, it has been ignored and not considered for evaluation of the composition of α and β phases. Also due to fine size and possible error due to overlap of α either above or below it in the thin foils, the composition of β phase may be slightly underestimated than that of α phase. It is also clearly observed from the above figure that the Ta equivalent of β phase is always higher than that of the alloy composition (Ta equivalent = 6.8) and that of α phase is lower.

The above observations have been rationalized from the knowledge of $\beta \rightarrow \alpha$ transformation temperature domains of the alloy at different cooling rates. It is discussed in section 5.8 that the transformation starts (T_s) and finish (T_f) temperatures decrease as the cooling rate increase. It is also to be noted that the finish temperature

(T_f) does not correspond to 100% α phase formation, but has been normalized for a microstructure of predominantly α phase with a small amount of retained β phase. The decrease of both T_s and T_f with increase in cooling rates implies that for low cooling rates the $\beta \rightarrow \alpha$ transformation domain lies at high temperature regime which shifts to lower temperature regime as the cooling rate increases. It is also known that [40, 41], when an isomorphous alloy is cooled continuously from high temperature single phase field, through a low temperature two phase field, the composition of the two phases at any temperature deviates from the equilibrium solvus lines. As a result, both α and β solvus lines shift towards lower compositions and the magnitude of shift increases at lower temperatures due to sluggish kinetics of diffusion. This has been schematically illustrated in Fig. 5.18.

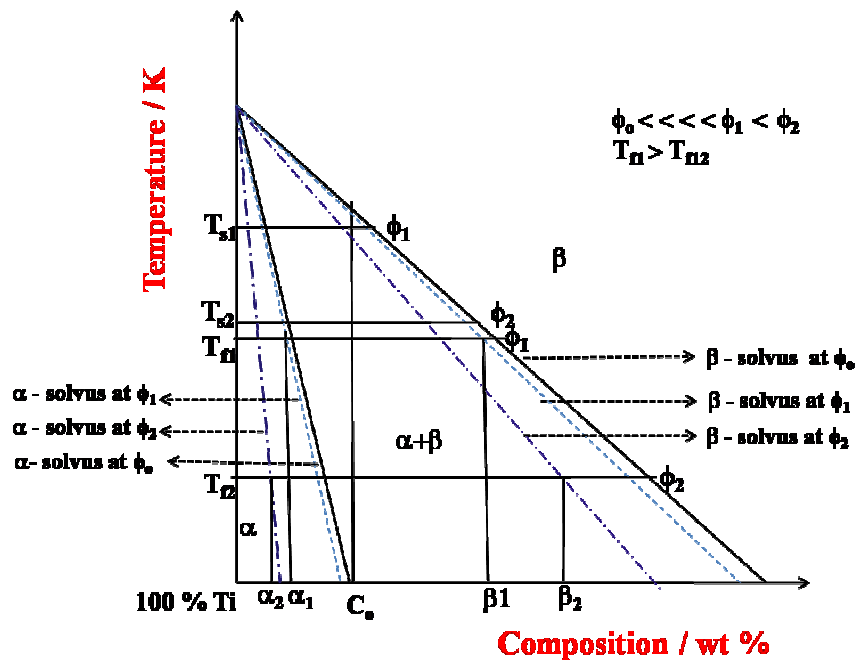


Figure 5.18 Schematic illustration of the effect of cooling rate in shifting of α and β solvus lines under non equilibrium conditions

The equilibrium solvus lines correspond to isothermal conditions ($\phi_0 \approx 0 \text{ K min}^{-1}$). The transformation start and finish temperatures of the alloy is high (T_{s1} and T_{f1}) for a low

cooling rate (ϕ_1) and the composition of α and β phases are represented as α_1 and β_1 respectively at T_{f1} . At a higher cooling rate (ϕ_2), the transformation start and finish temperatures of the alloy are lowered (T_{s2} and T_{f2}) and the composition of α and β phases are represented as α_2 and β_2 respectively at T_{f2} . Due to this difference in the finish temperatures, it is observed that β_2 would always be higher than β_1 and α_2 would always be lower than α_1 . At intermediate cooling rates, the composition of α and β phases would be between α_1 and α_2 , β_1 and β_2 respectively corresponding to their finish temperatures. The composition as well as the volume fraction of α and β phases measured in this study corresponds to the finish temperature for each cooling rate.

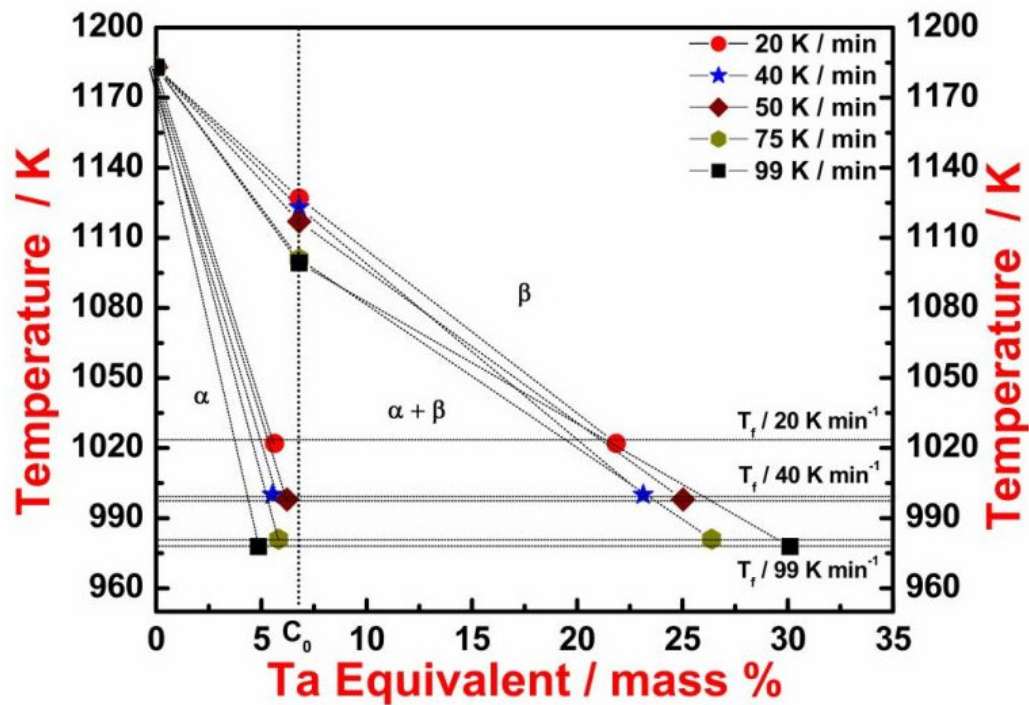


Figure 5.19 Variation of composition of α and β phases at transformation finish (T_f) temperature with cooling rate in Ti-5mass%Ta-1.8 mass% Nb alloy.

In **Fig. 5.19** the composition of α and β phases at the transformation finish temperatures is shown, when the Ti-5Ta-1.8Nb alloy is cooled from the single β phase field through the $\alpha+\beta$ phase field at different cooling rates. When the alloy is cooled

from the β phase field, the concentration of both α and β phases increases as temperature decreases. However, due to the reasons explained above, the α and β solvus lines would be shifted towards lower concentrations of Ta equivalent with increase in cooling rate as shown in **Fig. 5.18**. Hence, the composition of retained β phase at a low finish temperature of the transformation at a cooling rate of 99 K min^{-1} is higher than at a cooling rate of 20 K min^{-1} whose transformation finish temperature is high. This description clearly explains the observed behavior of increase in composition of β phase with cooling rate. The limitation in the present study is that, due to availability of only partial information on this ternary Ti-Ta-Nb phase diagram [42], the composition of α and β phases are expressed as Ta equivalent to superimpose and extrapolate to a pseudo binary diagram. However, for the purpose of understanding the observed trend in microchemical variations, this approach can be justified.

As seen from the experimentally measured composition (**Fig. 5.17**), the compositional changes in β phase with cooling rate manifests itself significantly than that in α phase. This is due to the sluggish diffusion of Ta and Nb in α phase as compared to the β phase at any temperature [43, 44]. Also the solubility of Ta and Nb in α phase is much lower than that of β phase at any temperature.

5.10.2 Secondary transformations of high temperature β phase on continuous cooling

A detailed TEM observation is made on the microstructure of the alloy cooled at 20, 40, 50, 75 and 99 K min^{-1} and the microstructure of the alloy cooled at 40 K min^{-1} is shown in **Fig. 5.20**. Bright Field (BF) image (**Fig. 5.20(a)**) of the same shows a lamellar $\alpha+\beta$ microstructure. Analysis of the SAD pattern from this region given in **Fig. 5.20(b)** confirms the presence of α phase along $[\bar{1}10\bar{1}]$ zone axis. From the Dark Field (DF) image acquired with $(0\bar{1}\bar{1})_{\alpha}$ reflection as shown in **Fig. 5.20(c)**, it is observed that

within the β lamella some regions are highlighted. This suggests the decomposition of the primary β phase to alternate lamellae of α and β phases.

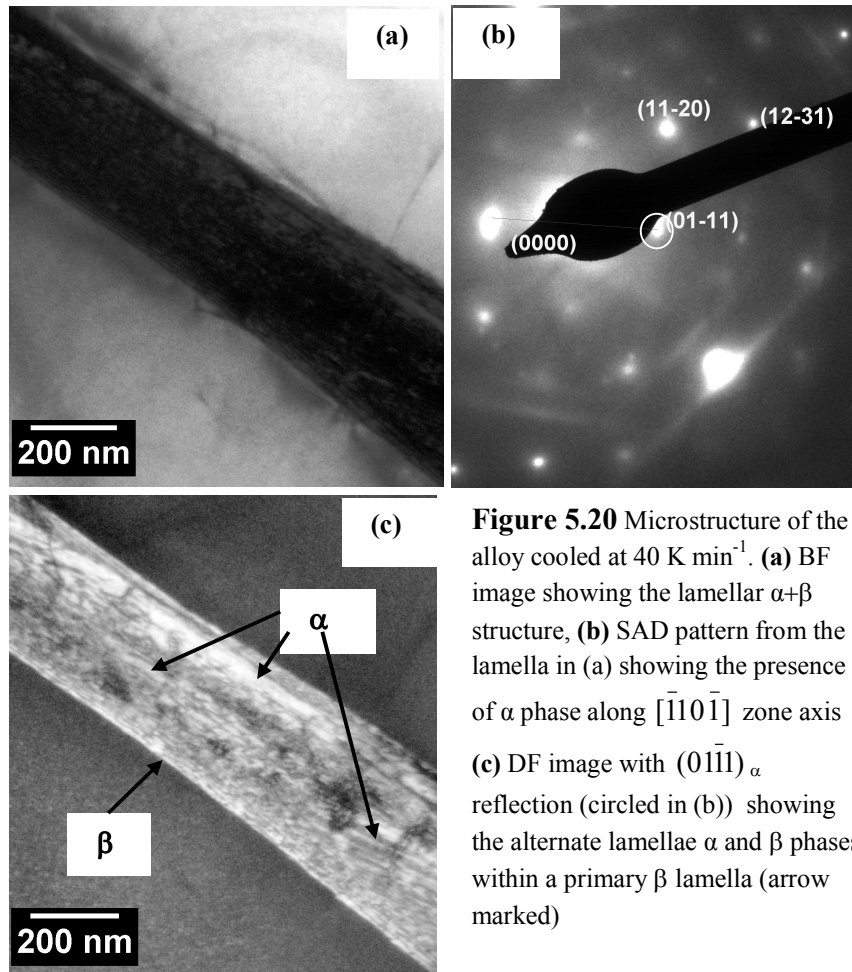


Figure 5.20 Microstructure of the alloy cooled at 40 K min^{-1} . **(a)** BF image showing the lamellar $\alpha+\beta$ structure, **(b)** SAD pattern from the β lamella in (a) showing the presence of α phase along $[\bar{1}10\bar{1}]$ zone axis **(c)** DF image with $(0\bar{1}1)_\alpha$ reflection (circled in (b)) showing the alternate lamellae α and β phases within a primary β lamella (arrow marked)

Fig. 5.21 shows the DF image of microstructure of the alloy cooled at 20, 50 and 75 K min^{-1} . It is observed that the regions inside the β lamella is highlighted suggesting the decomposition of primary β phase into lamellar $\alpha+\beta$ structure. From these observations, it can be implied that the cooling rates from 20 to 75 K min^{-1} are low enough to promote the precipitation of α phase within the primary β phase through a diffusional transformation.

In **Fig. 5.22**, a detailed TEM characterization of the alloy cooled at 99 K min^{-1} is shown. **Fig. 5.22 (a)** corresponds to the BF image of the alloy cooled at 99 K/min . It

shows the presence of a mottled contrast within the β lamella. Analysis of the SAD pattern from this region in **Fig. 5.22 (b)** shows the presence of β phase along $[113]$ zone axis. Analysis of the extra reflections in the SAD pattern confirmed that they belong to the hexagonal ω phase along $[\bar{1}213]$ zone axis. **Fig. 5.22 (c)** shows the key to the SAD pattern. DF image (**Fig. 5.22 (d)**) with $(10\bar{1}0)_{\omega}$ reflection clearly highlights fine ellipsoidal particles of ω phase within retained β . Examination of few other regions showed the presence of fine plates within the retained β lamellae as shown in **Fig. 5.22 (e)**. Analysis of the SAD pattern from this region (**Fig. 5.22 (f)**) indicated that the plates possess an orthorhombic structure, which could be the orthorhombic martensite forming in β rich Ti alloys [45, 46]. These observations suggest that a cooling rate of 99 K min^{-1} is high enough to induce the secondary diffusionless transformations within the primary β phase [47].

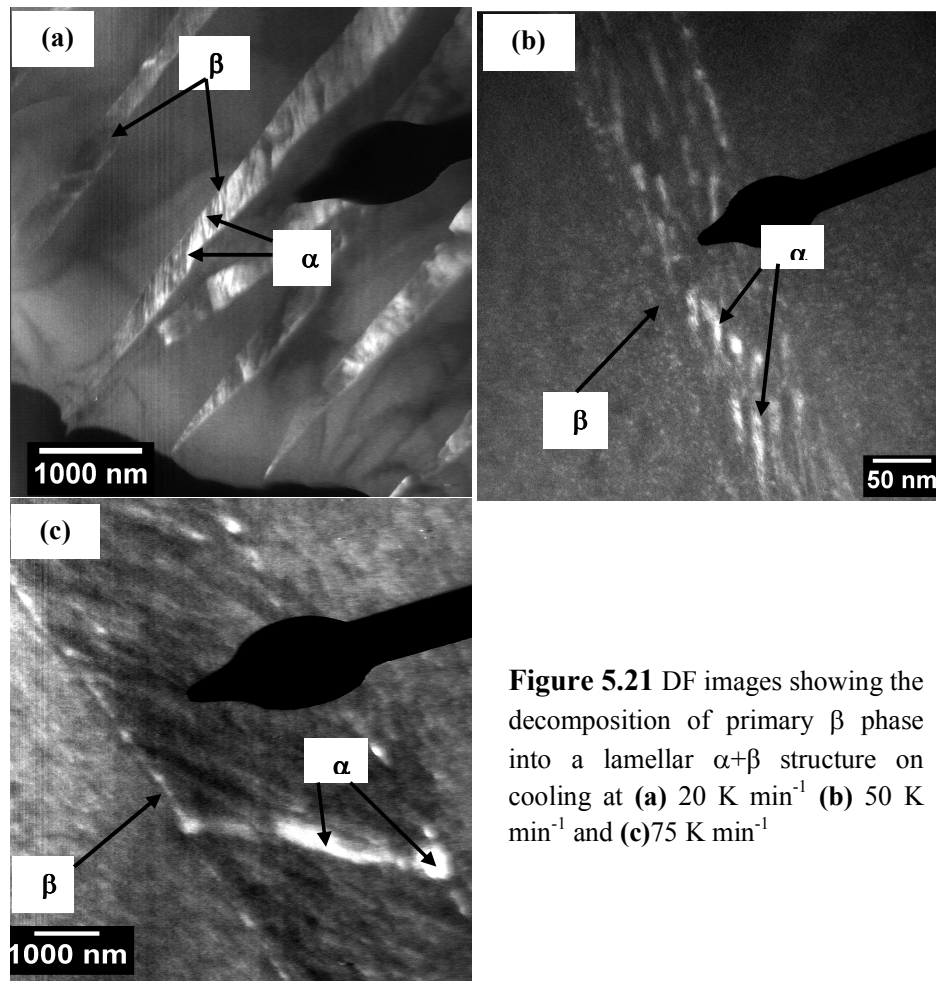


Figure 5.21 DF images showing the decomposition of primary β phase into a lamellar $\alpha+\beta$ structure on cooling at (a) 20 K min^{-1} (b) 50 K min^{-1} and (c) 75 K min^{-1}

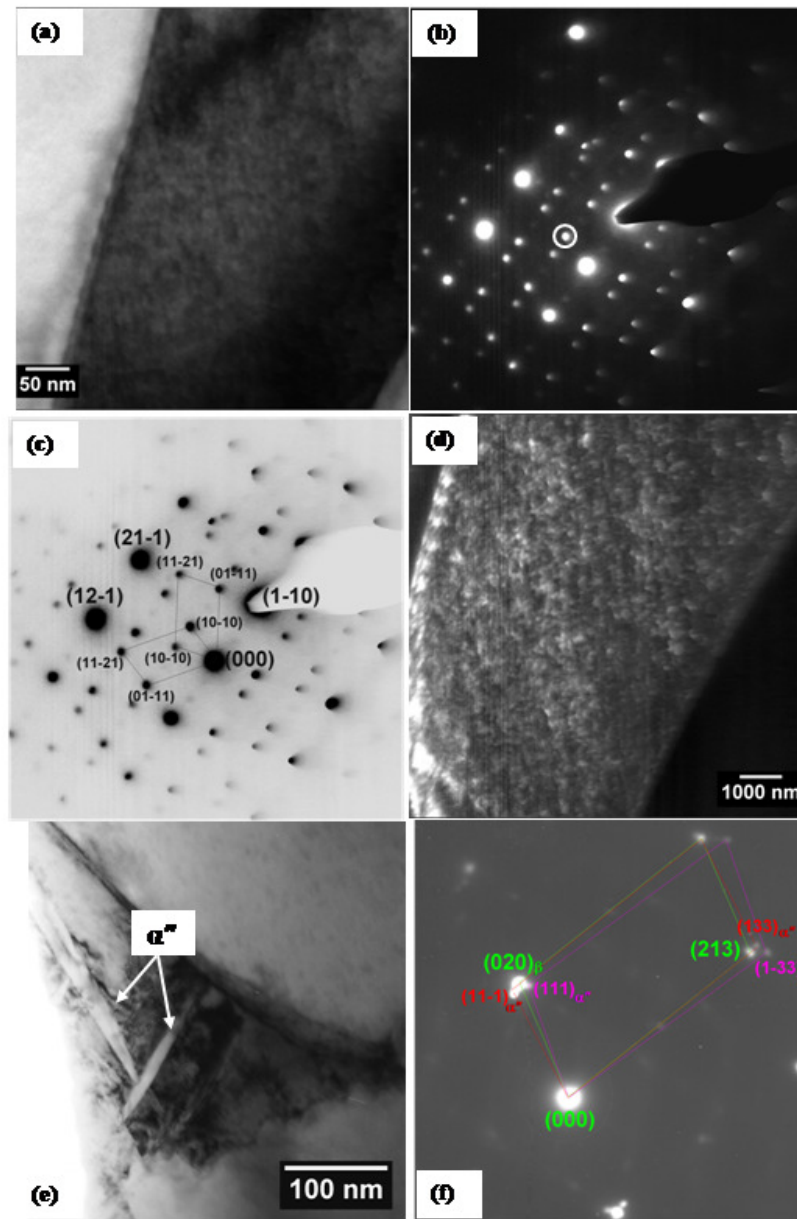


Figure 5.22 (a) BF image of β lamella of the alloy cooled at 99K min^{-1} showing a mottled contrast (b) & (c) SAD pattern and its key confirming the presence of two different variants of ω along $[\bar{1}2\bar{1}3]$ zone axis; (d) DF image taken with $(10\bar{1}0)_{\omega}$ reflection (circled in (b)) showing fine ω particles; (e) BF image of β lamella with fine plate like features within it and (f) SAD pattern confirming the presence of two different variants of face centered orthorhombic martensite α'' along $[3\bar{2}1]$ and $[3\bar{1}2]$

It is well known that, in titanium alloys both the cooling rate and the concentrations of the solutes [48, 49] dictate the mode of transformation either

diffusional resulting in formation of equilibrium α and β phase or the diffusionless transformation resulting in martensites (α' , α'' and ω). It is observed that at cooling rates from 20 to 75 K min⁻¹, the primary β decomposes into fine $\alpha+\beta$ structure through a diffusional transformation, while at a cooling rate of 99 K min⁻¹, the β phase undergoes a diffusionless transformation resulting in the formation of α'' and ω phases. Hence, in the present study, the high compositional enrichment of β phase during continuous cooling at 99 K min⁻¹ has been favourable for the transformation of β phase to orthorhombic martensite (α'') and omega (ω) phases. This is in accordance with literature, where the formation of orthorhombic martensite and omega phases is reported [46, 50] in Ti and Zr alloys which are fairly rich in β stabilizers. The formation of ω phase in this alloy at this cooling rate along with orthorhombic martensite confirms unambiguously that it is athermal ω and not isothermal ω which forms during aging at temperatures <773 K. The observation both ω and α'' phases in the alloy cooled at 99 K min⁻¹, suggests that these transformations are competitive to each other.

It is reported [51] that addition of every wt% Ta and Nb reduces the M_s temperature of pure Ti (1128 K) by 4.5 and 10.5 K respectively. This empirical calculation of M_s temperature corresponding to the composition of retained β phase showed a decrease from 986 to 921K with increase in cooling rate from 20-99 K min⁻¹. This is in agreement with literature, where it is reported [52] that at cooling rates lower than the critical cooling rate, M_s temperature decreases with increase in cooling rate. Thus the M_s temperature is sensitive to composition of β phase and cooling rate. Low solute enrichment and low cooling rates of 20-75 K min⁻¹ has promoted only diffusional α precipitation, despite the high M_s temperatures. However, a high solute enrichment and high cooling rate of 99 K min⁻¹ has resulted in formation of a orthorhombic martensite within the β lamellae as reported in β rich Ti alloys [46].

5.11 Conclusions

- i. An accurate determination of the temperature dependence of the enthalpy increment for Ti -5 mass% Ta – 1.8 mass% Nb has been made in the temperature range from 463 to 1457 K using inverse drop calorimetry. The measured data are subjected to standard analytical treatment to obtain specific heat values for α and β phases.
- ii. The drop calorimetry study clearly attested to the occurrence of the $\alpha \rightarrow \beta$ phase transformation in the temperature range from 1072 K to 1156 K. This temperature interval for the $\alpha \rightarrow \beta$ phase transformation has also been confirmed by microstructural studies.
- iii. The $\alpha \rightarrow \beta$ phase transformation kinetics is assumed to follow the KJMA description of a diffusion-limited reaction. The apparent activation energy for the overall phase change is estimated to be $295 \text{ kJ}\cdot\text{mol}^{-1}$.
- iv. The latent heat associated with the phase transformation or the transformation enthalpy is estimated to be $76 \text{ J}\cdot\text{g}^{-1}$. The corresponding change in specific heat $\Delta^\circ C_p$ is estimated as $904 \text{ J}\cdot\text{kg}^{-1}\cdot\text{K}^{-1}$.
- v. The measured specific heat values for the α phase are reasonably approximated by the Neumann-Kopp rule.
- vi. The on-heating and cooling phase transformation has been investigated as a function of heating and cooling rate varying between $3\text{-}99 \text{ K min}^{-1}$ for Ti-5 mass% Ta-1.8 mass % Nb using differential scanning calorimetry.
- vii. The $\alpha \leftrightarrow \beta$ transformation temperatures exhibited a non-linear variation with heating and cooling rate.
- viii. The kinetics of $\alpha \rightarrow \beta$ and $\beta \rightarrow \alpha$ phase transformation is described by non-isothermal version of KJMA model. The effective activation energy for $\alpha \rightarrow \beta$

phase transformation is found to be 280-300 kJ mol⁻¹ which is suggestive of bulk diffusion of the solutes in the matrix and for $\beta \rightarrow \alpha$ phase transformation varies between 80-110 kJ mol⁻¹ which suggests that grain boundary diffusion govern the transformation.

- ix. CHT and CCT diagram are generated for Ti-5 mass% Ta-1.8 mass% Nb alloy.
- x. At all cooling rates, a lamellar $\alpha+\beta$ structure is observed suggesting that a diffusional $\beta \rightarrow \alpha$ transformation is primarily operative.
- xi. With increase in cooling rate, the microstructural parameters like size of GB α , α and β lamellae show a systematic reduction and the microhardness value shows an increasing trend. Also the volume fraction of metastable retained β is observed to decrease with increase in cooling rate.
- xii. The Ta and Nb content in retained β phase increases with cooling rate.
- xiii. A high cooling rate of 99 K min⁻¹ and higher solute enrichment of β phase at this cooling rate is found to promote secondary diffusionless transformation of β phase to a mixture of face centred orthorhombic and omega phases. However, the low solute enrichment of β phase at low cooling rates from 20 to 75 K min⁻¹ inhibits a diffusionless transformation of β phase resulting only in the precipitation of diffusional α phase.

References

- [1] K. Kapoor, V. Kain, T. Gopalkrishna, T. Sanyal and P. K. De, *J. Nucl. Mater.* 322 (2003) 36-44.
- [2] K. Kiuchi, H. Hayakawa, Y. Takagi and M. Kikuchi, *Proc. Fourth Int. Conf. Nuclear Fuel Reprocessing and Waste Management, RECOD '94*, Vol. III, London, April 24-28, 1994.
- [3] S. Malinov, P. Markovsky and W. Sha, *J Alloys Comp.* 333 (2002) 122-132.
- [4] C. Angelier, S. Bein and J. Bechet, *Metall. Mater. Trans. A* 28 (1997) 2467-2475.
- [5] S. Malinov, W. Sha and P. Markovsky, *J alloys Comp.* 348 (2003) 110-118.
- [6] S. Bein and J. Bechet, *J. Phys. IV* 6 (C1) (1996) 99 – 108.
- [7] S. Malinov, P. Markovsky, W. Sha and Z. Guo, *J Alloys Comp.* 314 (2001) 181-192.
- [8] T. Karthikeyan, R. Mythili, S. Saroja and M. Vijayalakshmi, *Metals Mater. Processes.* 18 (2006) 269-282.
- [9] S. Saroja, M. Vijayalakshmi and Baldev Raj, *Trans. Indian Inst. Metals.* 61 (2008) 389-398.
- [10] R. Mythili, S. Saroja, M. Vijayalakshmi and V.S. Raghunathan, *J. Nucl. Mater.* 345 (2005) 167 -183.
- [11] R. Mythili, A. Ravi Shankar, S. Saroja, V.R. Raju, M. Vijayalakshmi, R.K. Dayal, V.S. Raghunathan and R. Balasubramaniam, *J. Mater. Sci.* 42 (2007) 5924-5935.
- [12] R. Mythili, S. Saroja and M. Vijayalakshmi, *Mater. Sci. Engg. A.* 454-455 (2007) 43–51.
- [13] R. Mythili, V. Thomas Paul, S. Saroja, M. Vijayalakshmi and V. S. Raghunathan, *Mater. Sci. Engg. A.* 390 (2005) 299-312.
- [14] T. Karthikeyan, Arup Dasgupta, S. Saroja, R. Khatirkar, M. Vijayalakshmi and I. Samajdar, *Mater. Sci. Engg. A* 485 (2008) 581-588.
- [15] T. Karthikeyan, Arup Dasgupta, R. Khatirkar, S. Saroja, I. Samajdar and M. Vijayalakshmi, *Mater. Sci. Engg. A* 528 (2010) 549-558.
- [16] V. Anbarasan, B. Jeyaganesh, S. Raju, S. Murugesan, E. Mohandas, U. Kamachi Mudali and Geetha Manivasagam, *J. Alloys Comp.* 463 (2008) 160 – 167.
- [17] A. J. Prabha, S. Raju, B. Jeyaganesh, Arun Kumar Rai, Madhusmita Behera, M. Vijayalakshmi, G. Paneerselvam and I. Johnson, *Physica B* 406 (2011) 4200-4209

- [18] Madhusmita Behera, S. Raju, B. Jeyaganesh, R. Mythili and S. Saroja, *Int. J. Thermophys.* 31 (2010) 2246-2263.
- [19] S. Raju, B. Jeyaganesh, A. Banerjee and E. Mohandas, *Mater. Sci. Engg. A* 465 (2007) 29-37.
- [20] F. Liu, F. Sommer and E. J. Mittemeijer, *Int. Mater. Rev.* 52 (2007) 193-212.
- [21] M.J. Starink, *J. Mater. Sci.* 32 (1997) 6505 – 6512.
- [22] G. Ruteinberg, E. Woldt and A.K. Petford-Long, *Thermochim. Acta* 378 (2001) 97-105.
- [23] G. Grimvall, *Thermophysical Properties of Materials*, North-Holland, Amsterdam.oxford. New york .Tokyo, p.146
- [24] M.W. Chase, C.A. Davis, J. R. Downey, J. Frurip, McDonald RA and Syverud AN. JANAF Thermochemical Tables 3rd ed. *J. Phy. Chem. Ref. Data.* 14 (1985): p.1601, p.1811,p.1819, p.1820.
- [25] S. Malinov, Z. Guo, W. Sha and A. Wilson. *Metall. Mater. Trans. A* 32 (2001) 879-887.
- [26] F. Liu, C. Yang, G. Yang and Y. Zhou, *Acta mater.* 55 (2007) 5255-5267.
- [27] F. Liu, F. Sommer, and E.J. Mittemeijer, *J. Mater. Sci.* 39 (2004) 1621-1634.
- [28] F. Liu, F. Sommer, C. Bos and E.J. Mittemeijer, *Int. Mater. Rev.* 52 No. 4 (2007) 193-212.
- [29] S. Malinov, P. Markovsky, W. Sha and Z. Guo, *J Alloys Comp.* 314 (2001)181-192.
- [30] S.Malinov, W. Sha and P. Markovsky, *J alloys Comp.* 348 (2003) 110-118.
- [31] S. Malinov, Z. Guo, W. Sha and A. Wilson. *Metall Mater. Trans. A* 32 (2001) 879-887
- [32] S. Malinov, P. Markovsky and W. Sha, *J Alloys Comp.* 333 (2002) 122-132.
- [33] R. A. Perez, F. Dymont, G. Garcia Bermudez, D. Abriola and M. Behar, *Appl. Phys. A* 76 (2003) 247-250.
- [34] M. Koppers, C. Herzig, M. Friesel and Y. Mishin. *Acta Mater.* 45 (1997) 4181-4191.
- [35] F.J. Gil and J. A. Planell, *Scripta Metall. Mater.* 25 (1991) 2843-2848.
- [36] F.J. Gil and J. A. Planell, *Mater. Sci. Engg. A* 283 (2000) 17-24.
- [37] W. Gang, Z. De-chang and L. Zhong-wu, *Trans. Nonferrous Met. Soc. China* 22 (2012) 1711-1716
- [38] R. Ding, Z.X. Guo and A. Wilson, *Mater. Sci. Engg. A* 327 (2002) 233-245.

- [39] H. M. Flower, Mater. Sci. Techno. 6 (1990) 1082-1092.
- [40] J.C. Zhao and M.R. Notis, J. Phase Equilib. 14 (1993) 303-315.
- [41] L. Kaufman and M. Cohen, Trans. AIME 206 (1956) 1393-1401.
- [42] Li Na and W.H. Warnes, IEEE Trans. Appl. Superconductivity 11 No.1 (2001) 3800-3803.
- [43] D. Ansel, I. Thibon, M. Boliveau and J. Debuigne, Acta Mater. 46 No. 2 (1998) 423-430.
- [44] R. A. Perez, F. Dymont, G. Garcia Bermudez, D. Abriola and M.Behar, Applied Phys. A 76 (2003) 247-250.
- [45] A.V. Dobromyslov and V.A. Elkin, Mater. Sci. Engg. A 438-440 (2006) 324-326.
- [46] A.V. Dobromyslov, Mater. Sci. Forum 546-549 (2007) 1349-1354.
- [47] Madhusmita Behera, R. Mythili, S. Raju and S. Saroja, Accepted in J Alloys Comp.
- [48] S. A. Souza, R. B. Manicardi, P.L.Ferrandini, C.R.M. Afonso, A. J. Ramirez and R. Caram, J. Alloys Comp. 504 (2010) 330-340.
- [49] F. J. Gil, M.P.Ginbera, J.M. Manero and J.A. Planell, J. Alloys Compd. 329 (2001) 142-152.
- [50] B.S. Hickman, J Mater. Sci. 4 (1969) 554-563.
- [51] R. Mythili, V. Thomas Paul, S. Saroja, M. Vijayalakshmi and V.S. Raghunathan, Mater. Sci. Engg. A 390 (2005) 299-312.
- [52] E.W. Collings, *Applied Superconductivity, Metallurgy and Physics of Titanium Alloys*, Vol. 1, Plenum Press, NewYork and London, 1998, p 23.

Chapter – 6

Summary

&

Scope for future work

6.1 Summary of the work

This thesis has aimed at investigating the high temperature phase stability and phase transformation energetics and kinetics of Ti-Ta and Ti-Ta-Nb alloys. This study has been undertaken to provide the important thermo-kinetic data that are much relevant for a proper design of $\alpha+\beta$ Ti alloys for various applications in chemical and biomedical industries. For the present study the drop calorimetry and differential scanning calorimetry are used as major experimental tools which are supplemented by the metallographic characterization.

In the present study, an accurate measurement of enthalpy increment as a function of temperature has been made in the temperature range of 463-1257 K for Ti-xTa (x=5, 10, 15 & 20 mass %) alloys using inverse drop calorimetry. The results of this measurement showed the temperature range of α , $\alpha+\beta$ and β phase stability. The measured enthalpy increment has been subjected to a standard analytical expression to obtain the heat capacity as a function of temperature. The $\alpha\rightarrow\beta$ phase transformation temperature, $\alpha\rightarrow\beta$ phase transformation enthalpy and heat capacity have been obtained in the present study. The results of this study are supplemented by the metallography and hardness measurement, which revealed the implication of the transformation characteristics. A compilation of the thermodynamic properties of Ti-Ta alloys from 0-1257 K have been obtained by combining the high temperature experimental data with simulated one in the low temperature. The drop calorimetry results have been modeled using self consistent Debye model.

The kinetics of $\alpha\rightarrow\beta$ on heating and $\beta\rightarrow\alpha$ on cooling of Ti-xTa (x=5, 10, 15 & 20 mass %) alloys has been studied using differential scanning calorimetry. The $\alpha\leftrightarrow\beta$ phase transformation start and finish temperatures have been measured as a function of heating and cooling rate. This study has revealed the kinetic asymmetry with respect to

the heating or cooling induced $\alpha \leftrightarrow \beta$ phase transformation. In addition, the role of increasing Ta concentration in affecting the diffusional kinetics has been elucidated here. The calculated enthalpy of phase transformation $\Delta^\circ H_{tr}^{\alpha \rightarrow \beta}$ showed that the $\Delta^\circ H_{tr}^{\alpha \rightarrow \beta}$ value decreases with increase in Ta concentration. Also, the entropy ($\Delta^\circ S_{tr}^{\alpha \rightarrow \beta}$) for the $\alpha \rightarrow \beta$ phase change is calculated using an empirical relation.

The DSC processed kinetic data both for $\alpha \rightarrow \beta$ and $\beta \rightarrow \alpha$ transformation have been modeled using KJMA formalism. This modeling yields the values for the apparent activation energy (Q_{eff}) for the $\alpha \rightarrow \beta$ and $\beta \rightarrow \alpha$ transformation as a function of Ta concentration. The activation energy for the $\alpha \rightarrow \beta$ phase transformation is found to be more as compared to $\beta \rightarrow \alpha$ transformation. It is found that the apparent activation energy for the $\alpha \rightarrow \beta$ phase transformation exhibited an increasing trend with Ta concentration. The observed kinetic disparity between $\alpha \rightarrow \beta$ and $\beta \rightarrow \alpha$ transformation is attributed to the role of Ta diffusion during the transformation. In the present study, the continuous heating transformation and continuous cooling transformation diagram has also been generated for Ti-xTa (x=5, 10, 15 & 20 mass %) alloys.

The studies carried out for Ti-Ta alloys using calorimetry has helped in getting an insight into the transformation mechanism and kinetics in a Ti-Ta-Nb alloy of industrial importance, especially for the nuclear waste reprocessing applications. Besides, the calorimetric characterization, a systematic microstructural characterization has been carried out using conventional microscopy on samples cooled at different cooling rates in order to understand its effect on microstructure evolution and the microstructural parameters like grain boundary α , α and β lamella thickness, volume fraction of α and β phases etc. Transmission Electron Microscopy characterization of the transformation product has also been made to understand the mechanism of phase change with varying cooling rates. TEM study showed the effect of cooling rate on composition variation of

the constituent phases. TEM study also revealed the role of solute enrichment and cooling rate in evolution of different metastable products through competitive transformation mechanism.

6.2 Scope for future work

The present study involved predominately the work carried out using calorimetry as the major technique and limited microstructural characterization with hardness as the supplementary tools.

- i. The present calorimetric characterization of thermodynamics and kinetics of phase transformations in Ti-Ta alloys has been carried out for low concentration of Ta. Similar study can be made on Ta rich Ti-Ta alloys.
- ii. A detailed Transmission Electron Microscopy characterization of the transformation product as a function of different cooling rate in Ti-Ta binary alloys is necessary to obtain valuable insights into the mechanistic aspects of phase transformation. The orientation relationship developed between α and β phases can give information with respect to the strain energy concentration that is involved in the microstructure evolution.
- iii. It is also envisaged that the High temperature X-Ray Diffraction (HTXRD) characterization will add further input to the analysis of high temperature phase stability and phase transformation and thermophysical properties of Ti-Ta binary and Ti-Ta-Nb ternary alloys, which can be studied in future.
- iv. An extension of the present work can also include assessment of the experimentally obtained thermodynamic data using ThermoCalc methodology.

PUBLICATIONS

Ph. D. WORK:

a. Journal

1. **Madhusmita Behera**, S. Raju, B. Jeyaganesh, R. Mythili, and S. Saroja, “A study on thermal properties and α (hcp) \rightarrow β (bcc) phase transformation energetics in Ti - 5 mass% Ta - 1.8 mass% Nb Alloy using inverse drop calorimetry”, Int. J. Thermophys., 31 (2010) 2246-2263.
2. **Madhusmita Behera**, R. Mythili, S. Raju, and S. Saroja, “Effect of cooling rate on mechanism of $\beta \rightarrow \alpha$ phase transformation on continuous cooling in Ti-5Ta-1.8Nb alloy”, J. Alloys Compd., 553 (2013) 59-68.
3. **Madhusmita Behera**, S. Raju, Arun Kumar Rai, and S. Saroja, “Calorimetry investigation of phase stability and thermal property in Ti – 5 mass% Ta Alloy”, DOI 10.1007/s12666-013-0250-1
4. **Madhusmita Behera**, S. Raju, R. Mythili, and S. Saroja, “High Temperature Drop Calorimetry Measurements of Enthalpy Increment in Ti-x Ta (X = 5, 10, 15, 20 mass %) Alloys” accepted in J Phy. Chem. solids 2013.
5. **Madhusmita Behera**, S. Raju, R. Mythili, and S. Saroja, “Kinetics of $\alpha \leftrightarrow \beta$ phase transformation in Ti-x Ta (X = 5, 10, 15, 20 mass %) alloys, communicated to J. Alloys Compd 2013.
6. **Madhusmita Behera**, R. Mythili, S. Raju, and S. Saroja, Characterization of $\alpha \leftrightarrow \beta$ phase transformation kinetics in Ti – 5 mass% Ta – 1.8 mass% Nb using Differential Scanning Calorimetry”, to be communicated.

b. CONFERENCE PROCEEDINGS

1. **Madhusmita Behera**, B. Jeyaganesh, S. Raju, R. Mythili, Arun Kumar Rai and S. Saroja, “Drop calorimetry study on Ti – 5 wt% Ta – 1.8 wt% Nb alloy”, Proceedings of the 17th DAE - BRNS National Symposium on Thermal Analysis, (THERMANS 2010), 46-48.
2. **Madhusmita Behera**, S. Raju, B. Jeyaganesh, R. Mythili, and S. Saroja, “A differential scanning calorimetry study of α (hcp) \leftrightarrow β (bcc) phase transformation kinetics in Ti - 5 wt.% Ta alloy”, Proceedings of the International Symposium for Research Scholars, (ISRS- 2010), 243-246.

c. CONFERENCE PRESENTATIONS

1. **Madhusmita Behera**, B. Jeya Ganesh, R. Mythili, S. Raju and S. Saroja, “A study of $\alpha \leftrightarrow \beta$ phase transformation in Ti - 5 wt. % Ta - 1.8 wt. % Nb alloy using Differential Scanning Calorimetry”, presented in Structure and Thermodynamics

of Emerging Materials (STEM- 2009).

2. **Madhusmita Behera**, B. Jeya Ganesh, R. Mythili, S. Raju and S. Saroja, “Phase transformation kinetics in Ti - 4.4 wt. % Ta - 1.8 wt. % Nb alloy using differential scanning calorimetry”, presented in 63rd ATM, 16th – 17th November 2009, Science city, Kolkata.
3. **Madhusmita Behera**, R. Mythili, S. Raju and S. Saroja, “Study of $\beta \rightarrow \alpha$ Phase transformation on continuous cooling from the β phase field in a Ti-5%Ta-1.8%Nb alloy” presented in 3rd National Symposium for Material Research Scholars, (MR10), 7-8th May 2010, IIT Bombay, Mumbai.
4. **Madhusmita Behera**, S. Raju, B. Jeyaganesh, R. Mythili, and S. Saroja, “Thermal stability and thermal property studies on Ti-5Ta & Ti - 5Ta-1.8Nb (mass%) alloy”, presented in 19th European Conference on Thermophysical Properties (19 ECTP), 28th August – 1st September 2011, Thessaloniki, Greece.
5. **Madhusmita Behera**, S. Raju, Arun Kumar Rai and S. Saroja, “Calorimetric investigation of phase stability and thermal Property in Ti – 5 mass% Ta Alloy”, presented in International Symposium for Research Scholars, (ISRS-2012), 13th - 15th December 2012, IIT Madras, Chennai, Tamil Nadu.

Related Work:

Journal

1. A. Josephine Prabha, S. Raju, B. Jeyaganesh, Arun Kumar Rai, **Madhusmita Behera**, M. Vijayalakshmi, G. Paneer Selvam and I. Johnson, “Thermodynamics of $\alpha'' \rightarrow \beta$ phase transformation and heat capacity measurements in Ti – 15 at % Nb alloy”, Physica B, 406 (2011) 4200-4209.

CONFERENCE PROCEEDINGS

1. A. Josephine Prabha, S. Raju, B. Jeyaganesh, Arun Kumar Rai, **Madhusmita Behera**, M. Vijayalakshmi, and I. Johnson, “Drop Calorimetry characterization of a Ti-32.7 mass% Nb alloy having a significant amount of non-equilibrium β at room temperature”, Proceedings of the International Symposium for Research Scholars, (ISRS- 2010), 62-65.